Modifying the Electronic Properties and Magnetic Interactions of the Two-Dimensional Material Silicene

Tobias G. Gill
toby.gill.09@ucl.ac.uk

Submitted in partial fulfilment of the
requirements for the degree of
Doctor of Philosophy
at
University College London

SUPERVISORS

Cyrus F. Hirjibehedin
London Centre for
Nanotechnology
Department of Physics
Department of Chemistry
University College London
UK
c.hirjibehedin@ucl.ac.uk

Yukiko Yamada-Takamura
School of Materials Science
JAIST
Japan
yukikoyt@jasit.ac.jp

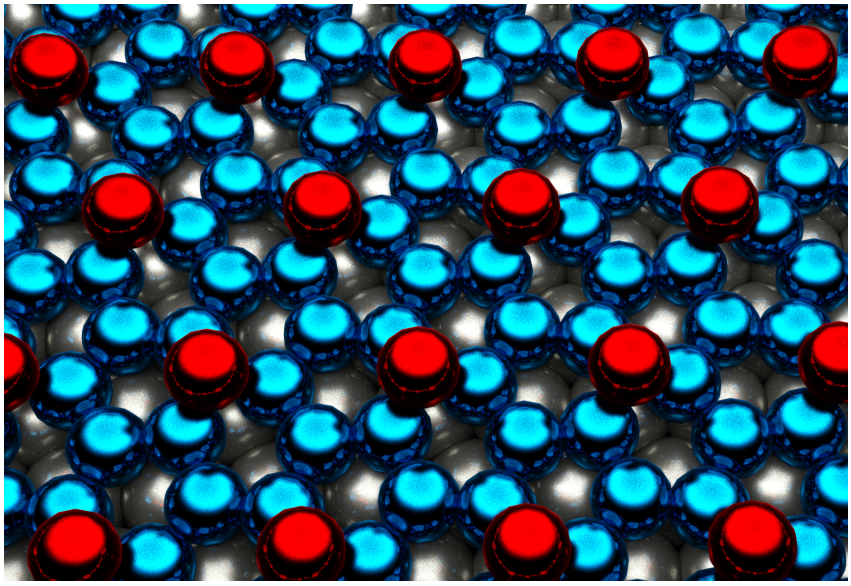

I, Tobias Gill confirm that the work presented in this thesis is my own. Where information has been derived from other sources, I confirm that this has been indicated in the thesis.

Abstract

As the pursuit for more powerful electronic devices progresses, individual components have had to be produced at ever smaller dimensions. Today, conventional technologies are at the edge of feasibility as they approach a fundamental limit at the atomic scale. Much research is aimed at overcoming the barrier to atomic scale devices, and indeed some of the explosion of interest into two-dimensional materials over the past decade has its roots in this goal. Graphene, the first atomically thin two-dimensional material, has since been followed by a growing number of intriguing materials with a wide variety of interesting properties, many of which may prove useful in technological devices. One of these two-dimensional materials is silicene, the silicon analogue to graphene that shares many of its properties. Moreover, owing to it being made of silicon, it may be more easily integrated into existing industrial processes.

In this thesis, silicene grown upon conductive zirconium diboride is investigated by scanning tunnelling microscopy and spectroscopy. It is found that the structural and electronic properties of epitaxial silicene can be fine-tuned by depositing small amounts of silicon on its surface. However, with continued silicon deposition a significant change is observed: the additional silicon leads to the formation of a layered metallic silicon nanostructure that could be utilised as an atomically precise metallic contact to silicene. Beyond this, the magnetic interactions of individual cobalt atoms on the silicene surface are investigated and it is found that the combination of the semiconducting silicene surface with the metallic zirconium surface yields an unusual spatially distributed Kondo effect. When cobalt atoms are in close proximity to one another on the silicene surface, they exhibit an incredibly strong indirect exchange (RKKY) interaction even at significant separations above 1 nm. The results in this thesis highlight the rich array of phenomena that can manifest in two-dimensional materials and point towards potential future developments for atomic scale electronic and spintronic devices.

Acknowlegements

Just over four years ago I returned from the European synchrotron radiation facility in Grenoble having experienced my first true taste of scientific research. I would describe it as tiring. It was then that Cyrus offered me the first of many opportunities that would ultimately lead me to this point. I don't know if it was the sleep deprivation that made me accept, but for this and your guidance over the years I owe you a great deal.

One of the many great opportunities I have had, has been to collaborate with Yukiko and Antoine at JAIST. I would like to thank both JAIST, and the UCL Department of Chemistry, Molecular Modelling and Materials (M3S) CDT for funding; in particular Zhimei for all your help. Yukiko and Antoine, thank you for all your support, both in our work and in making sure I was well taken care of in Japan.

That I can just about operate an STM is in no small part due to the team here at the LCN. Foremost, Ben and Henning without you two I would be far worse at this all than I am. Steven, Holly, Asif, Manuel, Neil, Philipp, Tingbing, Kitiphat, Taylor, Alex, Reyes, Jenny, Fadi, and Roland thank you all for making the STM community so enjoyable over the years. Phil thank you for patiently tolerating my inane questioning.

To my family, I would like to thank you all (there's so many of you!). Dad, thank you for your faith in me. Mum, thank you for always being the voice of reason in my ear. Graham, thank you for always being calm even when I was not. Bridie, Sam, and Miranda, I can always rely on you to bring me back down to the ground when my head gets too big. Jemima, Ollie, Bea, and Tilly, thank you for providing a wonderful sanctuary. Amy, Jack, and Kate, thank you for the drunken texts and calls asking me to explain science to people in random pubs (okay this was mostly Jack), but thank you all for always being interested and listening to my boring replies. Kate and Dylan, thank you for taking good care of the old man.

To my friends Matt, Hazel, Emily, Geoff, Toria, Alex, Sophie, Adam, Rob, Imogen, Mimi, Belle, Eammon, Ezster, Joe, Abi, Will, Alex, Isobel, Dana, Craig, Dave, and Sal, when science has been gray I've always been able to turn to any one you for a smile, thank you.

Lastly the most important and most difficult to fully express. I would not have made it here if it were not for Abi. Thank you for your endless support and patience when I could not even be on the same continent as you. When I was on the same continent, thank you for always welcoming me with a smile as I returned home late from the lab. Thank you for all the laughter, all the tears, and everything in between.

Contents

1 Introduction **6**

2 Scanning Tunnelling Microscopy **10**

2.1 Introduction 10

2.2 Tunnelling Theory 11

2.2.1 Bardeen Tunnelling Model 11

2.2.2 Tersoff-Hamann 18

2.3 Scanning Tunnelling Spectroscopy 20

2.3.1 Lock-in Amplifier Measurements 21

2.4 STM Measurements 22

2.4.1 Constant Current Topography 22

2.4.2 Constant Height Topography 23

2.4.3 Spatially Resolved Spectroscopy 23

2.5 Inelastic Tunnelling 25

2.6 Experimental Systems 28

2.6.1 Omicron VT-STM 28

2.6.2 Omicron Cryogenic STM 29

3 Silicene Surfaces **31**

3.1 Free-standing Silicene 31

3.1.1 Graphene Band Structure 31

3.1.2 Silicene Band Structure 37

3.2 Silicene on Ag(111) 40

3.2.1 (3×3) Reconstruction 40

3.2.2 $(\sqrt{3} \times \sqrt{3})$R30^o Reconstruction 42

3.3 Silicene on ZrB_2 Thin Films 45

3.4 Other Epitaxial Silicene Systems 50

3.4.1 Silicene on Ir(111) 50

3.4.2 Silicene on ZrC 51

3.4.3 Silicene on Bulk ZrB_2 52

3.5 Multi-Layer Silicene on Ag(111) 53

4 Magnetic Interactions **57**
4.1 Exchange Interaction . . . 57
4.2 Zeeman Effect . . . 59
4.3 Magnetic Anisotropy . . . 60
4.4 The Kondo Effect . . . 61
4.4.1 Electron Scattering . . . 61
4.4.2 The Anderson $S = \frac{1}{2}$ Impurity Model . . . 74
4.4.3 Single Atom Kondo . . . 79
4.5 Indirect Exchange Interaction . . . 84

5 Single Domain Silicene on ZrB_2 **86**
5.1 Experimental Systems . . . 87
5.2 Silicene Sample Preparation . . . 87
5.2.1 Ultra-High Vacuum Preparation . . . 88
5.2.2 Silicon Deposition . . . 89
5.3 Removal of Domain Boundaries on Si Deposition . . . 91
5.4 Preservation of Atomic Structure . . . 92
5.5 Conclusion . . . 94

6 Enhanced Conductivity in Layered Silicon Nanostructures Grown on Silicene/ZrB_2 **95**
6.1 Layered Silicon Nanostructure . . . 97
6.2 Electronic Properties of Layered Silicon Nanostructure . . . 101
6.3 Conclusion . . . 103
6.4 Future Work . . . 103

7 Single Cobalt Atoms on Silicene/ZrB_2 **107**
7.1 Co atom binding site . . . 109
7.2 Electronic Structure of Co atoms on Silicene/ZrB_2 . . . 111
7.3 Rotation of Silicene Domain Boundaries . . . 115
7.4 Reversible switching of Co atoms on silicene/ZrB_2 . . . 117
7.5 Conclusion . . . 118

8 Spatially Distributed Kondo Effect of Single Cobalt Atoms on Silicene 119
8.1 Magnetic Field Dependence . . . 124
8.2 Temperature Dependence . . . 127
8.3 Individual Co Atoms on Silicene/ZrB_2: A possible p-wave Kondo Effect . 128
8.4 Cobalt Atom Kondo Lobe Asymmetry . . . 129
8.5 Domain Boundary Modification of Kondo Temperature . . . 134
8.6 Influence of Co Atom Switching on Kondo Effect . . . 140
8.7 Conclusion . . . 141

8.8 Future Work 142

9 Parity Symmetry Breaking in the Two-Impurity Anderson Model 143

9.1 Cobalt Dimers on the 2D material Silicene/ZrB_2 145
9.2 Spectroscopic Measurements of Cobalt Dimers 152
9.3 Anisotropic RKKY interaction of Co Dimers 154
9.4 Parity Breaking in the Antiferromagnetic Regime 157
9.5 Conclusion 162
9.6 Future Work 163

10 Conclusion 165

Chapter 1

Introduction

From a technological view point, the modern era has been defined by miniaturisation in information storage and information processing. An excellent example of such trends can be seen for the case of the transistor. In 1947, Bardeen, Brattain, and Schockley developed the world's first transistor at Bell Labs (**Fig. 1.1a**) [1]. Their breakthrough, for which they were later awarded the Nobel prize in physics for, was to use a semiconductor crystal to reliably control the flow of electricity across a junction. Unlike contemporary counterparts, such as valves, the transistor allowed for rapid miniaturisation: cutting the block of semiconductor in half allows for two smaller transistors to be made. Nearly 70 years of scientific and engineering developments have followed until today, when individual groups of transistors can be constructed at the nanoscale. **Figure 1.1b** shows a scanning electron micrograph of a transistor cluster in Intel's latest i7 processors [2]. As a result, the entire processor (**Fig. 1.1c**),which is approximately the same size as the original transistor itself, now contains billions of individual transistors [2, 3].

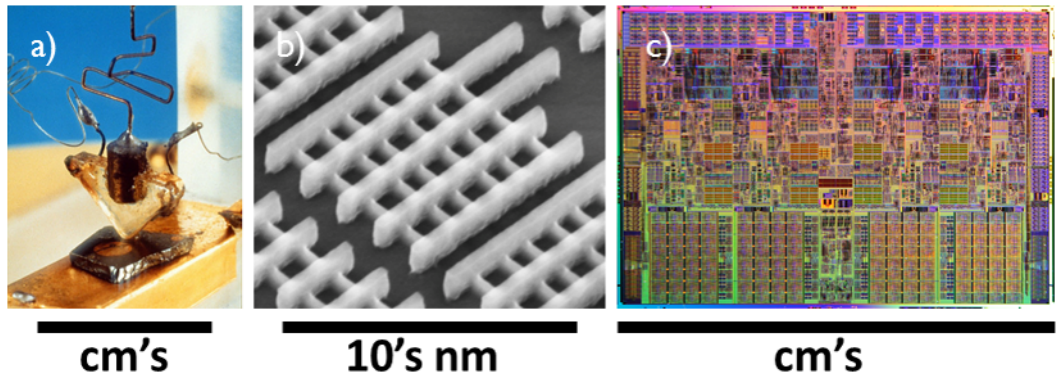

Figure 1.1: Miniaturisation of the transistor.
(a) Picture of the first transistor constructed at Bell Labs in 1947 from a Germanium crystal and gold foil. [2] (b) Scanning electron microscope image of a modern transistor array in Intel's latest i7 processor. (c) Picture of a modern Intel i7 processor, which is the same size as the original transistor, but contains billions of transistors. [2, 3]

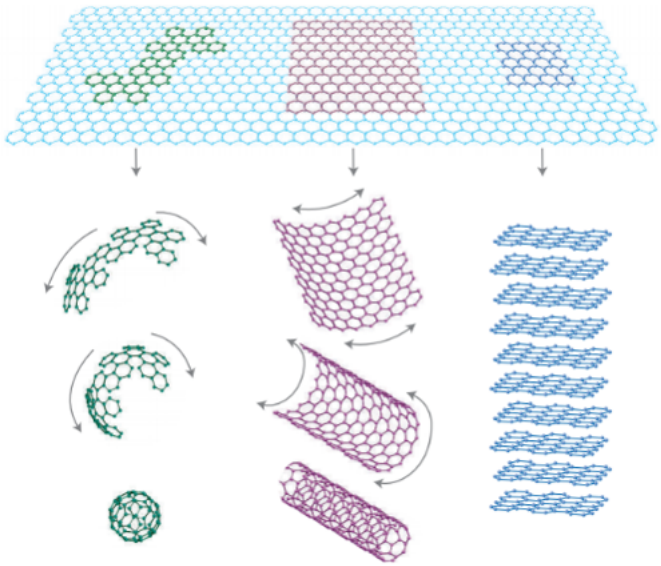

Figure 1.2: Model of graphene lattice forming the basis of all sp^2 hybridised carbon allotropes.[4]

However, continued miniaturisation has reached a problem at the nanscale, namely that the fundamental limit of atomic scaled devices is fast approaching. As material dimensions reach the nanoscale, quantum phenomena that manifest at these dimensions become more prominent and begin to interfere with the operation of traditional device designs [5].

It is therefore necessary to investigate new device paradigms and architectures that make use of these quantum phenomena to allow for continued progress. One avenue of particular interest is research into atomically thin two-dimensional (2D) materials. The past decade of research into atomically thin 2D materials originates from the initial work of Geim and Novoselov, who discovered the 2D allotrope of carbon, graphene [6]. Graphene is a single atomic layer of carbon, where the atoms form a honeycomb lattice. Novoselov and Geim later received the Nobel prize in physics for their discovery of this revolutionary material that exhibits extraordinary mechanical and electronic properties [4, 7]. Since the discovery of graphene, a great many new and intriguing atomically thin 2D materials have been discovered, and predicted. These range from molybdenum disulphide, that has interesting electro-optic properties [8, 9], to phosphorene, a 2D allotrope of phosphorus that may have a highly tunable band gap [10].

One 2D material of particular interest is silicene, the newly discovered silicon allotrope that is a 2D honeycomb of silicon atoms, and as such is analogous to graphene [11, 12]. Perhaps the most distinctive property of graphene is the behaviour of charge carriers around the Fermi energy as *"massless"* Dirac fermions [7]. It is this, previously unique, electronic structure that results in the manifestation of exciting properties in graphene, such as ballistic transport, and the anomalous quantum Hall effect [7]. Unlike graphene, silicene is predicted to exist in a buckled structure, where the two triangular sub-lattices

are offset to one another due to the preference of silicon to sp^3 hybridise - as is the case in bulk 'diamond-like' silicon - over the sp^2 configuration required for planar honeycomb structures. However, despite this fundamental difference in the structures of silicene and graphene, silicene is predicted to exhibit the electronic properties of its carbon namesake, but with the added benefit of being comprised of silicon, the material of choice within the information technology industry [13].

This thesis explores how the structural, electronic, and magnetic properties of silicene can be studied and tuned by the sub-monolayer and monolayer addition of metallic and semiconducting material. The primary tool used to investigate these systems is scanning tunnelling microscopy (STM). Therefore, Chapter 2 provides an introduction to the physics behind the STM and the experimental procedures used to acquire information on structural, electronic, and magnetic properties at the atomic scale.

Initially silicene was discoverd on Ag (111) by Vogt *et. al* [11], but has since been produced on a number of substrates [12, 14–16]. The predicted buckling of free-standing silicene is found to be influenced by interactions with the surface, resulting in substrate specific reconstruction that alter its electronic properties. An overview of theoretical and experimentally realised silicene systems is provided in Chapter 3. Particular focus is given to silicene formed on the $ZrB_2(0001)$ surface, as this is the substrate of choice in this thesis.

One of the main aims of this thesis is to probe and modify the magnetic properties of silicene on ZrB_2. Chapter 4 provides an overview of the magnetic phenomena that will be required to interpret the results presented later in the thesis. Detailed focus is given to the Kondo effect, a phenomenon that will feature heavily in the work presented.

Chapter 5 is the first of the experimental chapters, where it is shown that the electronic and structural properties of silicene on $ZrB_2(0001)$ are robust to the incorporation of additional Si atoms into the atomic lattice, though the additional Si also removes the striped domain boundaries unique to this form of silicene. In contrast, Chapter 6 shows that continued Si deposition onto the silicene/ZrB_2 surface leads to a significant change in both the structural and electronic properties of the silicene. Most strikingly, the semiconducting silicene transitions to a metallic silicon nanostructure.

A route to inducing novel magnetic behaviour into two dimensional materials, such as graphene, has been to deposit magnetic metal atoms on to the surface [17, 18]. However, the chemically inert properties of graphene have required significant modification of the surface to induce highly correlated effects [19]. In contrast the greater reactivity of silicene, owing to its mixed sp^2-sp^3 hybridisation, may provide an alternative substrate to combine desirable magnetic properties with the unique electronic properties of atomically thin 2D materials. In Chapter 7 it is shown that individual Co atoms can be deposited onto silicene/ZrB_2 at low temperatures without causing a reconstruction of the surface. The Co atoms are found to significantly hybridise with the silicene substrate, which

is used to probe the structural properties of silicene and confirm previously predicted models. It is also found that the Co atoms can be switched between a bi-stable binding configuration.

The magnetic properties of Co atoms on the silicene/ZrB_2 surface are investigated in Chapter 8 and Chapter 9. Traditionally the exchange scattering processes that give rise to the Kondo effect for individual magnetic adsorbates are considered to be s-wave like and isotropic [20]. For Co atoms on the silicene/ZrB_2 surface an unusual spatially distributed Kondo effect is found that may result from higher angular momentum, p- or d-wave like scattering. Finally, a highly anisotropic indirect exchange (RKKY) interaction is found between pairs of Co atoms in close proximity to one another, similar to when they are placed on simple metallic surfaces [21–29]. Unlike in these other systems the strength of the interaction is significantly increased, indicating significant contribution to the interaction from the 2D states of the silicene/ZrB_2 surface. In addition a substantial asymmetry is observed in antiferromagnetically coupled Co dimers that breaks the parity symmetry of the two impurity Anderson model. The magnetic properties of Co atoms on silicene/ZrB_2 could allow for large magnetic structures to be constructed that also introduce new degrees of freedom through parity dependent coupling.

A conclusion of the thesis is provided in Chapter 10. Also given is a perspective to future work, including the potential to deposit other semiconducting materials, magnetic atoms, and molecules.

Chapter 2

Scanning Tunnelling Microscopy

2.1 Introduction

The scanning tunnelling microscope (STM) allows for the structural, electronic, and magnetic properties of individual atoms and molecules to be probed. The STM, developed by Binnig and Rohrer at IBM – for which they later received a Nobel prize in 1986 [30] – is a deceptively simple tool. The STM makes use of the fact that at sufficiently small separations, sub-nanometer, the probability of electrons to quantum mechanically tunnelling across a vacuum barrier between two metals is significant enough to measure a current. Figure 2.1 shows a model of the STM, where an atomically sharp metallic tip is placed within a few angstroms of a conductive surface. With a voltage, V applied between the tip and sample a tunnel current, I can be measured. A real space image of a surface can then be constructed by scanning the tip across the surface and recording the tunnel current as a function of position. In this chapter we will address the key phenomena and theoretical models that underpin how the STM is able to probe structural, electronic and magnetic properties at the atomic scale.

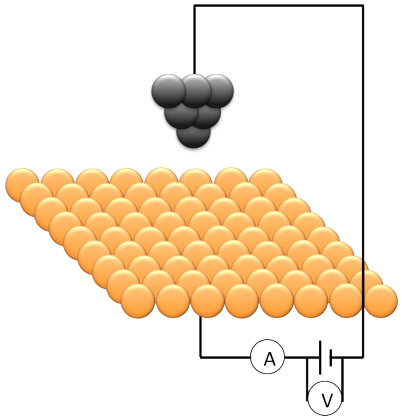

Figure 2.1: Model of a STM.
An atomically sharp metallic tip is placed within a few atomic distances of a conductive substrate with a bias voltage, V, applied across the junction. A tunnelling current can then be measured from the electrons that quantum mechanically tunnel between the tip and surface.

2.2 Tunnelling Theory

In classical mechanics a particle with kinetic energy, E_{kin} is completely confined within a potential well of energy, V_{pot} if $E_{kin} < V_{pot}$. There is a zero probability of finding the particle outside of the potential well. However, when the same problem is considered quantum mechanically it becomes apparent that despite the particle having less energy than is required to escape the potential well, it is still possible to find the particle out-side of the confining space. The physics of this phenomena, that lies at the heart of how an STM works, is captured by a simple one-dimensional (1D) tunnelling model.

2.2.1 Bardeen Tunnelling Model

Here a brief description of the Bardeen tunnelling model, as applied to STM, is given; for a more detailed derivation see the work of Gottleib and Wesoloski [31]. Within Bardeen's model the tunnelling current is considered to manifest from the cumulative effect of many independent scattering events that transfer electrons from one side of the barrier to the other. Knowledge of the electronic states of the two electrodes allows for one to derive a formula for the tunnel current that is equal to the net rate of electron transfer, multiplied by the electron charge e.
To apply the Bardeen tunnelling model to STM we need to make a small number of approximations. Two approximations from perturbation theory are that:

- tunnelling is weak enough to be described by a first-order approximation;
- electronic states in the tip and sample are approximately orthogonal.

Additionally Bardeen made the approximations that:

- electron-electron interactions can be ignored;
- occupation distributions in the tip and sample are unaffected by tunnelling;
- both the tip and sample are in electrochemical equilibrium.

Under the approximation that electron-electron interactions can be neglected, single-electron Hamiltonians can be used to describe states in the tip and sample independently. These sample and tip Hamiltonians have the form,

$$\mathbf{H}_s\psi = -\frac{\hbar^2}{2m}\nabla\psi(\mathbf{r}) + V_s(\mathbf{r})\psi(\mathbf{r}) \tag{2.1}$$

and

$$\mathbf{H}_t\phi = -\frac{\hbar^2}{2m}\nabla\phi(\mathbf{r}) + V_t(\mathbf{r})\phi(\mathbf{r}), \tag{2.2}$$

respectively, where ∇ is the gradient function, $V_s(\mathbf{r})$ and $V_t(\mathbf{r})$ are the potentials of the sample and tip. To describe the simple form of these potentials the space of the STM

is split into three regions: the sample, the barrier, and the tip. The sample potential $V_s(\mathbf{r}) = V(\mathbf{r})$ in the sample and barrier region, and is equal to zero in the tip region. The opposite is then true for the tip potential $V_s(\mathbf{r})$.

To begin, consider an electron that at time $t = 0$ is in a sample state ψ. The state then evolves as a state $\psi(t)$, where in an independent system the evolution would be determined by **eqn. 2.1** such that $\mathbf{H}_s\psi = E_s\psi$ and therefore $\psi(t) = e^{-itE_s/\hbar}\psi$. For the *real* combined system, under the approximation that tunnelling is a weak perturbation for small enough t, the time evolution of $\psi(t)$ can be approximated by,

$$\psi(t) = e^{-itE_s/\hbar}\psi \; + \; \sum_k a_k(t)\phi_k, \tag{2.3}$$

where

$$a_k(t) = \langle \phi_k | \psi(t) \; - \; e^{-itE_s/\hbar}\psi \rangle, \tag{2.4}$$

such that the sum in **eqn. 2.3** is the projection of $\psi(t) - e^{-itE_s/\hbar}\psi$ onto the space of the tip bound states. The tip bound states are defined by **eqn. 2.2** with $\mathbf{H}_t\phi_k \; = \; E_k\phi_k$. At this point a further approximation has been introduced, since the states of the tip do not actually span the entirety of the space.

It is now the goal of the model to approximate the coefficients $a_k(t)$, which will define the tunnelling probability. The initial coefficient $a_k(0)$ can trivially be determined from **eqn. 2.4**.

$$\begin{aligned} a_k(0) \; &= \; \langle \phi_k | \psi(0) \; - \; e^{-i(0)E_s/\hbar}\psi \rangle \\ a_k(0) \; &= \; \langle \phi_k | \psi \; - \; e^0\psi \rangle \\ a_k(0) \; &= \; 0. \end{aligned} \tag{2.5}$$

To learn about the other a_k coefficients the time-dependent Schrödinger equation of the STM system can be evaluated in two ways. First **eqn. 2.3** is substituted into the time-dependent Schrödinger equation to get,

$$\begin{aligned} i\hbar\frac{\partial}{\partial t}\psi(\mathbf{r},t) \; &= \; \mathbf{H}\psi(\mathbf{r},t) \\ &= \; \mathbf{H}(e^{-itE_s/\hbar}\psi) \; + \; \sum_k a_k(t)\mathbf{H}\phi_k \\ &= \; e^{-itE_s/\hbar}(\mathbf{H}_s \; + \; (\mathbf{H} \; - \; \mathbf{H}_s))\psi \; + \; \sum_k a_k(t)(\mathbf{H}_t \; + \; (\mathbf{H} \; - \; \mathbf{H}_t))\phi_k \\ &= \; e^{-itE_s/\hbar}(E_s\psi \; + \; (\mathbf{H} \; - \; \mathbf{H}_s)\psi) \; + \; \sum_k a_k(t)(E_k\phi_k \; + \; (\mathbf{H} \; - \; \mathbf{H}_t)\phi_k). \end{aligned} \tag{2.6}$$

The second approach takes the time derivative of **eqn. 2.3** leading to,

$$\begin{aligned}\frac{\partial}{\partial t}\psi(t) &= \frac{\partial}{\partial t}e^{-itE_s/\hbar}\psi \;+\; \sum_k \frac{\partial}{\partial t}a_k(t)\phi_k \\ &= \frac{-iE_s}{\hbar}e^{-itE_s/\hbar}\psi \;+\; \sum_k \frac{\partial}{\partial t}a_k(t)\phi_k \\ i\hbar\frac{\partial}{\partial t}\psi(t) &= E_s e^{-itE_s/\hbar}\psi \;+\; i\hbar\sum_k \frac{\partial}{\partial t}a_k(t)\phi_k.\end{aligned} \tag{2.7}$$

Combining **eqn. 2.6** and **eqn. 2.7** gives,

$$\begin{aligned}&E_s e^{-itE_s/\hbar}\psi \;+\; i\hbar\sum_k \frac{\partial}{\partial t}a_k(t)\phi_k \\ &\qquad = e^{-itE_s/\hbar}(E_s\psi \;+\; (\mathbf{H} \;-\; \mathbf{H}_s)\psi) \;+\; \sum_k a_k(t)(E_k\phi_k \;+\; (\mathbf{H} \;-\; \mathbf{H}_t)\phi_k) \\ i\hbar\sum_k \frac{d}{dt}a_k(t)\phi_k &= e^{-itE_s/\hbar}(\mathbf{H}-\mathbf{H}_s)\psi \;+\; \sum_k a_k(t)(E_k\phi_k \;+\; (\mathbf{H} \;-\; \mathbf{H}_t)\phi_k).\end{aligned} \tag{2.8}$$

Now taking the inner product on both sides with ϕ_j gives,

$$\begin{aligned}i\hbar\sum_k \frac{d}{dt}\langle\phi_j|a_k(t)|\phi_k\rangle &= e^{-itE_s/\hbar}\langle\phi_j|\mathbf{H} \;-\; \mathbf{H}_s|\psi\rangle \\ &\qquad + \;\sum_k (\langle\phi_j|a_k(t)E_k|\phi_k\rangle \;+\; a_k(t)\langle\phi_j|\mathbf{H} \;-\; \mathbf{H}_t|\phi_k\rangle) \\ i\hbar\frac{d}{dt}a_j(t) &= e^{-itE_s/\hbar}\langle\phi_j|\mathbf{H} \;-\; \mathbf{H}_s|\psi\rangle \;+\; a_j(t)E_j \\ &\qquad + \;\sum_k a_k(t)\langle\phi_j|\mathbf{H} \;-\; \mathbf{H}_t|\phi_k\rangle.\end{aligned} \tag{2.9}$$

The equation above is insolvable due to the final summation. However, the Bardeen model approximates that tunnelling is a weak perturbation and therefore assumes that $a_k(t)$'s that are zero at $t = 0$ remain very small for small values of t. Within these assumptions the final sum in **eqn. 2.9** can be neglected. Indeed it would also be reasonable to neglect the second term $a_j(t)E_j$, but this is not required to make the equation solvable and so it is kept to improve the accuracy of the model. **Equation 2.9** therefore simplifies to,

$$i\hbar\frac{d}{dt}a_j(t) \;=\; e^{-itE_s/\hbar}\langle\phi_j|\mathbf{H} \;-\; \mathbf{H}_s|\psi\rangle \;+\; a_j(t)E_j. \tag{2.10}$$

Since $a_j(0) = 0$, the solution to the above differential equation becomes,

$$a_j(t) \;=\; \frac{e^{-itE_s/\hbar} \;-\; e^{-itE_j/\hbar}}{E_s \;-\; E_j}\langle\phi_j|\mathbf{H} \;-\; \mathbf{H}_s|\psi\rangle. \tag{2.11}$$

Therefore $|a_j(t)|^2$ can be expressed as,

$$\begin{aligned} |a_j(t)|^2 &= \left(\frac{e^{-itE_s/\hbar} - e^{-itE_j/\hbar}}{E_s - E_j}\right)\left(\frac{e^{-itE_s/\hbar} - e^{-itE_j/\hbar}}{E_s - E_j}\right)|\langle\phi_j|\mathbf{H} - \mathbf{H}_s|\psi\rangle|^2 \\ &= \frac{e^0 - e^{(E_j - E_s)\frac{it}{\hbar}} - e^{(E_s - E_j)\frac{it}{\hbar}} + e^0}{(E_s - E_j)^2}|\langle\phi_j|\mathbf{H} - \mathbf{H}_s|\psi\rangle|^2 \\ &= \frac{2 - e^{(E_j - E_s)\frac{it}{\hbar}} - e^{-(E_j - E_s)\frac{it}{\hbar}}}{(E_s - E_j)^2}|\langle\phi_j|\mathbf{H} - \mathbf{H}_s|\psi\rangle|^2, \end{aligned} \tag{2.12}$$

and since,

$$\begin{aligned} \sin^2(x/2) &= \frac{e^{ix/2} - e^{-ix/2}}{2i}\cdot\frac{e^{ix/2} - e^{-ix/2}}{2i} \\ &= \frac{e^{ix} + e^{-ix} - e^0 - e^0}{4i^2} \\ 4\sin^2(x/2) &= 2 - e^{ix} - e^{-ix}, \end{aligned} \tag{2.13}$$

$|a_j(t)|^2$ becomes,

$$|a_j(t)|^2 = \frac{4\sin^2\left(\frac{(E_j - E_s)t}{2\hbar}\right)}{(E_j - E_s)^2}\cdot|\langle\phi_j|\mathbf{H} - \mathbf{H}_s|\psi\rangle|^2 \tag{2.14}$$

Now that the form of $|a_j(t)|^2$ is known it is possible to relate this to the transition probabilities $|\langle\phi_j|\psi(t)\rangle|^2$. Starting from **eqn. 2.3** $\langle\phi_j|\psi(t)\rangle$ is given by,

$$\begin{aligned} \langle\phi_j|\psi(t)\rangle &= \langle\phi_j|e^{itE_s/\hbar}|\psi\rangle + \sum_k\langle\phi_j|a_k(t)|\phi_k\rangle \\ &= \langle\phi_j|\psi\rangle e^{-itE_s/\hbar} + a_j(t)\ . \end{aligned} \tag{2.15}$$

Here the approximation that sample and tip states are nearly orthogonal is used to assume that $\langle\phi_j|\psi\rangle$ is small compared to $a_j(t)$. Then the most significant contribution to the transition probability $|\langle\phi_j|\psi(t)\rangle|^2$ is given by $|a_j(t)|^2$, where the rate of electrons, initially in the sample, scattering into a tip state is approximated by,

$$\frac{d}{dt}\sum_j|a_j(t)|^2 = \frac{d}{dt}4\sum_k\frac{\sin^2\left(\frac{(E_j - E_s)t}{2\hbar}\right)}{(E_j - E_s)^2}\cdot|\langle\phi_j|\mathbf{H} - \mathbf{H}_s|\psi\rangle|^2 \tag{2.16}$$

Fermi's Golden Rule, and the Origin of Elastic Tunnelling

The above description of the scattering rate (**eqn. 2.16**) describes the transfer of electrons, initially in the sample, into the tip; owing to the symmetry of the tunnelling

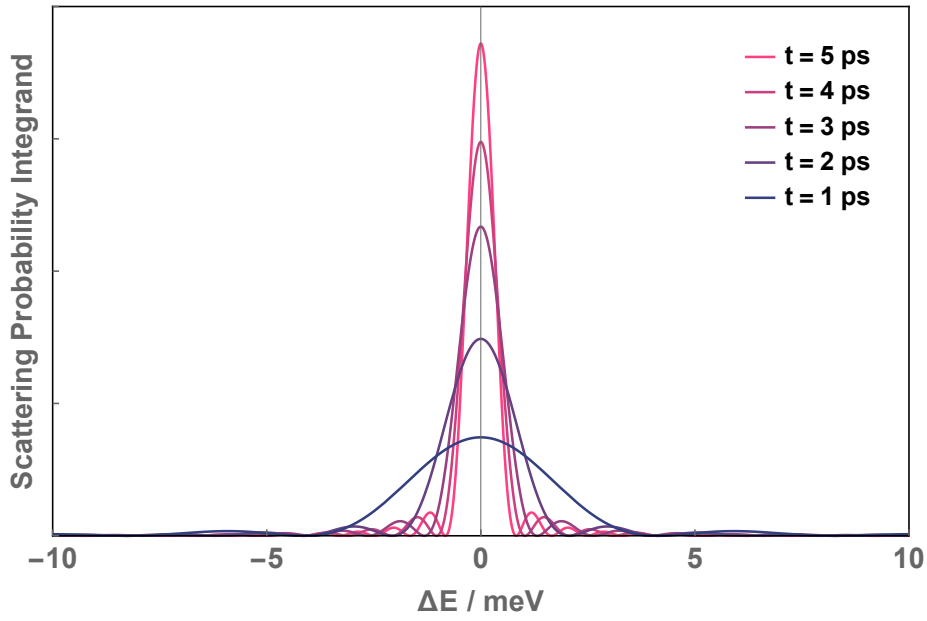

Figure 2.2: Origin of elastic-tunnelling condition.
Shown here are plots of the integrand in **eqn. 2.19** for different values of time t. As t approaches infinity the integrand approaches a delta function centred upon $(E_j - E_s) = 0$. Thus provided the lifetime of the tunnelling process is on the order of a few pico seconds an elastic tunnelling condition is enforced.

barrier it is also valid for the opposite process. Additionally, the derivation so far accounts for electrons scattering into isolated tip states, yet in reality the tip electronic states exist in a continuum.

The sum in **eqn. 2.16** can be re-written as.

$$\sum_k P_t(E_k - E_s) M^2(\phi_k, \psi), \tag{2.17}$$

where,

$$\begin{aligned} M^2(\phi_k, \psi) &= |\langle \phi_k | \mathbf{H} - \mathbf{H}_s | \psi \rangle|^2 \\ P_t(x) &= \frac{\sin^2(xt/2\hbar)}{x^2}. \end{aligned} \tag{2.18}$$

$P_t(x)$ is non-negative and

$$\int P_t(x) dx = \frac{\pi t}{2\hbar}, \tag{2.19}$$

with the most significant contribution to the integral coming from the $-2h/t < x < 2h/t$ interval. It is here that the elastic nature of the tunnelling phenomena can be seen. **Figure 2.2** shows plots of $P_t(x)$ for different values of t. One can see that the function is a maximum for zero change in energy between the initial and final states. Moreover as the time scale is increased the function sharpens around zero such that elastic tunnelling is required for time scales on the order of pico-seconds. With sufficiently large enough

values of t the energy interval $-2h/t < x < 2h/t$ becomes so narrow that the tip energy levels E_k appear to be distributed with a constant density, such that a *density of states* (DOS), $\rho_t(E_s)$ can be defined. N_{E_s} then denotes the number of tip energy states within the energy interval $-2h/t + E_s < x < 2h/t + E_s$. Setting,

$$M^2(\psi) = \frac{1}{N_{E_s}} \sum_{k:|E_k - E_s| < \frac{2h}{t}} M^2(\phi_k, \psi), \tag{2.20}$$

such that $M^2(\psi)$ effectively represents the average value of $M^2(\phi_k, \psi)$ over the energy interval of $-2h/t + E_s < x < 2h/t + E_s$. **Equation. 2.17** can then be approximated using Fermi's Golden Rule by,

$$\begin{aligned}
\sum_k P_t(E_k - E_s) M^2(\phi_k, \psi) &\approx \sum_{k:|E_k - E_s| < \frac{2h}{t}} P_t(E_k - E_s) M^2(\phi_k, \psi) \\
&\approx M^2(\psi) \sum_{k:|E_k - E_s| < \frac{2h}{t}} P_t(E_k - E_s) \\
&\approx M^2(\psi)\rho_t(E_s) \int_{-2h/t}^{2h/t} P_t(E) dE \\
&\approx M^2(\psi)\rho_t(E_s) \int_{-\infty}^{\infty} P_t(E) dE \\
&= M^2(\psi)\rho_t(E_s) \frac{\pi t}{2\hbar}
\end{aligned} \tag{2.21}$$

Now substituting this approximation for the sum back into **eqn. 2.16** gives,

$$\begin{aligned}
\frac{d}{dt} \sum_j |a_j(t)|^2 &\approx \frac{d}{dt} 4 \left(\frac{\pi t}{2\hbar} \rho_t(E_s) M^2(\psi) \right) \\
&= \frac{2\pi}{\hbar} \rho_t(E_s) M^2(\psi)
\end{aligned} \tag{2.22}$$

The above equation describes the total rate of electrons in a sample state ψ scattering into tip states of comparable energy, or equally the reverse process. However, this is assuming that every electron in an initial state has an available final state to scatter into. Pauli exclusion tells us that each state can be occupied by a single electron and therefore knowledge of the tip and sample state occupation distributions must be accounted for. Under the assumption that the occupation distributions of the tip and sample are unaffected by tunnelling it is reasonable to describe the system with Fermi-Dirac distributions of the form,

$$f_{E_F}(x) = \frac{1}{e^{(x - E_F)/k_B T} + 1}, \tag{2.23}$$

where E_F is the Fermi level, T is temperature, and k_B is the Boltzman constant. The

sample-tip and tip-sample electron scattering rates are therefore given by,

$$\frac{2\pi}{\hbar}\left[f_{E_F^s}(E_s)\left(1 - f_{E_F^t}(E_t)\right)\right]\rho_t(E_s)M^2(\psi) \tag{2.24}$$

and

$$\frac{2\pi}{\hbar}\left[\left(1 - f_{E_F^s}(E_s)\right)f_{E_F^t}(E_t)\right]\rho_t(E_s)M^2(\psi) \tag{2.25}$$

respectively, where the rates have been multiplied by the probabilities of there being an occupied initial state and unoccupied final state. Finally a tunnel current can be defined by taking the difference between tip-sample and sample-tip scattering rates, summing over all sample states ψ_n, and multiplying by the fundamental charge constant e to give,

$$I = \frac{4\pi e}{\hbar}\sum_n[(1 - f_{E_F^s}(E_n)f_{E_F^t}(E_n)) - f_{E_F^s}(E_n)(1 - f_{E_F^t}(E_n))]\rho_t(E_s)M^2(\psi) \tag{2.26}$$

which simplifies to,

$$I = \frac{4\pi e}{\hbar}\sum_n\left[f_{E_F^t}(E_n) - f_{E_F^s}(E_n)\right]\rho_t(E_n)M^2(\psi_n) \tag{2.27}$$

where the additional factor of 2 comes from the fact that each state can accommodate a spin-up and spin-down electron. Again assuming that the tunnelling matrix element $M^2(\psi)$ does not significantly depend upon energy then the sum in **eqn. 2.27** can be approximated using Fermi's Golden Rule to give,

$$I = \frac{4\pi e}{\hbar}\int_{-\infty}^{\infty}\left[f_{E_F^t}(E) - f_{E_F^s}(E)\right]\rho_s(E)\rho_t(E)M^2dE, \tag{2.28}$$

where $\rho_s(E)$ is the sample density of states, and M^2 is the average value of $M(\psi)$ over all sample states E_n in the infinitesimal energy range dE (similar to $M^2(\psi)$ in **eqn. 2.20**). **Equation 2.28** therefore describes how the tunnelling current is due to the transfer of electrons from filled states one side of the junction to empty states on the other. The sign - or direction - of the tunnel current is then dependent on the difference in tip and sample Fermi levels. If an STM tip was brought into tunnelling contact with a metallic surface as described simply by **eqn. 2.28** electron transfer would occur until the two electrodes reached equilibrium, i.e. the difference between their electronic distributions was zero. In practicality a bias V is applied across the junction such that the tunnel current is given by,

$$I = \frac{4\pi e}{\hbar}\int_{-\infty}^{\infty}\left[f_{E_F^t}(E - eV) - f_{E_F^s}(E)\right]\rho_s(E)\rho_t(E - eV)M^2dE. \tag{2.29}$$

Tunnelling Current at Low Temperature

At zero temperature the Fermi-Dirac distributions of the tip and sample reduce to Heavyside step functions where,

$$f_{E_F}(x) = \begin{cases} 1 & \text{if } x < E_F \\ 0 & \text{if } E_F < x \end{cases} \quad \text{for } T = 0. \tag{2.30}$$

Therefore the tunnel current is given by,

$$I \;=\; \frac{4\pi e}{\hbar} \int_{E_F^{min}}^{E_F^{max}} \rho_s(E)\rho_t(E - eV)M^2 dE \tag{2.31}$$

where $E_F^{min} = min\{E_F^s, E_F^t\}$ and $E_F^{max} = max\{E_F^s, E_F^t\}$. Provided that $k_B T$ is smaller than the desired energy resolution of the experiment **eqn. 2.31** is still a valid approximation for for finite T.

2.2.2 Tersoff-Hamann

To go beyond the formalism of Bardeen, outlined above, it is required to take into account the geometry of the STM tip. In general the specific geometry of the tip will be unknown in a given experiment, however, the Tersoff-Hamann approximation considers the tip as a s-like wave function centred at the tip apex $\overrightarrow{r}^T$ [32, 33]. It can then be stated that the tunnelling current is proportional to the applied bias, tip density of states, and the sample density of states at the position of the tip.

$$I(V) \propto V\, \rho^T(\varepsilon)\, \rho^S(\varepsilon, \overrightarrow{r}^T) \tag{2.32}$$

For STM measurements performed at higher biases, the above approximation of a constant energy-independent transfer matrix is not valid. A simplified model for approximating the energy-dependant tunnelling matrix, replaces the tunnelling matrix, $|M|^2$ with a tunnelling probability, $T(\varepsilon, eV, z)$ [34]. At T = 0 K the current is then given by the integral of the tunnelling probability over all possible energies.

$$I(V, x, y) = \frac{4\pi e}{\hbar} \int_0^{eV} d\varepsilon \rho^S(E_F^S + \varepsilon)\rho^T(E_F^T - eV + \varepsilon)T(\varepsilon, eV, z), \tag{2.33}$$

where the Wentzel-Kramers-Brillouin approximation is utilised to calculate the transmission probability assuming a trapezoid shape of the tunnelling barrier.

$$T(\varepsilon, eV, z) \propto exp\left(-\frac{2z\sqrt{2m_e}}{\hbar}\sqrt{\frac{\Phi^T + \Phi^S}{2} + \frac{eV}{2} - \varepsilon}\right) \tag{2.34}$$

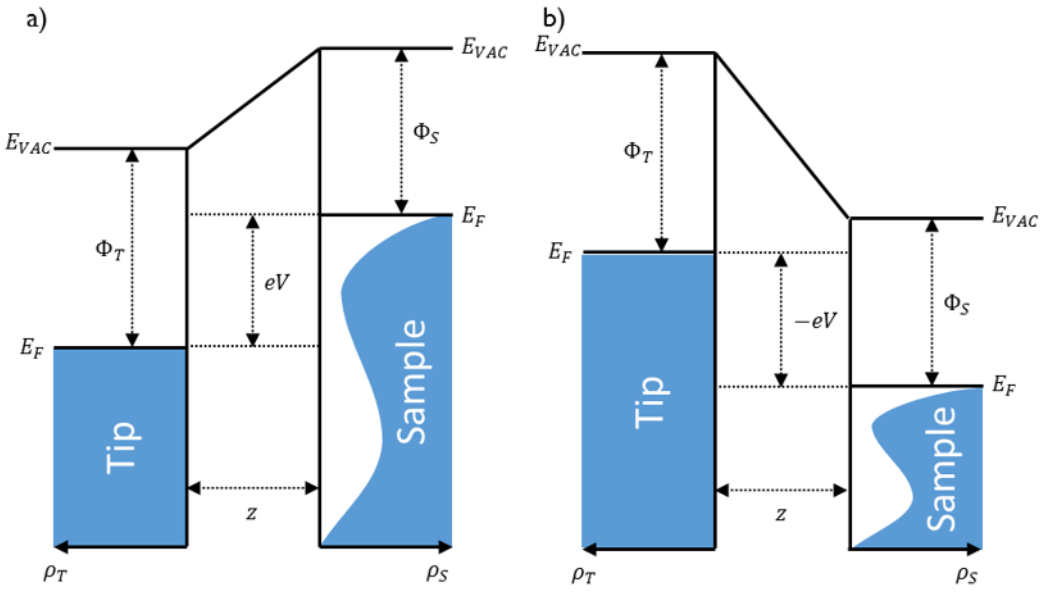

Figure 2.3: Model of an STM tunnelling junction at $T = 0$ K.
Tip and sample density of states ρ_T and ρ_S are are denoted by the blue regions, the shapes are chosen to signify the assumption that ρ_T is featureless. The vacuum level E_{VAC}, i.e. the energy required to ionise an electronc from the tip and sample lies Φ_T and Φ_S above the Fermi levels E_F of the tip and sample. A positive voltage V is applied between the tip and sample, where the effect on a) positive and b) negative charges is shown.

Here the tunnelling barrier is defined by the tip and sample work functions, Φ^T, and Φ^S, and the tip-sample separation, z. The effect of the applied bias, V and electron energy, ε on the barrier height are also included. A diagrammatic model of the STM tunnelling junction under these approximations is shown in **Fig. 2.3**.

At finite temperatures the tunnelling current is given by,

$$I(V,x,y) = \frac{4\pi e}{\hbar}\int_0^{eV} d\varepsilon\ [f_T(\varepsilon - eV) - f_S(\varepsilon)]\,\rho_S(\varepsilon)\rho_T(\varepsilon - eV)T(\varepsilon, eV, z) \qquad (2.35)$$

where the Fermi-Dirac functions effectively act to smear the Fermi seas of the tip and sample around the Fermi level.

2.3 Scanning Tunnelling Spectroscopy

Scanning tunnelling spectroscopy (STS) is one of the most important and powerful features of an STM. The high spatial and energy resolution of the STM allows for the LDOS of a surface to be probed at well defined positions and energies. The LDOS can be approximated from the derivative of the tunnelling current, with respect to the applied bias. This derivative can be expressed from **eqn. 2.35**, using Leibnitz's rule.

$$\begin{aligned}\frac{\partial}{\partial V}I(x,y,V) \propto \int_0^{eV} & f_T(\varepsilon - eV)\rho_S(\varepsilon)\rho_T(\varepsilon - eV)\frac{\partial}{\partial V}T(\varepsilon,V,z) \\ & + f_T(\varepsilon - eV)\rho_S(\varepsilon)\left(\frac{\partial}{\partial V}\rho_T(\varepsilon - eV)\right)T(\varepsilon,V,z) \\ & + \left(\frac{\partial}{\partial V}f_T(\varepsilon - eV)\right)\rho_S(\varepsilon)\rho_T(\varepsilon - eV)T(\varepsilon,V,z) \\ & - f_S(\varepsilon)\rho_S(\varepsilon)\rho_T(\varepsilon - eV)\left(\frac{\partial}{\partial V}T(\varepsilon,V,z)\right) \\ & - f_S(\varepsilon)\rho_S(\varepsilon)\left(\frac{\partial}{\partial V}\rho_T(\varepsilon - eV)\right)T(\varepsilon,V,z)\,d\varepsilon\end{aligned} \tag{2.36}$$

The above equation can be simplified if it is assumed that the LDOS of the tip and the transmission probability are both constant, such that their derivatives are zero, a valid approximation for small energy values ($\varepsilon \ll \Phi^T \, and \, \Phi^S$). **Equation. 2.36** therefore becomes

$$\frac{dI}{dV}(V,x,y) \propto \int_0^{eV}\left(\frac{\partial}{\partial V}f_T(\varepsilon - eV)\right)\rho^S(x,y,\varepsilon)\,d\varepsilon \tag{2.37}$$

As $T \to 0$ the Fermi-Dirac function derivative becomes a delta function. As a result at low temperatures the derivative of the tunnelling current becomes,

$$\frac{dI}{dV}(V,x,y) \propto \rho_S(\varepsilon - eV) \tag{2.38}$$

Practically this measurement can be achieved in a number of ways. The most obvious and easily implemented is to perform I(V) spectra at a given point on the surface. This is done by placing the tip above a surface feature of interest at a height defined by the set point current, and voltage, I_0 and V_0. The feedback loop is then deactivated and the tunnelling current is recorded, whilst the bias is swept from its start to final value. This I(V) curve can then be numerically differentiated to give the dI/dV curve, that is proportional to the LDOS. However, even after averaging of repeated I(V) curves the signal to noise ratio of numerical differentiated data can be high. As such, a lock-

in technique can be used to directly measure the derivative of the tunnelling current providing a direct measurement of the LDOS.

2.3.1 Lock-in Amplifier Measurements

The lock-in amplifier can be used to perform high signal-to-noise ratio spectroscopic measurements, by isolating the tunnelling current derivative at a low noise frequency environment [35]. This is achieved with application of a small sinusoidal voltage with an amplitude, V_m and frequency, ω_m, to the direct current bias, V_{DC}. Thus the tunnel junction bias is given by,

$$V_T = V_{DC} + V_m sin(\omega_m t). \tag{2.39}$$

Assuming the Tersoff-Hamann approximation (see *equation 2.32*), the tunnelling current is given by,

$$I \propto \int_0^{e(V_{DC}+V_m sin(\omega_m t))} \rho^S(\varepsilon) d\varepsilon \tag{2.40}$$

Eqn. 2.40 can be expanded in a Taylor series around the point $t = 0$ yielding

$$I(t) \propto \sum_{n=0}^{\infty} \frac{(V_m)^n}{n!} I^n(V) sin^n(\omega_m t), \tag{2.41}$$

where $I^n(V)$ is the n-th derivative of the tunnelling current, I at the voltage, V. The algebraic identity for the sine function is applied to directly obtain the Fourier series of the tunnelling current.

$$\begin{aligned} I(t) &\propto \sum_{n=0}^{\infty} \frac{(V_m)^n}{n!} I^n(V) \sum_{k=0}^{n} \frac{1}{2^n} \binom{n}{k} cos\left[(n-2k)\left(\omega_m t - \frac{\pi}{2}\right)\right] \\ &= \sum_{n=0}^{\infty} A_n sin(n\omega_m t + \phi_n) \end{aligned} \tag{2.42}$$

In general only the low harmonics of the Fourier series will have a non-negligible amplitude, A_n. In fact it is the direct current part of the series, A_0 that commonly has the highest amplitude with contributions from the alternating current harmonic, A_1. For a nearly linear $I(V)$ curve it is an accurate approximation to assume all higher harmonics are comparatively small.

The amplitude of the alternating current modulation frequency, A_1 is explicitly given, up to the fifth order by,

$$A_1 = V_m I^{(1)}(V) + \frac{1}{8} V_m^3 I^{(3)}(V) + \frac{1}{96} V_m^5 I^{(5)}(V) + ... \tag{2.43}$$

It is therefore seen that the first term of the alternating current modulation, A_1 is

proportional to the first derivative of the tunnelling current and thus the LDOS of the sample. This first derivative can be calculated from the normalised integral of the alternating tunnelling current, over the time, $\tau \gg 2\pi\omega_m^{-1}$ and multiplied by a reference signal, $sin(\omega_m t + \phi)$.

$$\frac{dI}{dV}(V) = \frac{2}{V_m \tau} \int_0^\tau sin(\omega_m t + \phi) I(t) dt \tag{2.44}$$

Practically, owing to capacitances in the STM junction and electronics the reference signal must be phase shifted, such that only the resistive tunnelling current is measured. The phase shift required to minimise the capacitive current, conventionally, is determined by retracting the tip such that only the capacitive current is detected and then adjusting the phase so that the integral above vanishes. However, in the Omicron STM systems (see **section 2.6**) the modulation voltage is applied to the tip, through the pre-amplifier. The pre-amplifier contains a complex capacitive compensation circuitry that this technique is impractical. Consequentially the both the capacitive and resistive current channels are recorded (they are approximately 90^o phase shifted to one another) and the phase shift is adjusted to minimise the capacitive contribution.

The strength of the lock-in technique for measuring dI/dV spectra comes from the ability to shift the derivative measurement from zero frequency - as is the case for numerical differentiation of an I(V) curve - towards the modulation frequency f_m. This modulation frequency can be chosen such that it is decoupled from experimental noise sources, including mechanical and electronic interferences. Whilst this is the case for the idealised model, even for finite measurements times, τ the addition of components from higher and lower frequencies is still relatively low. It is therefore still able to provide better signal to noise ratios, compared to numerical differentiation.

2.4 STM Measurements

2.4.1 Constant Current Topography

Conventionally STM imaging is performed in what is called *constant current mode*, where a constant tunnelling current is achieved during scanning by utilisation of a feedback loop that controls the tip-sample separation. From the Bardeen tunnelling model (see **subsection 2.2.1**) it is known that the tunnelling current is dependant on not only the tip-sample separation, but also the density of states in both the tip and sample. Consequentially the images recorded are typically a convolution of topographic and electronic effects.

2.4.2 Constant Height Topography

An alternative topographic measurement is to maintain the tip height at a constant value as it is scanned across the surface. Upon an atomically flat region of a sample the contrast provided by the STM would then only be dependent on changes in the LDOS. However, without the use of a feedback loop, significant changes in the sample topography could catastrophically cause the tip to crash into the sample. This measurement technique is therefore only used in special situations.

2.4.3 Spatially Resolved Spectroscopy

In **section 2.3** it has been shown how the STM can be used to perform spectroscopic measurements in order to gain insight into the electronic properties of the STM junction. An additional strength of the STM is that the spatial variation in spectroscopic features can be explored. There are two techniques for acquiring comprehensive spatially resolved spectroscopic measurements referred to here as dI/dV maps and dI/dV slices [1]. The differences between these techniques are qualitatively similar to those between constant height and constant current topographic measurements. Details of the two are given below.

dI/dV Maps

A dI/dV map is a logical progression upon conventional STS measurements, in which a STS spectrum is recorded at sub-set of pixels in an STM image. Just like in a conventional STS measurement the set point current and voltage are set, then the feedback loop is disengaged and the current is recorded as a function of applied bias. In doing so a high energy resolution map of the entire area can be produced. However, since at typical STS curve can take on the order of 1 minute to acquire these measurements can take a substantial period of time. For example a map with 64×64 spatial pixels and a single spectrum acquisition time of 10 seconds would take over 11 hours. These long acquisition time become prone to drift from thermal gradients. A dI/dV map therefore can be used to give high energy resolution, but relatively low spatial resolution.

dI/dV Slices

An alternative approach to obtaining spatially resolved spectroscopic measurements is to perform a dI/dV slice. In these measurements the STM is operated as though a standard topographic measurement is being performed, i.e. a constant current is maintained by altering the tip height above the surface. However, in addition to the

[1] There is little consensus in the literature as to the name of these measurements. So it is noted that they may be referred to in a number of different ways

direct current voltage the an alternating voltage is added to the junction such that a lock-in measurement of the differential conductance is made simultaneously (see **subsection 2.3.1**. Unlike in a standard spectroscopic measurement the dI/dV signal is only acquired for the set point voltage (broadened by the modulation). Therefore a dI/dV slice provides a comparitavely rapid high spatial resolution image at a single energy.

2.5 Inelastic Tunnelling

So far the elastic tunnelling of electrons across the STM junction has been considered. However, it is possible for inelastic tunnelling processes to occur, in which energy is lost via an excitation process. Examples of these mechanisms include phonon,[36, 37] spin, [38–46] and rotational [47, 48] excitations . In **Fig. 2.4a** a model of an STM junction is shown, where an applied bias V_T separates the tip and sample Fermi levels E_F by an energy eV_T. As has been previously discussed electrons will elastically tunnel across the junction; this process is denoted by the horizontal line in **Fig. 2.4a**. Should eV_T be greater than the excitation energy Δ, then an additional tunnelling pathway becomes possible in which tunnelling electrons lose an energy Δ during the process as denoted by the lower set of lines in **Fig. 2.4a**. The inelastic processes alter the tunnelling junction often adding an alternative tunnelling route so that the rate of electron transfer across the junction is increased. In this case the total current will be equal to the sum of the elastic and inelastic components.

In **subsection 2.2.1** it was shown that the sample-tip and tip-sample tunnelling rates are given by **eqn. 2.24** and **eqn. 2.25** respectively. Similarly the inelastic rates W can be defined as,

$$\begin{aligned} W_{s\to t} &= \frac{4\pi}{\hbar}\int_{-\infty}^{\infty} dE_t \int_{-\infty}^{\infty} dE_s \left[f_{E_F^s}(E_s)\left(1 - f_{E_F^t}(E_t)\right)\right] \\ &\qquad \times \rho_s(E_s)\rho_t(E_t)M^2(\psi)\delta(E_s - E_t + eV - \Delta) \\ &= \frac{4\pi}{\hbar}\int_{-\infty}^{\infty} dE \left[f_{E_F^s}(E)\left(1 - f_{E_F^t}(E + eV - \Delta)\right)\right] \rho_s(E)\rho_t(E + eV - \Delta)M^2 \end{aligned} \tag{2.45}$$

and

$$\begin{aligned} W_{t\to s} &= \frac{4\pi}{\hbar}\int_{-\infty}^{\infty} dE_t \int_{-\infty}^{\infty} dE_s \left[\left(1 - f_{E_F^s}(E_s)\right) f_{E_F^t}(E_t)\right] \\ &\qquad \times \rho_s(E_s)\rho_t(E_t)M^2(\psi)\delta(E_t - E_s + eV + \Delta) \\ &= \frac{4\pi}{\hbar}\int_{-\infty}^{\infty} dE \left[\left(1 - f_{E_F^s}(E + eV + \Delta)\right) f_{E_F^t}(E)\right] \rho_s(E + eV + \Delta)\rho_t(E)M^2 \end{aligned} \tag{2.46}$$

where the addition of the delta functions enforces the inelastic process. By taking the difference of **eqn. 2.46** and **eqn. 2.45**, multiplying by e and integrating over all states

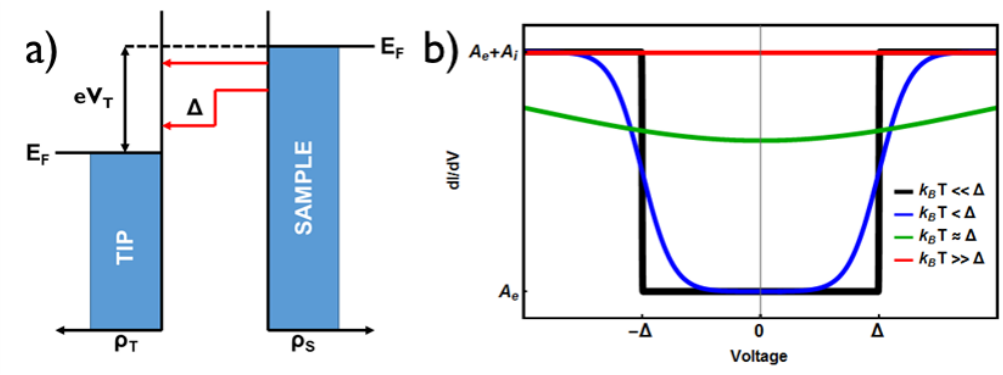

Figure 2.4: Model of inelastic tunnelling in an STM junction.
(a) Model of an STM junction, where the tip and sample Fermi levels E_F, are separated by the bias voltage V, ρ_T, and ρ_S are the tip and sample DOS respectively. The elastic tunnelling pathway is signified by the topmost horizontal arrow, where the energy of the initial and final states are equivalent. The inelastic tunnelling is denoted by the lower horizontal lines, where energy Δ is lost to an excitation resulting in the final state being at a lower energy. (b) Model dI/dV curves of an inelastic tunnelling feature for different temperature, excitation energy ratios.

the total inelastic tunnelling current is then given by,

$$I_i = \frac{4\pi}{\hbar}\int_{-\infty}^{\infty} dE\, M^2 \Big(\Big[\big(1 - f_{E_F^s}(E+eV+\Delta)\big)\, f_{E_F^t}(E)\rho_s(E+eV+\Delta)\rho_t(E)\Big] - \Big[f_{E_F^s}(E)\Big(1 - f_{E_F^t}(E+eV-\Delta)\Big)\rho_s(E)\rho_t(E+eV-\Delta)\Big]\Big) \tag{2.47}$$

The total tunnelling current is then given by the addition of the elastic (**eqn. 2.29**) and inelastic (**eqn. 2.47**) currents. It can then be shown that the derivative of the tunnel current, with respect to voltage, is given by [49, 50],

$$\frac{\partial I}{\partial V} = A_e + A_i\left[F\left(\frac{eV+\Delta}{k_BT}\right) + F\left(\frac{eV-\Delta}{k_BT}\right)\right], \tag{2.48}$$

where

$$F(x) = \frac{1+(x-1)e^x}{(e^x-1)^2} \tag{2.49}$$

A_e is a constant that represents the elastic contribution to the conductance, and similarly A_i gives the inelastic contribution. In **Fig. 2.4b** a model showing the influence of inelastic tunnelling on differential conductance measurements is shown for different temperature regimes. When $k_BT << \Delta$ (black) and $V < \Delta$ the conductance is solely comprised of the elastic component A_e. However, once the voltage is increased to $V \geqslant \Delta$ the inelastic tunnelling pathway becomes accessible and a jump in the conductance occurs to $A_e + A_i$. These steps in the dI/dV signal are observed symmetrically around the Fermi level at $V = \pm\Delta$. As the temperature is increased (blue) the Fermi seas of the tip and sample smear broadening the inelastic steps. From the second derivative of

the tunnelling current it can be shown that the intrinsic width of the inelastic steps is given by $\Gamma = 5.2\, k_B T$ [49, 50]. Increasing the temperature further to $k_B T \approx \Delta$ (green) causes the steps to become quite indistinguishable, until eventually for $k_B T >> \Delta$ (red) the conductance is flat at $A_e + A_i$.

2.6 Experimental Systems

In this section the experimental STM systems, located at the London Centre for Nanotechnology (LCN), that have been used to produce the data for this thesis are described. Both STM systems were produced by Omicron Nanotechnology (now Scienta Omicron). The first is the Omicron variable temperature scanning tunnelling microscope (VT-STM) and the second is the Omicron Cryogenic STM. Both systems operate in ultra high vacuum (UHV), with base pressures in the range of 1×10^{-9} to 1×10^{-11} mbar.

Figure 2.5: Picture of the Cyrogenic STM at the London Centre for Nanotechnology.

2.6.1 Omicron VT-STM

The VT-STM is a two chamber system, with a fast entry load lock that can be independently vented and pumped to maintain the main system UHV. The preparation chamber contains standard surface preparation tools such as Ar sputter guns, radiative filament heating, and direct current heating, where an electrical current is passed through the sample . In addition there is as a high flux Si evaporator. The evaporator houses an entire intrinsic Si wafer as a source, using direct current heating to sublimate Si atoms. A close-by radiative filament is used to pre-heat the wafer to a temperature at which it will conduct. The second chamber of the VT-STM system holds the microscope. As the name suggests the VT-STM can be operated at a range of temperatures from room temperature up to $1500\,\mathrm{K}$, via direct current heating of the sample. To stabilise the STM head an eddy current damping stage is employed, where metal teeth feed between permanent magnets around that edge of the stage.

2.6.2 Omicron Cryogenic STM

The Cryogenic STM, shown in **Fig. 2.5** is a pumped ^{4}He system with a base temperature of 1.8 K. It has superconducting magnets that allow for magnetic fields of up to 6 T perpendicular to the sample, or a vectored field with up to 2 T perpendicular and 1 T parallel to the sample. The vectored magnetic field is achieved by a solenoid magnet for the perpendicular field and two split coil magnets in x and y. The magnets are housed at the centre of a triple walled vacuum chamber in a large cryostat that holds 135 L of liquid helium. A vacuum space separates the helium and liquid nitrogen (LN_2) cryostats and a furher vacuum space before the external wall of the system. A capillary feeds from the bottom of the LHe cryostat to the 1 K pot that is thermally coupled to the STM head. The STM head sits in a warm bore that allows for the STM to be operated in over a temperature range of 1.8 to 400 K whilst independently maintaining the magnets below their superconducting transition. The downside of this arrangement is that the Omicron Cryogenic STM has a high liquid helium consumption on the order of 1 L/hour. The external magnetic field precludes the possibility of using a similar eddy current damping stage like in the VT-STM. Consequentially, the Cryogenic STM is often operated with at least 1 T in-plane or perpendicular to the sample to induce eddy current dampening. In addition to the standard surface preparation tools detailed in **subsection 2.6.1** the cryogenic STM has two metal evaporators, and a molecular evaporator. One metal evaporator is located in the preparation chamber and allows for depositions onto room temperature, or heated samples. The second is mounted onto the STM chamber itself and can be aligned directly towards the STM head allowing for metal atoms to be deposited onto surfaces below 30 K. The molecule evaporator is located in the load-lock that can be independently baked to reach clean UHV conditions and allows for sublimation of molecules onto room temperature samples.

Spectroscopic Resolution

The spectroscopic resolution of an STS measurement can be limited by a number of factors that include temperature broadening, lock-in modulation voltage, and the effective tunnelling electron temperature.

The thermodynamic base temperature of an experimental system will set a fundamental limit on the resolution of a measurement based upon Fermi-Dirac statistics. A standard operating temperature of the Omicron Cryogenic STM is around 3 K, which approximately corresponds to an energy of 0.3 meV. As such provided that the other sources of broadening in a given experiment are less this they can be considered negligible.

Application of a modulation voltage on top of the direct current voltage, when performing lock-in spectroscopic measurements induces a broadening, or smearing, of the measured energy. It is therefore necessary to consider the relative magnitude of this effect in comparison to the energetic width of the spectroscopic features that are to be

measured. For example, if the aim of an experiments is to determine the width of a semiconductors band gap, on the order of $\approx 1\,eV$, then a modulation bias of $V_m \approx 10\,meV$ would have little impact. However, measurements of narrow resonances, for instance Kondo resonances (see **section 4.4**), that may have a width on the order of a few millielectron volts will require significantly reduced modulation biases. A complication to this is that the magnitude of the lock-in dI/dV signal is proportional to the magnitude of the modulation bias used. Therefore, in any given experiment it is important to optimise the modulation voltage used such that it has negligible broadening of the spectroscopic feature, but is maximised as much as possible to increase the lock-in signal. This can be simply achieved by performing multiple spectra on the same feature with different modulation amplitudes and checking for changes in the observed width.

Similarly to modulation broadening, electrical noise in the STM junction can act to reduce the experimental resolution of an STS measurement. In general the cumulative effect of all sources of broadening can be considered to act as an effective temperature that similarly to the thermodynamic temperature of the system will limit the experimental resolution. The effective electronic temperature of the Omicron Cryogenic STM is $3.5 - 4.5\,\mathrm{K}$ based upon fits of the superconducting gap of $NbSe_2$ [51] and a comparison of the evolution of the spectrum of Co atoms on $Cu_2N/Cu(001)$ [28]. The observed discrepancy in effective temperature and the thermodynamic base temperature of 3 K is considered to likely arise from radio frequency noise that enters the system due to incomplete shielding and filtering.

Chapter 3

Silicene Surfaces

3.1 Free-standing Silicene

The first theoretical consideration of a 2D honeycomb lattice of silicon atoms came in 1994 from Takeda and Shiraishi [52] with the concept later revisited by Guzmán-Verri and Lew Yan Voon in 2007 [53], whom first coined the term 'silicene'. The tight-binding approach of Guzmán-Verri and Lew Yan Voon predicted analogous electronic properties of silicene to graphene and as such it is useful to review the band structure of graphene, before comparison to silicene.

3.1.1 Graphene Band Structure

Here a short summary of the band structure of graphene and the significant properties arising from this are provided; for a detailed review of the electronic properties of graphene see A. H. Castro Neto et al.[7].

The honeycomb lattice of graphene can be considered to be formed from two indistinguishable carbon triangular sub-lattices A (blue), and B (yellow) as shown in **Fig. 3.1**. It is therefore possible to define a two atom per unit cell basis, with real space lattice vectors

$$\mathbf{a_1} = \frac{a}{2}(3, \sqrt{3}) \quad \mathbf{a_2} = \frac{a}{2}(3, -\sqrt{3}), \tag{3.1}$$

where $a \approx 1.42$Å is the carbon-carbon bond length [7]. Thus the reciprocal-lattice vectors are given by

$$\mathbf{b_1} = \frac{2\pi}{3a}(1, \sqrt{3}) \quad \mathbf{b_2} = \frac{2\pi}{3a}(1, -\sqrt{3}). \tag{3.2}$$

Additionally the three nearest-neighbour real space vectors, shown in **Fig. 3.1**, are defined as,

$$\delta_\mathbf{1} = \frac{a}{2}(1, \sqrt{3}) \quad \delta_\mathbf{2} = \frac{a}{2}(1, -\sqrt{3}) \quad \delta_\mathbf{3} = -a(1, 0), \tag{3.3}$$

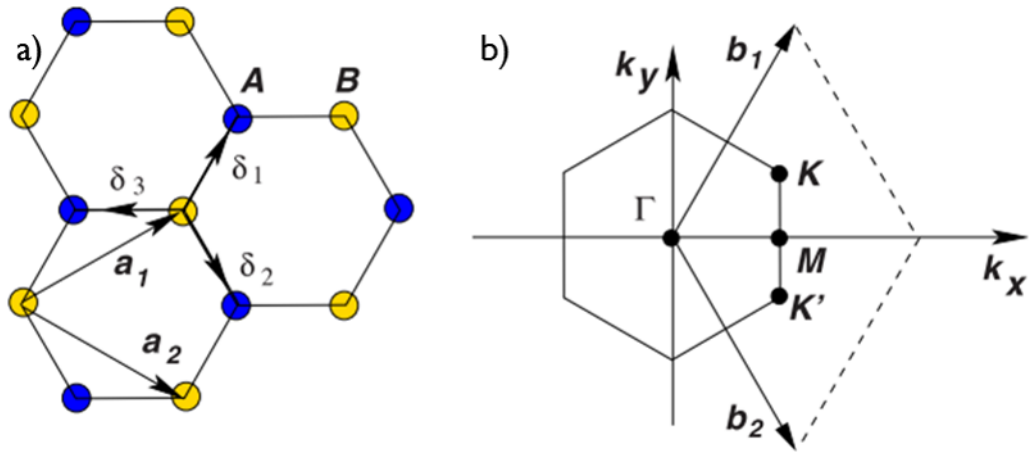

Figure 3.1: Graphene unit cells.
(a) Schematic model of the graphene honeycomb lattice, formed from two identical triangular sublattices A(blue) and B(yellow). The real space lattice vectors $\mathbf{a}_1$ and $\mathbf{a}_2$ are shown along with the nearest-neighbour vectors δ_i, $i = 1, 2, 3$. (b) Corresponding Brillouin zone and reciprocal lattice vectors $\mathbf{b}_1$ and $\mathbf{b}_2$. Also highlighted are the Dirac cone locations at the K and K' points.[7]

while the six second-nearest neighbours are given by,

$$\delta_{\mathbf{1}}' = \pm\mathbf{a_1} \qquad \delta_{\mathbf{2}}' = \pm\mathbf{a_2} \qquad \delta_{\mathbf{3}}' = \pm(\mathbf{a_2} - \mathbf{a_1}). \tag{3.4}$$

If at first it is considered that electrons in graphene can only hop between nearest-neighbour carbon atoms then a tight-binding Hamiltonian can be written as (units are chosen such that $\hbar = 1$)

$$H = -t \sum_{\langle i,j\rangle,\sigma} (a^\dagger_{\sigma,i} b_{\sigma,j} + b^\dagger_{\sigma,j} a_{\sigma,i}), \tag{3.5}$$

where $a_{i,\sigma}(a^\dagger_{i,\sigma})$ annihilates (creates) an electron with spin $\sigma(\sigma = \uparrow, \downarrow)$ on site $\mathbf{R_i}$ on sublattice A (an equivalent definition is used for sublattice B), t($\approx 2.8eV$) is the nearest-neighbour hopping energy (hopping between different sublattices)[7]. The tight-binding eigenvectors can then be written in the form of a spinor, where the components correspond to the electron amplitudes on the A and B atoms within in the unit cell, with respect to a reference point $\mathbf{R}_i^0$. For convenience $\mathbf{R}_i^0$ is defined at the A atom, and B lies δ_1 from A. The eigenfunctions therefore have the form,

$$\begin{pmatrix} \alpha_{\sigma,\mathbf{k}} \\ \beta_{\sigma,\mathbf{k}} \end{pmatrix} = \sum_{i,\sigma} e^{i\mathbf{k}\cdot\mathbf{R}_i^0} \begin{pmatrix} a^\dagger_{i,\sigma} e^{-\frac{i}{2}\mathbf{k}\cdot\delta_1} \\ b^\dagger_{i,\sigma} e^{\frac{i}{2}\mathbf{k}\cdot\delta_1} \end{pmatrix}. \tag{3.6}$$

The Hamiltonian then has the **k**-representation,

$$\mathbf{H_k} = \begin{pmatrix} 0 & \Delta_{\mathbf{k}} \\ \Delta^*_{\mathbf{k}} & 0 \end{pmatrix}, \tag{3.7}$$

where

$$\Delta_{\mathbf{k}} = -t \sum_{l=1}^{3} e^{i\mathbf{k}\cdot\delta_l} \tag{3.8}$$

is the sum of hopping terms to the three nearest neighbours. From $\mathbf{H_k}$ it can be trivially seen that the eigenvalues are given by,

$$\begin{aligned} |\mathbf{H_k} - \varepsilon_{\mathbf{k}}| &= 0 \\ \varepsilon^2_{\mathbf{k}} - \Delta^*_{\mathbf{k}}\Delta_{\mathbf{k}} &= 0 \\ \varepsilon_{\mathbf{k}} &= \pm|\Delta_{\mathbf{k}}|. \end{aligned} \tag{3.9}$$

$\Delta_{\mathbf{k}}$ can then be explicitly evaluated for nearest-neighbour vectors,

$$\begin{aligned} \Delta_{\mathbf{k}} &= -t\left(e^{i\mathbf{k}\cdot\frac{a}{2}(1,\sqrt{3})} + e^{i\mathbf{k}\cdot\frac{a}{2}(1,-\sqrt{3})} + e^{i\mathbf{k}\cdot -a(1,0)}\right) \\ &= -t\left(e^{i\frac{a}{2}(k_x+\sqrt{3}k_y)} + e^{i\frac{a}{2}(k_x-\sqrt{3}k_y)} + e^{-iak_x}\right) \\ &= -t\left(e^{i\frac{a}{2}k_x}\cdot e^{i\frac{\sqrt{3}a}{2}k_y} + e^{i\frac{a}{2}k_x}\cdot e^{i\frac{\sqrt{3}a}{2}k_y} + e^{-iak_x}\right) \\ &= -te^{-iak_x}\left(1 + e^{i\frac{3a}{2}k_x}\cdot e^{i\frac{\sqrt{3}a}{2}k_y} + e^{i\frac{3a}{2}k_x}\cdot e^{-i\frac{\sqrt{3}a}{2}k_y}\right) \\ &= -te^{-iak_x}\left(1 + e^{i\frac{3a}{2}k_x}\left(e^{i\frac{\sqrt{3}a}{2}k_y} + e^{-i\frac{\sqrt{3}a}{2}k_y}\right)\right) \\ &= -te^{-iak_x}\left(1 + 2e^{i\frac{3a}{2}k_x}cos(\frac{\sqrt{3}a}{2}k_y)\right). \end{aligned} \tag{3.10}$$

Next $|\Delta_{\mathbf{k}}|^2$ can be evaluated,

$$\begin{aligned} |\Delta_{\mathbf{k}}|^2 &= -te^{-iak_x}\left(1 + 2e^{i\frac{3a}{2}k_x}cos(\frac{\sqrt{3}a}{2}k_y)\right)\cdot -te^{iak_x}\left(1 + 2e^{-i\frac{3a}{2}k_x}cos(\frac{\sqrt{3}a}{2}k_y)\right) \\ &= t^2e^0\left[1 + 2e^{-i\frac{3a}{2}k_x}cos\left(\frac{\sqrt{3}a}{2}k_y\right) + 2e^{i\frac{3a}{2}k_x}cos\left(\frac{\sqrt{3}a}{2}k_y\right) + 4e^0cos^2\left(\frac{\sqrt{3}a}{2}k_y\right)\right] \\ &= t^2\left[1 + 4cos\left(\frac{3a}{2}k_x\right)cos\left(\frac{\sqrt{3}a}{2}k_y\right) + 4cos^2\left(\frac{\sqrt{3}a}{2}k_y\right)\right] \\ &= t^2\left[1 + 4cos\left(\frac{3a}{2}k_x\right)cos\left(\frac{\sqrt{3}a}{2}k_y\right) + \left(2 + 2cos\left(\sqrt{3}ak_y\right)\right)\right] \\ &= t^2\left[3 + 4cos\left(\frac{3a}{2}k_x\right)cos\left(\frac{\sqrt{3}a}{2}k_y\right) + 2cos\left(\sqrt{3}ak_y\right)\right], \end{aligned} \tag{3.11}$$

so that the electron dispersion is given by,

$$\varepsilon_{\mathbf{k}} = \pm t \left[3 + 4cos\left(\frac{3a}{2}k_x\right) cos\left(\frac{\sqrt{3}a}{2}k_y\right) + 2cos\left(\sqrt{3}ak_y\right) \right]^{\frac{1}{2}}. \tag{3.12}$$

Since the low energy excitations of a system often dominate the electronic properties it is useful to examine the calculated dispersion around the Fermi level. Solving **eqn. 3.12** for **k**, where $\varepsilon_{\mathbf{k}} = 0$ gives the **K** and **K'** points,

$$\mathbf{K} = \left(\frac{2\pi}{3a}, \frac{2\pi}{3\sqrt{3}a}\right), \qquad \mathbf{K}' = \left(\frac{2\pi}{3a}, -\frac{2\pi}{3\sqrt{3}a}\right) \tag{3.13}$$

that sit at the corners of the Brillouin zone (see **Fig. 3.1**). For convenience a new lattice vector **q** is defined that is measured relative to the **K**-point,

$$\mathbf{q} = \mathbf{k} - \mathbf{K}. \tag{3.14}$$

Therefore **eqn. 3.10** can be redefined to give,

$$\begin{aligned}
\Delta_{\mathbf{q}} &= -te^{-ia\left(q_x + \frac{2\pi}{3a}\right)} \left[1 + 2e^{i\frac{3a}{2}\left(q_x + \frac{2\pi}{3a}\right)} cos\left(\frac{\sqrt{3}a}{2}\left(q_y + \frac{2\pi}{3\sqrt{3}a}\right)\right)\right] \\
&= -te^{-iaq_x}e^{-i\frac{2\pi}{3}} \left[1 + 2e^{i\frac{3a}{2}q_x}e^{i\pi} cos\left(\frac{\sqrt{3}a}{2}q_y + \frac{\pi}{3}\right)\right] \\
&= -te^{-iaq_x}e^{-i\frac{2\pi}{3}} \left[1 - 2e^{i\frac{3a}{2}q_x} cos\left(\frac{\sqrt{3}a}{2}q_y + \frac{\pi}{3}\right)\right] \\
&= -te^{-i\frac{2\pi}{3}} \left[e^{-iaq_x} - 2e^{i\frac{a}{2}q_x} cos\left(\frac{\sqrt{3}a}{2}q_y + \frac{\pi}{3}\right)\right]
\end{aligned} \tag{3.15}$$

It is now the goal to expand **eqn. 3.15** about $\mathbf{q} = 0$, i.e. the **K** point at which the Fermi level lies. This is achieved with a Taylor expansion of the form,

$$\Delta_{\mathbf{q}} \approx q_x \left[\frac{\partial \Delta_{\mathbf{q}}}{\partial q_x}\right]_{\mathbf{q}=0} + q_y \left[\frac{\partial \Delta_{\mathbf{q}}}{\partial q_y}\right]_{\mathbf{q}=0}. \tag{3.16}$$

The partial derivatives are given by,

$$\frac{\partial \Delta_{\mathbf{q}}}{\partial q_x} = -te^{-i1\frac{2\pi}{3}} \left[-iae^{-iaq_x} - iae^{i\frac{a}{2}q_x} cos\left(\frac{\sqrt{3}a}{2}q_y + \frac{\pi}{3}\right)\right] \tag{3.17a}$$

$$\frac{\partial \Delta_{\mathbf{q}}}{\partial q_y} = -te^{-i\frac{2\pi}{3}} \left[\sqrt{3}ae^{i\frac{a}{2}q_x} sin\left(\frac{\sqrt{3}a}{2}q_y + \frac{\pi}{3}\right)\right]. \tag{3.17b}$$

When evaluated at $\mathbf{q} = 0$ **eqn. 3.17a** and **eqn. 3.17b** give,

$$\left[\frac{\partial \Delta_{\mathbf{q}}}{\partial q_x}\right]_{\mathbf{q}=0} = \frac{3}{2} iat\, e^{-i\frac{2\pi}{3}} \tag{3.18a}$$

$$\left[\frac{\partial \Delta_{\mathbf{q}}}{\partial q_y}\right]_{\mathbf{q}=0} = -\frac{3}{2} at\, e^{-i\frac{2\pi}{3}}. \tag{3.18b}$$

The low energy expansion is therefore,

$$\begin{aligned} \Delta_{\mathbf{q}} &\approx q_x \left(i\frac{3a}{2} t\, e^{-i\frac{2\pi}{3}} \right) + q_y \left(-\frac{3}{2} at\, e^{-i\frac{2\pi}{3}} \right) \\ &\approx i\frac{3a}{2} t \left(q_x + iq_y\right)\, e^{-i\frac{2\pi}{3}}. \end{aligned} \tag{3.19}$$

Here it is noted that if the expansion was performed about **K'** then,

$$\begin{aligned} \Delta_{\mathbf{q}}(\mathbf{K'}) &= -i\frac{3a}{2} t (q_x - iq_y) e^{i\frac{2\pi}{3}} \\ &= \Delta^*_{\mathbf{q}}(\mathbf{K}), \end{aligned} \tag{3.20}$$

which demonstrates the helicity of the graphene dispersion relations. More illustratively the Hamiltonian can be re-written with these expressions to give,

$$\begin{aligned} \mathbf{H} &= \frac{3a}{2} t \begin{pmatrix} 0 & q_x + iq_y \\ q_x - iq_y & 0 \end{pmatrix} \\ &= \frac{3a}{2} t\, \boldsymbol{\sigma} \cdot \mathbf{q}, \end{aligned} \tag{3.21}$$

where $\boldsymbol{\sigma}$ are the usual Pauli matricies. It can now be seen that electrons around the **K**− and **K'**−points have an opposite spin-like property known as pseudo-spin or valley number. The electronic dispersion can then be calculated from **eqn. 3.9** as,

$$\begin{aligned} \varepsilon_{\mathbf{q}} = |\Delta_{\mathbf{q}}| &= \left[-i\frac{3}{2} at \left(q_x - iq_y\right)\, e^{i\frac{2\pi}{3}} \cdot i\frac{3}{2} at \left(q_x + iq_y\right)\, e^{-i\frac{2\pi}{3}} \right]^{\frac{1}{2}} \\ &= \left[-i^2 \frac{9}{4} (at)^2 \left(q_x^2 + iq_x q_y - iq_x q_y - i^2 q_y^2\right) e^0 \right]^{\frac{1}{2}} \\ &= \left[\frac{9}{4} (at)^2 \left(q_x^2 + q_y^2\right) \right]^{\frac{1}{2}} \\ &= \pm\frac{3}{2} at \left(q_x^2 + q_y^2\right)^{\frac{1}{2}} \\ &= \pm v_F |\mathbf{q}|, \end{aligned} \tag{3.22}$$

where $v_F = 3at/2$ is the Fermi velocity, the plus, and minus signs refer to the upper (π^*) and lower (π) bands respectively, and $|\mathbf{q}|$ is the magnitude of $\mathbf{q}$. $\varepsilon_{\mathbf{q}}$ is symmetric about the Fermi level, and linearly dependent on only the magnitude of $\mathbf{q}$. It is this relationship that

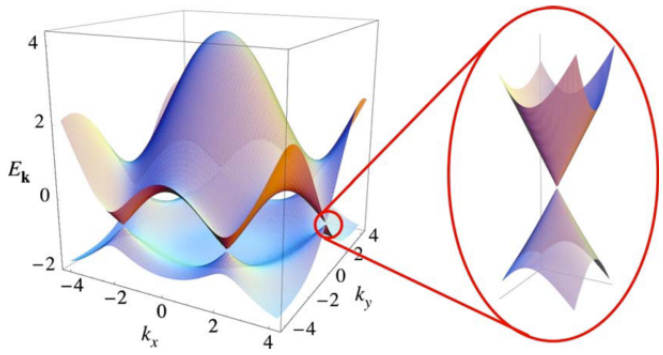

Figure 3.2: Graphene Band Stucture.
(Left) Full electronic dispersion energy spectrum (in units of t) for t=2.7 eV and t'=-0.2t. (Right) Zoom in of the energy bands close to one of the Dirac points.[7]

forms the so called Dirac cones of graphene. The most striking difference between Dirac cones and the conventional Fermi velocity of a metal, $v_F = \sqrt{2E/m}$, where m is the electron mass, and E is the energy, is that the Fermi velocity of graphene is independent of both energy and momentum. Charge carriers in graphene therefore behave as "massless" Dirac fermions, with an experimentally determined[54] Fermi velocity $v_F \approx \frac{1}{300}c \approx 1 \times 10^6\,\mathrm{ms}^{-1}$, where c is the speed of light [7].

So far only the nearest-neighbour hopping of electrons has been considered. However it is also reasonable to examine how the electronic dispersion of graphene is influenced by next-nearest-neighbour hopping, where the Hamiltonian is now given by,

$$H = -t \sum_{\langle i,j\rangle,\sigma} (a^\dagger_{\sigma,i} b_{\sigma,j} + b^\dagger_{\sigma,j} a_{\sigma,i}) - t' \sum_{\langle\langle i,j\rangle\rangle,\sigma} \left(a^\dagger_{\sigma,i} a_{\sigma,j} + b^\dagger_{\sigma,i} b_{\sigma,j} + a^\dagger_{\sigma,j} a_{\sigma,i} + b^\dagger_{\sigma,j} b_{\sigma,i} \right), \tag{3.23}$$

where t' is the next-nearest-neighbour hopping energy.

In a similar procedure to that outlined above for nearest-neighbour hopping, the Hamiltonian including nearest- and next-nearest-neighbour hopping can be expanded around the K point, this time to second order in **q** to give,

$$\varepsilon_\pm(\mathbf{q}) \approx 3t' \pm v_F|\mathbf{q}| - \left(\frac{9t'a^2}{4} \pm \frac{3ta^2}{8} sin(3\theta_\mathbf{q}) \right) |\mathbf{q}|^2, \tag{3.24}$$

where,

$$\theta_\mathbf{q} = arctan\left(\frac{q_x}{q_y}\right) \tag{3.25}$$

is the angle in momentum space. Hence t' acts to shift the energy position of the Dirac point and breaks electron-hole symmetry. **Figure 3.2** shows a plot of the graphene band dispersion in **eqn. 3.24** showing the six-fold symmetry of the Brillouin zone. The zoom in on the right hand side focuses around one of the **K**-points revealing the linear dispersion of the Dirac cones.

3.1.2 Silicene Band Structure

The original tight-binding model of silicene by Guzmán-Verri and Lew Yan Voon [53] considered a planar hexagonal lattice of silicon atoms and as such predicted electronic properties almost identical to that of graphene. *Ab initio* calculations of silicene reveal that the two sublatticies of silicene are expected to be offset to one another (see **Fig. 3.3**), due to the intermediary sp^2/sp^3 hybridisation of the silicon atoms [55–57]. Therefore to examine the band structure of silicene it is necessary to use a tight-binding model that includes the effects of spin-orbit coupling and the periodic potential of the buckled lattice [58, 59]. Presented here is a short overview on the comprehensive work on silicene tight-binding models, in particular the work of C. -C. Lie [60] and M. Ezawa [58].

The two sublattices, A (yellow) and B (red), are now buckled with respect to one another with a vertical separation of $2l$ (see **Fig. 3.3**). Spin-orbit coupling (SOC) in the Pauli equation can be written in generic form,

$$\begin{aligned} \mathbf{H}_{SO} &= \frac{1}{4}\left(\boldsymbol{\nabla} V \times \mathbf{p}\right) \cdot \boldsymbol{\sigma} \\ &= -\left(\mathbf{F} \times \mathbf{p}\right) \cdot \boldsymbol{\sigma} \end{aligned}, \tag{3.26}$$

where V is the potential energy, $\boldsymbol{\nabla}$ is the gradient function, $\mathbf{F}$ is the force, $\mathbf{p}$ is the momentum, and $\boldsymbol{\sigma}$ are the Pauli matrices.

The SOC coupling interactions of silicene are similar to those that would be expected for graphene. Although, often in graphene these effects are ignored as it can genrally be assumed that the spin-orbit interactions are weak [60]. Owing to mirror symmetry about nearest-neighbours the SOC is zero (**Fig. 3.3c**). However, the next-nearest-neighbour in-plane SOC is non-zero (**Fig. 3.3c**) and by symmetry is given as,

$$\begin{aligned} \mathbf{H}_{SO1} &= i\gamma_2 \left(\mathbf{F}_{\parallel} \times \mathbf{d}_{i,j}\right) \cdot \boldsymbol{\sigma} \\ &= i t_2 v_{i,j} \boldsymbol{\sigma}_z, \end{aligned} \tag{3.27}$$

where $v_{i,j} = \frac{\mathbf{d}_i \times \mathbf{d}_j}{|\mathbf{d}_i \times \mathbf{d}_j|}$, γ_2 and t_2 are undetermined parameters, and $\mathbf{d}_i$ and $\mathbf{d}_j$ are the two nearest bonds connecting next-nearest neighbours $\mathbf{d}_{i,j}$. Where silicene differs from graphene is that due to the sub-lattice buckling the perpendicular SOC is non-zero (see **Fig. 3.3d**). These interactions give rise to an additional component in the Hamiltonian of the form,

$$\begin{aligned} \mathbf{H}_{SO2} &= i\gamma_1 \left(\boldsymbol{\sigma} \times \mathbf{d}^0_{i,j}\right) \cdot \mathbf{F}^A_{\perp} \mathbf{e}_z \\ &= i t_1 \mu_{i,j} \left(\boldsymbol{\sigma} \times \mathbf{d}^0_{i,j}\right), \end{aligned} \tag{3.28}$$

where $\mathbf{d}^0_{i,j} = \mathbf{d}_{i,j}/|\mathbf{d}_{i,j}|$, γ_1, and t_1 are undermined parameters, and $\mu_{i,j} = \pm 1$ for the A and B sites.

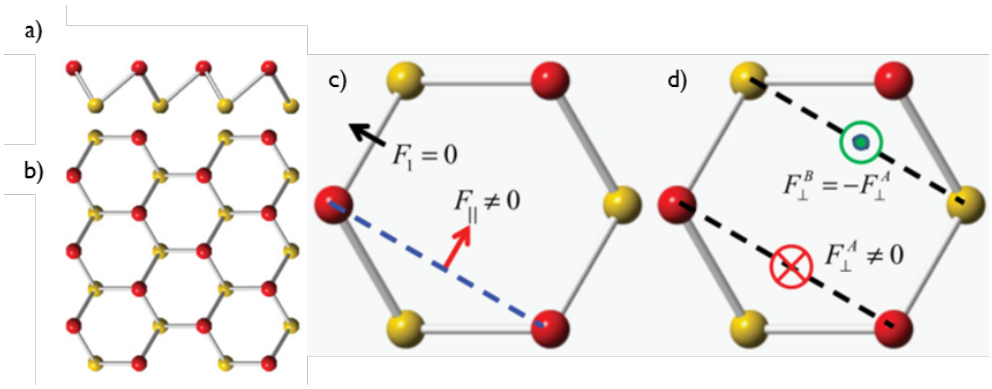

Figure 3.3: Silicene honeycomb lattice ball model.
(a) Side, and (b) top view showing how the two triangular sublatticies are displaced from one another inducing the characteristic buckling of the silicene lattice. The atomic intrinsic spin-orbit interactions of silicene showing (c) that the nearest-neighbour force F_1 is zero, and the in-plane next-nearest-neighbour force $F_{\parallel} \neq 0$. (d) The next-nearest-neighbour perpendicular forces obey $F_{\perp}^{B} = -F_{\perp}^{A}$. [60]

With the SOC interactions defined a complete Hamiltonian for silicene can be given as,

$$\begin{aligned} H = & -t \sum_{\langle i,j\rangle,\alpha} a_{i,\alpha}^{\dagger} b_{j,\alpha} + b_{j,\alpha}^{\dagger} a_{i,\alpha} \\ & + it_2 \sum_{\langle\langle i,j\rangle\rangle,\alpha,\beta} v_{i,j} \left(a_{i,\alpha}^{\dagger} \boldsymbol{\sigma}_{\alpha,\beta}^{z} a_{j,\beta} + b_{i,\alpha}^{\dagger} \boldsymbol{\sigma}_{\alpha,\beta}^{z} b_{j,\beta} + a_{j,\alpha}^{\dagger} \boldsymbol{\sigma}_{\alpha,\beta}^{z} a_{i,\beta} + b_{j,\alpha}^{\dagger} \boldsymbol{\sigma}_{\alpha,\beta}^{z} b_{i,\beta} \right) \\ & + it_1 \sum_{\langle\langle i,j\rangle\rangle,\alpha,\beta} \mu_{i,j} \Big(a_{i,\alpha}^{\dagger} \left(\boldsymbol{\sigma} \times \mathbf{d}_{i,j}^{0} \right)_{\alpha,\beta}^{z} b_{j,\beta} + b_{i,\alpha}^{\dagger} \left(\boldsymbol{\sigma} \times \mathbf{d}_{i,j}^{0} \right)_{\alpha,\beta}^{z} a_{j,\beta} \\ & \qquad + a_{j,\alpha}^{\dagger} \left(\boldsymbol{\sigma} \times \mathbf{d}_{i,j}^{0} \right)_{\alpha,\beta}^{z} b_{i,\beta} + b_{j,\alpha}^{\dagger} \left(\boldsymbol{\sigma} \times \mathbf{d}_{i,j}^{0} \right)_{\alpha,\beta}^{z} a_{i,\beta} \Big) , \end{aligned} \tag{3.29}$$

where the first term is the nearest-neighbour hopping, the second and third terms are then the next-nearest-neighbour hopping with effective and intrinsic Rashba SOC, respectively.

Using similar methods to those outlined in **section 3.1.1**, a low-energy effective Hamiltonian around the **K**-point can be derived from **eqn. 3.29** of the form [60],

$$\mathbf{H_q} \approx \begin{pmatrix} h_{11} & v_F \left(q_x + i q_y \right) \\ v_F \left(q_x - i q_y \right) & -h_{11} \end{pmatrix} , \tag{3.30}$$

where v_F, and h_{11} are,

$$v_F = \frac{\sqrt{3}a}{2} t \tag{3.31a}$$

$$h_{11} = -3\sqrt{3} t_2 \boldsymbol{\sigma}_z - \frac{3a}{2} t_1 \left(q_y \boldsymbol{\sigma}_x - q_x \boldsymbol{\sigma}_y \right) . \tag{3.31b}$$

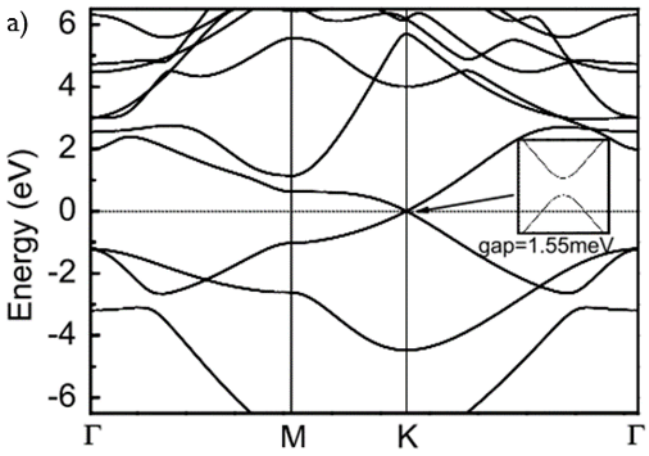

Figure 3.4: Band structure diagram of free-standing silicene.
Electronic dispersion along different high symmetry directions in the silicene BZ. Centred at the **K**-point is the linearly dispersing Dirac cone, that in silicene is intrinsically gapped by approximately 1.55 meV. [60]

The electron dispersion can then be obtained from $|\mathbf{H_q} - \varepsilon_\mathbf{q}\mathbf{1}| = 0$ to give,

$$\varepsilon_\mathbf{q} = \pm \left[h_{11}^2 + v_F^2|\mathbf{q}|^2\right]^{\frac{1}{2}}. \tag{3.32}$$

It is from **eqn. 3.32** that the fundamental difference between silicene and graphene can be seen. Evaluating **eqn. 3.32** for $\mathbf{q} = 0$ gives,

$$\varepsilon_{\mathbf{q}=0} = \pm 3\sqrt{3}t_2\boldsymbol{\sigma}_z. \tag{3.33}$$

It is therefore seen that unlike graphene, silicene has an intrinsic bandgap, at the **K**- and **K'**-points, which arises due to the lifting of the sublattice degeneracy. **Figure 3.4** shows a plot of the band structure for silicene, where the inset focuses on the gapped linear dispersion around the **K**-point.

In addition to the brief overview of SOC in silicene shown here, much work has investigated how the electronic properties of silicene are influenced by other interactions, such as with an external electric or magnetic field [58–67]. These investigations have found a rich array of different phenomena including a quantum spin hall effect [59, 65, 67], as well as other topological phase transitions [61, 63]. As such it is expected that experimentally realised forms of silicene will prove to provide an interesting playground for potentially novel electronic and magnetic effects. The following sections of this chapter will now provide a review of current experimental progress in the field of epitaxially grown silicene.

3.2 Silicene on Ag(111)

In 2012, Vogt, et. al. [11] demonstrated experimental evidence for the formation of a 2D hexagonal lattice of silicon atoms - silicene - upon a Ag(111) single crystal, which presented electronic structure similar to that of graphene. The initial uncertainty in the STM measurements of silicene on Ag (111) [68] were later elucidated to most likely be due to the sensitive growth parameters of this system, in particular substrate temperature [69]. However, it is now considered that, of the many possible atomic arrangements of the hexagonal lattice, the (3×3)[11], and $(\sqrt{3} \times \sqrt{3})$R30^o [70, 71] reconstructions, with respect to the silicene (1×1), exhibit electronic properties compatible with those of free-standing silicene. In both the (3×3) and $(\sqrt{3} \times \sqrt{3})$R30^o reconstructions, the formation of silicene upon Ag(111) is achieved by Si deposition from a sublimation source in ultrahigh vacuum (UHV) conditions [11, 70–74]. The differences in the two systems arise from a combination of temperature, deposition rate, and substrate effects that will be covered in the following sections.

3.2.1 (3×3) Reconstruction

The formation of (3×3) reconstructed silicene is achieved upon a Ag (111) single crystal. The Si deposition rate must be finely controlled ($\approx$ 1 ML/hr) and the Ag substrate kept between 220 - 260 ^{o}C [69]. Prepared in this manor, silicene sheets several hundereds of square nanometres are formed [11, 72, 75]. The STM images in **Fig. 3.5** show how the (3×3) reconstructed silicene is characterised by a hexagonal arrangement of triangular protrusions with a 1.14 nm periodicity. Density functional theory (DFT) calculations of silicene on Ag(111) elucidate that the contrast in STM images is a result of Si atoms sitting on top of Ag atoms, corresponding to a (4×4) and (3×3) reconstruction with respect to the Ag(111) and silicene lattices respectively (**Fig. 3.6**).

As is seen in **Fig. 3.6c** the triangular sublattices of silicene are buckled with respect to one another. Whilst the specific buckling of 0.075 nm is particular to this silicene

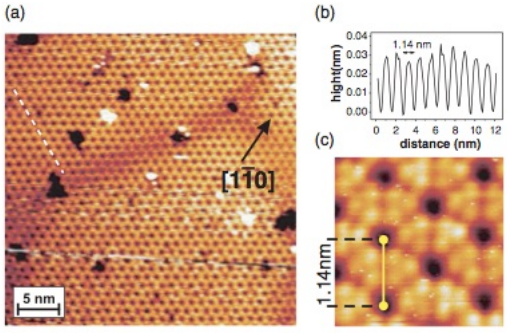

Figure 3.5: STM images of silicene on Ag(111).
(a) Large scale STM image of silicene upon Ag(111). (b) Topographic profile across silicene structure. (c) High resolution STM image of silicene superstructure upon Ag(111). [11]

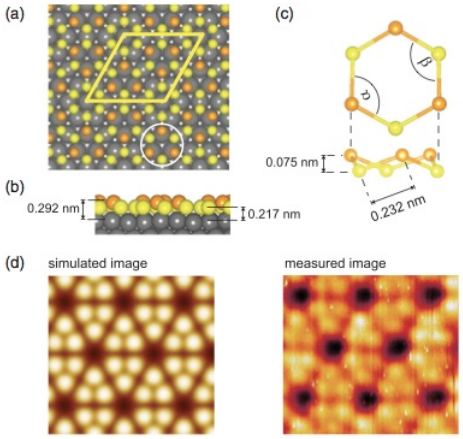

Figure 3.6: DFT results of silicene upon Ag(111).
(a) Positions of Si atoms (yellow and orange) in silicene (3x3) reconstruction on Ag(111) (gray). (b) Side view of (a). (c) Enlargement of silicene hexagon taken from white circle in (a) showing the sublattice buckling. (d) Comparison of simulated (left) and measured (right) STM images. [11]

- Ag(111) interface, free-standing silicene is predicted to exist in a buckled structure owing to a mixed sp^2-sp^3 atomic hybridisation of the silicon atoms [55, 57] (see **section 3.1.2**). Angle Resolved Photoelectron Spectroscopy (ARPES) measurements performed upon silicene on Ag(111) reveal a band structure similar to that of graphene [74, 76]. A model of the (1×1) Ag (blue), (1×1) silicene (black), and (3×3) silicene (red) Brillouin zones are shown in **Fig. 3.7a**. It can be seen that the (1×1) silicene K^{Si} point aligns with the (3×3) silicene Γ_{11} point that back folds to the Γ_{00} point. The (3×3) silicene Γ_{02} point also aligns with the (1×1) silicene M^{Ag} point that again back folds to the Γ_{00} point. Due to the alignments of these different high symmetry points in the silicene/Ag Brillouin zone the ARPES spectra in **Fig. 3.7b**, recorded at the (1×1) Ag M_{Ag} point, reveals the highly dispersive gapped Dirac cone of the silicene lattice [74]. From this linear dispersion a Fermi velocity comparable to that of graphene at 1.3 x 10^{-6} ms^{-1} is determined [74, 76].

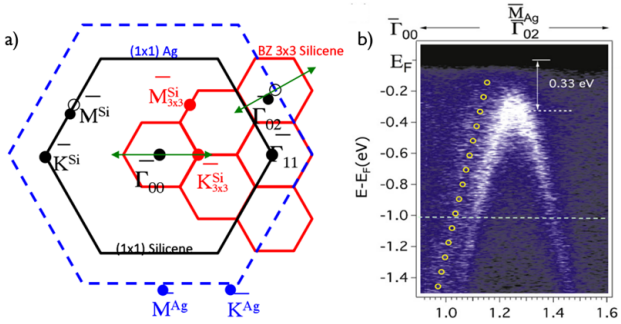

Figure 3.7: ARPES measurements of (3×3)−reconstructed Silicene on Ag(111).
(a) Model of the (1×1) Ag (blue), (1×1) silicene (black), and (3×3) silicene (red) Brillouin zones, showing how the (1×1) Silicene K^{Si} point back folds onto the (3×3) silicene Γ point. (b) ARPES spectrum of the silicene/Ag(111) surface recorded at the Γ_{02} point along the $\Gamma - M_{ag} - \Gamma$ direction, dotted line represents the Ag substrate 'sp' band. [74]

3.2.2 $(\sqrt{3} \times \sqrt{3})$R30^o Reconstruction

The $(\sqrt{3} \times \sqrt{3})$R30^o reconstruction of silicene on Ag (111), shown in **Fig. 3.8c**, is formed with higher silicon deposition rates than in the case of the (3×3) reconstruction. The substrate is kept at $\approx 220\,^o$C (similarly to the (3×3) growth) and a 3 ML/hr deposition rate employed [70, 71]. Under these parameters, large silicene sheets are formed 0.263 nm above the Ag (111) surface and it is seen that carpeting over Ag (111) step edges occurs. This can be seen in **Fig. 3.8a** and the corresponding line profile in **Fig. 3.8b**.

The origin of $(\sqrt{3} \times \sqrt{3})$R30^o reconstruction is considered in **Fig. 3.9**, where models of the free-standing AB corrugated silicene (see **Fig. 3.9a**) and an AB$\bar{\text{A}}$ corrugated structure (see **Fig. 3.9b**) are compared. The former of these two configurations is covered in **section 3.1.2**, whilst the latter is formed by one atom in the $(\sqrt{3} \times \sqrt{3})$ unit cell (green) being displaced below the plane of the AB configuration. The experimentally determined 0.64 nm periodicity of the $(\sqrt{3} \times \sqrt{3})$R30^o reconstruction is $\approx 4\%$ smaller than theoretical values of free-standing silicene [55, 59] and as such the Ag (111) substrate may act to contract the silicene lattice; stabilising the $(\sqrt{3} \times \sqrt{3})$R30^o reconstruction. DFT calculations of a contracted silicene lattice reveal how the AB$\bar{\text{A}}$ buckling stablises the hexagonal lattice for supercell periodicities below 0.635 nm (see **Fig. 3.9c**), within the experimental uncertainty for the measured periodicity. The $(\sqrt{3} \times \sqrt{3})$R30^o reconstruction can therefore be interpreted as imaging the A (red) atoms in the AB$\bar{\text{A}}$ buckling model, as highlighted by the blue hexagon in **Fig. 3.9d**.

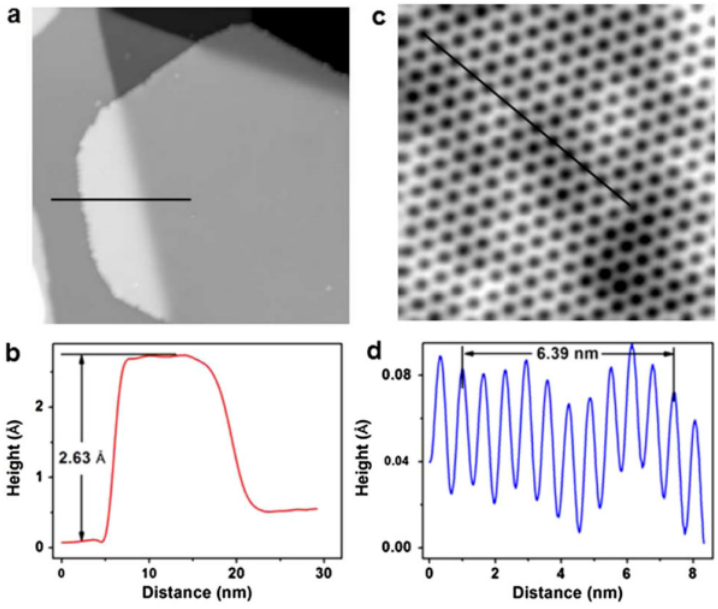

Figure 3.8: STM measurements of $(\sqrt{3} \times \sqrt{3})$R30^o silicene on Ag(111).
(A) Large scale image (65 nm $\times$ 6 nm) of silicene on Ag (111) crossing two substrate steps. (B) Line profile indicated by the black line in (A). (C) High resolution image (10 nm $\times$ 10 nm) revealing the honeycomb $(\sqrt{3} \times \sqrt{3})$R30^o reconstruction of silicene on Ag (111). (D) Line profile indicated in (C) by the black line revealing the atomic corrugation.[70]

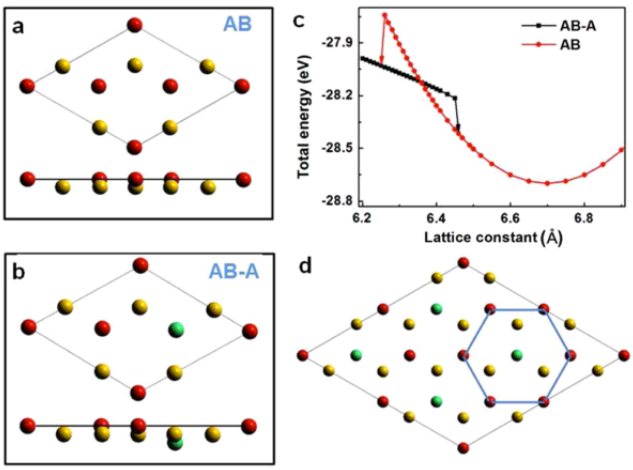

Figure 3.9: DFT model of $(\sqrt{3} \times \sqrt{3})$ reconstructed silicene on Ag(111). (a),(b) Top and side views of the lattice geometry of AB buckled silicene and $(\sqrt{3} \times \sqrt{3})$, AB$\bar{\text{A}}$ silicene. Red, yellow, and green balls correspond to A, B, and $\bar{\text{A}}$ atoms respectively. (c) Total energy of $(\sqrt{3} \times \sqrt{3})$ lattice in AB (red) and AB$\bar{\text{A}}$ (black) configurations, revealing that for $a < 6.35$ Å the AB$\bar{\text{A}}$ buckling is energetically favoured. (d) The blue hexagon details how the AB$\bar{\text{A}}$ buckling generates the $(\sqrt{3} \times \sqrt{3})$R30^o reconstruction. [70]

Electronic characterisation of the $(\sqrt{3} \times \sqrt{3})$R30^o reconstructed silicene surface has been achieved by dI/dV scanning tunnelling spectroscopy (STS), as shown in **Fig. 3.10a** [70]. In addition to the noteable peak at 0.9V, a dip in the dI/dV specta is observed at 0.5 V. Similar features are observed in graphene and are attributed to the energetic potsition of the Dirac point [77, 78]. Evidence for the presence of Dirac fermions in the $(\sqrt{3} \times \sqrt{3})$R30^o reconstruction of silicene on Ag (111) comes from quasi-particle interference (QPI) patterns upon the surface. **Figure 3.10b** shows an STM image of a second silicene layer on the $(\sqrt{3} \times \sqrt{3})$R30^o surface. Visible in the dI/dV images of the surface at various energies (see **Fig. 3.10c-e**) are standing wave patterns radiating out from the island. If it is considered that these arise from intravalley quasi-particle scattering (within a constant energy circle of the Dirac cone), then a plot of $E \ vs \ \frac{\kappa}{2}$, where κ is the interference pattern wavelength will yield the quasi-particle dispersion. As is shown in **Fig. 3.10f** this relationship is linear, as is expected for Dirac fermions. The Fermi velocity determined for this system is comparable to that of graphene at $V_F = (1.2 \pm 0.1) \times 10^6$ ms^{-1} and in agreement with ARPES measurements on (3×3) reconstructed silicene on Ag (111).

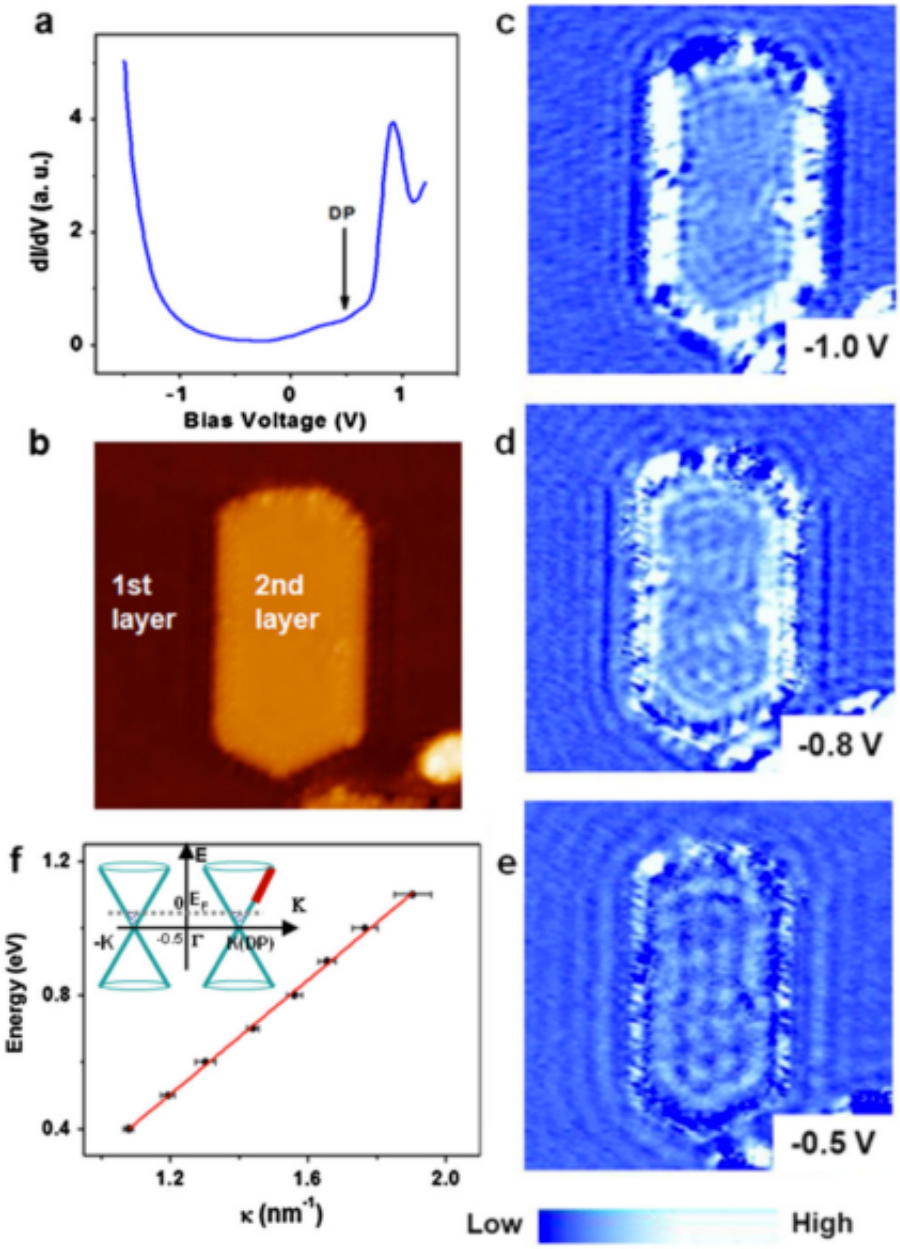

Figure 3.10: Silicene quasi-particle interference patterns.
(a) dI/dV spectroscopy taken at 77 K. The position of the Dirac point is labelled. (b) STM image (40 nm $\times$ 40 nm) of 1 ML silicene surface with a second layer island taken at -1.0V. (c),(d), and (r) dI/dV maps of the same area as (b) taken at -1.0 V, -0.8 V, and -0.5 V respectively. (f) Energy dispersion as function of quasi-particle interference pattern wavelength. (INSET) Schematic of the total band structure, with the experimental data highlighted in red and Fermi level position highlighted in grey.[70]

3.3 Silicene on ZrB_2 Thin Films

Silicene on zirconium diboride (ZrB_2) is formed by a unique surface segregation technique developed by Fleurence at al. [12]. An epitaxial thin film of ZrB_2 is grown on a Si (111) wafer by ultra high vacuum-chemical vapour epitaxy (UHV-CVE), where the film growth is monitored by *in-situ* reflection high energy electron diffraction (RHEED) [79]. Si (111) substrates are thermally prepared by direct current heating starting with an initial degas at 500^{o}C for 10 hours and then several flashes to 1200^{o}C in order to remove the SiO_2 layers. Once a clear Si (111) - (7×7) reconstruction is observed by RHEED, the substrate is held at 900^{o}C, whilst $Zr(BH_4)_4$ is introduced to the chamber, with a pressure of 7×10^{-5} Pa maintained for the entirety of the growth time. Thermal decomposition of $Zr(BH_4)_4$ at the Si (111) surface over the period of between 100-150 minutes leads to the formation of a ZrB_2(0001) thin film of an approximate 50 nm thickness [80].

The ZrB_2/Si(111) sample is then removed from the growth UHV chamber and exposed to atmospheric conditions upon transfer to characterisation UHV systems. The formation of silicene on the ZrB_2 (0001) surface is achieved by annealing the sample, via direct current heating, to 800^{o}C for between 5-10 hours. The high temperature removes the oxide layers, and allows for silicon segregation from the underlying Si (111) wafer to spontaneously form a self terminating monolayer of silicene upon cooling [12]. **Figure 3.11a** shows a typical STM image of a silicene/ZrB_2/Si (111) surface, where a (2×2) reconstruction - with respect to the underlying ZrB_2 (0001) surface [80] - and linear, regularly aligned stress relief domains are observed running along the ZrB_2 $[11\bar{2}0]$ direction [12].

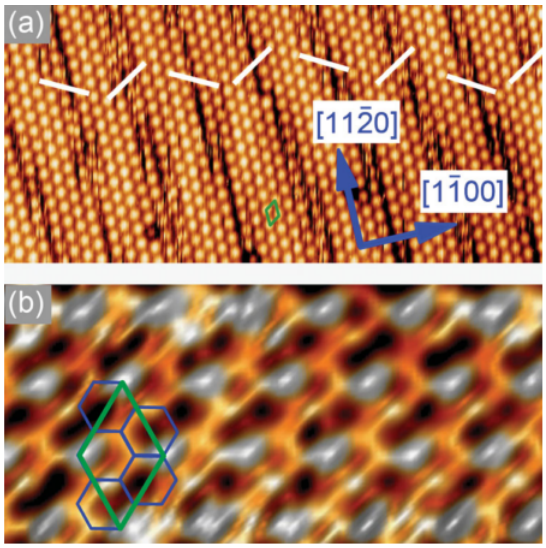

Figure 3.11: STM images of silicene on ZrB_2.
STM image of the (2×2)-reconstructed ZrB_2 (0001) surface. (a) 20 nm $\times$ 9.5 nm, I = 55 pA, V_s = 700 mV, (b) 4.2 nm $\times$ 2 nm, I = 600 pA, V_s = 100 mV. The white lines emphasise the direction of offsets between successive domains. The (2 x 2) UC and the honeycomb mesh are emphasized by green and blue solid lines, respectively. [12]

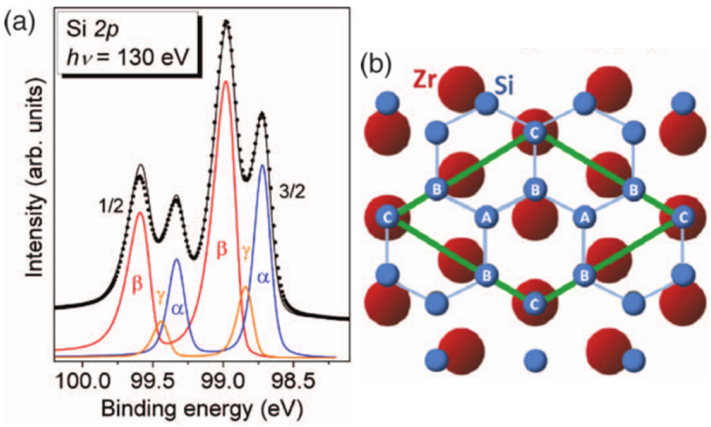

Figure 3.12: Core-level photoelectron spectroscopy of silicene on ZrB_2.
(a) Surface-sensitive Si(2p) photo-electron spectrum at normal emission. Chemical states identified by peak fitting are labelled as α, β, and γ. The three states are then attributed to Si atoms A, B, and C respectively in (b) from the relative spectral intensities. (b) Model of the silicene ($\sqrt{3} \times \sqrt{3}$) R30^o reconstruction on the ZrB_2 (0001) surface. [81]

Surface-sensitive core-level X-ray photoelectron spectroscopy performed on the sample demonstrates the presence of Si at the surface [12, 81]. **Figure. 3.12a** shows a spectrum of the silicene surface where the Si(2p) states are split into three chemical environments labelled α, β, and γ. The approximate $2:3:1$ intensity ratio of these three doublets, in conjunction with the high resolution STM image in **Fig. 3.11b** is used to give an in-plane model of the Si atoms in **Fig. 3.12b**, where the α, β, and γ components are attributed to the A, B, and C atoms respectively. Using this model the more common resolution STM measurements in **Fig. 3.11a** can be interpreted as a silicene ($\sqrt{3} \times \sqrt{3}$) R30^o reconstruction, where contrast is produced by Si atoms sitting directly on top of Zr atoms (**Fig. 3.12b**).

Further investigations into the X-ray photon energy dependence of the α, β, and γ intensity ratios revealed an oscillatory behaviour, as can be seen in **Fig. 3.13b**. From this the relative intensities can be normalised with respect to the total Si 2p intensity as a function of photon energy and an average for the ratio can be determined (see inset in **Fig. 3.13b**). The intensity ratio is then given as $2.3:3.4:0.3$. The average intensity ratio shows a substantial deviation from the idealised model of $2:3:1$, in particular the γ, or C atom, component is significantly under-represented. The ball model from which the idealised ratio can be derived from does not account for the domain boundary structure. Since it is also known that the C Si atoms, sitting directly on top of Zr atoms, have the weakest binding energy [12] it can be considered that these will be the most affected by the domain boundaries. As a result a chemical shift from the γ peak core-level excitations could be expected due to silicon C atoms that are not bound directly atop Zr atoms. The greater full width half maximum of the β component, with respect to the α and γ peaks may therefore be due to a 'hidden' shifted γ component [81]. Finally it is noted that the form of the Si(2p) spectrum for silicene on ZrB_2 is clearly

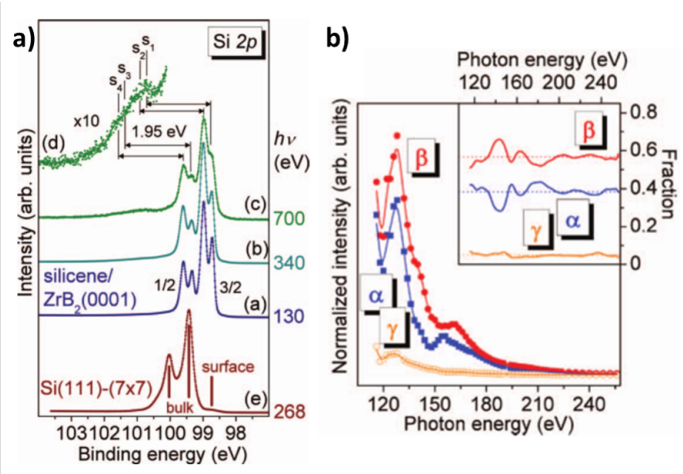

Figure 3.13: Photon energy dependence of Core-level photoelectron spectra of silicene. (a) Si 2p photoelectron spectra of silicene on ZrB_2 obtained at different photon energies: (blue) $h\nu = 130\,\text{eV}$, (light green) $h\nu = 340\,\text{eV}$, (green) $h\nu = 700\,\text{eV}$. (dark green) Magnification of $h\nu = 130\,\text{eV}$ spectrum. (red) Si 2p spectrum of Si(111)-(7×7) surface measured with $h\nu = 268\,\text{eV}$. (b)Spectral intensities of the α, β, and γ components as a function of photon energy, normalised to the photon flux. Inset shows the relative intensities of the α, β, and γ components as normalised to the total Si 2p intensity. The averaged intensities are shown as the dotted lines. [81]

very different to that of bulk Si(111) or the surface states of the (7×7) reconstruction (see the red curve in **Fig. 3.13a**).

To learn more about the out-of-plane buckling of the silicene lattice on ZrB_2 a series of comprehensive DFT investigations have been performed [12, 82–84]. Initially there were two possible candidate structures; one known as the *'buckled-like'* phase, and the second as *'planar-like'*. Through these studies it was shown that the striped domain boundary structure [83], and electronic band structure [84] could be well explained by the *planar-like* silicene structure and consequently it is the currently accepted model.

In *planar-like* silicene on ZrB_2 five out of six of the silicon atoms in the $(\sqrt{3} \times \sqrt{3})$ reconstructed silicene lattice lie in a single plane, with the sixth raised above by approximately 1.5 Å(see **Fig. 3.14b**)[82]. With respect to the underlying Zr surface the Si atoms bind in three positions: the hollow site, near-bridge site, and directly on top of a Zr atom. The three binding sites are 2.30 Å, 2.31 Å, and 3.89 Å above the Zr surface respectively.

Angle resolved ultraviolet photoelectron spectroscopy (ARUPS) measurements taken along the silicene(ZrB_2) $\bar{\Gamma} - K$ $(\bar{\Gamma} - M - \bar{\Gamma})$ surface directions, as a function of in-plane electron wave number $k_{\parallel}$ are shown in **Fig. 3.15a**. **Figure 3.15b** show the same spectra, but where guiding curves are used to highlight features. Surface states well known to correspond to the unperturbed Zr-terminated ZrB_2 (0001) surface are denoted as"$S_{1,2}$" [80, 85] and are an indication to the low level of hybridisation between the silicene layer and the underlying Zr surface [86]. The features denoted with "X_{1-10}" are therefore associated with the silicene sheet. The dispersive nature of the "X_2" feature, which is

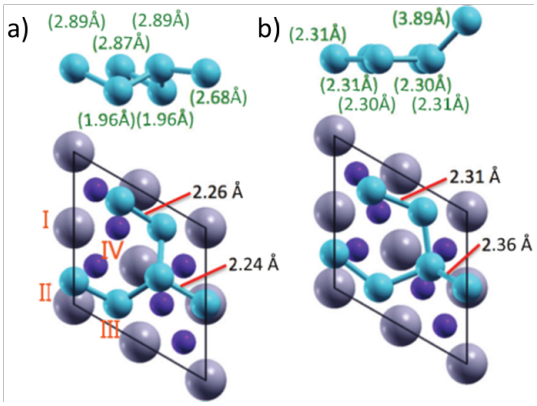

Figure 3.14: Ball models of candidate silicene/ZrB_2 surfaces.
Top and side views of silicene ball models corresponding to (a) Buckled-like silicene and (b) Planar-like silicene. [82]

centred at the expected silicene K-point, bares resemblance to the predicted Dirac cones of unreconstructed free-standing silicene [52, 53, 55, 57]. However, here the opening of an approximately 250 meV gap indicates that the specific buckling and hybridisation of silicene on ZrB_2 surface has altered the Dirac cone into a π-band feature. In **Fig. 3.15c** the band structure of *planar-like* silicene as calculated by DFT is shown,where a significant agreement is found with the experimentally obtained APRES spectra [83].

Figure 3.16 show a DFT model of the striped domain boundary structure of silicene on ZrB_2. In the center of the domains the silicene structure is identical to that in **Fig. 3.14b**. However, approaching the domain boundary Si atoms deviate from the ideal positions eventually forming a distorted hexagonal structure, essentially skipping a Si 'up' atom. As a result the silicene lattice rotates by 180^o upon transition across a domain boundary. An investigation into the phonon dispersion of an infinite, domain-free, silicene lattice formed on ZrB_2 revealed the presence of an instability [84]. Centred upon the high symmetry M point of the brillouin zone is a zero energy phonon mode. Accordingly,

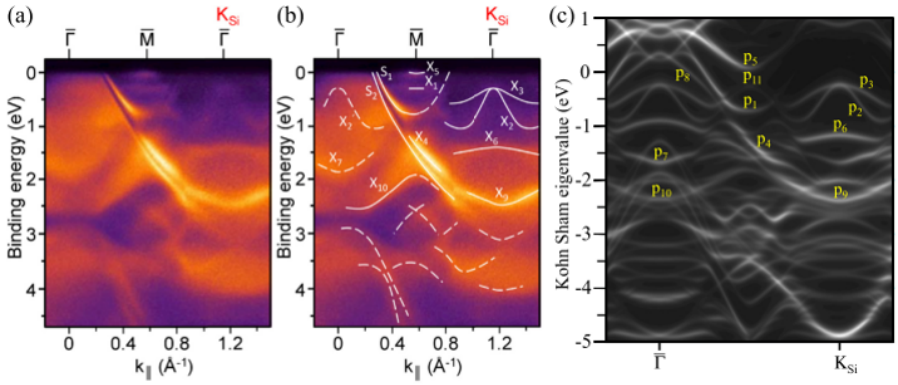

Figure 3.15: Comparison of ARPES and calculated band structure for silicene on ZrB_2.
(a) ARPES spectra of silicene on ZrB_2 taken along the silicene(ZrB_2) $\bar{\Gamma} - K(\bar{\Gamma} - M - \bar{\Gamma})$ directions. (b) Same as in (a), but with guiding curves. (c) DFT calculated band structure of *planar-like* silicene. [83]

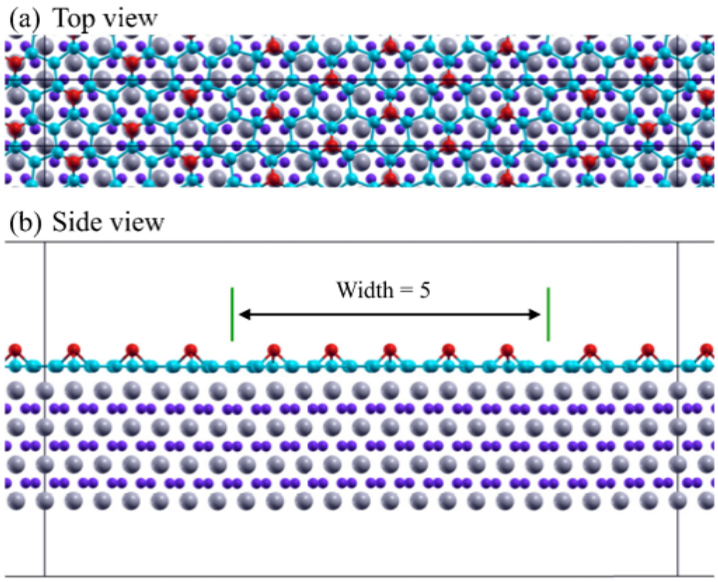

Figure 3.16: DFT model of the stripe-domain structure of silicene/ZrB_2. (a) Top view of the silicene structure showing how the domain boundaries are formed from lower density distorted hexagons. (b) Side view that highlights how the reduced density is achieved by 'skipping' a Si 'up' atom. [84]

the surface 'engineers' a shortening of the brillouin zone, by forming the striped domains, moving the high symmetry point away from the unstable phonon mode. **Figure 3.17** shows a graph of the formation enthalpy for silicene sheets with different widths. A maximally stable formation is found for domains 5 Si 'up' atoms wide. Crucially, all investigated widths, including a domain-free surface, are stable, with respect to bulk Si clustering. It is therefore expected to observe silicene domains with varied widths.

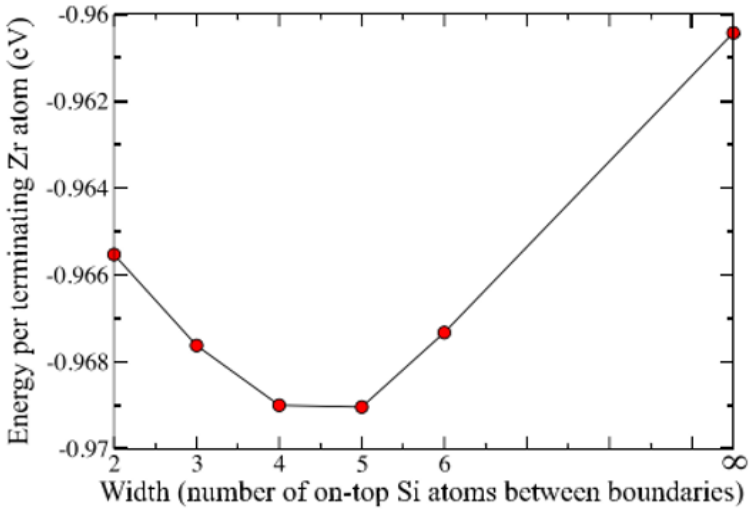

Figure 3.17: Stability of the silicene domain boundary width. The formation enthalpy per terminating Zr atom versus the stripe width.[84]

3.4 Other Epitaxial Silicene Systems

So far the experimental results for silicene on Ag(111), and ZrB_2(0001) thin films have been reviewed. These works comprise the majority of experimental research on silicene, but here for completeness investigations into silicene upon Ir(111), ZrC, and bulk ZrB_2 substrates are briefly reviewed.

3.4.1 Silicene on Ir(111)

Silicene on Ir (111) is produced in a similar manner to that of silicene on Ag (111): silicon is sublimated by direct current heating of a Si wafer onto the Ir (111) surface. However, in contrast to the Ag (111) system, deposition is carried out with the substrate at room temperature. Post deposition, the Ir (111) sample is annealed to 670 K for 30 mins [14]. **Figure 3.18a** shows a large scale STM image of the silicene on Ir (111) surface. A higher resolution image of the surface in **Fig. 3.18b** reveals a $(\sqrt{3} \times \sqrt{3})$ reconstruction of the silicene surface. LEED measurements performed on the surface shows that this $(\sqrt{3} \times \sqrt{3})$ reconstruction corresponds to a $(\sqrt{7} \times \sqrt{7})$ periodicity of the underlying Ir (111) substrate [14].

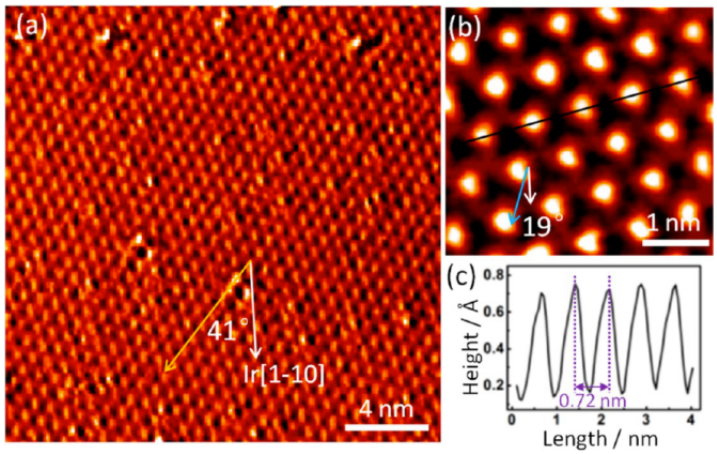

Figure 3.18: STM measurements of silicene on Ir(111).
(A) STM image of silicene on Ir (111), (V_0 = -1.45 V, I_0 = 0.25 nA). (B) High resolution STM image of $(\sqrt{3} \times \sqrt{3})$ silicene reconstruction, (V_0 = -1.5 V, I_0 = 0.05 nA). (C) Line profile indicated by the black line in (B) showing the periodicity of the $(\sqrt{3} \times \sqrt{3})$ structure.[14]

To confirm the presence of a silicene like layer on the Ir surface, DFT calculations were peformed. **Figure 3.19** shows the results where the $(\sqrt{3} \times \sqrt{3})$ reconstruction is given by a significant buckling of the relevant Si atoms [14]. This provides tantalising evidence for a third silicene system, although further characterisation is required to deduce the electronic structure of this silicene like layer.

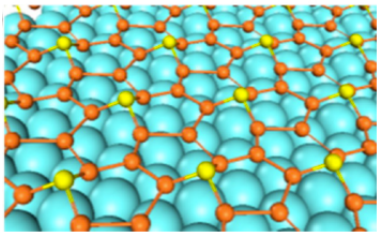

Figure 3.19: DFT model of silicene on Ir(111).
Perspective view of DFT results, revealing the buckling of the $(\sqrt{3} \times \sqrt{3})$ silicene reconstruction.[14]

3.4.2 Silicene on ZrC

Aizawa, *et. al* have shown that silicene can be grown upon a Zirconium Carbide (111) (ZrC) thin film [15]. The ZrC(111) surface is grown upon a Niobium Carbide (NbC) single crystal by electron beam heated evaporation of a sintered ZrC rod. Si is then deposited onto the ZrC(111) surface by direct current heating of a Si wafer with a deposition rate of $5 \times 10^{17} \mathrm{m}^{-2}\mathrm{s}^{-1}$, corresponding to 0.03 Si(111) double layers per second. RHEED, HREELS, and DFT have be used to investigate the Si surface that forms confirming the presence of a honeycomb Si lattice. In particular the phonon dispersion of the silicene sheet has been probed to infer experimental details that is then used to produce a model structure. **Figure 3.20** shows a DFT model of the silicene/ZrC(111) surface. it can be seen that a $(\sqrt{3} \times \sqrt{3})$ reconstruction of the silicene lattice matches a (2×2)reconstruction of the ZrC(111) surface. The lattice matching between the ZrC(111) surface and free-standing silicene lattice is greater than that of ZrB_2(0001) such that no domain boundary structure is observed.

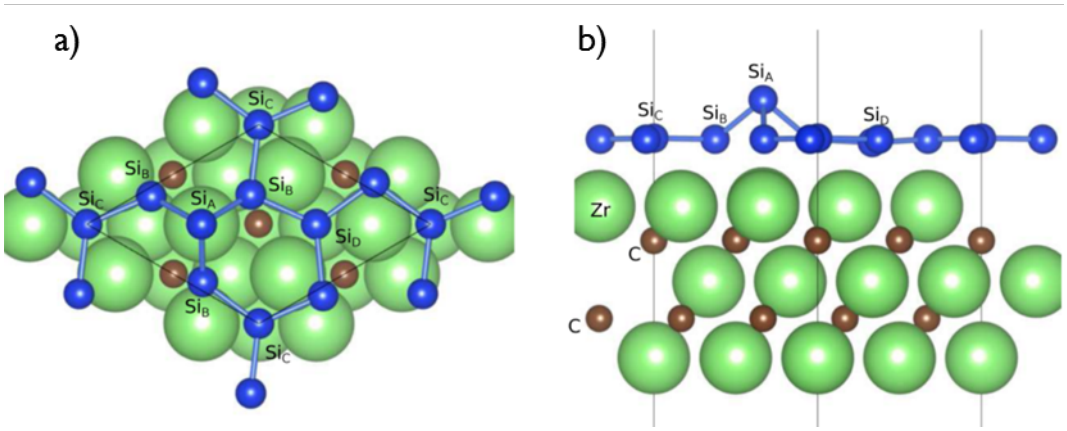

Figure 3.20: DFT model of silicene on ZrC(111).
(a) Top view of the silicene/ZrC(111) surface showing the three Si binding sites, Si_A, Si_B, and i_C at the Zr 'atop', Zr bridge and Zr hollow sites respectively. (b) Side view of the silicene/ZrC(111) surface revealing the buckled structure of the silicene lattice. [15]

3.4.3 Silicene on Bulk ZrB_2

Recently Aizawa *et. al* have performed analogous measurements, to those for silicene on ZrC(111), for silicene on bulk ZrB_2 [16]. Unlike other investigations into silicene on ZrB_2, where thin films have been used (see **section 3.3**), a ZrB_2 single crystal is used as the substrate. ZrB_2 single crystal rods are grown using radio-frequency heated floating zone methods [16]. A small sample disk is cut from the crystal and mirror polished. In vacuum, degassing to $1500\,\mathrm{K}$ is followed by repeated flashing to $> 2500\,\mathrm{K}$ to form a clean $ZrB_2(0001)$ surface. To form the silicene surface Si is deposited by direct current heating of a Si wafer using RHEED to confirm the presence of the $(\sqrt{3} \times \sqrt{3})\mathrm{R30}^o$ reconstructed silicene lattice. DFT models of the silicene surface have been used to calculate the phonon dispersion relationship of silicene on ZrB_2, which is then compared to experimentally obtained results from HREEL measurements. **Figure 3.21** highlights the key result from these investigations that indicate a good agreement between the calculated and measured phonon dispersion relations.

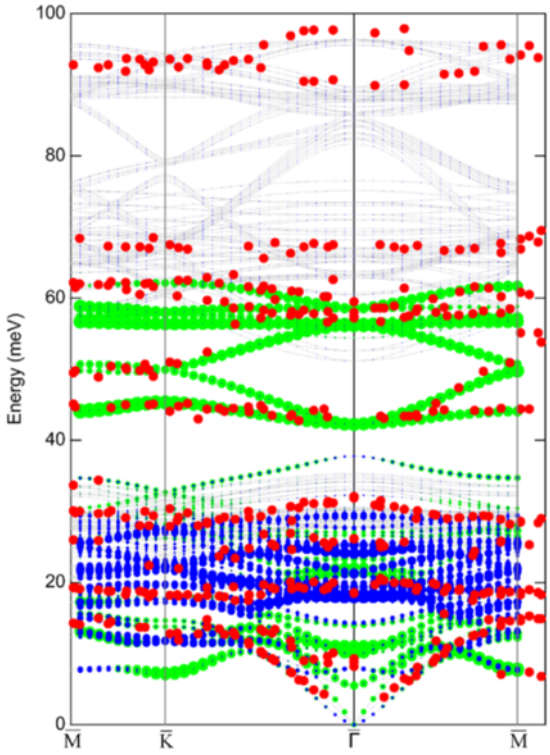

Figure 3.21: Comparison of calculated and experimentally obtained silicene/ZrB_2(0001) phonon dispersion.
Calculated phonon dispersion of silicene on ZrB_2(0001) surface (gray) compared to experimental data (red dots). The phonon partial density of states of the vertical/longitudinal component of silicene is indicated by tghe blue/green markers, respectively. Marker areas are proportional to the partial density of states. [16]

3.5 Multi-Layer Silicene on Ag(111)

The interactions between silicene and its supporting substrate heavily influence it's buckling and consequentially have a dramatic impact on the electronic properties of the observed surface. For graphene it has previously been observed that the electronic properties can be greatly influenced by producing multilayer structures [7] and in other layered materials such as the transition metal dichalcogenide MoS_2 interesting opto-electric transitions have been found [8, 87]. First principles investigations into multilayer silicene reveal that the expected electronic band dispersion of multi-layer free-standing silicene is greatly dependant on the stacking order of the silicene layers [88] and other investigations suggest that the effect of the substrate will influence these properties further [89]. Furthermore, there have been predictions for multi-layer silicene of interesting physical phenomena including a tunable bandgap [90], superconductivity [91], and behaviour as a quasi-topological insulator [64].

Recently De Padova, et al.[92] demonstrated that further Si deposition onto the (3×3) silicene reconstruction on Ag (111) can produce large areas of a new surface that could be multi-layer silicene. These new structures exhibit a $(\sqrt{3} \times \sqrt{3})\mathrm{R30^o}$ reconstruction with respect to the silicene (1×1) lattice. A similar surface is also observed with continued Si deposition onto the $(\sqrt{3} \times \sqrt{3})\mathrm{R30^o}$ silicene monolayer [14, 93]. The STM image in **Fig. 3.22** shows an island of $(\sqrt{3} \times \sqrt{3})\mathrm{R30^o}$ bilayer silicene that is approximately 0.2 nm above the (3×3) reconstructed monolayer.

Figure 3.23a-left shows a model of the silicene, (1×1) (black), (3×3) (red), $(\sqrt{3} \times \sqrt{3})\mathrm{R30^o}$ (green), and Ag (111) (blue) Brillouin zones. It is seen that the $\bar{K}$ point of the silicene (1×1) maps back onto the $\bar{\Gamma}$ point of the $(\sqrt{3} \times \sqrt{3})\mathrm{R30^o}$ reconstruction. **Figure 3.23b,c**

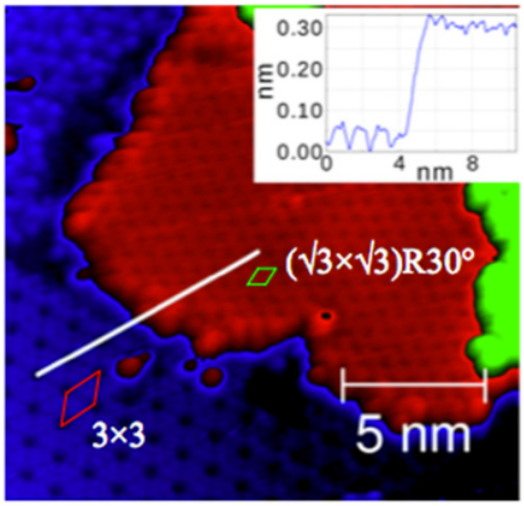

Figure 3.22: Multilayer silicene on Ag(111).
STM image of the multi-layer silicene surface grown on Ag (111) ($V_0 = -1.1V, I_0 = 0.33nA$). An island of $(\sqrt{3} \times \sqrt{3})\mathrm{R30^o}$ reconstructed silicene is ≈ 0.2 nm above the (3×3) monolayer silicene reconstruction.[94]

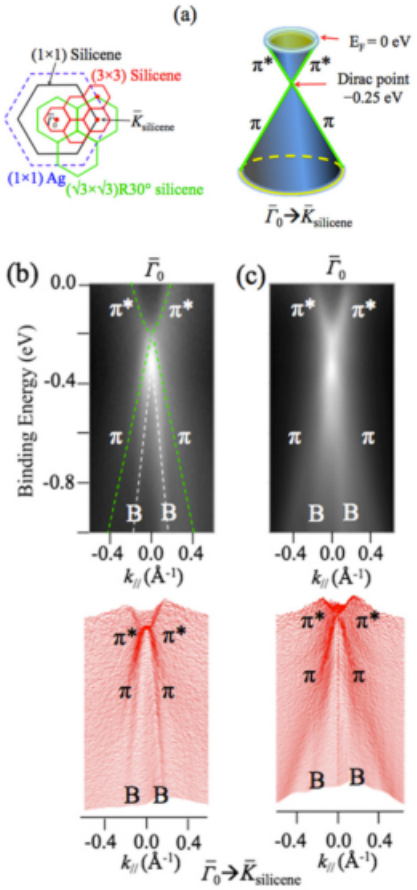

Figure 3.23: ARPES measurements of multi-layer silicon structures on Ag(111). Dirac cones for multilayer $(\sqrt{3} \times \sqrt{3})R30^o$ silicene islands on top the (3×3) monolayer. (A) LEFT: scheme of the Ag(111) (1×1) (blue), silicene (1×1) (black), silicene $(\sqrt{3} \times \sqrt{3})R30^o$ (green) Brillouin zones. RIGHT: Diagram of a Dirac cone, indicating the positions of the Dirac point and Fermi level for bilayer silicene on Ag (111). (B),(C) TOP: Band dispersion around $\bar{\Gamma}_0$ for 1.5 ML and 3 ML surfaces. BOTTOM: Waterfall of band dispersion line profiles to emphasise the Dirac cones.[94]

shows ARPES spectra performed along the $\bar{\Gamma}_0 - \bar{K}$ direction of the silicene surface providing a detailed electronic characterisation for 1.5 ML and 3 ML silicene surface respectively. The 1.5 ML spectra corresponds to a combination of the (3×3) and $(\sqrt{3} \times \sqrt{3})\mathrm{R30^o}$ reconstructions, whilst the 3 ML coverage is solely for the $(\sqrt{3} \times \sqrt{3})\mathrm{R30^o}$ surface. The spectra show that the multilayer surfaces still exhibit a linearly dispersive $\pi - \pi^*$ band structure, centred at the $\bar{K}$ point of the silicene Brillouin zone. This feature is associated to the Dirac cone of the multi-layer structure, **Fig. 3.23a-right** shows a schematic that shows the Dirac point is shifted -0.25 eV from the Fermi level. These results provide evidence for the formation of a layered silicon structure, that still at the 3 ML level exhibits electronic properties consistent with those expected for free-standing silicene.

The conductivities of the multi-layer silicon structures have been investigated by STS, and transport measurements [95]. **Figure 3.24a-c** show scanning electron microscopy (SEM) images of the Ag(111) surface at different Si coverages. The Si deposition

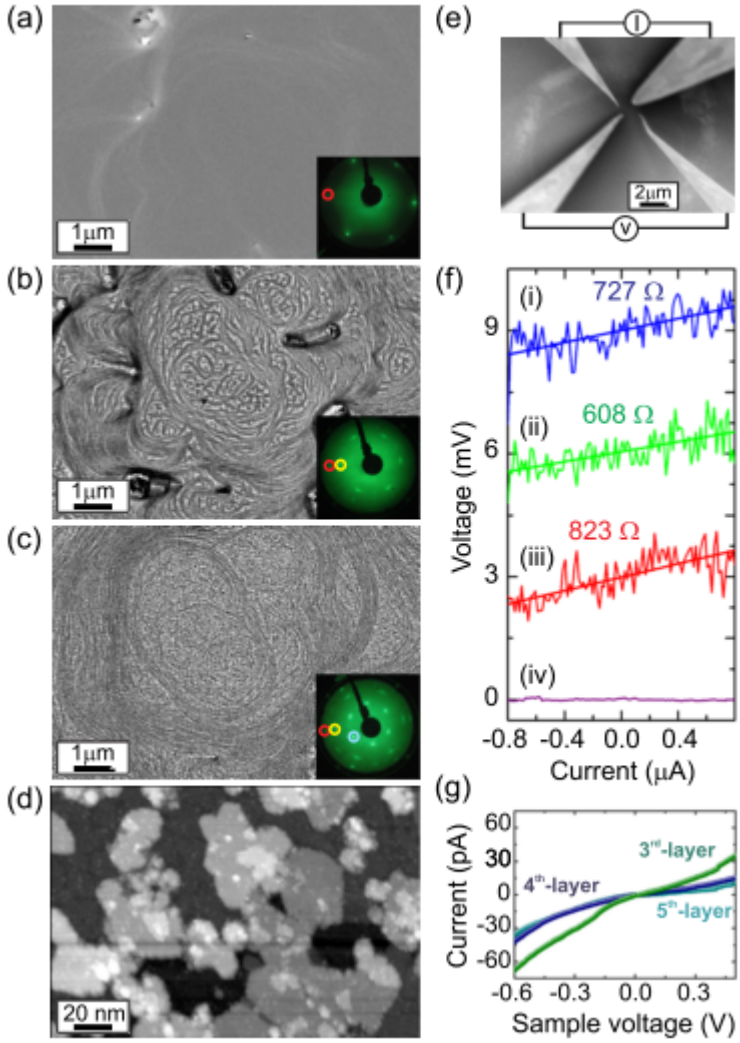

Figure 3.24: Morphology and conductivity of silicene surfaces on Ag(111). Evolution of the surface morphology as a function of the Si coverage on the A(111) surface observed by scanning electron microscopy. (a) Bare Ag surface. (b) Ag surface with $<$1 ML Si coverage. (c) Ag surface with $>$1 ML Si coverage. (d) Insets show LEED patterns where the red, yellow, and blue circles highlight the (1×1) Ag(111), (3×3) monolayer silicene, and $(\sqrt{3} \times \sqrt{3})$R30^o multi-layer silicon structures. (d) STM image of multilayer silicene surface similar to (c). Transport measurements of multilayer silicon structures. (e) SEM image of multi-layer silicon being contacted with four tungsten tips in a refion of the silver substrate surrounded by a blurred grey contour, corresponding to large step bunches. (f) Set of V-I curves measured on the multi-layer silicon with a square arrangement of the four probes. All the curves have been shifted for clarity. Curve (iv) highlights the occurrence of a short circuit by the Ag(111) suface due to the stronger compression of the multi-layer with the STM tips. (g) I(V) curves measured with STS on three adjacent silicon layers showing the $(\sqrt{3}\times\sqrt{3})$R30^o structure (V_0=-1.8V, I_0=1 nA)/ [95]

causes substantial changes to the surface morphology significantly increasing surface roughness. However, in the STM image of **Fig. 3.24d** shows that there are still large atomically flat areas. In **Fig. 3.24e** an SEM image of the surface shows four tungsten tips contacting the silicon surface. Transport measurements performed through these contacts are shown in **Fig. 3.24f**; the sheet resistance calculated from these is given as $6.5\,\mathrm{k}\Omega$ [95]. STS measurements performed on surfaces at different Si thickness's reveal that the conductivity of the Si structures decreases with increasing thickness. This is attributed to an increased decoupling between the Ag substrate and the silicon surface [95].

These results indicate that there are interesting electronic differences between the mono- and multi-layer Si structures that warrants further investigation. However, complementary studies have highlighted the need for caution as the observed silicene multilayers on Ag(111) bear significant resemblance to bulk Ag terminated Si(111) [96, 97]. It will therefore be of interest to investigate the effects of greater Si deposition onto other epitaxial silicene systems.

Chapter 4

Magnetic Interactions

It is the aim of this thesis to investigate the electronic and magnetic properties of epitaxial silicene. Although there have been predictions of interesting magnetic interactions intrinsic to free-standing silicene [61, 62], it is likely that for epitaxial systems magnetism will have to be induced by some means. Perhaps one of the most simple routes is to deposit magnetic adatoms onto the silicene surface, similarly to investigations of magnetism on epitaxial graphene [17–19]. It is therefore of interest to provide a summary of the magnetic interactions and effects that can manifest when magnetic atoms are placed upon conductive substrates, such as exchange, the Zeeman effect, and magnetic anisotropy. The majority of this chapter will focus upon the Kondo effect, and RKKY interaction as these phenomena are of key importance to interpreting the later experimental results of this thesis.

4.1 Exchange Interaction

The Pauli exclusion principles requires the total wave function of a pair of identical fermions to be antisymmetric with respect to exchange [98]. Consider a hydrogen like molecule where the electrons have a total wave function Ψ_T that can be expressed as the product of their spin and spatial wave functions ϕ and $\psi(\mathbf{r})$ respectively. An antisymmetric and symmetric linear combination of the spatial wave functions can be given by,

$$\Psi_A(\mathbf{r}_1, \mathbf{r}_2) = \frac{1}{\sqrt{2}} \left[\psi_a(\mathbf{r}_1)\psi_b(\mathbf{r}_2) - \psi_a(\mathbf{r}_2)\psi_b(\mathbf{r}_1)\right], \tag{4.1a}$$

$$\Psi_S(\mathbf{r}_1, \mathbf{r}_2) = \frac{1}{\sqrt{2}} \left[\psi_a(\mathbf{r}_1)\psi_b(\mathbf{r}_2) + \psi_a(\mathbf{r}_2)\psi_b(\mathbf{r}_1)\right], \tag{4.1b}$$

where orthogonality of the two electrons spatial wave functions $\psi_a(\mathbf{r})$ and $\psi_b(\mathbf{r})$ has been assumed. From the isolated Hamiltonian,

$$H_0 = -\frac{\hbar^2}{2m}(\nabla_1^2 + \nabla_2^2) - \frac{e^2}{\mathbf{r}_1} - \frac{e^2}{\mathbf{r}_2}, \tag{4.2}$$

the exchange interaction can be expressed as a perturbation,

$$H_{ex} = \frac{e^2}{\mathbf{R}_{ab}} + \frac{e^2}{\mathbf{r}_{12}} - \frac{e^2}{\mathbf{r}_{a1}} - \frac{e^2}{\mathbf{r}_{b2}} \tag{4.3}$$

where $\mathbf{R}_{ab}$ is the internuclear separation, such that the total Hamiltonian is $H = H_0 + H_{ex}$. The eigenvalues of the spatial Hamiltonian are then,

$$E_\pm = E_0 + \frac{C \pm J_{ex}}{1 \pm B}, \tag{4.4a}$$

$$C = \int \psi_a(\mathbf{r}_1)^2 \left(\frac{1}{\mathbf{R}_{ab}} + \frac{1}{\mathbf{r}_{12}} - \frac{1}{\mathbf{r}_{a1}} - \frac{1}{\mathbf{r}_{b2}}\right) \psi_b(\mathbf{r}_2)^2 d^3\mathbf{r}_1 d^3\mathbf{r}_2, \tag{4.4b}$$

$$B = \int \psi_b(\mathbf{r}_2)\psi_a(\mathbf{r}_2) d^3\mathbf{r}_2, \tag{4.4c}$$

$$J_{ex} = \int \psi_a^*(\mathbf{r}_1)\psi_b^*(\mathbf{r}_2) \left(\frac{1}{\mathbf{R}_{ab}} + \frac{1}{\mathbf{r}_{12}} - \frac{1}{\mathbf{r}_{a1}} - \frac{1}{\mathbf{r}_{b2}}\right) \psi_b(\mathbf{r}_1)\psi_a(\mathbf{r}_2) d^3\mathbf{r}_1 d^3\mathbf{r}_2, \tag{4.4d}$$

where C, B, and J_{ex} are the Coulomb, overlap, and exchange integrals respectively. From **eqn. 4.4** it can be seen that the exchange of the particles can act to reduce the energy of the system by an amount J_{ex} behaving as though it were a force.

Now consider the spin of the two electrons, again taking linear combinations of the two independent wavefunctions to give,

$$\phi_A(1,2) = \frac{1}{\sqrt{2}} \left(\phi_\uparrow(1)\phi_\downarrow(2) - \phi_\uparrow(2)\phi_\downarrow(1)\right) \tag{4.5a}$$

$$\phi_S(1,2) = \frac{1}{\sqrt{2}} \left(\phi_\uparrow(1)\phi_\downarrow(2) + \phi_\uparrow(2)\phi_\downarrow(1)\right). \tag{4.5b}$$

where ϕ_A gives the $\mathbf{S} = 0$ singlet state, and ϕ_S gives the $\mathbf{S} = 1$ triplet state. Now combining the spatial and spin wave functions gives,

$$\Psi_T^{singlet} = \phi_A(1,2)\Psi_S(\mathbf{r}_1, \mathbf{r}_2) \tag{4.6a}$$

$$\Psi_T^{triplet} = \phi_S(1,2)\Psi_A(\mathbf{r}_1, \mathbf{r}_2). \tag{4.6b}$$

Equation 4.6 shows that the spatially symmetric states that typically have a greater Coulomb interaction due to greater spatial confinement, can lower the total energy by anti-aligning the spins. The opposite is true for the more spatially diffuse triplet state.

4.2 Zeeman Effect

The Zeeman effect describes the energetic splitting of degenerate spin states due to their interaction with a magnetic field [99]. The interaction energy is given by,

$$H_{Zeeman} = -g\mu_B \mathbf{S} \cdot \mathbf{B}, \tag{4.7}$$

where g is the Landé g-factor, $\mu_B = 5.788 \times 10^{-2}$ meV·T^{-1} is the Bohr magneton, **B** is the magnetic field, and **S** is the total spin. **Figure 4.1** shows a diagram of the zeeman splitting of a spin-$1/2$ doublet. The linear splitting of the spin $+1/2$ (up arrow) and spin $-1/2$ (down arrow) as a function of magnetic field is seen.

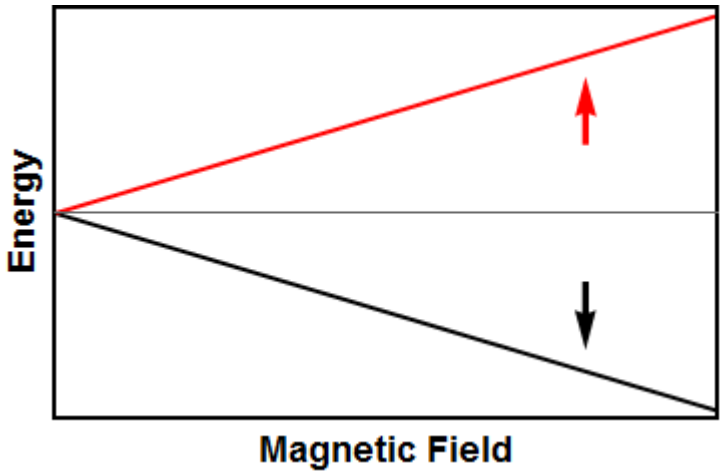

Figure 4.1: Zeeman splitting of an S=1/2 doublet.

4.3 Magnetic Anisotropy

The degeneracy of spin states can lifted by the interactions of the magnetic moment with it's surrounding environment, an interaction that is known as the crystal field effect [99]. The interactions with the surrounding environment can be complex, but can be approximated by a Hamiltonian of the form,

$$H_{CF} = \mathbf{S} \cdot \mathbf{D} \cdot \mathbf{S}, \tag{4.8}$$

where **D** is a real, symmetric tensor. By defining an appropriate axis with the eigenvectors of **D**, the Hamiltonian can be expressed as,

$$H_{CF} = D_{xx}S_x^2 + D_{yy}S_y^2 + D_{zz}S_z^2 \tag{4.9}$$

where S_x, S_y, and S_z are the spin matrices along the axis. Since the Hamiltonian will be unaffected by the addition of a constant, it can be simplified by,

$$\begin{aligned} H_{CF} &= D_{xx}S_x^2 + D_{yy}S_y^2 + D_{zz}S_z^2 - \frac{1}{2}(D_{xx} + D_{yy})(S_x^2 + S_y^2 + S_z^2) \\ &= \left[D_{zz} - \frac{1}{2}\left(D_{xx} + D_{yy}\right)\right] S_z^2 + \frac{1}{2}\left(D_x - D_y\right)\left(S_x^2 - S_y^2\right) \\ &= DS_z^2 + E\left(S_x^2 - S_y^2\right). \end{aligned} \tag{4.10}$$

In a system with axial symmetry the $D_{xx} = D_{yy}$ and as a result $E = 0$. The parameter D therefore acts to split the $(2S + 1)$ multiplet of spin states. The eigenvectors of the system with axial symmetry are therefore the same as those for S_z, and the corresponding eigenvalues are,

$$\varepsilon(m) = Dm^2 - \frac{1}{3}S(S + 1), \tag{4.11}$$

where $|m\rangle$ are the eigenvectors of S_z. For $D > 0$ the anisotropy favours lower m states, but with $D < 0$ the ground state is given by the higher spin projection configurations. If E is then treated perturbatively then it can be considered to mix, or tunnel, between states [99].

4.4 The Kondo Effect

Generally the resistance of a simple metal can be defined by electron-phonon scattering, phenomenologically described by the Bloch-Grüneisen formula[100, 101];

$$\rho(T) = \rho(0) + A\left(\frac{T}{\Theta_R}\right)^5 \int_0^{\frac{\Theta_R}{T}} \frac{x^5}{(e^x - 1)(1 - e^{-x})} dx \tag{4.12}$$

where, $\rho(0)$ is the residual scattering due to impurities, A is a constant, T is temperature, Θ_R is the Debye temperature[1]. As the temperature is reduced it would be expected that the resistivity of the metal would saturate at a value determined by the residual scattering of impurities. However, in 1934 *W. J. Hass* and *J. van Den Berg* detected an anomalous increases in the resistance of gold when cooled to approximately 8 K [103]. It took over 30 years for a theoretical understanding of the phenomena to emerge. *J. Kondo* explained the low temperature logarithmic increase in resistance as a consequence of conduction electrons exchange scattering off magnetic impurities in the host metal [104]. Later it was also shown that the effect can be interpreted by the Anderson model, upon a canonical transformation.

In this section the theoretical basis upon which to understand the Kondo effect is outlined, where emphasis is given to the determination of properties that can be directly accessed by experimental systems. In particular the results pertinent to the investigation of single magnetic atoms on conductive substrates by scanning tunnelling spectroscopy will be given. For a more complete description of the following overviews see [20, 105].

4.4.1 Electron Scattering

At the heart of the Kondo effect is a spin-flip electron scattering process that effectively anti-ferromagnetically couples the conduction band electrons of the metal host to the magnetic moment of the impurity. *J. Kondo* showed how the s-d electron scattering model could be used to gain insight into the observed logarithmic increase in resistance of dilute magnetic alloys at low temperatures. Here a brief overview of the use of Greens functions as applied to basic scattering theory is provided. Although the techniques outlined are not directly applicable to the more complex perturbation theory used by J. Kondo, what shall be apparent are certain general features of scattering and so called virtual resonances. The Anderson model, as applied to Kondo theory, will then be outlined to gain greater insight into the microscopic scattering processes at play that give rise to the Kondo effect.

[1] The Debye temperature is the highest temperature that can be achieved by a single normal vibration of the electrons in a crystal. It is proportional to the number density of atoms and the effective speed of sounds in the crystal [102]

Green Functions

In the following discussions of scattering processes it will be of use to define and to become familiar with the application of Green functions[2]. One of the most simple example of these are the single-particle Green functions that are related to single creation or annihilation operators of a system. The goal of this approach is define the single-particle spectral function that gives information upon the single-particle excitations of the system. The spectral function can also be associated to the density of states of the system, a property that can be directly probed by scanning tunnelling spectroscopy.

Given a differential operator L that has a set of complete eigenvectors $\Psi_n(x)$ and eigenvalues λ_n such that,

$$L\Psi_n(x) = \lambda_n \Psi_n(x), \tag{4.13}$$

and completeness is defined as,

$$\delta(x - x') = \sum_{n=0}^{\infty} \Psi_n^{\dagger}(x)\Psi_n(x'), \tag{4.14}$$

it is in principle possible to construct a Green's function $G(x, x')$ from the eigenvectors and eigenvalues that satisfy,

$$\begin{aligned} LG(x, x') &= \delta(x - x') \\ &= \sum_{n=0}^{\infty} \Psi_n^{\dagger}(x)\Psi_n(x'). \end{aligned} \tag{4.15}$$

It then follows that

$$G(x, x') = \sum_{n=0}^{\infty} \frac{\sum_{n=0}^{\infty} \Psi_n^{\dagger}(x)\Psi_n(x')}{\lambda_n}, \tag{4.16}$$

since application of L to each side of this equation yields the completeness relation, as assumed. From **eqn. 4.16** it can be seen that by finding the solution of $G(x, x')$ one can in principle learn about the eigenvectors and eigenvalues of a system. For example let us examine the time-dependent Schrödinger equation

$$i\hbar \frac{\partial}{\partial t}\Psi(x) = H\Psi(x). \tag{4.17}$$

This equation can be rearranged into,

$$\left(i\hbar \frac{\partial}{\partial t} - H\right)\Psi(x) = 0, \tag{4.18}$$

where it is now clear that this has a form such that L in **eqn. 4.15** is equal to the

[2] A simple introduction to the use of Greens functions in scattering theory can be found in reference [98]

bracketed section on the left hand side of the above equation. It is therefore possible to examine the properties of the time-dependent Schrödinger equation of a system by solving **eqn. 4.18** and **eqn. 4.15** for G.

Single-Particle Green Functions

In an interacting many-particle system the ground state eigenvector can be denoted in Dirac notation as $|\Psi(t=0)\rangle$. Importantly $|\Psi(t=0)\rangle$ is time-independent such that,

$$H\,|\Psi(t=0)\rangle = E_0\,|\Psi(t=0)\rangle\,. \tag{4.19}$$

Then let $\psi(x,t)$ denote the field operator that annihilates a field quantum at space-spin point x at time t, and $\psi(x,t)^\dagger$ be the corresponding creation operator. The fermion single-particle Green functions can then be defined as,

$$G^{\pm}(x,t;x',t') \equiv \mp i\Theta(t \mp t')\langle\{\psi(x,t),\psi^\dagger(x',t')\}\rangle, \tag{4.20}$$

where the $\{...\}$ is the standard anti-commutator and the minus(plus) sign denotes the retarded(advanced) Green function . It is noted here that owing to the step function Θ the retarded(advanced) Green function is nonzero only for $t > t'(t < t')$. For later convenience the greater and lesser Green functions are defined,

$$G^{>}(x,t;x',t') \equiv -i\langle\psi(x,t)\psi^\dagger(x',t')\rangle, \tag{4.21}$$

$$G^{<}(x,t;x',t') \equiv i\langle\psi^\dagger(x',t')\psi(x,t)\rangle. \tag{4.22}$$

The retarded and advanced Green functions can then be expressed in terms of the greater and lesser Green functions,

$$G^{R}(x,t;x',t') = \Theta(t-t')\left[G^{>}(x,t;x',t') - G^{<}(x,t;x',t')\right], \tag{4.23}$$

$$G^{A}(x,t;x',t') = \Theta(t'-t)\left[G^{<}(x,t;x',t') - G^{>}(x,t;x',t')\right]. \tag{4.24}$$

Grand Canonical Ensemble

To understand the Kondo effect it is necessary to consider a macroscopic system with many particles in thermodynamic equilibrium at a temperature T. In general there are two ensembles to describe the thermal and quantum average $\langle...\rangle$ of many-body systems. The first, and more simple, is the canonical ensemble in which the number of particles N is fixed, but the system can exchange energy with an external reservoir. The second is the grand canonical ensemble in which the system can exchange both particles and energy

with a reservoir. As a result the chemical potential μ, which determines the average number of particles in the system, must be considered in addition to the temperature. For an arbitrary operator A, the quantum statistical-mechanical average or expectation value can be defined as,

$$\langle A \rangle = \frac{1}{Z} \sum_n \langle n| A |n\rangle e^{-\beta E_n}, \tag{4.25}$$

where $|n\rangle$ are the normalised eigenstates of the Hamiltonian H with eigenvalues E_n, $\beta = 1/k_B T$, and $Z = \sum_n e^{-\beta E_n}$ is the partition function. Using the density matrix,

$$\rho = \frac{1}{Z} e^{-\beta(H-\mu N)}, \tag{4.26}$$

where

$$Z = Tr(e^{-\beta(H-\mu N)}). \tag{4.27}$$

the expectation value can then be defined as,

$$\langle A \rangle = Tr(\rho A). \tag{4.28}$$

In these equations N is the number operator that counts the total number of particles in the system. To evaluate the trace in **eqn. 4.28** the basis set of $H - \mu N$ should be used, which corresponds to measuring the single-particle energies with respect to the chemical potential. The time dependence of an arbitrary operator A is then defined as,

$$A(t) \equiv e^{i(H-\mu N)t} A e^{-i(H-\mu N)t}. \tag{4.29}$$

For brevity, in the following sections the operator $H - \mu N$ will be simplified to H, with its eigenvectors and eigenvalues written as $|n\rangle$ and E_n respectively, such that

$$H |n\rangle = E_n |n\rangle . \tag{4.30}$$

Spectral Function for Non-interacting Electrons

In the Kondo effect the electrons of the system behave in a highly correlated manner, but as a first step the **k**-space Green functions for a simplistic system of noninteracting electrons will be investigated. Although this seems like a significant simplification it can be shown [20] that in general it is a reasonable approximation to consider the electrons in a metal, close to the Fermi Level, to behave as non-interacting particles. The Hamiltonian for this system has the form,

$$H_0 = \sum_{\mathbf{k},\sigma} \epsilon_{\mathbf{k}} c^\dagger_{\mathbf{k},\sigma} c_{\mathbf{k},\sigma} \tag{4.31}$$

where, $c^\dagger_{\mathbf{k},\sigma}$ and $c_{\mathbf{k},\sigma}$ are the creation and annihilation operators of Bloch states $\phi_{\mathbf{k},\sigma}(r)$ with wavevector $\mathbf{k}$, spin σ, and energy $\epsilon_{\mathbf{k}}$. The subscript 0 denotes that this is the Hamiltonian of a non-interacting system. $c^\dagger_{\mathbf{k},\sigma}$ and $c_{\mathbf{k},\sigma}$ obey the standard fermion anti-commutator relations,

$$\{c_{\mathbf{k}\sigma}, c^\dagger_{\mathbf{k'},\sigma'}\} = c_{\mathbf{k}\sigma}c^\dagger_{\mathbf{k'},\sigma'} + c^\dagger_{\mathbf{k'},\sigma'}c_{\mathbf{k}\sigma} = \delta_{\mathbf{k},\mathbf{k'}}\delta_{\sigma,\sigma'} \tag{4.32a}$$

$$\{c_{\mathbf{k},\sigma}, c_{\mathbf{k'},\sigma'}\} = c_{\mathbf{k},\sigma}c_{\mathbf{k'},\sigma'} + c_{\mathbf{k'},\sigma'}c_{\mathbf{k},\sigma} = 0. \tag{4.32b}$$

H_0 is invariant under translation for $\mathbf{k}$, since the is no external potential, and σ. As such the Green functions of H will also be invariant in $\mathbf{k}$ and σ. The retarded Green function can therefore be expressed as,

$$G^R_0(\mathbf{k},\sigma;t-t') = -i\Theta(t-t')\langle\{c_{\mathbf{k}\sigma}(t), c^\dagger_{\mathbf{k},\sigma}(t)\}\rangle, \tag{4.33}$$

To express the above Green function the time dependence of the fermion operators must be determined. Since,

$$c_{\mathbf{k},\sigma}(t) = e^{iHt}c_{\mathbf{k},\sigma}e^{-iHt}, \tag{4.34}$$

the derivative with respect to time can be given as,

$$\begin{aligned}
\frac{d}{dt}c_{\mathbf{k},\sigma}(t) &= e^{iHt}\frac{d}{dt}\left(c_{\mathbf{k},\sigma}e^{-iHt}\right) + \frac{d}{dt}e^{iHt}\left(c_{\mathbf{k},\sigma}e^{-iHt}\right) \\
&= e^{iHt}\left(-ic_{\mathbf{k},\sigma}e^{-iHt}H\right) + iHe^{iHt}\left(c_{\mathbf{k},\sigma}e^{-iHt}\right) \\
&= i\left(He^{iHt}c_{\mathbf{k},\sigma}e^{-iHt} - e^{iHt}c_{\mathbf{k},\sigma}e^{-iHt}H\right) \\
&= i[H, c_{\mathbf{k},\sigma}(t)].
\end{aligned} \tag{4.35}$$

Making use of the fermion anticommutators in **eqn. 4.32** $[H, c_{\mathbf{k},\sigma}(t)]$ can be expressed as,

$$\begin{aligned}
[H, c_{\mathbf{k},\sigma}(t)] &= Hc_{\mathbf{k},\sigma}(t) - c_{\mathbf{k},\sigma}(t)H \\
&= \sum_{\mathbf{k'},\sigma}\epsilon_{\mathbf{k'}}c^\dagger_{\mathbf{k'},\sigma'}(t)c_{\mathbf{k'},\sigma'}(t)c_{\mathbf{k},\sigma}(t) - c_{\mathbf{k},\sigma}(t)\sum_{\mathbf{k'},\sigma'}\epsilon_{\mathbf{k'}}c^\dagger_{\mathbf{k'},\sigma'}(t)c_{\mathbf{k'},\sigma'}(t) \\
&= -\sum_{\mathbf{k'},\sigma}\epsilon_{\mathbf{k'}}c^\dagger_{\mathbf{k'},\sigma'}(t)c_{\mathbf{k},\sigma}(t)c_{\mathbf{k'},\sigma'}(t) - \epsilon_{\mathbf{k}}\left(1 - c^\dagger_{\mathbf{k},\sigma}(t)c_{\mathbf{k},\sigma}(t)\right)c_{\mathbf{k},\sigma}(t) \\
&= -\epsilon_{\mathbf{k}}\left(1 - c_{\mathbf{k},\sigma}(t)c^\dagger_{\mathbf{k},\sigma}(t)\right)c_{\mathbf{k},\sigma}(t) - \epsilon_{\mathbf{k}}\left(1 - c^\dagger_{\mathbf{k},\sigma}(t)c_{\mathbf{k},\sigma}(t)\right)c_{\mathbf{k},\sigma}(t) \\
&= -\epsilon_{\mathbf{k}}\left(\left(1 - c_{\mathbf{k},\sigma}(t)c^\dagger_{\mathbf{k},\sigma}(t)\right) + \left(1 - c^\dagger_{\mathbf{k},\sigma}(t)c_{\mathbf{k},\sigma}(t)\right)\right)c_{\mathbf{k},\sigma}(t) \\
&= -\epsilon_{\mathbf{k}}\left(2 - \left(c_{\mathbf{k},\sigma}(t)c^\dagger_{\mathbf{k},\sigma}(t) + c^\dagger_{\mathbf{k},\sigma}(t)c_{\mathbf{k},\sigma}(t)\right)\right)c_{\mathbf{k},\sigma}(t) \\
&= -\epsilon_{\mathbf{k}}\left(2 - (1)\right)c_{\mathbf{k},\sigma}(t) \\
&= -\epsilon_{\mathbf{k}}c_{\mathbf{k},\sigma}(t),
\end{aligned} \tag{4.36}$$

and therefore,

$$\frac{d}{dt}c_{\mathbf{k},\sigma}(t) = -i\epsilon_{\mathbf{k}}c_{\mathbf{k},\sigma}(t). \tag{4.37}$$

Following a similar procedure will also lead to,

$$\frac{d}{dt}c^{\dagger}_{\mathbf{k},\sigma}(t) = i\epsilon_{\mathbf{k}}c^{\dagger}_{\mathbf{k},\sigma}(t). \tag{4.38}$$

Now it is a matter of solving these differential equations.

$$\begin{aligned}
\frac{d}{dt}c_{\mathbf{k},\sigma}(t) &= -i\epsilon_{\mathbf{k}}c_{\mathbf{k},\sigma}(t) \\
\frac{1}{c_{\mathbf{k},\sigma}(t)}dc_{\mathbf{k},\sigma}(t) &= -i\epsilon_{\mathbf{k}}dt \\
\int \frac{1}{c_{\mathbf{k},\sigma}(t)}dc_{\mathbf{k},\sigma}(t) &= \int -i\epsilon_{\mathbf{k}}dt \\
ln(c_{\mathbf{k},\sigma}(t)) &= -i\epsilon_{\mathbf{k}}t + a \\
c_{\mathbf{k},\sigma}(t) &= e^{-i\epsilon_{\mathbf{k}}t+a} \\
c_{\mathbf{k},\sigma}(t) &= e^{-i\epsilon_{\mathbf{k}}t} + e^{a} \\
c_{\mathbf{k},\sigma}(t) &= Ae^{-i\epsilon_{\mathbf{k}}t}.
\end{aligned} \tag{4.39}$$

From **eqn. 4.34** for $t = 0$, $c_{\mathbf{k},\sigma}(0) = c_{\mathbf{k},\sigma}$ and therefore $A = c_{\mathbf{k},\sigma}$. This gives the simple form for the time dependent annihilation operator for noninteracting electrons,

$$c_{\mathbf{k},\sigma}(t) = e^{-i\epsilon_{\mathbf{k}}t}c_{\mathbf{k},\sigma}, \tag{4.40}$$

and a similar procedure gives the time dependent creation operator,

$$c^{\dagger}_{\mathbf{k},\sigma}(t) = e^{i\epsilon_{\mathbf{k}}t}c^{\dagger}_{\mathbf{k},\sigma}. \tag{4.41}$$

With the forms of the time dependent operators now known the greater Green function $G_0^{>}$ can be defined,

$$\begin{aligned}
G_0^{>}(\mathbf{k},\sigma;t-t') &= -i\langle c_{\mathbf{k},\sigma}(t)c^{\dagger}_{\mathbf{k},\sigma}(t')\rangle \\
&= -ie^{-i\epsilon_{\mathbf{k}}t}e^{-i\epsilon_{\mathbf{k}}t'}\langle c_{\mathbf{k},\sigma}c^{\dagger}_{\mathbf{k},\sigma}\rangle \\
&= -ie^{-i\epsilon_{\mathbf{k}}(t-t')}\langle c_{\mathbf{k},\sigma}c^{\dagger}_{\mathbf{k},\sigma}\rangle \\
&= -ie^{-i\epsilon_{\mathbf{k}}(t-t')}\left(1 - \langle c^{\dagger}_{\mathbf{k},\sigma}c_{\mathbf{k},\sigma}\rangle\right) \\
&= -ie^{-i\epsilon_{\mathbf{k}}(t-t')}\left(1 - \langle n_{\mathbf{k},\sigma}\rangle\right) \\
&= -ie^{-i\epsilon_{\mathbf{k}}(t-t')}\left(1 - n_F(\epsilon_{\mathbf{k}})\right),
\end{aligned} \tag{4.42}$$

where,

$$n_F(\omega) = \frac{1}{e^{\frac{\omega}{k_BT}}} \tag{4.43}$$

is the Fermi-Dirac distribution function. Calculation of the lesser Green function through similar procedures gives,

$$G_0^<(\mathbf{k},\sigma;t-t') = ie^{-i\epsilon_\mathbf{k}(t-t')}n_F(\epsilon_\mathbf{k}). \tag{4.44}$$

Now that the greater and lesser Green functions have been defined the retarded Green function can be calculated by,

$$\begin{aligned} G_0^R(\mathbf{k},\sigma;t-t') &= \Theta(t-t')\left[G_0^>(\mathbf{k},\sigma;t-t') - G_0^<(\mathbf{k},\sigma;t-t')\right] \\ &= \Theta(t-t')\left[-ie^{-i\epsilon_\mathbf{k}(t-t')}\left(1-n_F(\epsilon_\mathbf{k})\right) - ie^{-i\epsilon_\mathbf{k}(t-t')}n_F(\epsilon_\mathbf{k})\right] \\ &= -i\Theta(t-t')e^{-i\epsilon_\mathbf{k}(t-t')}. \end{aligned} \tag{4.45}$$

Next the Fourier transform of the system is taken to first yield,

$$\begin{aligned} \int\left(i\hbar\frac{\partial}{\partial t} - H\right)G_0^R(t-t')e^{\frac{i}{\hbar}\omega^+(t-t')}\,d(t-t') &= \int\delta(t-t')e^{\frac{i}{\hbar}\omega^+(t-t')}\,d(t-t') \\ \int i\hbar\frac{\partial}{\partial t}G_0^R(t-t')e^{i\frac{i}{\hbar}\omega^+(t-t')}\,d(t-t') - H\int G_0^R(t-t')e^{i\frac{i}{\hbar}\omega^+(t-t')} &= e^{i\frac{i}{\hbar}\omega^+(0)}. \end{aligned} \tag{4.46}$$

Then making use of,

$$\hat{f}(\nu) = \int f(x)e^{-i\nu x}\,dx, \tag{4.47a}$$

$$(i\nu)^n\hat{f}(\nu) = \int\frac{\partial^n}{\partial x^n}f(x)e^{-i\nu x}\,dx \tag{4.47b}$$

eqn. 4.46 becomes,

$$\begin{aligned} i\hbar\left(-\frac{i}{\hbar}\omega^+\right)G_0^R(\omega) - HG_0^R(\omega) &= 1, \\ \left(\omega^+ - H\right)G_0^R(\omega) &= 1, \end{aligned} \tag{4.48}$$

where $\omega^+ = \omega + i\eta$ and η is a positive infinitesimal. Now the operator equation of the system is given by,

$$\left(\omega + i\eta - H\right)G_0^R(\omega) = I. \tag{4.49}$$

Now the Fourier transform of G_0^R is explicitly taken to express the Lehmann, or spectral, representation of the retarded Green function $G_0^R(\omega)$ to give

$$\begin{aligned} G_0^R(\mathbf{k},\sigma;\omega) &= \int_{-\infty}^{\infty}dt\,e^{i\omega t}\left(-i\Theta(t)e^{-i\epsilon_\mathbf{k}t}\right) \\ &= -i\int_0^\infty dt\,e^{i(\omega-\epsilon_\mathbf{k})t}. \end{aligned} \tag{4.50}$$

Equation 4.50 does not converge at its upper limit; to overcome this we let $\omega \to \omega + i\eta$, where $\eta = 0^+$ is a positive infinitesimal. Redefining G_0^R to be,

$$\begin{aligned} G_0^R(\mathbf{k},\sigma;\omega) &= -i\int_0^\infty dt\, e^{i(\omega-\epsilon_\mathbf{k}+i\eta)t} \\ &= -\frac{i}{i(\omega-\epsilon_\mathbf{k}+i\eta)}\left[e^{i(\omega-\epsilon_\mathbf{k}+i\eta)t}\right]_0^\infty \\ &= -\frac{1}{\omega-\epsilon_\mathbf{k}+i\eta}\left[e^{i(\omega-\epsilon_\mathbf{k})t}e^{-\eta t}\right]_0^\infty \\ &= -\frac{1}{\omega-\epsilon_\mathbf{k}+i\eta}\left[\left(e^{i(\omega-\epsilon_\mathbf{k})t}\cdot 0\right)-(1\cdot 1)\right] \\ &= \frac{1}{\omega-\epsilon_\mathbf{k}+i\eta} \end{aligned} \tag{4.51}$$

Now that the retarded Green function has been calculated in its spectral form the spectral function $A(\mathbf{k},\sigma,\omega)$ can be expressed as,

$$A(\mathbf{k},\sigma,\omega) = -\frac{1}{\pi} Im\left(G_0^R(\mathbf{k},\sigma,\omega)\right). \tag{4.52}$$

Making use of,

$$\begin{aligned} Im\left(\frac{1}{x+i\eta}\right) &= -\frac{\eta}{x^2+\eta^2}, \\ &= -\pi\delta(x), \end{aligned} \tag{4.53}$$

and **eqn. 4.51** the spectral function for the system of non-interacting electrons is given by,

$$A(\mathbf{k},\sigma,\omega) = \delta(\omega-\epsilon_\mathbf{k}). \tag{4.54}$$

In the non-interacting system the spectral function is only non-zero when $\omega = \epsilon_\mathbf{k}$, the energy of a particle in a state $(\mathbf{k},\sigma)$ from H_0.

Finally from the spectral function the single-particle density of states (DOS) can be defined by summing over all $\mathbf{k}$,

$$DOS(\omega) = \frac{1}{\Omega}\sum_{\mathbf{k},\sigma} A(\mathbf{k},\omega), \tag{4.55}$$

where Ω is the reciprocal space volume of the system.

In this section it has been shown how one can use the Green functions of a system to evaluate a number of interesting physical properties of that system. In the case of a non-interacting system of electrons the Green functions are somewhat trivial to derive, but in general this is not the case. At the end the DOS of the non-interacting system of electrons has been calculated, this value is directly experimentally obtained from scanning tunnelling spectroscopy, differential conductance (dI/dV) measurements. So from this

it is clear how scanning tunnelling spectroscopy can yield interesting information on the a system.

Potential Scattering and the Friedel Sum Rule

In the previous section a detailed derivation of the spectral function and density of states of a system of non-interacting electrons was given. It is now the aim of this section to highlight the results obtained from similar techniques and show how these can be used to gain insight into the scattering processes that occur when an impurity ion is placed with a metal.

An impurity, within a host metal, can have an excess of charge, relative to the host, such that there is an effective Coulomb potential, $V_{imp}^{eff}(r)$. The charge of the impurity will be screened by electrons in the conduction band of the metal host. The combined Hamiltonian is given by,

$$H = \sum_{\mathbf{k},\sigma} \epsilon_{\mathbf{k}} c^{\dagger}_{\mathbf{k},\sigma} c_{\mathbf{k},\sigma} + \sum_{\mathbf{k},\mathbf{k'},\sigma} V_{\mathbf{k},\mathbf{k'}} c^{\dagger}_{\mathbf{k},\sigma} c_{\mathbf{k'},\sigma} \tag{4.56}$$

where, the first sum term is the same as for the unperturbed system (**eqn. 4.31**) and $V_{\mathbf{k},\mathbf{k'}} = \langle \mathbf{k} | V_{imp}^{eff} | \mathbf{k'} \rangle$. This Hamiltonian can be diagonalised into the form

$$H = \sum_{\alpha,\sigma} \epsilon_{\alpha} c^{\dagger}_{\alpha,\sigma} c_{\alpha,\sigma}, \tag{4.57}$$

where $c^{\dagger}_{\alpha,\sigma}(c_{\alpha,\sigma})$ is the creation(annihilation) operator of an eigenstate with energy ϵ_{α} and spin σ. In this form it is trivial to see from the previous section that the retarded Green function $G^{R}_{\alpha\alpha'}$ will have the form,

$$G^{R}_{\alpha\alpha'}(\alpha,\sigma;\omega) = \frac{\delta_{\alpha\alpha'}}{(\omega - \epsilon_{\alpha} + i\eta)}, \tag{4.58}$$

and that the density of states will be given by,

$$DOS(\omega) = -\frac{1}{\pi} Im\left(Tr(G^{R}(\omega))\right). \tag{4.59}$$

However, the particular property of interest to evaluate here is the change in density of states due to the impurity. To examine this perturbatively, H in the operator equation of **eqn. 4.49** can be redefined to $H = H_0 + V$, where H_0 and G^{R}_{0} are the Hamiltonian and respective Green function of the non-interacting system giving,

$$(\omega + i\eta - H_0 - V)\, G^{R}(\omega) = I. \tag{4.60}$$

Now using that from **eqn. 4.49** $G_0^R = (\omega + i\eta - H_0)^{-1}$ it can be seen that,

$$\begin{aligned}
(\omega + i\eta - H_0 - V)\, G^R(\omega) &= I \\
(\omega + i\eta - H_0)\, G^R(\omega) &= VG^R(\omega) + I \\
G_0^R(\omega)\,(\omega + i\eta - H_0)\, G^R(\omega) &= G_0^R(\omega)VG^R(\omega) + G_0^R(\omega) \\
G^R(\omega) &= G_0^R(\omega)VG^R(\omega) + G_0^R(\omega).
\end{aligned} \tag{4.61}$$

Equation 4.61 can be solved iteratively obtaining a solution as a power series in V of the form,

$$G^R(\omega) = G_0^R(\omega) + G_0^R(\omega)T(\omega^+)G_0^R(\omega), \tag{4.62}$$

where T is given by,

$$\begin{aligned}
T(\omega^+) &= V + VG_0^R(\omega^+)V + VG_0^R(\omega^+)VG_0^R(\omega^+)V + ... \\
&= V\left(I - G_0^R(\omega^+)V\right)^{-1}.
\end{aligned} \tag{4.63}$$

The change in the density of states induced by the impurity, $\rho_{imp}(\omega) = \rho(\omega) - \rho_0(\omega)$ can be given by,

$$\Delta\rho(\omega) = -\frac{1}{\pi} Im\left(Tr\left(G^R(\omega) - G_0^R(\omega)\right)\right) \tag{4.64}$$

From the matrix relation,

$$\begin{aligned}
Tr(ln(\mathbf{A})) &= ln(det(\mathbf{A})), \\
\frac{\partial}{\partial\omega} Tr\left(ln\left(\frac{\delta_{\alpha,\alpha'}}{\omega + i\eta - \epsilon_\alpha}\right)\right) &= \frac{\partial}{\partial\omega} ln\left(det\left(\frac{\delta_{\alpha,\alpha'}}{\omega + i\eta - \epsilon_\alpha}\right)\right) \\
-Tr\left(\frac{\delta_{\alpha,\alpha'}}{\omega + i\eta - \epsilon_\alpha}\right) &= \frac{\partial}{\partial\omega} ln\left(det\left(\frac{\delta_{\alpha,\alpha'}}{\omega + i\eta - \epsilon_\alpha}\right)\right)
\end{aligned} \tag{4.65}$$

therefore,

$$Tr(G^R(\omega)) = -\frac{\partial}{\partial\omega} ln\left(det\left(G^R(\omega)\right)\right). \tag{4.66}$$

The change in the denisty of states can then be re-expressed as,

$$\rho_{imp}(\omega) = \frac{1}{\pi} Im\left(\frac{\partial}{\partial\omega} ln\left(det\left(G^R(\omega)(G_0^R)^{-1}\right)\right)\right) \tag{4.67}$$

Then solving **eqn. 4.61** for $G^R(\omega)$,

$$\begin{aligned} G^R(\omega) &= G_0^R(\omega) + G_0^R(\omega)VG^R(\omega) \\ G^R(\omega)(G^R(\omega))^{-1} &= G_0^R(\omega)(G^R(\omega))^{-1} + G_0^R(\omega)VG^R(\omega)(G^R(\omega))^{-1} \\ I &= G_0^R(\omega)(G^R(\omega))^{-1} + G_0^R(\omega)V \\ \left(I - G_0^R(\omega)V\right) &= G_0^R(\omega)(G^R(\omega))^{-1} \\ \left(I - G_0^R(\omega)V\right) G^R(\omega) &= G_0^R(\omega)(G^R(\omega))^{-1}G^R(\omega) \\ \left(I - G_0^R(\omega)V\right) G^R(\omega) &= G_0^R(\omega) \\ G^R(\omega) &= \left(I - G_0^R(\omega)V\right)^{-1} G_0^R(\omega) \end{aligned} \tag{4.68}$$

and substituting into **eqn. 4.67** gives,

$$\rho_{imp}(\omega) = \frac{1}{\pi} Im \left(\frac{\partial}{\partial \omega} ln \left(det \left((I - G_0^R(\omega)V)^{-1} \right) \right) \right). \tag{4.69}$$

In the above equation $(I - G_0^R(\omega)V)^{-1}$ can be replaced by $T(\omega^+)$ since V is independent of ω giving,

$$\rho_{imp}(\omega) = \frac{1}{\pi} Im \left(\frac{\partial}{\partial \omega} ln \left(det T(\omega^+) \right) \right) \tag{4.70}$$

If the phase shift $\eta(\omega)$ is defined as,

$$\eta(\omega) = Arg\, det \left(T(\omega^+) \right), \tag{4.71}$$

then the change in density of states due to the impurity $\rho_{imp}(\omega)$ becomes,

$$\rho_{imp}(\omega) = \frac{1}{\pi} \frac{\partial \eta(\omega)}{\partial \omega}. \tag{4.72}$$

It can then be shown that the change in the number of electrons n_{imp} due to the incorporation of the impurity can be given by,

$$\begin{aligned} n_{imp} &= \int_{-\infty}^{\epsilon_F} \rho_{imp}(\omega)\, d\omega, \\ &= \frac{\eta(\omega)}{\pi}, \end{aligned} \tag{4.73}$$

where ϵ_F is the Fermi level and it is assumed $\eta(-\infty) = 0$. The total number of electronic states induced below the Fermi level by the impurity must be sufficient to screen the effective charge of the impurity. The impurity nucleus and core electrons will have an excess charge, relative to the metal, ΔZe and therefore $n_{imp} = \Delta Z$. This requirement on n_{imp} is known as the Friedel sum rule, and must be imposed self consistently in simplified models such as this, where the complete long range Coulomb interactions between the impurity and conduction electrons are not directly considered.

In the case of a spherically symmetric impurity potential it can be shown that the change in the density of states induced by the impurity can be given by,

$$\Delta\rho(r) \approx -\frac{1}{2\pi^2 r^3}\sum_l (2l+1)(-1)^l cos\left(2k_F r + \eta_l(\epsilon_F)\right) sin\left(\eta_l(\epsilon_F)\right), \tag{4.74}$$

where l is the angular momentum quantum number of the potential, and k_F is the Fermi wave vector. From **eqn. 4.74** it is possible to see that although the screening of the impurity potential will be at the atomic scale there will also be oscillations in the screening cloud of wavelength $1/2k_F$. These Friedel oscillations in the local density of states of the impurity and surrounding metal can be directly measured by STM and are observed as standing waves around an impurity.

Virtual Bound States

If an impurity potential is very attractive it can induce a bound state below the Fermi level such that an electron becomes confined. The wavefunction of this impurity state would fall off exponentially with distance away from the impurity. However, it may be that the impurity potential is not sufficiently strong to create a bound state. In this case it may still be sufficient, for a time, to localise conduction band electrons around the impurity. Such a process can induce a narrow peak in the conduction band density of state at the impurity site due to resonant scattering. This narrow feature is known as a virtual bound state. In a virtual bound state electrons spend a relatively larger proportion of time around the impurity, but their wavefunctions tend to Bloch states far away from the impurity.

Consider a very localised potential,

$$V_{\mathbf{k},\mathbf{k'}} = V/N_s, \tag{4.75}$$

where $\epsilon_{\mathbf{k}}, \epsilon_{\mathbf{k'}} < D$, and D is the band width of the conduction density of states, and N_s is the total number of sites. Then starting from **eqn. 4.62** and taking matrix elements

to Block states gives,

$$
\begin{aligned}
G^R(\omega) &= G_0^R(\omega) + G_0^R(\omega)T(\omega^+)G_0^R(\omega) \\
\langle \mathbf{k}| G^R(\omega) |\mathbf{k'}\rangle &= \langle \mathbf{k}| G_0^R(\omega) |\mathbf{k'}\rangle + \langle \mathbf{k}| G_0^R(\omega)T(\omega^+)G_0^R(\omega) |\mathbf{k'}\rangle \\
G^R_{\mathbf{k},\mathbf{k'}}(\omega) &= \frac{\delta_{\mathbf{k},\mathbf{k'}}}{(\omega + i\eta - \epsilon_{\mathbf{k}})} + \sum_{\mathbf{k},\mathbf{k'}} \langle \mathbf{k}| G_0^R(\omega) |\mathbf{k}\rangle \langle \mathbf{k}| T(\omega^+) |\mathbf{k'}\rangle \langle \mathbf{k'}| G_0^R(\omega) |\mathbf{k'}\rangle \\
&= \frac{\delta_{\mathbf{k},\mathbf{k'}}}{(\omega + i\eta - \epsilon_{\mathbf{k}})} + \frac{1}{(\omega + i\eta - \epsilon_{\mathbf{k}})} \left(\sum_{\mathbf{k},\mathbf{k'}} \langle \mathbf{k}| \frac{V}{\left(I - G_0^R(\omega)V\right)} |\mathbf{k'}\rangle \right) \frac{1}{(\omega + i\eta - \epsilon_{\mathbf{k'}})} \\
&= \frac{\delta_{\mathbf{k},\mathbf{k'}}}{(\omega + i\eta - \epsilon_{\mathbf{k}})} + \frac{1}{(\omega + i\eta - \epsilon_{\mathbf{k}})} \left(\frac{V/N_s}{\left(1 - \sum_{\mathbf{k},\mathbf{k'}} \langle \mathbf{k}| G_0^R(\omega)V |\mathbf{k'}\rangle\right)} \right) \frac{1}{(\omega + i\eta - \epsilon_{\mathbf{k'}})} \\
&= \frac{\delta_{\mathbf{k},\mathbf{k'}}}{(\omega + i\eta - \epsilon_{\mathbf{k}})} + \frac{1}{(\omega + i\eta - \epsilon_{\mathbf{k}})} \left(\frac{V/N_s}{\left(1 - \sum_{\mathbf{k},\mathbf{k'},\mathbf{k''}} \langle \mathbf{k}| G_0^R(\omega) |\mathbf{k''}\rangle \langle \mathbf{k''}| V |\mathbf{k'}\rangle\right)} \right) \\
&\qquad \times \frac{1}{(\omega + i\eta - \epsilon_{\mathbf{k'}})} \\
&= \frac{\delta_{\mathbf{k},\mathbf{k'}}}{(\omega + i\eta - \epsilon_{\mathbf{k}})} + \frac{1}{(\omega + i\eta - \epsilon_{\mathbf{k}})} \left(\frac{V/N_s}{\left(1 - V/N_s \sum_{\mathbf{k},\mathbf{k''}} \langle \mathbf{k}| G_0^R(\omega) |\mathbf{k''}\rangle\right)} \right) \\
&\qquad \times \frac{1}{(\omega + i\eta - \epsilon_{\mathbf{k'}})} \\
&= \frac{\delta_{\mathbf{k},\mathbf{k'}}}{(\omega + i\eta - \epsilon_{\mathbf{k}})} + \frac{1}{(\omega + i\eta - \epsilon_{\mathbf{k}})} \left(\frac{V/N_s}{\left(1 - V/N_s \sum_{\mathbf{k},\mathbf{k''}} \frac{\delta_{\mathbf{k},\mathbf{k''}}}{(\omega + i\eta - \epsilon_{\mathbf{k''}})}\right)} \right) \frac{1}{(\omega + i\eta - \epsilon_{\mathbf{k'}})}.
\end{aligned}
\tag{4.76}
$$

From this the phase shift $\eta(\omega)$ is given by,

$$
\eta(\omega) = Arg\left(det\left(\frac{V/N_s}{1 - V/N_s \sum_{\mathbf{k''}} \frac{1}{\omega + i\eta - \epsilon_{\mathbf{k''}}}} \right) \right) \tag{4.77}
$$

then using the standard result,

$$
\begin{aligned}
\sum_{\mathbf{k}} \frac{1}{\omega + i\eta - \epsilon_{\mathbf{k}}} &= P \sum_{\mathbf{k}} \frac{1}{\omega - \epsilon_{\mathbf{k}}} - i\pi \sum_{\mathbf{k}} \delta(\omega - \epsilon_{\mathbf{k}}) \\
&= N_s \left(\Lambda(\omega) - i\pi\rho_0(\omega) \right),
\end{aligned}
\tag{4.78}
$$

where $N_s\Lambda(\omega) = P\sum_{\mathbf{k}} 1/(\omega - \epsilon_{\mathbf{k}})$ and P is the principle part integration,

$$
\eta(\omega) = Arg\left(\frac{V/V_s}{1 - V/N_s(N_s(\Lambda(\omega) - i\pi\rho_0(\omega)))} \right) \tag{4.79}
$$

and using,

$$
Arg(\frac{z_1}{z_2}) = Arg(z_1) - Arg(z_2) \tag{4.80}
$$

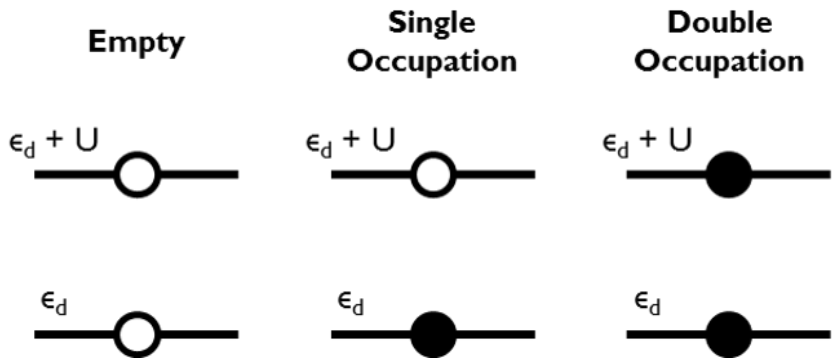

Figure 4.2: Occupation configurations for the Anderson model for $V_k = 0$.

then,

$$\begin{aligned}\eta(\omega) &= Arg(V/N_s) - Arg\left(1 - \frac{V}{N_s}\left(N_s(\Lambda(\omega) - i\pi\rho_0(\omega))\right)\right) \\ &= 0 - Arg\left(1 - V\Lambda(\omega) + i\pi\rho(\omega)V\right) \\ &= -tan^{-1}\left(\frac{\pi\rho_0(\omega)V}{1 - V\Lambda(\omega)}\right) \\ &= tan^{-1}\left(\frac{\pi\rho_0(\omega)V}{V\Lambda(\omega) - 1}\right).\end{aligned} \tag{4.81}$$

From here **eqn. 4.72** can be used to give the change in the density of states due to the impurity as,

$$\Delta\rho(\omega) = -V\frac{(1 - V\Lambda(\omega))\rho_0'(\omega) + V\rho_0(\omega)\Lambda'(\omega)}{(1 - V\Lambda(\omega))^2 + (\pi\rho_0(\omega))^2}, \tag{4.82}$$

where the prime denotes a derivative with respect to ω. **Equation 4.82** is valid if $1 - V\Lambda(\omega) = 0$ has no roots outside of the conduction band. In the case that a solution does exist within the conduction band, for example for $\omega = \epsilon_0$ then an expansion of $\Lambda(\omega)$ around ϵ_0 can be used to show that $\Delta\rho(\omega)$ has a Lorentzian form close to $\omega = \epsilon_0$.

$$\Delta\rho(\omega) = \frac{\Delta/\pi}{((\omega - \epsilon_0)^2 + \Delta^2)}, \tag{4.83}$$

where $\Delta = \pi\rho_0/\Lambda(\epsilon_0')$. Therefore in an STS experiment of a system where an impurity forms a virtual bound state it would be expected to observe a Lorentzian peak in the LDOS at ϵ_0.

4.4.2 The Anderson $S = \frac{1}{2}$ Impurity Model

The Anderson model considers a localised magnetic impurity coupled to a continuum of electrons and is described by the Hamiltonian,

$$H = H_0 + H_{impurity} + H_{hybrid} + H_{Coulomb} \tag{4.84}$$

where,

$$H_0 = \sum_{\mathbf{k},\sigma} \epsilon_{\mathbf{k}} c^\dagger_{\mathbf{k},\sigma} c_{\mathbf{k},\sigma}, \tag{4.85a}$$

$$H_{impurity} = \sum_{\sigma} \epsilon_d d^\dagger_\sigma d_\sigma, \tag{4.85b}$$

$$H_{hybrid} = \sum_{\mathbf{k},\sigma} \left(V_{\mathbf{k}} d^\dagger_\sigma c_{\mathbf{k},\sigma} + V^*_{\mathbf{k}} c^\dagger_{\mathbf{k},\sigma} d_\sigma \right), \tag{4.85c}$$

$$H_{Coulomb} = U \left(d^\dagger_\uparrow d_\uparrow d^\dagger_\downarrow d_\downarrow \right). \tag{4.85d}$$

$\epsilon_{\mathbf{k}}$ is the energy of a Bloch state with wave vector **k**. $c_{\mathbf{k},\sigma}$ and $c^\dagger_{\mathbf{k},\sigma}$ are the annihilation and creation operators of an conduction band electron with wave vector **k** and spin σ. d_σ and $d^\dagger_\sigma$ are the annihilation and creation operators of an electron in the impurity state with energy ϵ_d and spin σ. $V_{\mathbf{k}}$ describes the hybridisation of continuum, and impurity electrons and U is the Coulomb repulsion between two electrons in the impurity d states,

$$U = \int \phi^*_d(\mathbf{r}) \phi^*_d(\mathbf{r'}) \frac{e^2}{|\mathbf{r} - \mathbf{r'}|} \phi_d(\mathbf{r}) \phi_d(\mathbf{r'}) \, d\mathbf{r} d\mathbf{r'}. \tag{4.86}$$

To begin, consider the simplified case in which $V_{\mathbf{k}} = 0$ such that the impurity states are isolated from the conduction band. In this case the impurity can be either empty, singly occupied by an electron with spin σ ($\sigma = \uparrow \text{ or } \downarrow$) and energy ϵ_d, or doubly occupied with no net spin, and a total energy of $2\epsilon_d + U$ (**Fig. 4.2**). For there to be a magnetic moment on the impurity the two-fold degenerate singly occupied configuration must be the ground state. For the singly occupied configuration to be the ground state $\epsilon_d < \epsilon_F$ and $\epsilon_d + U > \epsilon_F$ so that double and zero occupation become unfavourable.

If the singly occupied configuration $|d^1_\sigma\rangle$ is the ground state of the impurity then the other configurations $|d^0\rangle$ and $|d^2\rangle$ are higher energy, excited states. Turning on $V_{\mathbf{k}}$ allows for the potential to mix conduction band and impurity states via **eqn. 4.85c** such that $|d^0\rangle = c^\dagger_{\mathbf{k},\sigma} d_\sigma |d^1_\sigma\rangle$ and $|d^2\rangle = d^\dagger_{-\sigma} c_{\mathbf{k},-\sigma} |d^1_\sigma\rangle$, where $-\sigma$ denotes the opposite spin state to σ. If it is further assumed that $\epsilon_d = \epsilon_F - U/2$ then two symmetric scattering processes can be defined as,

$$|d^1_{-\sigma}\rangle = d^\dagger_{-\sigma} c_{\mathbf{k'},-\sigma} c^\dagger_{\mathbf{k},\sigma} d_\sigma |d^1_\sigma\rangle \tag{4.87a}$$

$$|d^1_{-\sigma}\rangle = c^\dagger_{\mathbf{k'},\sigma} d_\sigma d^\dagger_{-\sigma} c_{\mathbf{k},-\sigma} |d^1_\sigma\rangle. \tag{4.87b}$$

These processes are diagrammatically shown in **Fig. 4.3**, where it is clear to see that both are spin flip scattering processes that effectively anti-ferromagnetically couple the conduction band electrons to the impurity magnetic moment. Typically U is of the order of electron-volts for a transition metal impurity in a metal host [20], and therefore these spin-flip events are virtual processes mediated by tunnelling. Furthermore, since these spin-flip scattering processes require there to be conduction band states with the

same energy that are both filled and empty in both spin-up and spin-down states, the scattering resonance can only occur at the Fermi level.

The Schrieffer-Wolff transformation can be used to approximate the Hamiltonian in **eqn. 4.85** by[106],

$$H \approx H_0 + \sum_{\mathbf{k},\mathbf{k}} V_{\mathbf{k}}^* V_{\mathbf{k'}} \left(\frac{1}{U + \epsilon_d - \epsilon_{\mathbf{k'}}} + \frac{1}{\epsilon_{\mathbf{k}} - \epsilon_d} \right) \times \left(d_\uparrow^\dagger d_\downarrow c_{\mathbf{k},\downarrow}^\dagger c_{\mathbf{k'},\uparrow} + d_\downarrow^\dagger d_\uparrow c_{\mathbf{k},\uparrow}^\dagger c_{\mathbf{k'},\downarrow} + \frac{1}{2} \left(d_\uparrow^\dagger d_\uparrow - d_\downarrow^\dagger d_\downarrow \right) \left(c_{\mathbf{k},\uparrow}^\dagger c_{\mathbf{k'},\uparrow} - c_{\mathbf{k},\downarrow}^\dagger c_{\mathbf{k'},\downarrow} \right) \right). \tag{4.88}$$

Equation 4.88 is therefore equivalent to the Kondo Hamiltonian [104],

$$H = H_0 + \sum_{\mathbf{k},\mathbf{k'}} J_{\mathbf{k},\mathbf{k'}} \left(S^+ c_{\mathbf{k},\downarrow}^\dagger c_{\mathbf{k'},\uparrow} + S^- c_{\mathbf{k},\uparrow}^\dagger c_{\mathbf{k'},\downarrow} + S_z \left(c_{\mathbf{k},\uparrow}^\dagger c_{\mathbf{k'},\uparrow} - c_{\mathbf{k},\downarrow}^\dagger c_{\mathbf{k'},\downarrow} \right) \right), \tag{4.89}$$

where,

$$J_{\mathbf{k},\mathbf{k'}} = V_{\mathbf{k}}^* V_{\mathbf{k'}} \left(\frac{1}{U + \epsilon_d - \epsilon_{\mathbf{k'}}} + \frac{1}{\epsilon_{\mathbf{k}} - \epsilon_d} \right) \tag{4.90}$$

and

$$S^+ = d_\uparrow^\dagger d_\downarrow, \tag{4.91a}$$
$$S^- = d_\downarrow^\dagger d_\uparrow, \tag{4.91b}$$
$$S_z = \frac{1}{2} \left(d_\uparrow^\dagger d_\uparrow - d_\downarrow^\dagger d_\downarrow \right). \tag{4.91c}$$

Similarly the conduction band operators can be defined as an effective spin-1/2 system with,

$$S_{\mathbf{k},\mathbf{k'}}^+ = c_{\mathbf{k},\uparrow}^\dagger c_{\mathbf{k'},\downarrow} \tag{4.92a}$$
$$S_{\mathbf{k},\mathbf{k'}}^- = c_{\mathbf{k},\downarrow}^\dagger c_{\mathbf{k'},\uparrow} \tag{4.92b}$$
$$S_{\mathbf{k},\mathbf{k'}}^z = \frac{1}{2} \left(c_{\mathbf{k},\uparrow}^\dagger c_{\mathbf{k'},\uparrow} - c_{\mathbf{k},\downarrow}^\dagger c_{\mathbf{k'},\downarrow} \right), \tag{4.92c}$$
$$\tag{4.92d}$$

giving,

$$H = H_0 + \sum_{\mathbf{k},\mathbf{k'}} J_{\mathbf{k},\mathbf{k'}} \mathbf{S}_d \cdot \mathbf{S}_{\mathbf{kk'}} \tag{4.93}$$

where $\mathbf{S}_d$ is the spin of the impurity and $\mathbf{S}_{\mathbf{kk'}}$ is the net effective spin of the conduction band electrons in the vicinity of the impurity. For scattering around the Fermi level

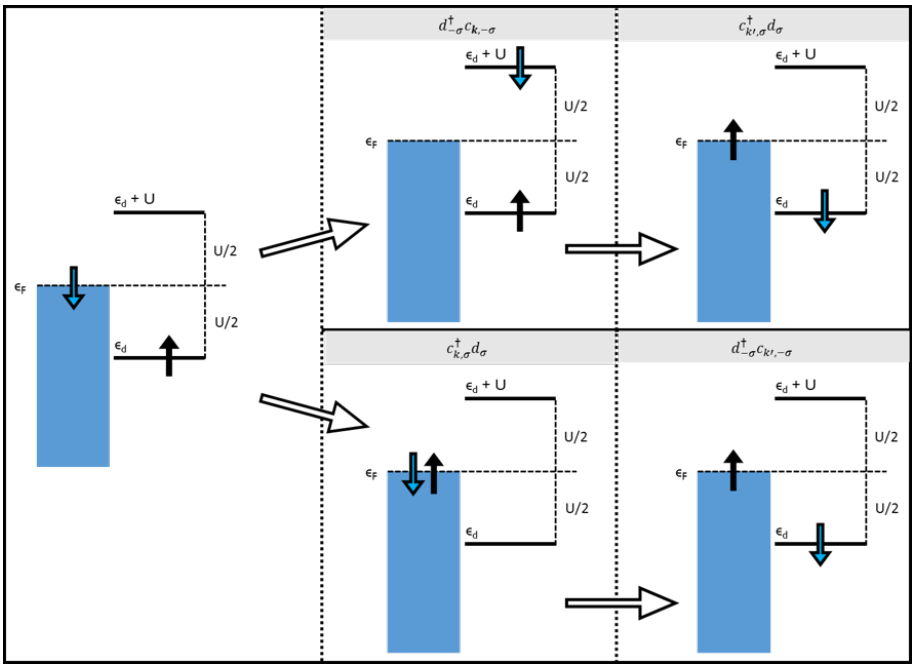

Figure 4.3: Diagrammatic representation of Kondo scattering in the Anderson Model. (a) To begin consider the impurity to be singly occupied by a spin up electron with energy ϵ_d (black arrow), and a spin down electron of the continuum at the Fermi level ϵ_F (blue arrow). A zero energy scattering process that flips the spin of the impurity can occur through one of two routes. Route 1: (b) The spin down electron from the continuum (blue) hops to the impurity doubly occupied state with energy $\epsilon_d + U$. (d) The spin up electron that was originally on the impurity (black) then hops to the continuum at the Fermi level leaving the spin down electron (blue) in the impurity singly occupied state. Route 2: (c) The spin up electron of the impurity (black) hops to the continuum at the Fermi level. (e) The spin down electron (blue) then hops from the continuum to the singly occupied impurity state with energy ϵ_d.

$\epsilon_{\mathbf{k}} \approx \epsilon_{\mathbf{k'}} \approx \epsilon_F$, therefore **Eqn. 4.90** can be re-arranged to,

$$J_{\mathbf{k}_F} = \frac{|V_{\mathbf{k}_F}|^2 U}{(U + \epsilon_d - \epsilon_F)(\epsilon_F - \epsilon_d)} \tag{4.94}$$

and since the requirement for a singly occupied configuration was $U + \epsilon_d > \epsilon_F$ and $\epsilon_d < \epsilon_F$ **Eqn. 4.94** will always be positive. The conduction band electrons will be antiferromagentically coupled to the impurity spin. The result of this is to form a many-body macroscopic singlet ground state in which a cloud of conduction band electrons are responsible for effectively screening the magnetic moment of the impurity. *J. Kondo* showed that the formation of this resonance at the Fermi level is responsible for the logarithmic increase in resistance of dilute magnetic metal alloys upon cooling the system below a characterstic temperature T_K [20],

$$T_K = D\sqrt{\frac{2\Delta}{\pi D}} exp\left(-\frac{1}{2J\rho_0}\right), \tag{4.95}$$

where Δ is the width of the ϵ_0 state. In terms of the Anderson model T_K can be

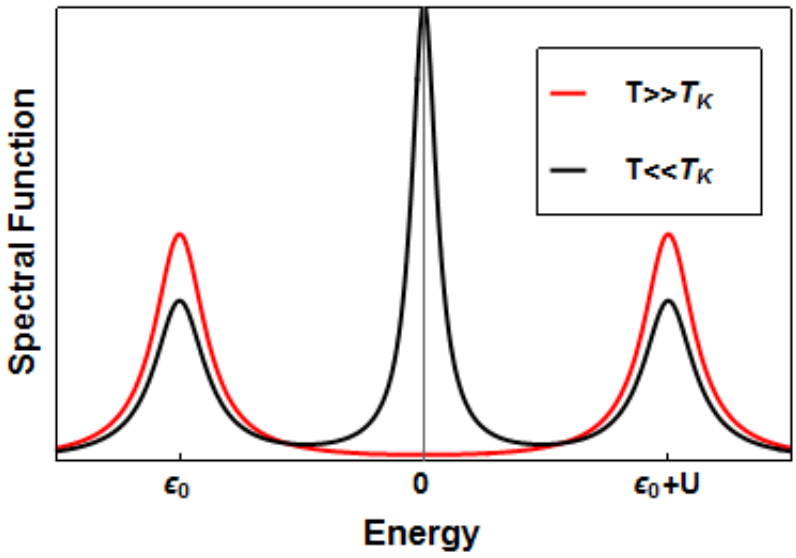

Figure 4.4: Sketch of the spectral function of a Kondo impurity. At temperatures well above T_K (Red) the spectral function has two resonances, one below the Fermi level at ϵ_0 and the other above at $\epsilon_0 + U$. For temperatures significantly below T_K (black) a third, Kondo resonance appears at the Fermi level. The width of the resonance is proportional to the Kondo temperature.

expressed as [107, 108],

$$T_K = \frac{1}{2}\left(\Gamma U\right)^{1/2} exp\left(\frac{\pi\epsilon_d(\epsilon_d + U)}{\Gamma U}\right), \tag{4.96}$$

where Γ is the width if the impurity levels, broadened by the virtual tunnelling processes.

By considering the effect of these spin-flip scattering processes *J. Kondo* made a breakthrough in the understanding of why there was a minimum in the resistance of magnetic impurities in metals. However, the perturbation theory used breaks down becoming divergent as $T \rightarrow 0\,K$. To go beyond this a number of new many-body techniques have been developed including numerical renormalisation group (NRG)[109, 110], quantum Monte Carlo (QMC) [111], and non-crossing approximation (NCA) [112] all of which provide a detailed understanding of the spectral function of the Kondo system. Well above T_K the spectral function contains two resonances, one corresponding to ϵ_0 below the Fermi level and the other above the fermi level at $\epsilon_0 + U$. Upon cooling to well below T_K the system condenses into the Kondo singlet and a third resonance, the Kondo resonance, appears at the Fermi level; the width of which is proportional to the Kondo temperature T_K.

4.4.3 Single Atom Kondo

At the turn of the century there was a resurgence of interest in the Kondo effect as new experimental paradigms opened up the possibility to investigate individual Kondo impurities. Transport measurements of quantum-dot devices operated in the Coulomb blockade regime allow for precise control over the parameter space of the Anderson model [113, 114], while STM measurements of individual magnetic impurities on metallic surfaces [115, 116] for the first time allowed for the Kondo effect to be investigated in real space. Much of the seminal work in this area was later reviewed by L. K. Kouwenhoven[108]. In the previous section (**section 4.4.1**) it was shown how in principle the spectral function can be related to the density of states of a system, a property that is directly accessible by STM experiments. In practicality STM actually measures a projected density of states via weak coupling to the STM tip. The result is that the impurity d-states may be too locally confined to be directly probed by the STM, but rather the influence of the impurity upon the density of states of the conduction band electrons can be used to infer details of the Kondo effect.

One of the first examples of single impurity Kondo formed by an individual magnetic atom came from Co atoms on an Au (111) surface [115]. In this work it was highlighted that the STS curves obtained for individual magnetic impurities must be understood in the context of Fano interference [117]. The measured density of states is formed by an interference between two tunnelling pathways: one through the impurity Kondo resonance, and the second directly into the continuum of states of the host metal.

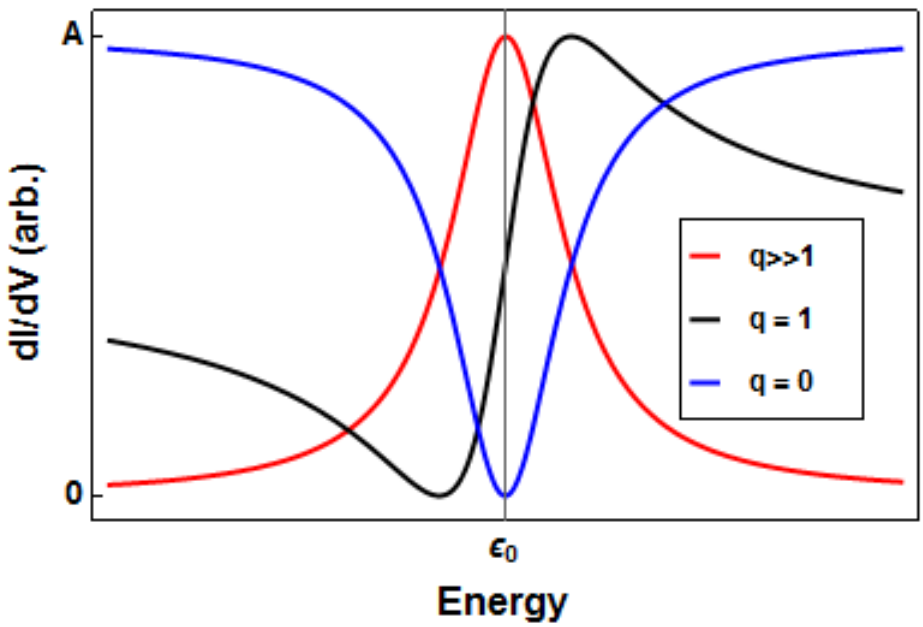

Figure 4.5: Fano resonance lineshapes for different q-factors. Plots of **eqn. 4.97** with $C = 0$, and $q >> 1$ (red) for the majority of tunnelling into the resonance, $q = 1$ (black) for an equal tunnelling ratio, and $q = 0$ (blue) for tunnelling solely into the continuum.

To model an STS curve acquired from a single magnetic atom on a surface the Fano equation can be defined as,

$$\frac{dI}{dV} = \frac{A}{1+q^2}\frac{(q+x)^2}{1+x^2} + C, \tag{4.97}$$

where

$$x = \frac{\epsilon - \epsilon_0}{\Gamma/2}, \tag{4.98}$$

A is the resonance amplitude, ϵ is energy, ϵ_0 is the resonance position, Γ is the resonance full width at half maximum (FWHM), C is an offset, and q is the q-factor. The q-factor describes the ratio of tunnelling through the Kondo resonance versus directly into the continuum; the key forms of this equation are shown in **Fig. 4.5**. If all of the tunnelling is directly into the continuum $q = 0$ and the Fano lineshape is an anti-resonance. $q = 1$ describes an equal tunnelling ratio such that the Fano lineshape is an $'S'$ like curve. Finally, if tunnelling is predominantly through the Kondo resonance $q >> 1$ and the Fano equation reduces to the a Lorenztian lineshape, as one would expect for the virtual scattering resonance (see **section 4.4.1**). A detailed investigation of the Fano equation in the context of STS experiments on single magnetic atoms can be found in [118].

Temperature Dependent Measurements

The observation of a zero bias resonance formed by a single magnetic impurity on a metallic host, is in of its self, not sufficient to confirm the presence of the Kondo effect. A common experimental procedure for the verification of the Kondo effect is to use an external magnetic field to split the spin degeneracy of the Kondo resonance, via the Zeeman Effect (see **section 4.2**). However, if the intrinsic width of the resonance is greater than the accessible Zeeman energies ($\approx 0.1\,\mathrm{mV/T}$) then it can be difficult to reliably determine the resonance splitting. Alternatively, the temperature dependence of the intrinsic resonance width can be used to verify the Kondo effect.

To determine the intrinsic width of a spectroscopic feature in STS at finite temperatures it is necessary to consider the effects of Fermi-Dirac temperature broadening. In **eqn. 2.37** it can be seen that the effect of finite temperatures is effectively a convolution of the derivative of the Fermi-Dirac distribution with the DOS of the sample. **Figure 4.6** shows plot of the derivative of the Fermi-Dirac function for a series of temperatures. At very low temperatures the function reduces to an effective Dirac delta function, and the broadening of the DOS will be negligible. However, as the temperature increases the function becomes wider, and will therefore smear the DOS over a greater energy range. For a hypothetical DOS feature that is a delta function the broadening due to Fermi-Dirac effects is $3.2k_BT$, where k_B is the Boltzmann constant and T is temperature [119].

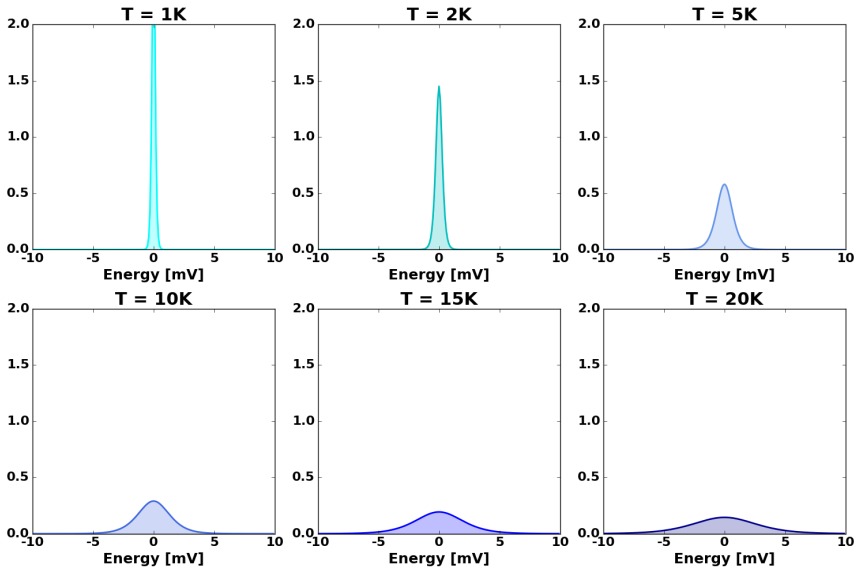

Figure 4.6: Derivative of Fermi-Dirac distribution at varied tempertures.
Plots of the derivative of the Fermi-Dirac distrution function for a range of temperatures between 1 K and 20 K.

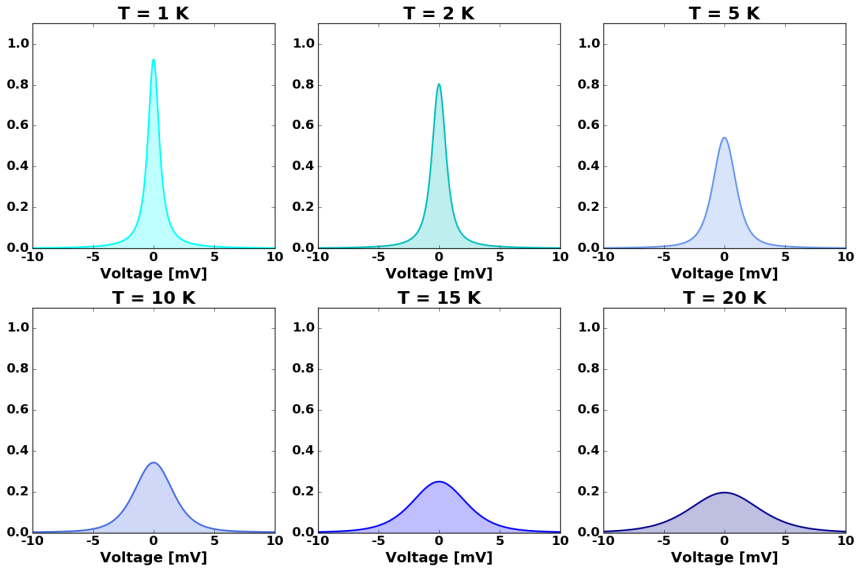

Figure 4.7: Fermi-Dirac broadening of a Lorentzian resonance.
Here the effect of Fermi-Dirac broadening upon a Lorentzian with a FWHM $= 1$ mV is considered. At 1 K the effect is negligible, however as the temperature is increased the broadening become more pronounced.

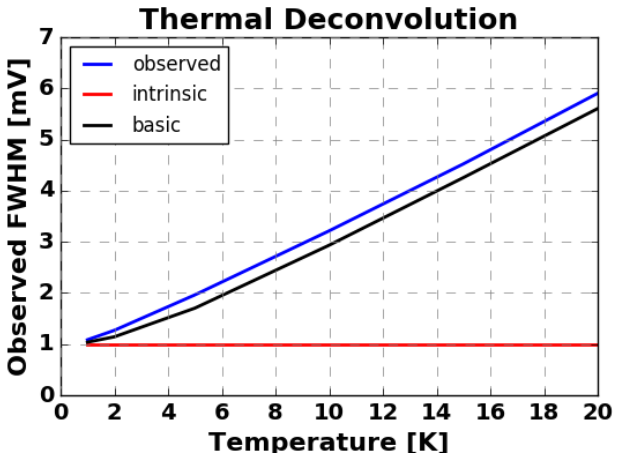

Figure 4.8: Fermi-Dirac de-convolution.
Plot of the results from a Fermi-Dirac de-convolution performed on the resonances in **Fig. 4.7**. Blue line shows the observed FWHM as determined by fitting to a Lorentzian. Red line shows the extracted intrinsic FWHM from the de-convolution process. Black line shows a *guess* for the observed width from **eqn. 4.99**

.

In the case of the Kondo effect the intrinsic DOS feature has a well defined analytical form, namely the Fano resonance described above (see **eqn 4.97**) that in some cases reduces to a Lorentzian form. **Figure 4.7** shows plots of a Lorentzian resonance, with an intrinsic FWHM$= 1$ mV, convoluted with the Derivative of the Fermi-Dirac distribution over a range of temperatures. The plots highlight that at elevated temperatures the observed width of a spectroscopic feature is dominated by the Fermi-Dirac temperature broadening.

To extract the intrinsic width of an observed spectroscopic feature the reverse process to that used in **Fig. 4.7** can be used; whereby at a given temperature the known Fermi-Dirac derivative function can be de-convolved from the experimental feature of a known form, but unkown parameters. For example, in **Fig. 4.8** the results of the de-convolution process performed upon the broadened resonances in **Fig. 4.7** are shown. The blue line shows the observed FWHM of the resonances in **Fig. 4.7**, as determined by fitting to a Lorentzian, and in red the intrinsic width of the resonance after de-convolution is shown. As is expected the extracted intrinsic width is constant at 1 mV. Additionally, a simple *guess* of the Fermi-Dirac broadening is shown determined from a simple squared addition of the form,

$$\Gamma_{observed} = \sqrt{\Gamma^2_{intrinsic} + (3.2k_BT)^2}. \tag{4.99}$$

In this hypothetical case the FWHM of the intrinsic resonance has been fixed at a constant, as would be the case for any simple DOS feature. However, for a Kondo resonance the intrinsic width also increases with temperature. The rate of broadening with temperature for a magnetic atom coupled to a 3D metal is determined by Fermi

liquid theory such that the intrinsic width in **eqn. 4.99** is given by [120],

$$\Gamma_{intrinsic} = \sqrt{(2\pi k_B T)^2 + (2k_B T_K)^2}, \tag{4.100}$$

where T_K is the Kondo temperature. Therefore experimental verification of the Kondo effect can be achieved by performing temperature deconvolution and comparing the observed change in intrinsic FWHM to that expected from **eqn. 4.100**.

4.5 Indirect Exchange Interaction

In the previous sections it has been shown how a magnetic impurity can exhibit an exchange interaction with the conduction band of a host metal. Under a specific set of parameters this interaction can lead to the formation of the Kondo effect (see **section 4.4**), but the antiferromagnetic interaction at the heart of the Kondo effect is a general feature of magnetic impurities in a metal. The question then arises as to what will happen when multiple magnetic moments are in close proximity to one another. Ruderman and Kittel [121], Kasyua [122], and Yosida [123] showed that an indirect exchange interaction can occur, where spatially separated magnetic impurities interact via the conduction band electrons.

To begin consider a conduction band of non-interacting electrons with wave vector **k** described by Bloch states,

$$\phi_{\mathbf{k}}(\mathbf{r}) = e^{i\mathbf{k}\cdot\mathbf{r}} u_{\mathbf{k}}(\mathbf{r}), \tag{4.101}$$

where $u_{\mathbf{k}}$ is periodic in the lattice and $\phi_{\mathbf{k}}(r)$ is normalised for large volumes V by,

$$1 = \frac{1}{V} \iiint d\tau \, \phi^*_{\mathbf{k}} \phi_{\mathbf{k}}. \tag{4.102}$$

Exchange interactions between the spins of the magnetic impurities $\mathbf{S}_i$ and conduction band electrons **s** will scatter Block states of **k** to **k'**. The matrix element of these interactions at $\mathbf{r} = \mathbf{R}_i$ is given by,

$$\mathbf{s} \cdot \mathbf{S}_i \Delta_{\mathbf{kk'}} e^{i(\mathbf{k}-\mathbf{k'})\cdot\mathbf{R}_i}, \tag{4.103}$$

where

$$\Delta_{\mathbf{kk'}} = \iiint d\tau \, \phi^*_{\mathbf{k'}}(\mathbf{r}) \Delta \phi_{\mathbf{k}}(\mathbf{r}) = \Delta^*_{\mathbf{k'k}} \tag{4.104}$$

and Δ is the strength of interaction. Treating Δ as a small perturbation upon a conduction band filled, in both spin states, from $\mathbf{k} = 0$ to the Fermi level $\mathbf{k}_F$, then the interaction between two impurities i and j at $\mathbf{r} = \mathbf{R}_i$ and $\mathbf{r} = \mathbf{R}_j$ is given by,

$$H(\mathbf{R}_{ij}) = -(\mathbf{s}\cdot\mathbf{S}_i)(\mathbf{s}\cdot\mathbf{S}_j) \int_0^{\mathbf{k}_F} \frac{d\mathbf{k}}{(2\pi)^3} \int_{\mathbf{k}_F}^{\infty} \frac{d\mathbf{k'}}{(2\pi)^3} \frac{\Delta_{\mathbf{kk'}} \Delta_{\mathbf{k'k}} e^{i(\mathbf{k}-\mathbf{k'})\cdot\mathbf{R}_{ij}}}{E(\mathbf{k'}) - E(\mathbf{k})} + c.c. \tag{4.105}$$

where the interaction has been mediated by the double scattering of an electron from **k** to **k'** and then to **k**. Assuming that scattering is not strongly dependent on **k** and that the most significant contributions come from $\mathbf{k'} \approx \mathbf{k} \approx \mathbf{k}_F$,

$$\Delta_{\mathbf{kk'}} \Delta_{\mathbf{k'k}} \approx |\Delta_{k_F k_F}|^2. \tag{4.106}$$

Next summing over all spin states and performing angular integrations and assuming

that $E(k)$ only depends on the magntiude of k gives,

$$H(R_{ij}) = -\frac{\mathbf{S}_i \cdot \mathbf{S}_j |\Delta_{k_F k_F}|^2}{(2\pi)^4 R_{ij}^2} \int_{-k_F}^{k_F} k\, dk e^{ikR_{ij}} \left[\int_{k_F}^{\infty} + \int_{-\infty}^{-k_F} \frac{e^{ik'R_{ij}} k' dk'}{E(k') - E(k)} \right]. \quad (4.107)$$

It can then be shown that **eqn. 4.107** can be expressed as [121],

$$H(R_{ij}) = -\frac{\mathbf{S}_i \cdot \mathbf{S}_j}{4} \frac{|\Delta_{k_F k_F}|^2 m^*}{(2\pi)^3 R_{ij}^4 \hbar^2} \left[2k_F R_{ij} cos(2k_F R_{ij}) - sin(2k_F R_{ij}) \right], \quad (4.108)$$

where it has been assumed that the effective mass of electrons does not vary significantly for values of k around k_F, such that $E(k) = \hbar^2 k^2 / 2m^*$.

Eqn. 4.108 shows that two spatially separated spins $\mathbf{S}_i$ and $\mathbf{S}_j$ become effectively exchange coupled. The sign of the exchange coupling is dependent on the separation of the two impurities, relative to the Fermi wave vector of the continuum, through the trigonometric functions in the brackets. Therefore, the two impurities can be either ferromagnetically or antiferromagnetically coupled with the magnitude of the interaction decaying rapidly with greater separation. It can now be seen that the RKKY interaction can lead to long range magnetic order in a material. Of particular interest in the work presented within this thesis is when the Kondo effect and RKKY interactions are both present.

Chapter 5

Single Domain Silicene on ZrB_2

The formation of epitaxial silicene upon the (0001) surface of ZrB_2 occurs spontaneously, in a self-terminating manner, due to the segregation of Si atoms from the underlying silicon substrate at temperatures in excess of $800\,^oC$ [12]. Compared to free-standing silicene, the silicene lattice on ZrB_2 is compressed by approximately 5 %, producing a commensuration between the $Zr(2 \times 2)$ lattice and a $(\sqrt{3} \times \sqrt{3})$ reconstruction of the silicon honeycomb lattice. To accommodate this in-plane strain the silicene sheet adopts a buckling specific to the silicene/ZrB_2 interface, where one in six of the silicon atoms, per unit cell, is raised above the plane formed by the others [82]. The effect of this buckling is to transform the Dirac cones, of free-standing silicene, into parabolic π-electronic bands separated by a band gap [12, 84]. Additionally the strain introduced by the $(\sqrt{3} \times \sqrt{3})$ reconstruction produces a highly ordered array of striped domains [12] that density functional theory calculations suggest arise to avoid a critical phonon instability [83]. The same domain structure is also observed in silicene upon a $ZrB_2(0001)$ single crystal surface formed through Si deposition [16]. In the case of more lattice-matching interfaces, such as that of silicene grown upon Ag(111)[11] and ZrC(111)[15, 16] single crystal surfaces, no domain structures are observed. Despite the silicene lattices upon all these varied surfaces exhibiting numerous reconstructions, the electronic properties remain similar. The robust nature of the silicene lattice to these structural deformations can therefore be utilised to fine-tune its properties between different regimes. The striped domains of the silicene/ZrB_2 surface can be advantageously used to template linear chains of organic molecules [124], however in other applications, such as those that utilise the transport properties of silicene [125] it may be more beneficial to produce a domain-free surface. In this chapter, it is demonstrated that the striped domains of silicene on ZrB_2 can be removed upon deposition of a small amount of Si atoms, to form large single-domain silicene sheets. The comparison of the structural and electronic properties between both silicene sheets indicates that the domain structure introduces very little change to the atomic structure. These results further demonstrate the flexibility of silicene suggesting that the fine-tuning of properties can be achieved in a single

experimental system.

The work reported here is the result of a collaboration between the authors of the publication *Single-domain epitaxial silicene on diboride thin films*[126]. The author of this report performed the STM experiments, and was directly involved in the acquisition of supporting core-level photoelectron spectroscopy and ARPES data. LEED measurements were performed by Yukiko Yamada-Takamura.

5.1 Experimental Systems

Changes in the surface structure were characterised at room-temperature by STM and LEED. The dynamic evolution of the surface structure during the deposition of Si atoms was investigated using the spectroscopic low-energy electron microscopy (Elmitec SPE-LEEM) end-station located at BL U5UA of the National Synchrotron Light Source (NSLS, Brookhaven National Laboratory, Upton, NY, USA). Changes in bonding and electronic structure upon Si deposition, core-level photoelectron spectroscopy and angle-resolved photoelectron spectroscopy (ARPES) were carried out at BL13B of the Photon Factory synchrotron radiation facility located at the High-Energy Accelerator Research Organization (KEK, Tsukuba, Japan), using photon energies ($h\nu$) of 130 eV and 43 eV, respectively. For ARPES, the total energy resolution was better than 35 meV as determined from the broadening of the Fermi level. At this end-station, the electric field vector of the light was at the fixed angle of 25^o with respect to the photoelectron analyser.

5.2 Silicene Sample Preparation

In this section the preparation of silicene/ZrB_2 samples for STM investigations will be detailed. Terminology and procedures will be referenced to the Omicron STMs used in the acquisition of data for this thesis, but in general should be applicable to any standard UHV system. What will not be detailed is the procedures required to grow ZrB_2 thin films on Si(111) wafers; for this see Fleurence *et al.*[12].

The ZrB_2 thin film is grown upon an approximately 1 cm square Si(111) wafer. These can be either cleaved or sawed into 1 cm by 0.25 cm sections for use in STM experiments (**Fig. 5.1a**). These samples can then be mounted upon direct current annealing compatible sample holders, an example of which is shown in **Fig. 5.1b**. The sample holder shown is for the Omicron Cryogenic STM, where all metal components are molybdenum. However, the diagram in **Fig. 5.1c** highlights the important components that can be transferred to other systems. In vacuum a high voltage contact is made to the left hand side of the sample. The bevelled ceramic washers ensure that the HV contact and foil are electrically isolated from the base and screw mounts. The sample therefore provides the only route to ground. For semiconducting samples, such as Si,

the resistance is sufficient to then provide a means to directly heat the sample via the current. It is noted here that for the Omicron VT-STM there is a tolerance level for the total height of the sample holder that should be checked before loading samples into the vacuum system.

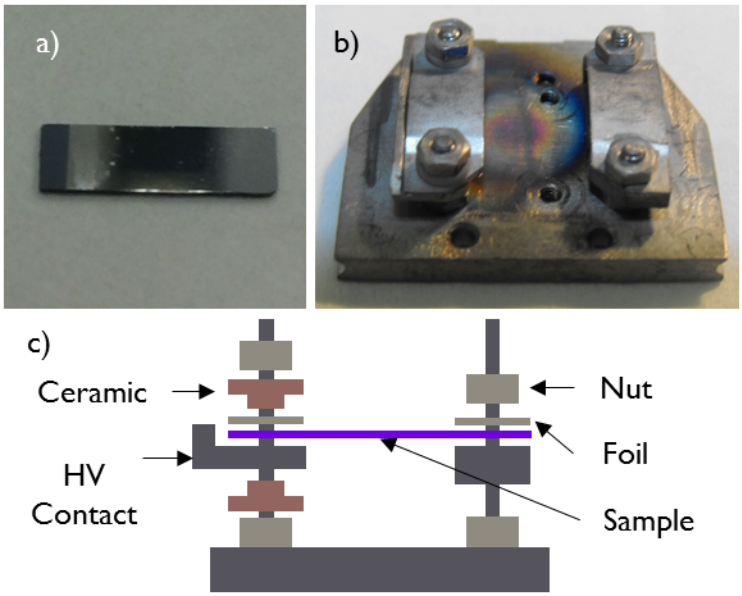

Figure 5.1: Silicene/ZrB_2 sample preparation.
(a) Picture of a ZrB_2/Si(111) sample after being sawed to 1 cm by 0.25 cm size for use in direct current sample holder. (b) Photograph of the direct current sample holder for the Cyrogenic STM (no sample is mounted). (c) Exploded, side view, schematic diagram of the Omicron Cryogenic STM direct current sample holder. The crucial components are the bevelled ceramic washers that isolate the left hand side of the from the base plate.

5.2.1 Ultra-High Vacuum Preparation

To prepare the silicene/ZrB_2 samples for use in STM there are two *in-situ* steps, degassing, and high temperature annealing. Once a new sample has been loaded into the UHV system an initial degassing is required. The sample degas should be performed with a resistive filament that will ensure the entire sample holder is heated. Typically a temperature of approximately $500\,^{\circ}$C is used, and the sample is left overnight. It is not uncommon for the pressure of the preparation chamber to peak at approximately 1×10^{-7} mbar. After an overnight degas the chamber pressure, with the sample still at $500\,^{\circ}$C will lower to approximately 1×10^{-9} mbar.

The next step is a high temperature direct current anneal to remove the oxide layers, and form the silicene surface. If possible a pyrometer should be aligned upon the sample for the direct current anneal, using an emissivity value for Si (0.63 [127]). Typically, the contact resistance of silicene/ZrB_2 samples in the direct current sample holders, in air at room temperature, can range between $2 - 40\,\Omega$. Although the resistance may change after the degassing procedure it is not always the case. More usually the contact

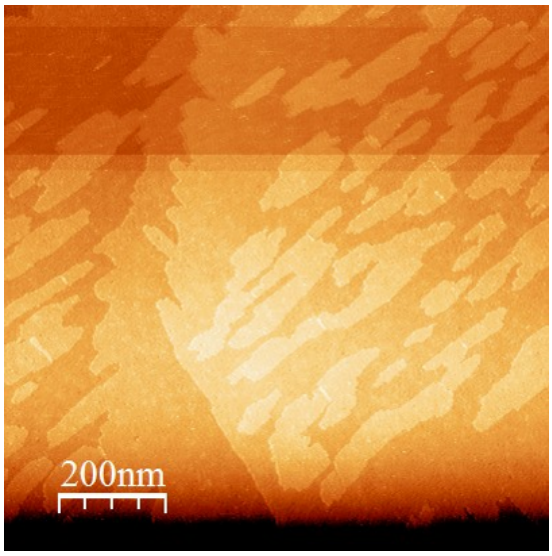

Figure 5.2: STM image of Si(100) surface used for Si deposition calibration. The Si deposited onto the Si(100) surface can be seen to grow as islands. Area analysis is used to determine the amount of Si deposited and therefore the flux at the sample.

resistance will only change during the direct current anneal. It is noted that often, when the resistance is high to begin with, the initial voltage required to pass a current through the sample is high, as is expected. However, in these samples the resistance will often drop suddenly after only a few seconds, which can lead to an excessive current passing through the sample. It is therefore recommended that the power supply be maintained in current limiting mode. The direct current anneal should be performed in a step wise manner with 0.1 A increments in the current until $800\,^{\circ}$C, so that a high quality vacuum can be maintained throughout the procedure. The resistance of the sample will lower as the temperature increases, and the actual values for current and voltage used will differ depending on sample dimensions and initial contact resistance; typical values for $800\,^{\circ}$C are around 1.5 A and 5.8 V. Upon heating the first notable dull glow of the sample will occur at around $500\,^{\circ}$C (≈ 0.7 A, ≈ 6.5 V), and then at the preparation temperature of $800\,^{o}$ the entire sample will glow bright orange. It is noted that the temperature across the sample is often not uniform with some areas appearing brighter(hotter) than others. It is generally found from pyrometer measurements that the hottest part is at the edge of the HV contact. Once the sample preparation temperature has been achieved it should be maintained for at least four hours, but preferably overnight, especially if it is the first preparation of the sample.

5.2.2 Silicon Deposition

Silicon deposition onto the silicene/ZrB_2 surface in STM experiments has been performed using SUSI silicon sublimation source (SUSI-63, MBE-Komponenten GmbH), where ultra-high purity Si is used as a sublimation source. The Si source is preheated to

approximately $450\,^{\circ}$C with a nearby filament, such that a current flow though the source. Then a direct current is used to heat the Si source to a Si sublimation temperature of $970\,^{\circ}$C; typical values used to obtain this temperature were 45 A and 4.7 V. For the deposition, samples are held in front of the evaporator, in UHV, approximately 30 cm from the source. The Si flux has been calibrated by measuring the surface area of new island growth on a Si(100) surface in STM measurements. An example of an image used in this analysis is shown in **Fig. 5.2**. The calculated coverage was found to correspond to 3.84 monolayers (ML) of Si(100) per minute (4.43×10^{15} atoms/min). Since 1 ML of Si(100) is equivalent to 0.78 ML of Si(111), and 1 ML of Si(111) is equivalent to 0.5 layers (L) of silicene, the flux can be converted to layers of silicene, giving approximately 1.5 Ls of silicene per minute. The Si depositions onto the silicene/ZrB_2 surfaces presented in this thesis were done with the sample maintained at approximately $310\,^{\circ}$C. The sample was then slowly cooled to room temperature after deposition, before STM measurements were performed.

5.3 Removal of Domain Boundaries on Si Deposition

The evolution of the surface structure as silicon was deposited onto the striped-domain silicene surface was monitored in real-time by LEEM in the μ-LEED mode using a 2-μm-selected-area aperture. The μ-LEED pattern and STM image in **Fig. 5.3a** and **Fig. 5.3c** were taken prior to silicon deposition. The $(\sqrt{3} \times \sqrt{3})$ spots of the reconstructed silicene surface are split in the μ-LEED pattern, due to the striped-domains of the spontaneously formed silicene surface. Within the STM image the $(\sqrt{3} \times \sqrt{3})$ reconstruction is observed as circular protrusions and the domain boundaries as dark lines that run along the $ZrB_2[11\bar{2}0]$ direction.

Soon after the Si deposition began the μ-LEED pattern in **Fig. 5.3b** was acquired. The fractional splitting of the $(\sqrt{3} \times \sqrt{3})$ spots completely disappears. Repeated deposition procedures were performed at different substrate temperatures between 210^{o}C and 370^{o}C, where the striped-domain surface was regenerated each time by annealing to 800$^{\circ}C$. For each temperature the amount of Si required to complete the transition differed between 3$\dot{}$% and 5 % of a silicene layer (L) (1.73×10^{15}cm^{-2}) at 210^{o}C (60 secs deposition) and 370^{o}C (90 secs deposition) respectively. STM observations taken after the transition (approximately 0.1 Ls deposition at 320^{o}C with a higher Si flux of 1.5 Ls/min) reveal the disappearance of the striped-domains, while the $(\sqrt{3} \times \sqrt{3})$ reconstruction is preserved (**Fig. 5.3d**). The large scale STM image in **fig. 5.3e** confirms that the single-domains extend over large areas of the surface, with only a few domain boundaries. The domain boundaries that remain are qualitatively quite different to those on the as-grown silicene surface; they are no longer highly ordered, nor do they run along a crystallographic direction.

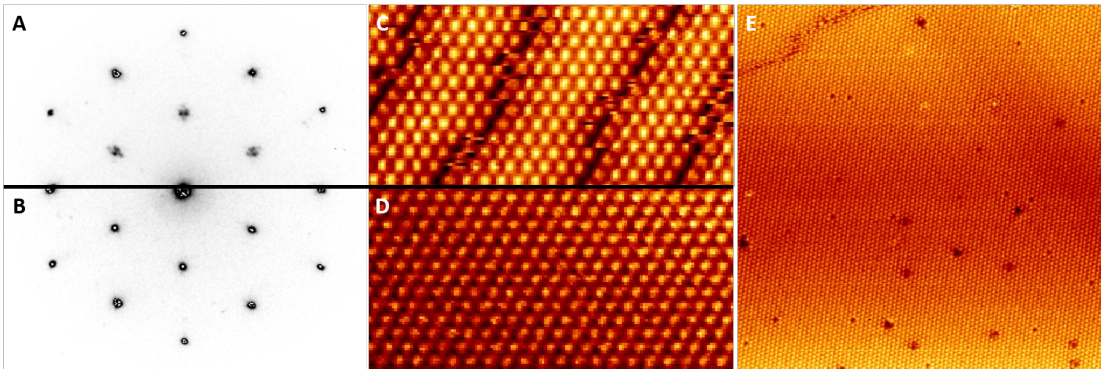

Figure 5.3: Comparison of silicene surfaces before and after Si deposition.
LEED patterns of (A) striped-domain silicene and (B) single-domain silicene. STM images (14 nm $\times$ 7 nm) of (C) striped-domain silicene (1.0 V, 50 pA) and (D) single-domain silicene (0.7 V, 50 pA) surfaces. Both LEED and STM indicate that the structural transition is limited to the removal of the domain boundaries. STM image in (E) shows how the single-domain silicene sheets extends over large areas (50 nm $\times$ 50 nm, 0.7 V, 50 pA).

5.4 Preservation of Atomic Structure

STM and μ-LEED measurements suggest the in-plane structural modification of the silicene sheet, induced by the deposition of silicon onto the surface, is limited to the removal of the domain boundaries. A core-level photoelectron spectrum of the as-grown stripe-domain silicene surface is shown as the black line in **Fig. 5.4b**. This spectrum, similar to previously observed spectra for silicene on ZrB_2 thin films [12, 81], can be decomposed into three significant contributions shown in blue, white, and green corresponding to the near-bridge, hollow, and 'up' Si atom binding sites respectively. The red line in **Fig. 5.4b** corresponds to a spectrum recorded after the domain boundaries have been removed by Si deposition producing the single-domain surface. Qualitatively it is observed that there is not a significant change to the spectrum in comparison to the stripe-domain silicene surface: there are two major Si 2p doublets, bluw and white, separated by 260 meV, which are attributed to the Si atoms that sit on the hollow, and near-bridge sites of the underlying Zr surface (see **Fig. 5.4a**). Quantitatively, small changes in the parameters of the peaks can be determined. The greatest intensity doublet, corresponding to the Si near-bridge atoms, has the $2p^{\frac{3}{2}}$ peak centred at 0 eV and lies 260 meV below the $2p^{\frac{1}{2}}$ peak for both surfaces. However, the near-bridge site Si atoms FWHM in the single-domain surface is 170 meV, notably reduced from the 200 meV for the same feature in the stripe-domain silicene surface. Similarly, the Si 2p doublet for the hollow site Si atoms has reduced in width to 150 meV, from 170 meV for the stripe-domain silicene surface. In addition the hollow site doublet has shifted

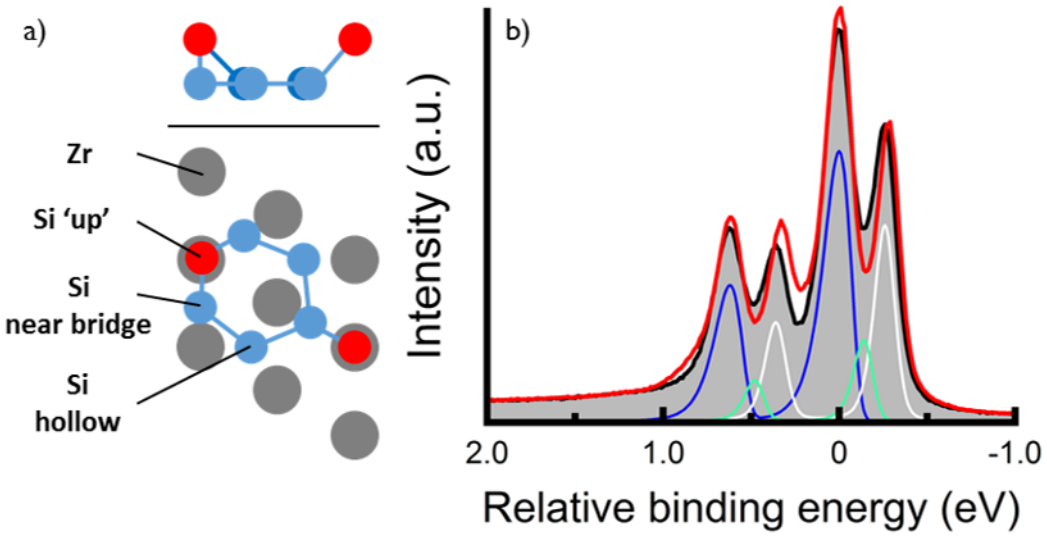

Figure 5.4: Core-level photoelectron spectra of the stripe- and single-domain silicene surfaces.
(a) Ball model of the silicene/ZrB_2 surface. (b) The spectrum of the stripe-domain silicene surface (black) is comprised of three Si 2p doublets as shown by the blue, green and white lines. A spectrum of the single-domain silicene surface is shown in red. Qualitatively little difference is observed between the two surfaces suggesting that there is no significant change in the silicene lattice buckling. [126]

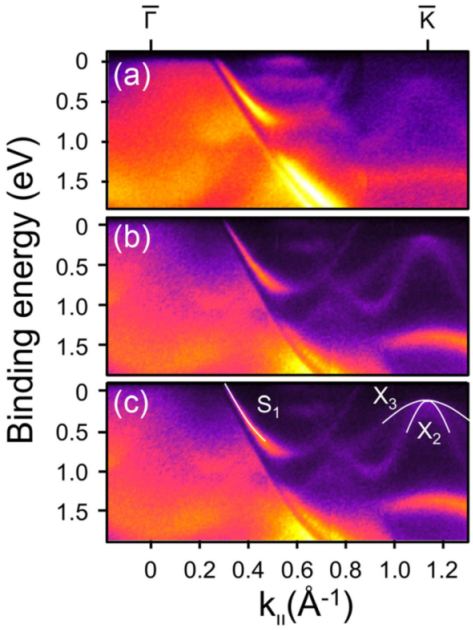

Figure 5.5: Comparison of ARPES for stripe- and single-domain silicene surfaces. ARPES spectra taken along the $\Gamma - K$ directions of the silicene (1×1) silicene lattice. (a) Stripe-domain and (b) single-domains silicene surfaces taken before and after Si deposition. Spectrum in (c) is the same as (b), but with silicene and Zr surface bands highlighted X_i and S respectively. [126]

towards lower binding energy by about 20 meV. It is proposed that the narrowing of the Si 2p doublets, upon Si deposition, could be due to the increased surface homogeneity as the domain boundaries are removed. The small binding energy shift of the hollow site Si atoms could be associated to an increased valence electron density at these sites or may be related to a binding energy shift of the 'up' Si atoms, which can only be estimated via fitting procedures [12, 81].

The small changes in the core-level photoelectron spectroscopy between the stripe- and single-domain silicene surfaces suggests that there is not a significant change in the chemical environment for Si atoms and as a results the buckling of the silicene lattice is not expected to have been modified. Corroboration of this interpretation is found in ARPES spectra taken prior to and after Si deposition. The ARPES spectrum taken along the $\Gamma - K$ direction of (1×1)-silicene in **Fig. 5.5a** was acquired from the stripe-domain silicene surface prior to Si deposition. As in previously reported examples the parabolic $\pi-$band centred at the (1×1)-silicene K point is visible [12]. After Si deposition the spectrum in **Fig. 5.5b** was obtained. Similarly to the core-level photo-electron spectroscopy, there is a strong similarity between the spectra for the two surfaces. **Figure 5.5c** shows the same spectrum as in **Fig. 5.5b**, but where the ZrB_2 surface state (S_1) and silicene bands ($X_{2,3}$) have been highlighted. While there has been little change to the ZrB_2 surface state from Si deposition the silicene bands have become sharper. It is suggested that the sharpening of these bands is related to the higher coherence of electrons at low binding energies in electronic states with long-

range order. It is noted that the silicene bands X_2 and X_3 in the single-domain silicene surface have also shifted to lower binding energy by approximately 50 meV, which may be related to changes in the stress distribution of the Si lattice upon removal of the domain boundaries.

5.5 Conclusion

The electronic properties of epitaxial silicene systems are defined by the interactions with their respective substrates that modify their atomic scale buckling [11, 12, 14–16]. In the case of silicene grown upon ZrB_2 the silicon lattice adopts a unique buckling where five out of six of the Si atoms in the honeycomb lattice lie in a single plane, with the sixth raised above this plane. As a result the silicene lattice is $(\sqrt{3} \times \sqrt{3})$ reconstructed and forms an array of highly ordered striped domain boundaries. LEED, and STM measurements performed upon the silicene/ZrB_2 surface prior to and after Si deposition onto the surface indicate that the additional silicon is incorporated into the silicene sheet, removing the domain boundaries. Core-level photoelectron spectroscopy and ARPES reveal that the chemical environment and electronic structure of the newly formed single-domain silicene sheet is not significantly changed in comparison to the stripe-domain surface.

Chapter 6

Enhanced Conductivity in Layered Silicon Nanostructures Grown on Silicene/ZrB_2

Silicene, a honeycomb lattice of silicon atoms, has been predicted to share many interesting properties with its carbon counterpart graphene [53]. Unlike graphene, however, the triangular sublattices of free-standing silicene are displaced out-of-plane with respect to one another [52, 59, 60]. As a consequence, the electronic structure of free-standing silicene is predicted to be more susceptibe to modification by external fields and the greater spin-orbit coupling in silicon results in a relatively large bandgap of 1.55 meV [59, 60].These electronic properties may therefore prove useful in nanoscale device fabrication [128–131]. Recent work has shown that silicene can be incorporated into a conventional field-effect transistor archtecture [125], a process that involves the complex etching of metallic contacts on the delicate silicene surface. It is therefore desirable to develop new techniques for patterning conductive contacts onto two-dimensional materials at the nanoscale.

To date silicene has been grown upon a number of metallic substrates [11, 12, 14–16, 70]. As with graphene [132–136], interactions with the underlying substrate are expected to play a significant role in enabling the tuning of the electronic properties [137]. In particular, when placed upon a surface, the specific buckling of the silicene lattice is heavily influenced by interactions with the substrate [11, 12, 14–16, 70]. For many layered materials, such as graphene [138–140] and various transition metal dichalcogenides like MoS_2 [8, 87], it has previously been observed that the electronic and electro-optic properties can change dramatically when going from the mono- to multi-layer regime. Similarly, multi-layered silicene is predicted to exhibit a broad range of interesting physical phenomena including a tuneable bandgap [90], superconductivity [91], and behaviour as a quasi-topological insulator [64]. Recent experiments studying multiple silicon layers deposited on Ag (111) show a $(\sqrt{3} \times \sqrt{3})$R30^o reconstruction, in contrast to the

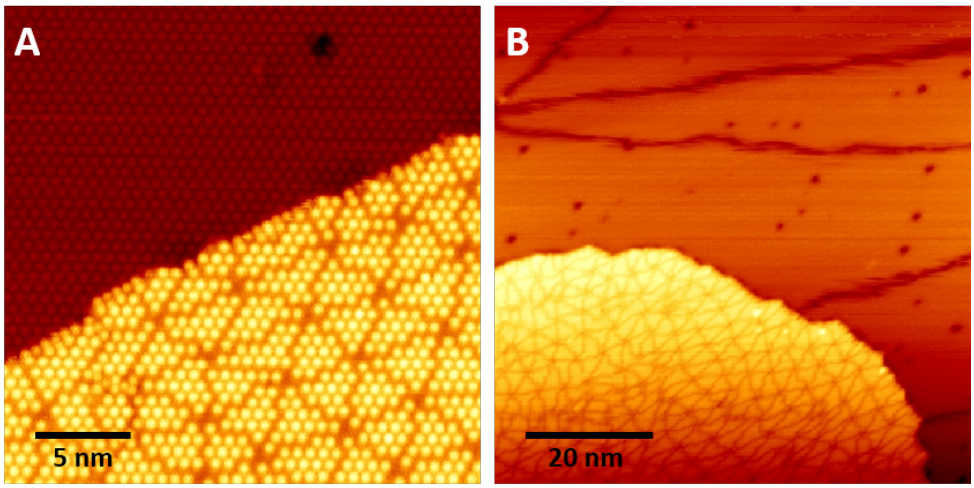

Figure 6.1: STM images of new silicon nanostructure growing on single-domain silicene/ZrB_2.
STM images acquired after a silicon deposition equivalent to 0.5 Ls of silicene. The high-resolution image in (A) reveals the triangular domain structure of the 2 L surface and that internally the same surface symmetry of the single-domain silicene sheet is retained. Large scale image in (B) shows that the new silicon nanostructure grows as a layer without forming large 3D clusters.

(3×3) reconstruction of the monolayer [94]. Remarkably, these multilayers are more metallic than the monolayer [95]. Comparison to Ag terminated Si (111), however, has highlighted the need for further investigation into these reconstructions [96, 97]. It is therefore of interest to investigate multilayer silicene candidates on other substrates, such as ZrB_2.

In this chapter we show that one or more layers of silicon deposited onto single-domain silicene formed on $ZrB_2(0001)$ thin films can cause substantial changes in the structural and electronic properties of the silicon surfaces. Using scanning tunnelling microscopy (STM) and spectroscopy (STS), low energy electron diffraction (LEED), we find that deposition of Si onto the single-domain silicene/ZrB_2 surface results in the formation of a novel layered silicon nanostructure displaying substantially different structural and electronic properties to both silicene and bulk silicon. The changes in electrical structure remain for deposition amounts as high as 9 Ls. These results illustrate the surprisingly rich array of structural and electronic properties that can be manifested in novel silicon nanostructures when utilising structurally tunable 2D substrates.

The work presented in this chapter results from the collaborative effort between the authors in the publication *Single-domain epitaxial silicene on diboride thin films*[126] and is currently being prepared for submission to an equivalent journal. The author of this thesis performed the STM experiments, and was directly involved in the acquisition of supporting core-level photoelectron spectroscopy and angle resolved photoelectron spectroscopy (ARPES). LEED measurements were performed by Yukiko Yamada-Takmura. For details of the sample preparation and Si deposition process see **section 5.2**.

6.1 Layered Silicon Nanostructure

The spontaneous formation of silicene on the ZrB_2(0001) surface exhibits a highly ordered striped domain structure [12]. In the previous chapter (**Chapter 5**) it has been demonstrated that additional silicon can be incorporated into the silicene sheet by depositing very small amounts of silicon onto the surface [126]. In doing so the striped domain structure is removed, but the structural and electronic properties of the silicene sheet are not significantly altered. **Figure 6.1** shows STM images of the silicene/ZrB_2 surface after a Si deposition equivalent to 0.5 Ls of silicene. In the top left-hand side of the image in **Fig. 6.1a** there is an area of single-domain silicene, within which the $(\sqrt{3} \times \sqrt{3})$-reconstruction of silicene on ZrB_2 (0001) can be observed as a triangular array of circular protrusions. The measured lattice constant of $a_{(\sqrt{3}\times\sqrt{3})} = 6.44 \pm 0.89$ Å is in good agreement with an expected value for the Zr (2×2) spacing of 6.37 Å[80, 141, 142]. Errors in distance measurements are estimated from the width of features in the Fourier transform of STM images. In the lower section of the image a second silicon layer is formed on top of the single-domain silicene sheet. The second silicon layer preserves a lattice with the same symmetry of the silicene $(\sqrt{3} \times \sqrt{3})$-reconstruction, but with a slightly increased lattice constant of $a^{2L}_{(\sqrt{3}\times\sqrt{3})} = 6.52 \pm 0.96$ Å; however, it displays a dramatically different quasi-ordered triangular-domain structure. The large scale STM image in **Fig. 6.1b** reveals that the new silicon nanostructure grows as an extended layer without forming large three-dimensional clusters.

Similar to the striped-domain silicene/ZrB_2 surface, atoms adjacent to the domain boundaries are observed to be mobile at room temperature. The atom mobility is directly observed by STM as a hopping of protrusions from one side of a domain boundary to the other. In the triangular-domain surface (**Fig. 6.2**), STM images recorded at the same surface position over time show that the hopping causes significant motion in the sides of the domains, yet the dark vertices remain fixed. Consequently, a good determination of the domain size can be made by Fourier transform measurement, yielding a value of

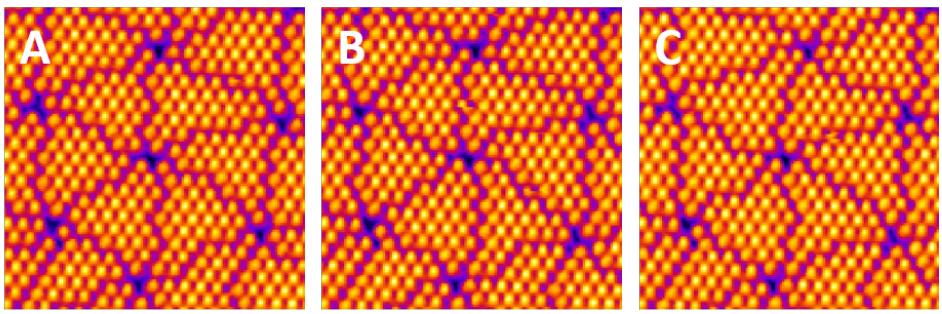

Figure 6.2: Si atom hopping at domain boundaries.
High resolution STM images of the 2 L silicon nanostructure taken at the same location (13 nm × 13 nm, $I_0 = 100\,pA$, $V_0 = -1.0\,V$. Over time individual hopping events result in significant changes in the shape of domain edges, however, the dark vertices of the triangular domains remain approximately fixed.

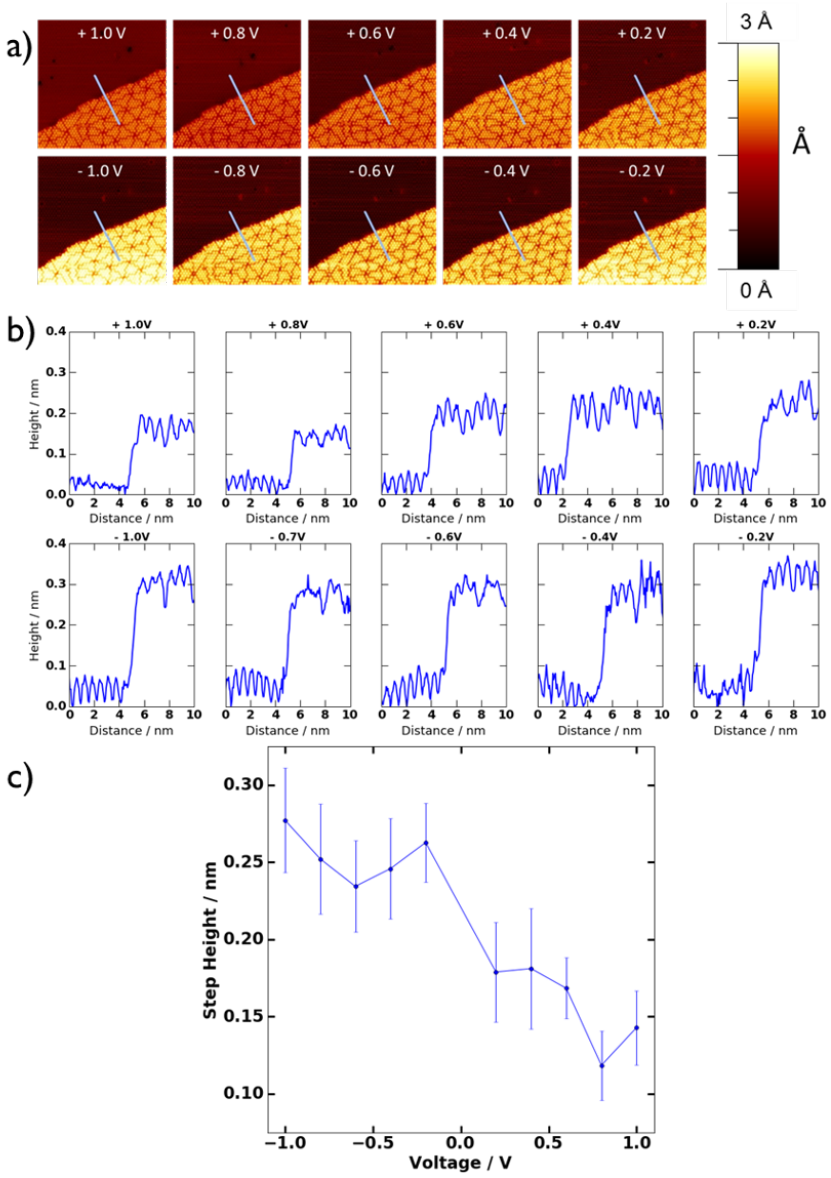

Figure 6.3: bias dependence of the 2 L silicon nanostructure height relative to the single-domain silicne surface.
(c) Graph of step heights measured from the line profiles in (b) corresponding to the blue lines in the STM images of (a). (30 nm × 30 nm, $\pm 1.0\,V$ $100\,pA$, $\pm 0.8\,V$ $80\,pA$, $\pm 0.6\,V$ $60\,pA$, $\pm 0.4\,V$ $40\,pA$, $\pm 0.2\,V$ $20\,pA$,

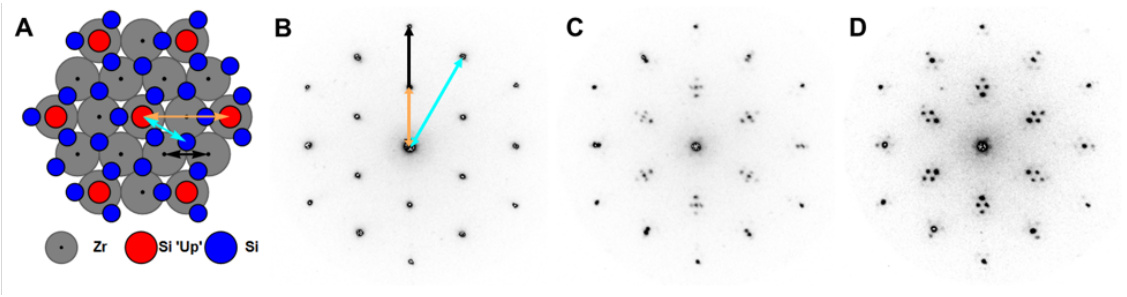

Figure 6.4: In-plane structural modification of the silicon surface upon Si deposition. μ-LEED pattern for (B) single-domain silicene surface, where the blue, orange, and black arrows correspond to the (1×1)-silicene, $(\sqrt{3} \times \sqrt{3})$-silicene, and (1×1)-ZrB_2(0001) spots associated to the equivalent distances in the real space ball model in (A). μ-LEED patterns(C) after Si deposition equivalent to 0.5 Ls of silicene, and (D) after Si deposition equivalent to 1.0 Ls of silicene.

3.96 ± 2.02 nm, where the large error is an indication to the variation in domain size.

The apparent height of the new layered silicon nanostructure relative to the domain-free silicene sheet as measured by STM is found to be heavily bias dependent, ranging approximately linearly from 0.30 nm to 0.15 nm over the voltage range of -1 V to 1 V (**Fig. 6.3**). This suggests that part of the apparent height difference arises from differences in the electronic structure of the two layers. Importantly, this distance is less than that of the ZrB_2 (0001) step height at 0.35 nm [142], and less than predicted values for multi-layer silicene [88, 90, 143]. The small interlayer spacing is an indication that the new layered silicon nanostructure is not formed from weakly Van der Waals coupled layers.

LEED measurements reveal that the in-plane structural modification upon formation of the triangular-domain surface influences the entire silicon structure. The single-domain silicene LEED pattern comprises of three significant contributions: the Zr (1×1), silicene (1×1), and silicene $(\sqrt{3} \times \sqrt{3})\mathrm{R}30^o$ spots, highlighted by the green, blue, and orange lines respectively, in the ball model of **Fig. 6.4a** and the LEED pattern of **Fig. 6.4b**. The LEED pattern is then monitored as the silicon deposition amount is increased. In **Fig. 6.4c, and d** the LEED patterns for 0.5 Ls and 1.0 Ls of deposited silicene are shown. While the spots attributed to the silicon structures are observed to vary throughout the process, the Zr (1×1) surface is not observed to change. Two important points should be noted from this: (i) the structural modification of the surface is limited to the silicon layers, and (ii) even at a complete 2 L coverage the LEED is sensitive to the entire silicon structure. A more quantitative analysis is provided in **Fig. 6.5**, where the Zr (1×1) LEED spot integrated intensity ratio, $I = I_\Theta/I_0$ is plotted as the Si coverage Θ is increased. After an initial slight increase, I decreases by approximately a third at a complete 1 L deposition amount. The inelastic mean-free path of electrons in a crystal is found to be largely independent of the material and for electrons of energies 20 - 200 eV the mean-free path is of order 5 - 10 Å[144]. Specifically, the intensity of emitted electrons will be reduced by a factor of $1/e$ ($\sim 34\%$) after travelling 5 - 10 Å. It can

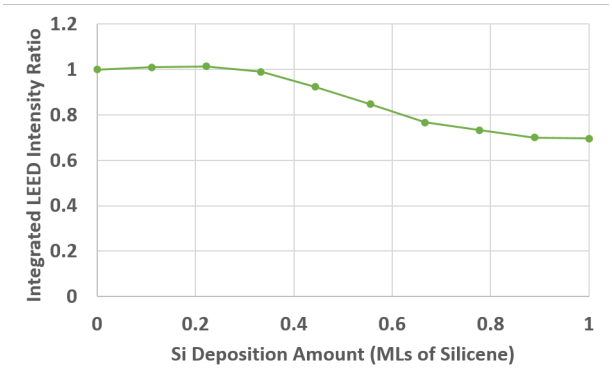

Figure 6.5: Reduction of (1×1)-Zr LEED spot intensity upon Si deposition.
Graph showing the reduction in the integrated LEED intensity ratio, $I = I_\Theta / I_0$, for the (1×1)-Zr spot.

therefore be concluded that the reduction in intensity of the Zr (1×1) spot is consistent with this simple model and that we should expect LEED to probe the first few atomic layers of the material.

At a deposition amount of 0.5 Ls of silicene, two new features are present (**Fig. 6.4c**). The first is the appearance of an additional silicene (1×1) spot with an approximately 15 % larger lattice constant. The second new feature is a diamond of satellite spots around the silicene $(\sqrt{3} \times \sqrt{3})$ spot; these are attributed to the triangular-domain pattern of the second layer. Finally at a complete 2 L coverage (**Fig. 6.4d**), in addition to the unaltered Zr (1×1) spots, the LEED pattern is solely comprised of features that are produced by the deposition process. The deposited silicon that forms the quasi-ordered triangular domain surface must therefore cause a restructuring of the two silicon layers since there is a complete disappearance of LEED features attributed to the single-domain silicene surface.

The small increase of the silicon (1×1) lattice parameter suggests that the triangular domain structure arises from a new epitaxial relationship between the Si and the ZrB_2 substrate. In the monolayer, the flexibility of the silicene sheet allows for additional silicon to be incorporated into the surface altering the stripe-domains [126, 145]. In the 2 L surface, the rigidity of the silicon bonding may force the silicon lattice to enlarge, diminishing the lattice matching between the Zr (2×2) and silicon $(\sqrt{3} \times \sqrt{3})$-reconstruction.

6.2 Electronic Properties of Layered Silicon Nanostructure

The electronic properties of the new layered silicon nanostructure with triangular domains have been investigated by STS. **Figure 6.6** compares the current as a function of applied bias voltage $I(V)$ above the surfaces with striped-domain, single-domain, 2 L, 3 L, and 10 L surfaces. There is little difference in the electronic structure between the striped-domain and single-domain surfaces within 1 V of the Fermi energy. However, a clear difference is observed between the monolayers and the 2 L triangular domain surface. In particular, there is a far greater relative current at negative bias (filled states) vs. positive bias (empty states).

Surprisingly, when the amount of deposited silicon is increased above 1 L, multiple quasi-ordered triangular domain silicon layers are observed in STM. **Figure 6.7a** shows an STM image of the silicon surface across a ZrB_2 terrace step after a 1.5 L deposition. The top layer - in the bottom right of the image is 0.35 nm (a ZrB_2 (0001) step) above the lowest layer on the terrace below, where STS spectra confirm that both layers have a conductance expected for the 2 L surface. A third layer of silicon can then be seen to have grown upon the lower terrace, with an apparent step height of 0.15 nm above the 2 L surface (step height profile shown in **Fig. 6.7b**); this apparent height is not expected to be significantly sensitive to the applied voltage owing to the similarity in electronic structure (**Fig. 6.6**). As with the step height of the 2 L surface above the single-domain silicene surface, the interlayer spacing of 0.15 nm is smaller than would be expected for weak van der Waals interactions between layers. STS performed on the third layer reveals little difference in electronic properties between the 3 L (green line) and 2 L (red line) surfaces (**Fig. 6.6**); however, the quasi-ordered triangular domain size increases by approximately 30 % in comparison to the 2 L surface. LEED measurements performed on the surface, as the silicon deposition amount is increased, show that the new layers do not alter the observed pattern. This, coupled with the observation that the same

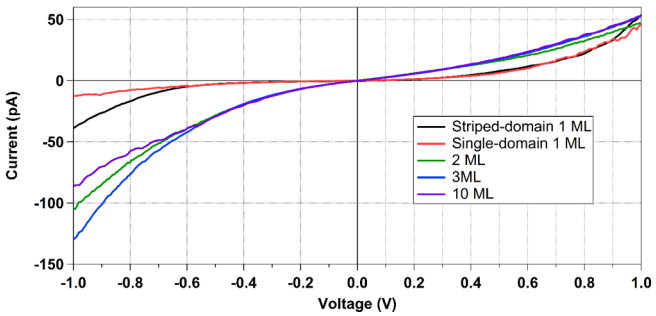

Figure 6.6: Scanning tunnelling spectra of silicene and silicon surfaces.
$I(V)$ curves taken above the stripe-domain (black), single-domain(red), 2 L silicon nanostructure (green), 3 L structure (blue), and 10 L surface - after a 9 L deposition amount - (purple). ($I_0 = 50\,pA$, $V_0 = 1.0\,V$).

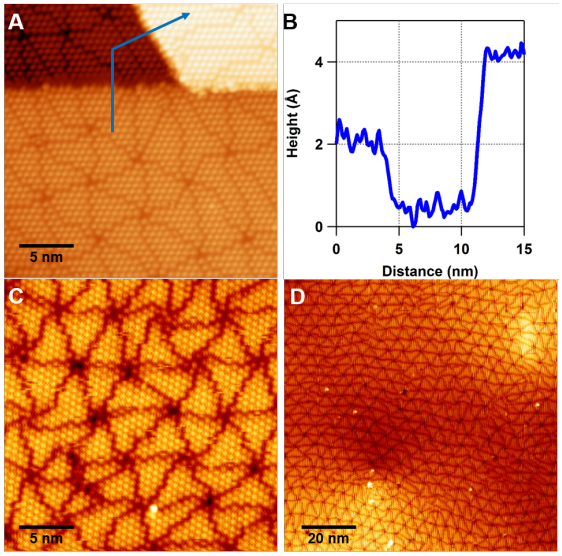

Figure 6.7: Silicon surfaces after significant Si depositions.
A) STM image of silicon surface after a Si deposition equivalent to 1.5 Ls of silicene. Three layers can be observed, at the lowest (top left) a 2 L silicon nanostructure is ~ 3.5 nm (a $ZrB_2(0001)$ step) below another $ZrB_2(0001)$ terrace also with a 2 L silicon nanostructure grown on top. In the bottom of the image another triangular domain silicon nanostructure (3 L) is observed ~ 1.5 nm above the 2 L surface ($I_0 = 50\,pA$, $V_0 = 1.0\,V$). B) Height profile of the blue line in (A). C) High resolution ($I_0 = 50\,pA, V_0 = 1.0\,V$) and D) large-scale ($I_0 = 20\,pA$, $V_0 = -1.0\,V$) STM images of the layered silicon nanostructure after a Si deposition amount equivalent to 9 Ls of silicene.

structure is observed by STM after a 9 L deposition (**Fig. 6.7c**), suggests that the new silicon nanostructure is stable and does not transition to conventional bulk silicon, even at significant thicknesses. We note here that although 9 Ls of silicene were deposited, the actual thickness of the silicon nanostructure is unknown. However, a small change in the STS spectrum of the 10 L surface at negative bias (**Fig. 6.6**) suggests that it is at least of a thickness greater than 3 Ls. In addition, we note that for these significant amounts of Si deposition the surface remains atomically flat over large areas as can be observed in **Fig. 6.7d**.

6.3 Conclusion

In conclusion, it has been shown that deposition of Si onto the single-domain silicene/ZrB2 surface forms a new layered silicon nanostructure with dramatically different structural and electronic properties. STM and LEED have shown that there is a restructuring of the silicon layers as the 2 L surface is grown upon the single-domain silicene surface. However, the exact structure of the new nanostructure is not easily determined and will require further investigation. LEED measurements indicate that there is still a hexagonal silicon lattice with a similar lattice constant (0.39 nm) to the silicene/ZrB_2 (1×1) unit cell (0.36 nm) that qualitatively describes the formation of the triangular domain boundaries.

A variety of silicon nanostructures are known, the properties of which vary greatly with crystallographic face [146], doping [147, 148], particle size [149], and morphology [149–151]. Application of significant pressures ($>$ 10 GPa) to Si induces a number of polymorphic phase transitions [152–154]. Interestingly, these structures are metallic, in stark contrast to semiconducting diamond Si found at room temperature. In this work an atomically sharp transition between electronically distinct silicon nanostructures has been found. As in the case of the single-domain silicene surface, this new Si nanostructure has finite conductance at the Fermi level indicating that the electronic structure is not that of bulk semiconducting silicon. It may therefore be that the new Si nanostructure could be used as a conductive contact to the single-domain silicene surface. To better understand the changes in electronic structure new investigations have been performed. The preliminary analysis and interpretation of these results will be discussed in the next section.

6.4 Future Work

LEED measurements of the layered silicon nanostructure have revealed that the in-plane symmetry of the lattice reflects that of the silicene/ZrB_2 surface. However, the small apparent step height (1.5 Å - 3.0 Å) of the layered silicon nanostructure, obtained by STM measured realtive to the single-domain silicene sheet, implies that the out-of plane arrangement of the new silicon structure is non-trivial. In order to gain new insights into the changes in the silicon environment core-level photoelectron spectroscopy has been performed upon the 2 L layered silicon nanostructure. The characterisation reveals that the binding energy of Si atoms in the new layered silicon nanostructure no longer represents the chemical environment that is a signature of silicene/ZrB_2 surface.

In **fig. 6.8a**, a core-level photoelectron spectrum for the single-domain silicene surface is shown (black line). Here we present a best fit achieved from two spin-orbit split doublets (red line). After removal of a Shirley background, the spectrum is fit by two asymmetric pseudo-Voigt doublets (green and blue) with the Si $2p^{\frac{3}{2}}$ peaks centred

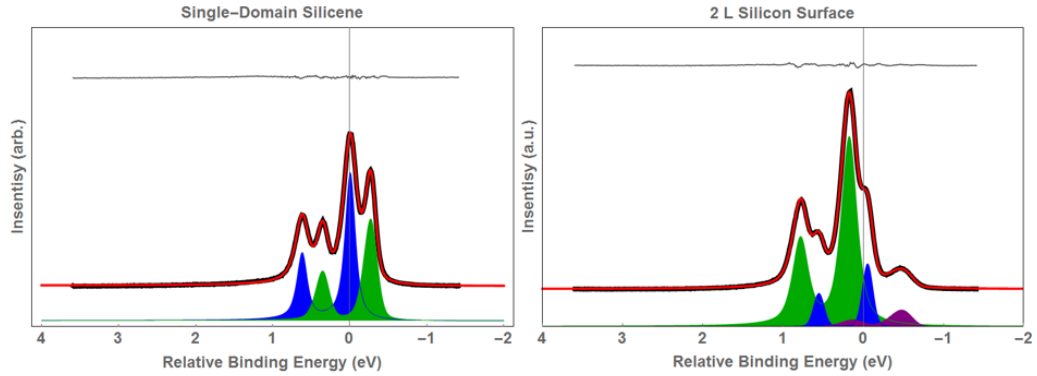

Figure 6.8: Silicene and layered silicon nanostructure core-level photoelectron spectroscopy.
Core-level photoelectron spectra for (LEFT) single-domain silicene, and (RIGHT) 2 L silicon nanostructure surfaces. Similarly to previously reported examples the single-domain silicene surface spectrum is well described by two Si 2p doublets. The spectrum recorded for the 2 L layered silicon nanostructure is notably different. The new features, well described in the main text, clearly detail a new chemical environment of the Si atoms in the layered silicon nanostructure.

at relative binding energies of 0 eV, and -272 eV. The $2p^{\frac{1}{2}}$ states are then found to lie 620.0 ± 0.5 meV above with branching ratios of 0.510 ± 0.004, and 0.437 ± 0.002, respectively. Strictly the branching ratios of the spin-orbit split doublets should be 0.5, deviation from this can be used as an indication of unaccounted for chemical states, such as the third component often used in fitting silicene/ZrB_2 spectra [12, 81]. The full width half maximum (FWHM) of the two doublets are 144 ± 1 meV, and 202 ± 1 meV, where the pseudo-Voigt, Gaussian to Lorentzian ratios are 0.76 ± 0.03, and 0.00 ± 0.02, with asymmetric parameters of 0.005 ± 0.005, and 0.035 ± 0.002. The amplitude ratio of the two peaks is 1.6 ± 0.1, close to an expected value of 2. Quoted errors are standard deviation generated from the fitting procedure.

Dramatic changes are seen between the single-domain and the 2 L surface core-level photoelectron spectrum (black line in **fig. 6.8b**). In comparison to the spectrum for the single-domain surface, two new states are present, one at lower binding energy and the other above the state at 0 eV that is present in both surfaces. Simultaneously, the higher binding energy state of the single-domain surface disappears. The 2 L spectrum is well described by a fit (red) composed of a set of three doublets (blue, green, and purple). The two new states have Si $2p^{\frac{3}{2}}$ relative binding energies centred at 173 eV, and -479 eV , where the $2p^{\frac{1}{2}}$ states are found 608.3 ± 0.4 meV higher. The branching ratios of the two new states are 0.40 ± 0.09 and 0.505 ± 0.007, with pseudo-Voigt, Gaussian to Lorentzian rations of 1.00 ± 0.08, and 0.68 ± 0.07; asymmetry parameters of 0.07 ± 0.02, and 0.00 ± 0.01, and FWHMs of 309 ± 7 meV, and 151 ± 2 meV respectively. The state at 0 eV, is found to have a branching ratio of 0.449 ± 0.004, pseudo-Voigt, Gaussian to Lorentzian ratio of 0.49 ± 0.01, FWHM of 217 ± 1 meV and an asymmetry parameter of 0.017 ± 0.003. The amplitude ratio of the three doublets is then, $1 : 4 : 12$. The

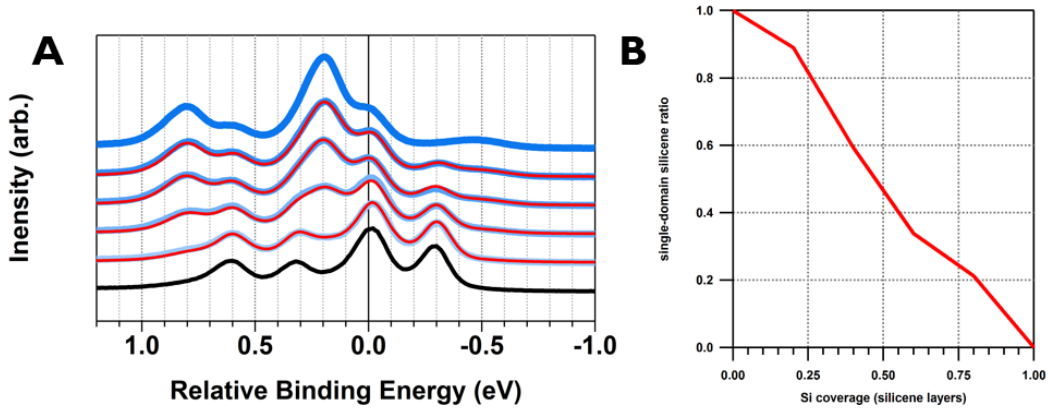

Figure 6.9: Si deposition dependence on core-level photoelectron spectra. (A) The spectrum of the single-domain silicene and 2 L layered silicon nanostructure surfaces are shown in black and dark blue at the bottom and top of the graph respectively. The intermediate curves are taken for intermediate Si deposition amounts between 0 L and 1 L of silicene. The red curves for these are fits that describe a linear combination of the two psuedo-voigt functions that independently detail the single-domain silicene and 2 L layered silicon nanostructure surfaces. (B) Plot of the ratio of single-domain silicene to 2 L layered silicon nanostructure core-level features as a function of Si coverage. A direct one-to-one conversion is found indicating that the Si deposition induces a complete structural transformation of the surface.

change in the spin-orbit coupling separation of $\approx$ 12 meV between the single-domain and 2 L surfaces hints to a significant change in the structure of the 2 L surface.

Figure 6.9 shows a series of core-level photoelectron spectra for intermediate silicon deposition amounts between the single-domain (bottom) and 2 L (top) surfaces. Each spectrum is fit (red lines) to a function that describes a linear combination of the two asymmetric pseudo-Voigt multiple doublet functions as detailed above that individually represent the single-domain and 2 L surface spectra. The high quality of this basic procedure can be seen in the good agreement between the experimental spectra and respective fits. As with the LEED measurements, this suggests that there is a significant change in the structural properties of the 2 L surface that destroys the single-domain silicene layer, which has a distinctly different chemical environment.

ARPES measurements have been performed to reveal the nature of the changes in electronic structure observed in both STS and core-level photoelectron spectroscopy. In **Fig. 6.10** an ARPES spectra taken along the ZrB_2 $(0001)-(1\times1)\,\Gamma-M-\Gamma$ direction is shown. In comparison to previously reported equivalent ARPES measurements on the stripe-domain [12] and single-domain [126] silicene surfaces, the new layered silicon is found to have additional bands crossing the Fermi level in the vicinity of the ZrB_2 $(0001)-(1\times1)$ M-point (vertical white line in **Fig. 6.10**), which corresponds to the K-point of the stripe- and single-domain silicene surfaces on ZrB_2. The greater density of states due to the additional bands crossing the Fermi level qualitatively suggest that the new layered silicon is metallic and that it will be more conductive than silicene.

In summary the results of the core-level photoelectron spectroscopy indicate that

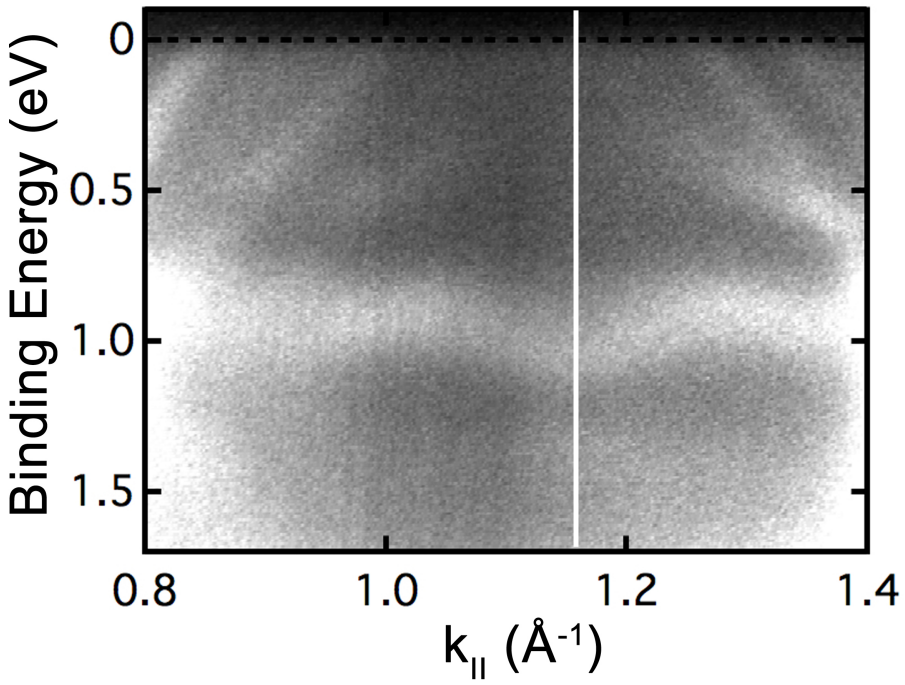

Figure 6.10: Valence electronic structure of new layered silicon nanostructure. ARPES spectra taken along the ZrB_2 $(0001)-(1\times1)\,\Gamma-M-\Gamma$ direction in the vicinity of the M-point, which corresponds to the K-point of single-domain (1×1) silicene on ZrB_2. Spectra reveal a pair of bands symmetrically separated in the vicinity of the ZrB_2 $(0001)-(1\times1)$ M-point (white vertical line) that cross ther Fermi level.

there is significant change in the chemical environment of Si atoms in the 2 L layered silicon nanostructure in comparison to single-domain silicene/ZrB_2. The transition in the shape of the sprectra for intermediate amounts of Si deposition corroborate the LEED observations that suggest a complete restructuring of the silicon lattice. ARPES measurements have then been used to show that these changes result in the formation of a metallic layered silicon surface. To further understand the origin of these new metallic bands new investigations into the atomic scale geometry of the layered silicon surface will be required.

Chapter 7

Single Cobalt Atoms on Silicene/ZrB_2

The adsorption of magnetic adatoms onto conductive substrates has been used to probe intriguing magnetic phenomena such as inelastic spin excitations [38, 39], magnetic ordering at domain boundaries [155, 156], skyrmions [157, 158], and highly correlated interactions such as the Kondo effect [115, 159]. The use of surfaces with non-trivial electronic structures opens the possibility to investigate even more exotic physics and so it is of great interest to explore the interactions between magnetic atoms and 2D surfaces. For example, transition metal atoms deposited upon free-standing silicene have been predicted to exhibit a number of interesting magnetic phenomena [145, 160–163] including a quantum anomalous Hall effect [164], and other topological states [165].

In this chapter it is demonstrated that silicene/ZrB_2 is robust to the deposition of individual Co atoms onto its surface. The structural and electronic properties of individual Co atoms on the silicene/ZrB_2 surface are investigated by STM and STS. A three-fold symmetric binding site of the Co atoms is found, which is shown to support existing DFT models of the silicene/ZrB_2 surface by directly observing the rotation of adjacent silicene domains. It is found that Co atoms on the silicene/ZrB_2 surface exhibit a bias dependent symmetry, indicating a strong level of hybridisation to the substrate. Finally, it is found that voltage pulse induced switching of Co atoms between a bi-stable binding configuration can occur.

Co atoms have been deposited upon a clean silicene/ZrB_2 sample by electron-beam bombardment (Omicron EFM 3 evaporator, V$= 780$ V, $I_{fil} = 1.83$ A, $I_{emission} = 13.0$ mA, $I_{flux} = 17.0$ nA) of a high purity Co rod (Goodfellow, CO007902 Cobalt, Rod Diameter: 2.0 nm, Rob Length: 45 mm, High Purity: $99.99+$%). The deposition is done directly onto the silicene sample while it is in the Cryogenic STM head and after it has been imaged at 2 K; this is done by lowering the sample into the room temperature part of the STM vacuum chamber. The head is continuously cooled, such that the substrate temperature does not exceed 30 K. Typical deposition times were between 10-30 seconds

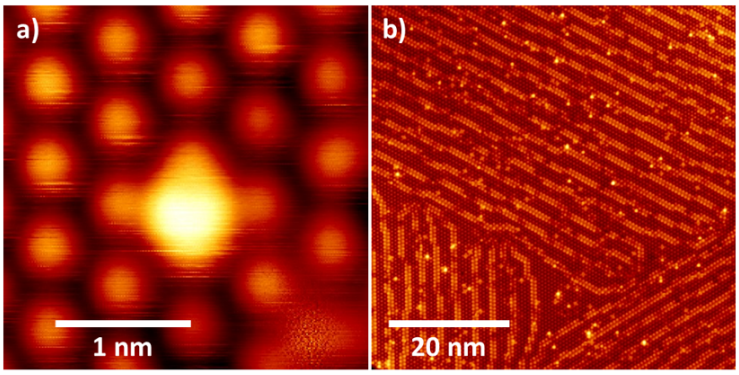

Figure 7.1: STM images Cobalt on silicene.
(a) High resolution STM image of an individual Co atom on silicene ($I_0 = 100\,pA$, $V_0 = -100\,mV$). (b) Large scale STM image of an area of silicene with many Co atoms bound on the surface ($I_0 = 100\,pA$, $V_0 = 100\,mV$).

to obtain coverages substantially below a monolayer. **Figure 7.1a** shows a typical STM image of an individual Co atom on the silicene/ZrB_2 surface. In the background the $(\sqrt{3}\times\sqrt{3})$R30^o reconstruction of the silicene lattice can been seen; a circular protrusion, approximately 0.5 nm in diameter, at the centre of the image is associated with the Co atom. A large scale STM image of silicene/ZrB_2 with many Co atoms absorbed on the surface is shown in **Fig. 7.1b**. The very low coverage of Co atoms does not cause any reconstruction of the silicene surface and allows for the investigation of single atoms.

Theoretical support has been provided by Nicolae Atodiresei, Vasile Caciuc, and Stefan Blügel at Forschungszentrum Jülich, Germany. First-principles density functional theory (DFT) [166] calculations have been carried out using the projector augmented wave method [167] pseudopotentials generated with the Perdew-Burke-Ernzerhof exchange correlation functional [168] as implemented in the VASP code [169, 170]. The silicene on ZrB_2(0001) was modelled by a slab consisting of 64 Si atoms on three Zr and two B atomic layers amounting to 308 substrate atoms using the stripe-like geometry proposed by Lee et al. [83]. For an energy cut-off of 500 eV and a Brillouin zone sampling by 4 k-points in the irreducible part of the Brillouin zone, the relaxed geometry for the silicene/ZrB_2(0001) system was obtained when the calculated forces were less than 10 meV/Å. Furthermore, simulated STM images were obtained using the Tersoff-Hamann theory [32].

7.1 Co atom binding site

The binding site of Co atoms on the silicene surface is determined using the structural model of Lee *et al.*[83]. This model allows for the unambiguous determination of the 'unseen' silicene (1×1) lattice by aligning the Si 'up' atoms of the model upon the nearest domain boundary (see **Fig. 7.2**). The validity of this model can be seen from the simulated STM images in **Fig. 7.3**. In **Fig. 7.4a** and **Fig. 7.4b** the same STM image of a Co atom on the silicene/ZrB_2 surface is shown, where in **Fig. 7.4b** a ball model of the silicene/ZrB_2 lattice (see **Fig. 7.4c**) has been overlaid and a high contrast colour scheme is used to emphasise the centre of the atom. From **Fig. 7.4b** it is possible to see that the centre of the Co atom lies approximately at the Si near-bridge atom highlighted in yellow.

DFT investigations of the transition metal atoms adsorbed onto free-standing silicene have predominantly found the silicene hollow site to be the most stable configurations [161, 162, 164, 165]. Other investigations have considered the substitutional doping of transition metal atoms [145, 160, 162], where the most stable configuration is heavily dependent upon the transition metal used. For Co deposited upon silicene/ZrB_2 it is seen that the Co atoms do not bind in the hollow site of the silicene lattice, but at the position of a Si near-bridge atom. It is difficult to make conclusive statement on the exact binding

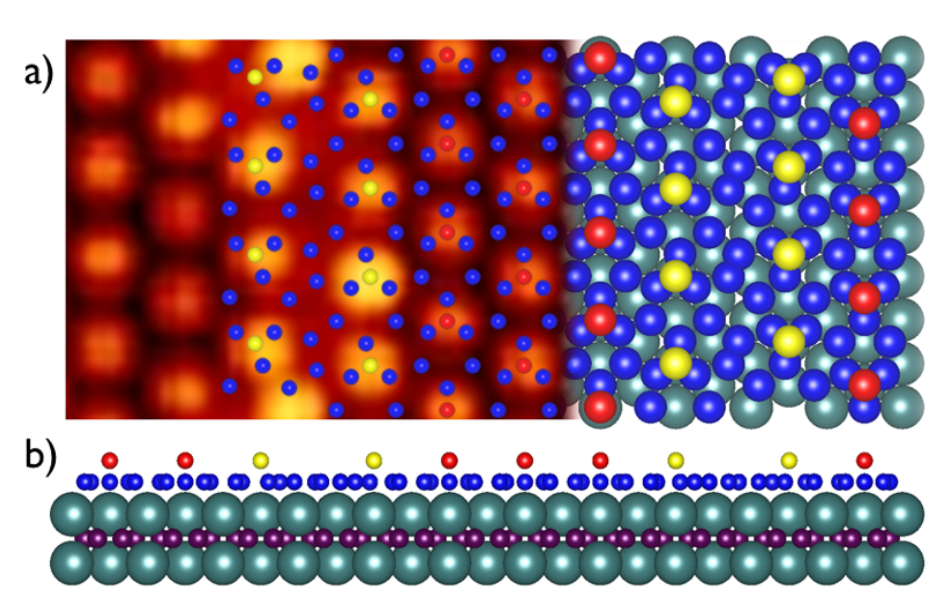

Figure 7.2: Silicene lattice assignment to STM images.
(a) Ball model of the striped domain boundary silicene/ZrB_2 surface from DFT calculations overlaid on to an equivalent STM image ($I_0 = 0.1\,nA$, $V_0 = -10\,mV$). (b) Side view of the DFT model in (a). For the DFT models in (a) and (b) the Zr, B, Si near bridge and Si hollow, and Si 'up' atoms are represented by the gray, purple, blue, and red balls. Yellow balls highlight Si 'up' atoms in the domain boundaries.

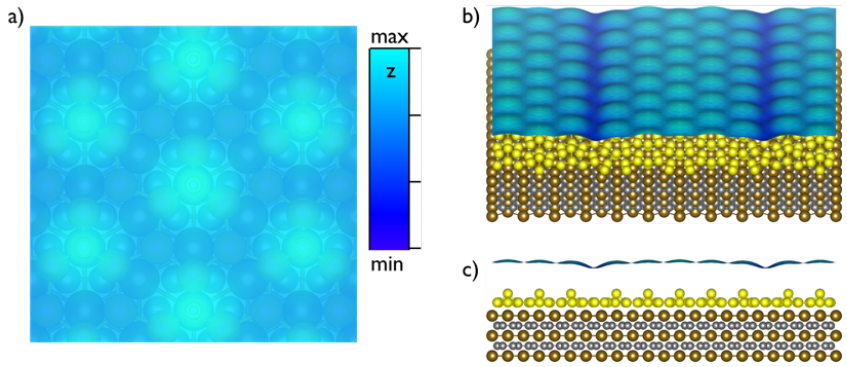

Figure 7.3: Simulated STM image of silicene/ZrB_2.
(a)Top, (b) oblique, and (c) lateral view of a contour showing the height of constant integgrated density of states from the Fermi energy to $+1$ eV, whcih corresponds to an STM topographic image that would be taken with a set point voltage of $+1$ V. A ball model of the silicene/ZrB_2 is also shown with Si (yellow), Zr (brown), and B (silver) atoms. The bright spots n the contour correspond to the Si 'up' atoms in the silicene surface.

configuration, especially because only one of the six atoms in the silicene unit cell can be imaged with STM. However, it is considered that the lack of any substantial distortion in the silicene lattice around the Co atom, and that the maximum temperature during deposition is 30 K are indications that the Co atom is not a substitutional dopant in the surface.

The preference of adsorbed Co atoms in DFT studies to bind in the hollow site is a result of the configuration providing the greatest Si coordination to the Co atom. The unique buckling of silicene on ZrB_2, where the Si 'up' atom is raised approximately 1.5 Å above the plane of the other Si atoms, may therefore provide an alternative binding site with greater Si coordination to the Co atoms. Later it will be demonstrated that the state of Co atoms on the surface is meta-stable, suggesting that the observed binding site may not be the ground state of the system (see **section 7.4**).

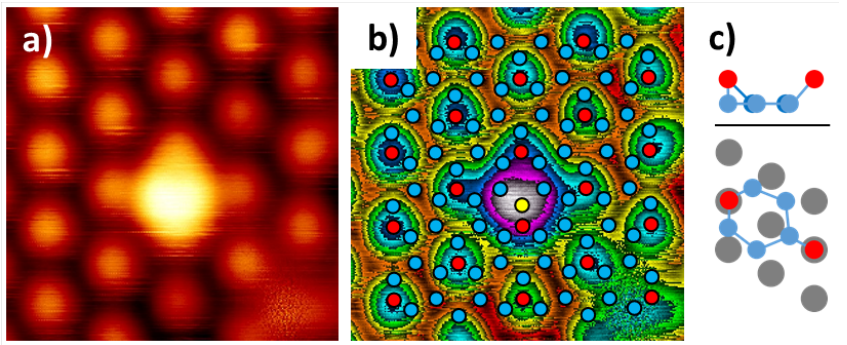

Figure 7.4: Binding site of cobalt monomer on silicene.
(a) STM image of a single Co atom on silicene/ZrB_2 ($I_0 = 0.1$ nA, $V_0 = -100$ mV). (b) Same as in (a), but with a high contrast colour scheme and silicene lattice ball model overlaid to highlight the binding site of the Co atom above the Si near-bridge site. (c) Side and top view of the silicene/ZrB_2 surface.

7.2 Electronic Structure of Co atoms on Silicene/ZrB_2

Transition metal atoms deposited upon metallic and thin insulating substrates are typically observed as circular protrusions by STM [171–173]. However, when atoms are placed upon or within semiconducting surfaces anisotropic patterns can be observed [174–176]. In this section bias dependent imaging and STS is used to investigate the electronic structure of Co atoms on the silicene/ZrB_2 surface. It is demonstrated that the observed symmetry of Co atoms changes significantly with bias voltage. In particular at certain voltages the Co atoms become anisotropic indicating a strong level of hybridisation with the silicene surface, similar to semiconducting [174–176] or molecular systems [177]. These anisotropic features indicate that the interactions between the semiconducting silicene surface, ontop of the metallic ZrB_2(0001) surface [80, 84, 85], are important for defining the properties of the adsorbed Co atoms.

Constant current STM measurements provide contrast through a convolution of electronic and topographic effects. It is possible to probe the electronic structure of surface features by imaging the same area at different bias voltages. Assuming that there is no change in the topography, any changes in the contrast of images can be attributed to different electronic features. **Figure 7.5** shows STM topographies of three Co atoms at ± 300 mV, ± 200 mV, and ± 100 mV. At negative bias voltages, filled states, the Co atoms are observed as circular protrusions on the surface with a decreasing diameter as the bias voltage approaches the Fermi level (see **Fig. 7.5a-c**). However, at positive bias, empty states, the Co atoms become increasingly anisotropic with increasing voltage (see **Fig. 7.5d-f**), elongating across the short axis of the silicene $(\sqrt{3} \times \sqrt{3})$ unit cell.

Further changes in the symmetry of the Co atoms are seen when the bias dependent imaging is focused around the Fermi level. **Figure 7.6a** and **Fig. 7.6d** show STM images of a Co atom at -100 mV and 100 mV respectively revealing the same symmetries as seen at the lower end of the voltage dependence in **Fig. 7.5**. For both the STM images at -50 mV and 50 mV (**Fig. 7.6b** and **Fig. 7.6e**) the Co atom is observed as an almost triangular feature slightly elongated along the short axis of the silicene unit cell. However, very close to the Fermi level at -3 mV and 3 mV in **Fig. 7.6c** and **Fig. 7.6f** the Co atom is resolved as two lobes with a nodal plane along the ZrB_2 $[11\bar{2}0]$ or silicene(1×1)-armchair direction.

The STM images in **Fig. 7.5** and **Fig. 7.6** are measurements proportional to the integrated density of states. As such, ignoring any topographic effects, the differences in observed symmetry of the Co atoms can be interpreted as imaging the LDOS that reflect the orbital symmetries of the Co-silicene interactions. The significant changes in the observed symmetry of individual Co atoms on silicene/ZrB_2 suggests that the Co atoms have a strong anisotropic interaction with the silicene surface. **Figure 7.7a** and **Fig. 7.7b** show STM images of a Co atom upon which the large voltage range STS

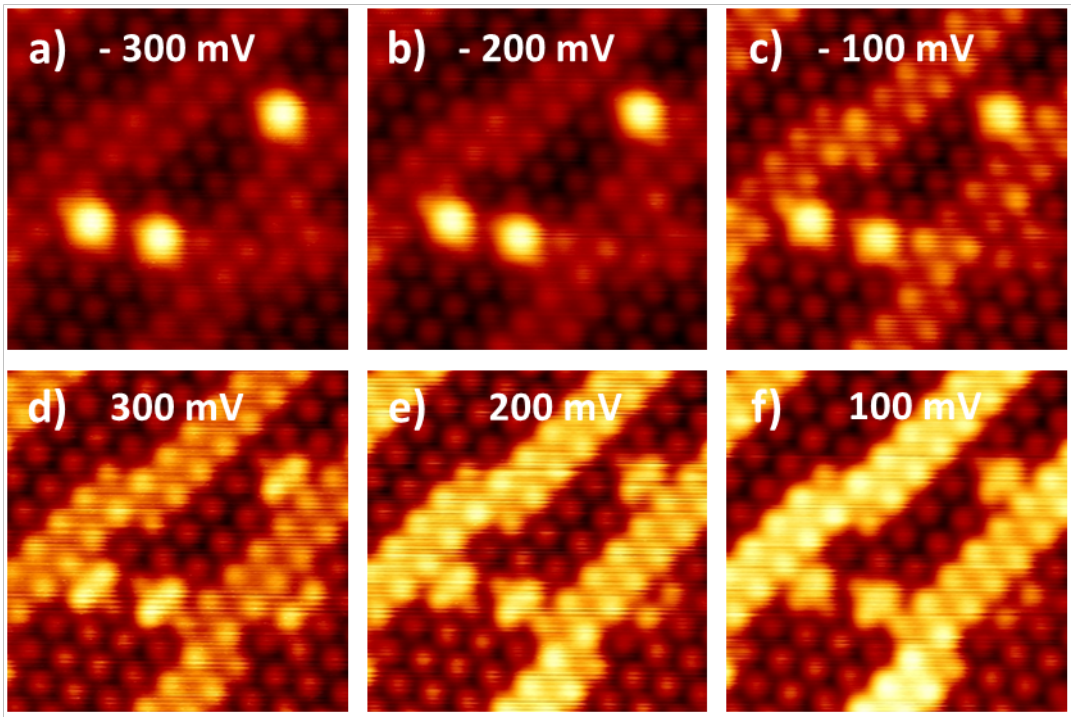

Figure 7.5: Voltage dependent STM images of Co on silicene/ZrB_2 far from the Fermi level.
High resolution STM images ($5.98\,\mathrm{nm} \times 5.98\,\mathrm{nm}$) of three Co atoms on silicene ZrB_2 ($I_0 = 100\,\mathrm{pA}$).

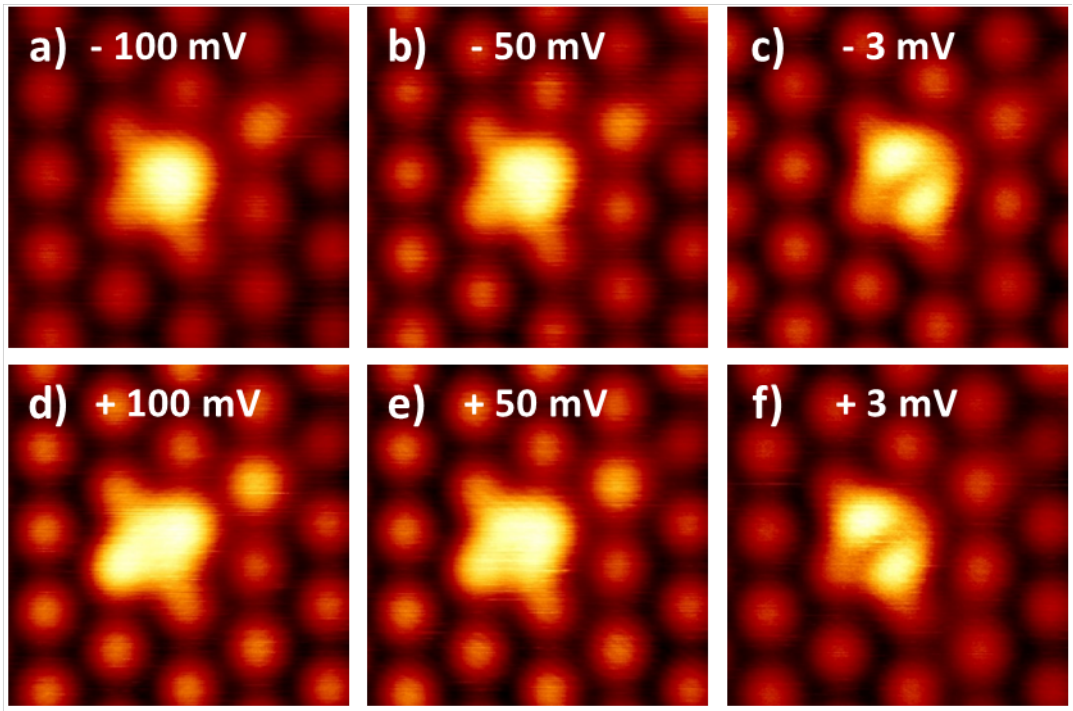

Figure 7.6: Voltage dependence of Co atoms on silicene.
(a-c, d-f) Bias depedent STM images of an individual Co atom on the silicene/ZrB2 surface (2.6 nm x 2.6 nm).(a, b, d, e) $I_0 = 100\,\mathrm{pA}$. (c, f) $I_0 = 10\,\mathrm{pA}$.

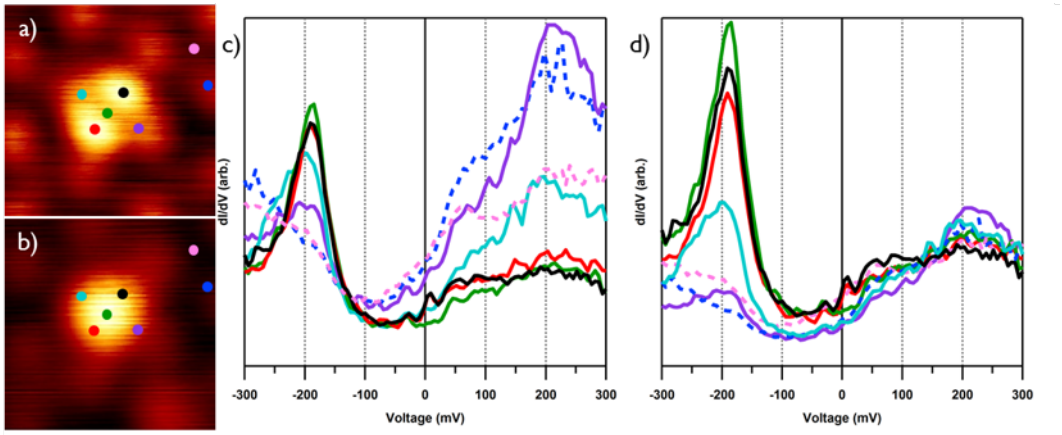

Figure 7.7: High voltage spectroscopic measurements of a individual Co atom on silicene/ZrB_2.
High resolution STM images of a Co atom on silicene/ZrB_2 $(1.7\,\mathrm{nm}\times1.7\,\mathrm{nm})$ (a) $V_0 = -3$ mV, $I_0 = 0.1$ nA, (b) $V_0 = -300$ mV, $I_0 = 0.5$ nA. (c) STS measurements of the Co atom in (a)&(b) ($V_0 = -0.3$ V, $I_0 = 0.5$ nA). Red, green, blue, and black curves taken at the Co: top lobe, centre, lower lobe, as shown in (a) and the silicene background. (d) Same as in (c), but where the spectra have been normalised to the filled states.

measurements in **Fig. 7.7c** were taken. STS point spectra were recorded at different locations on the Co atom and bare silicene surface as indicated by the coloured circles in **Fig. 7.7a** and **Fig. 7.7b**. In **Fig. 7.7c** the as recorded spectra are shown, where the set point current is in the filled states. To help emphasise the changes in the spectra at negative biases they have been re-normalised to the filled states in **Fig. 7.7d**. The integrated dI/dV from the Fermi level to the set point voltage is equal to the set point current. The re-normalisation is achieved by artificially enforcing this relationship for the opposite bias voltage, positive in the case of **Fig. 7.7d**.

In **Fig. 7.7d** it becomes very clear to see that the spectra recorded at the Co atom top lobe (black), centre (green), bottom lobe (red), left side (cyan), and right side (purple) all display a feature at approximately -190 mV that is not present at either of the two locations on the bare silicene surface (blue, and pink). In metallic systems the hybridisation between the surface and transition metal adatoms broadens the metal atom d-orbitals, typically to around a hundred milli-electron volts[120, 171–173, 178–182]. The Co atom feature is around 100 mV wide and is therefore expected to correspond to a d-orbital of the Co atom on silicene/ZrB_2. As should be expected the spatial symmetry of the feature at -190 mV matches that of the Co atoms in STM topographies at negative biases in **Fig. 7.5a-b**.

The STS curves in **Fig. 7.7c** are used to understand the origin of the elongated features in the STM images of Co atoms at large positive voltages (**Fig. 7.5d-f**). Logically, the spectra recorded at the Co atom lobes (black and red) and the Co centre (green) have a significantly reduced LDOS in comparison to the bare surface (blue and pink). What is not so clear is that the spectra recorded at the Co left side (cyan) and

right side (purple) do not have significantly different LDOS than the background spectra (blue and pink); in fact the left hand side has a diminished LDOS in comparison to the background. It is therefore likely that the contrast observed at positive biases, in empty states, is significantly influenced by the topography of the Co atom.

It has been shown that Co atoms on the silicene/ZrB_2 surface exhibit a strong bias dependent symmetry when observed by STM. Spectroscopic measurements have been used to identify electronic features of the Co atoms responsible for the observed topographic symmetries. Identification of a Co atom d-orbital suggest that the interactions between the Co atoms and the silicene/ZrB_2 surface are consistent with those of transition metal atoms on metallic substrates. However, the significant anisotropic changes in the observed symmetries of electronic features suggests that the Co atoms interact in a manner similar to semiconducting systems. Furthermore, from large voltage range STS measurements no electronic feature is found that could explain the two lobe structure of Co atoms at voltages close to the Fermi level. Later high resolution spectroscopic measurements are used to investigate the origin of these features (see **section 8**).

7.3 Rotation of Silicene Domain Boundaries

Silicene formed upon the $ZrB_2(0001)$ surface forms a $(\sqrt{3} \times \sqrt{3})R30^o$ reconstruction that is commensurate with respect to a $Zr(2\times2)$ lattice (see **section 3.3**). As such there are two equivalent phases of the silicene lattice, one a 180^o rotation of the other. DFT models of the striped domain structure of silicene/ZrB_2 have suggested that adjacent domains are of the opposite phase joined by a distorted lattice at the boundaries [83]. In this section it is shown how Co atoms bound on the silicene/ZrB_2 surface can be used to confirm the silicene domain rotation.

Co atoms are observed to bind at the Si near-bridge site of the silicene/ZrB_2 surface (see **section 7.1**). Owing to the three-fold symmetry of the silicene/ZrB_2 surface there are therefore three equivalent binding site upon the surface, each a 120^o rotation with respect to one another. **Figure 7.8** shows a STM image with an example of each of these three configurations. Also shown is a model representation of each of the configurations that highlights how the Co atom sits to one side of the silicene $(\sqrt{3} \times \sqrt{3})$ unit cell.

The configuration of Co atoms has been measured over a large areas of the silicene/ZrB_2 surface as shown in **Fig. 7.9**. It is found that Co atom configurations in adjacent domains are 180^o rotations of one another; the Co atom sits on the opposite side of the $(\sqrt{3} \times \sqrt{3})$ unit cell. No other difference is observed indicating that the Co atoms are bound on the same surfaces. It is therefore concluded that adjacent silicene domains are rotated with respect to one another. It is noted that this observation does not require knowledge of the 'hidden' atomic structure of the silicene lattice and can therefore be considered an independent confirmation of the model determined by Lee *et al.*[83].

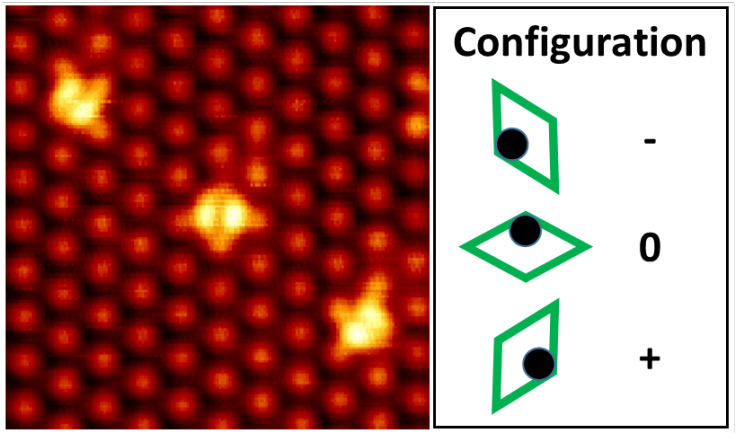

Figure 7.8: Binding configurations of Co atoms on silicene/ZrB_2.
(LEFT) STM image of three Co atoms bound on the silicene/ZrB_2 surface $(6\,\mathrm{nm}\times6\,\mathrm{nm}, V_0 = 10\,mV, I_0 = 0.5\,nA)$. Owing to the three-fold symmetry of the silicene surface, there are three equivalent binding sites each a 120^o rotation with respect to one another. (RIGHT) Each of the three configurations is labelled 0, $+$, or $-$.

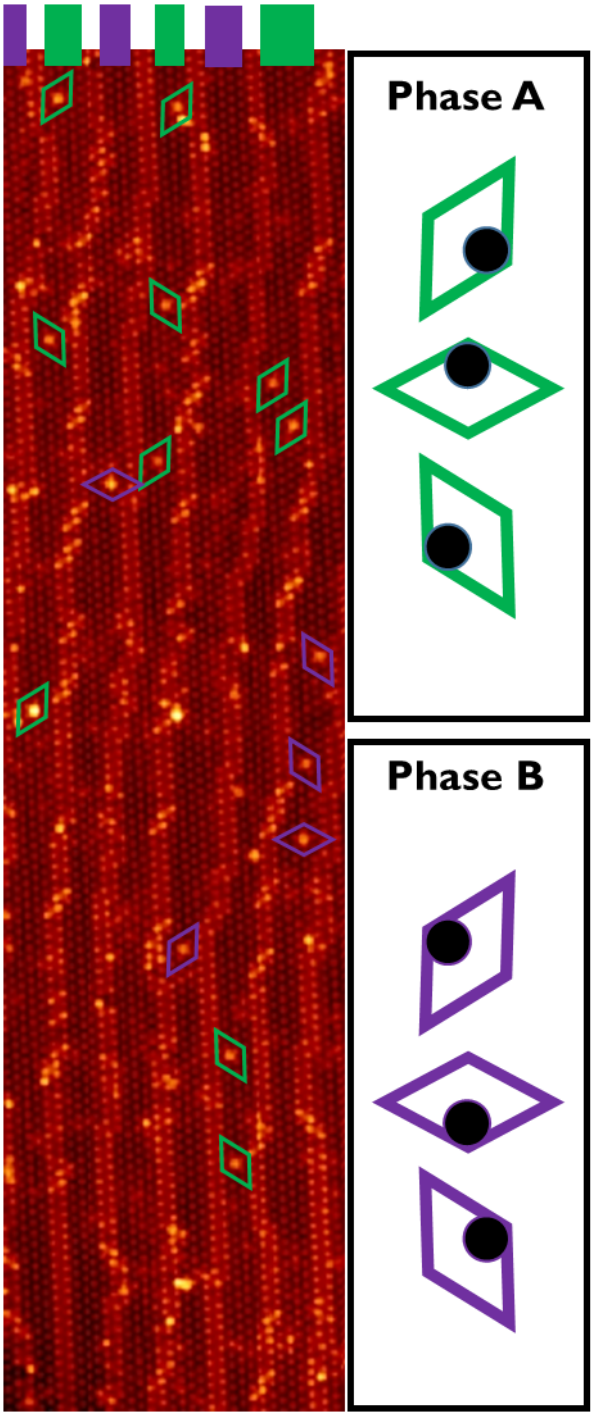

Figure 7.9: Co atom binding site rotation across silicene domains.
Large scale STM image of the silicene/ZrB_2 surface with Co atoms deposited upon it ($80\,\mathrm{nm} \times 20\,\mathrm{nm}$, $I_0 = 50\,\mathrm{pA}$, $V_0 = -100\,\mathrm{mV}$). The asymmetric binding of Co atoms in the silicene $(\sqrt{3} \times \sqrt{3})$ unit cell is used to define one of six configurations. The six configurations are found to belong to two phases that are 180^o rotations of one another.

7.4 Reversible switching of Co atoms on silicene/ZrB_2

The deposition of metal atoms onto surfaces can, in some systems, give mea-stable configurations that can be switched between using the STM tip. For example Co atoms on Cu_2N can be moved from the Cu to the N site via a voltage pulse dramatically changing the magnetic coupling to the substrate [28, 183]. Other examples of single atom switching have been observed for Au atoms on NaCl/Cu(111), where the STM is used to induce a change in the charge state of the atoms [184]. This section demonstrates that Co atoms on the silicene/ZrB_2 surface can be reversibly switched between two states that alters the hybridisation of the Co atom with the silicene surface.

After deposition onto the silicene/ZrB_2 surface Co atoms are observed to bind above the Si near-bridge site of the silicene lattice (see **section 7.1**). **Figure 7.10a** shows a typical example of an individual Co atom on silicene/ZrB_2 acquired at low bias, where the two lobes of the atom are clearly visible (see **section 7.2**). In **Fig. 7.10b** an STM image of the same Co atom, taken at the same set point parameters, is shown after a $0.4\,V$ pulse was performed above the centre of the atom. Now the Co atom is no longer a distinct pair of lobes, but is observed as heart shape. Upon switching there does not appear to be any induced distortion or alteration of the surrounding silicene lattice, nor has the Co atom moved significantly. Furthermore, when another $0.4\,V$ pulse is performed over the switched Co atom a second switching event occurs that transitions the Co atom back to the initial two lobe state (**Fig. 7.10c**).

The switching of Co atoms on the silicene/ZrB_2 can be repeated many times and has been observed on many different atoms. However, occasionally after a switching event the Co atom becomes fixed in one state and can no longer be altered. It is unclear whether this is due to a tip effect or that the Co atom is switched to a third more stable state. The low bias voltage required to switch the Co atoms also places a limit upon the voltage range of spectroscopic measurements.

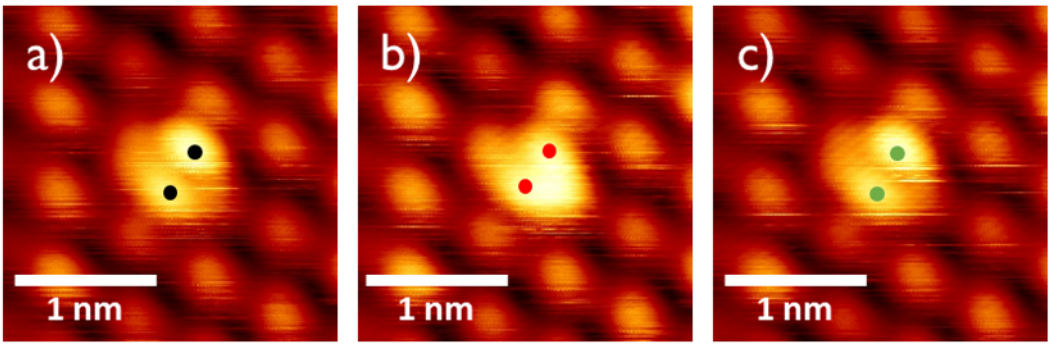

Figure 7.10: Reversible switching of Co atoms on the silicene/ZrB_2 surface.
STM images of the same Co atom on the silicene/ZrB_2 surface ($I_0 = 0.1\,nA$, $V_0 = -10\,mV$). (a) Prior to switching, (b) after switching with 0.4 V pulse, and (c) switched back to the initial state with a second 0.4 V pulse.

7.5 Conclusion

It has been shown that Co atoms can be deposited upon the silicene/ZrB_2 surface at very low coverages, such that individual atoms can be investigated by STM. Existing DFT model of silicene/ZrB_2 have been used to assign a binding site to Co atoms. Co atoms are found to sit above the Si near-bridge site of the silicene lattice. It is found that the Co atoms exhibit a significant bias dependent change to the observed symmetry between filled and empty states, and that at the Fermi level the atoms are imaged as a distinct two lobe structure with a central nodal plane running along the high symmetry $ZrB_2[11\bar{2}0]$ or silicene armchair directions. The observed changes in symmetry indicate that the Co atoms are strongly hybridised with the silicene/ZrB_2 surface. It is then demonstrated that the asymmetric binding of the Co atoms in the silicene $(\sqrt{3} \times \sqrt{3})$ unit cell allows for the direct observation of the rotation of adjacent silicene domains: a confirmation of a previously theoretically predicted model. Lastly, the bi-stable switching of Co atoms is briefly discussed, where it is found that the switching changes the low bias structure of Co atoms. These changes in the Co atom structure, as observed by STM, indicate that the switching alters the hybridisation of the Co atoms to the surface. It is also noted that the low bias voltage required to switch the Co atoms places an upper bound on the range of spectroscopic measurements that can be reliably performed.

Chapter 8

Spatially Distributed Kondo Effect of Single Cobalt Atoms on Silicene

When placed upon metallic substrates and cooled below a characteristic temperature scale T_K, individual magnetic impurities can form a many-body singlet ground state with a cloud of electrons in the host metal via the Kondo effect (see **section 4.4**). The Kondo effect created by single magnetic atoms upon simple metallic substrates is well understood (see **subsection 4.4.3**). However, the question of what happens when magnetic impurities are placed upon new 2D surfaces, such as graphene, is only starting to be answered. In the case of transition metals upon the (111) faces of noble metals, that host a 2D surface state, it has been shown that the Kondo screening is predominantly mediated by the bulk states of the surface [185]. In epitaxial graphene systems the Kondo effect has been observed upon an Ru(001) substrate, where the changes in electronic structure across the rippled moirè pattern are crucial to controlling the effect [19]. In this section it is shown how the 2D material silicene grown on ZrB_2 can be used to produce an unusual spatially distributed Kondo effect when individual Co atoms are placed upon the surface.

Cobalt atoms on the silicene/ZrB_2 surface exhibit a strong bias dependent symmetry when measured by STM (see **section 7.2**). At low biases, close to the Fermi level $-10\,\mathrm{mV} \lesssim V \lesssim 10\,\mathrm{mV}$, the Co atoms are observed as a two lobe structure that does not follow the symmetry of the closest d-orbital resonance (see **Fig. 7.7**). To explore the electronic structure of this feature high resolution STS spectra have been taken across the Co atom on the silicene/ZrB_2 surface. **Figure 8.1b** shows the STS spectra taken upon the left lobe (red), centre (green), and right lobe (black) of the Co atom in **Fig. 8.1a**, as well as the silicene background (blue). In each of the spectra taken atop the Co atom there are two significant features not present on the bare surface: symmetric steps/peaks at approximately $\pm 32\,\mathrm{mV}$ and a zero bias resonance. From the relative intensities of the zero bias resonances it is clear that the two lobe structure of the Co atoms is due to these features. The symmetric step/peak features are more

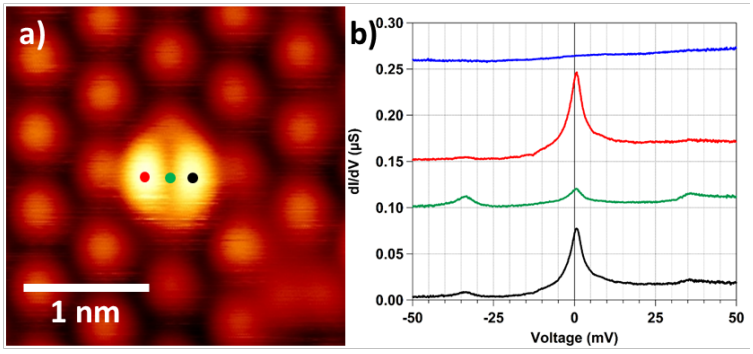

Figure 8.1: Spatially distributed Kondo resonance of a single Co atom on silicene/ZrB_2. (a) STM image of a single Co atom on the silicene/ZrB_2 surface ($V_0 = -3\,mV$, $I_0 = 50\,pA$, $V_{mod} = 0.5$ mV). (b) STS curves taken over: bare silicene (blue), Co atom left lobe (red), Co atom centre (green), and Co right lobe (black). Spectra have been offset for clarity. Locations are shown by coloured circles in (a). STS curves show that the Kondo resonance is centred upon the two lobes of the Co atom and not in the centre.

intense at the centre of the Co atom, although this could be a topographic artefact due to differences in tip-sample height at the set point parameters above the different areas of the Co atom. Symmetric features in STS curves are a strong indication of inelastic processes that can include spin [38, 39], phonon [36], rotational [47, 48],and plasmon [186] excitations. Typical energies for spin excitations are on the order of $0.1 - 100$ meV and exhibit variable increases in the total conductance [38, 39]. Phonon states are more generally in the tens of mV range with much lower intensities [36]. Futhermore, later it will be shown that no chanage is observed in the energy position of the steps in a magnetic field (see **section 8.1**), it is therefore likely the symmetric step/peaks of Co atoms on silicene/ZrB_2 are vibrational excitations.

The presence of a zero bias resonance in STS curves of a magnetic adatom upon a conductive substrate is highly indicative of the Kondo effect (see **section ??**). The functional form of the resonance is dependent on the ratio of tunnelling directly into the resonance versus tunnelling into the continuum of screening states (see **section 4.4.3**). When the tunnelling is predominantly through the resonance state the Fano equation (see **eqn. 4.97**) reduces to a simple Lorentzian. **Figure 8.2a** shows an example of a Co atom zero bias resonance that has been fit to a Lorentzian equation of the form,

$$\frac{dI}{dV} = A\frac{\left(\frac{\Gamma}{2}\right)^2}{\left(V-\epsilon_0\right)^2+\left(\frac{\Gamma}{2}\right)^2} + bV + c, \tag{8.1}$$

where A is the resonance amplitude, Γ is the resonance FWHM, V is the bias voltage, ϵ_0 is the resonance position, b is a background gradient in the dI/dV, and c is a background offset. **Equation 8.1** provides a good fit to the experimental data over a voltage range of approximately $-20\,\mathrm{mV} \lesssim V \lesssim 20\,\mathrm{mV}$, before effects of the inelastic steps become significant. **Figure 8.2b** shows a histogram of Co atom Kondo resonance widths taken

from approximately 50 atoms. The different colours in the histogram correspond to measurements taken with different STM tips. The distribution of widths is found by fitting to a Gaussian distribution to be 3.8 ± 0.4 mV.

To better determine the spatial extent of features in the STS curves of Co atoms dI/dV maps have been acquired. **Figure 8.3a** shows a topographic image of a Co atom on the silicene/ZrB_2 surface, upon which an STS spectrum was recorded at each pixel. **Figures 8.3b-j** show spatially resolved constant energy slices of these STS curves, where contrast is provided by the amplitude of the dI/dV signal. The zero bias dI/dV map (**Fig. 8.3b**) reveals the two lobe structure that was observed in bias dependent topographic images (see **Fig. 7.6**). Once the magnitude of the bias voltage increases to $|V| = 10$ mV the two lobe structure disappears and the Co atom is observed as a depression in the LDOS, relative to the surrounding silicene surface. At -30 mV the onset of the negative bias step in the dI/dV curve is seen. The step is centred upon the Co atom, in-between the two lobes of the Kondo resonance. The equivalent positive bias feature is hidden in the contrast due to the absolute conductance at positive bias being significantly less on the Co atom in comparison to the bare silicene surface. The influence of the step at negative biases continues to be observed up to the minimum voltage of -50 mV. On the positive bias side the Co atom is still observed as a relative depression with increasing diameter over the $10\,\mathrm{mV} < V < 50\,\mathrm{mV}$ voltage range.

The determination of whether or not a zero bias resonance is due to the Kondo effect can be achieved in one of two ways. The first is to use an external magnetic field to lift the spin degeneracy of the Kondo resonance, via the Zeeman effect. In this way a splitting, or broadening of the Kondo resonance should be observed that is proportional to the external field. Secondly the temperature dependence of a Kondo resonance can be examined. A normal density of states feature broadens according to Fermi-Dirac statistics, however a Kondo resonance will have an additional intrinsic level of temperature broadening.

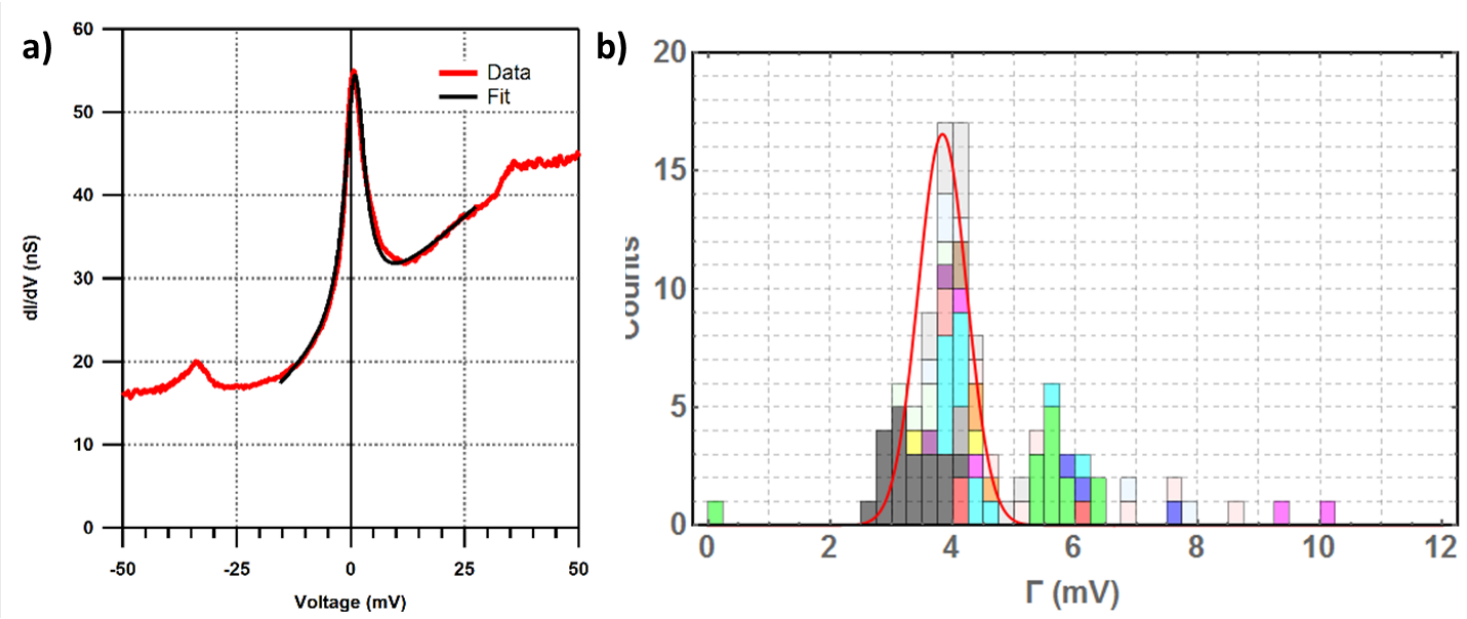

Figure 8.2: Fitting procedure for the Kondo resonance formed by individual Co atoms on silicene/ZrB_2.
(a) (red) STS curve taken on one of the lobes of a Co atom on silicene (V_0=-10 mV, I_0=100 pA, $V_{mod} = 0.5$ mV). (black) Fit to data using a Lorentzian line shape, see main text for details. (b) Histogram of Kondo resonance FWHM using Lorentzian fits taken from 50 Co atoms on silicene. Different colours denote data taken with different STM tips. Red curve is a best fit to a Gaussian distribution with $E_0 = 3.8$ mV and a standard deviation of 0.4 mV.

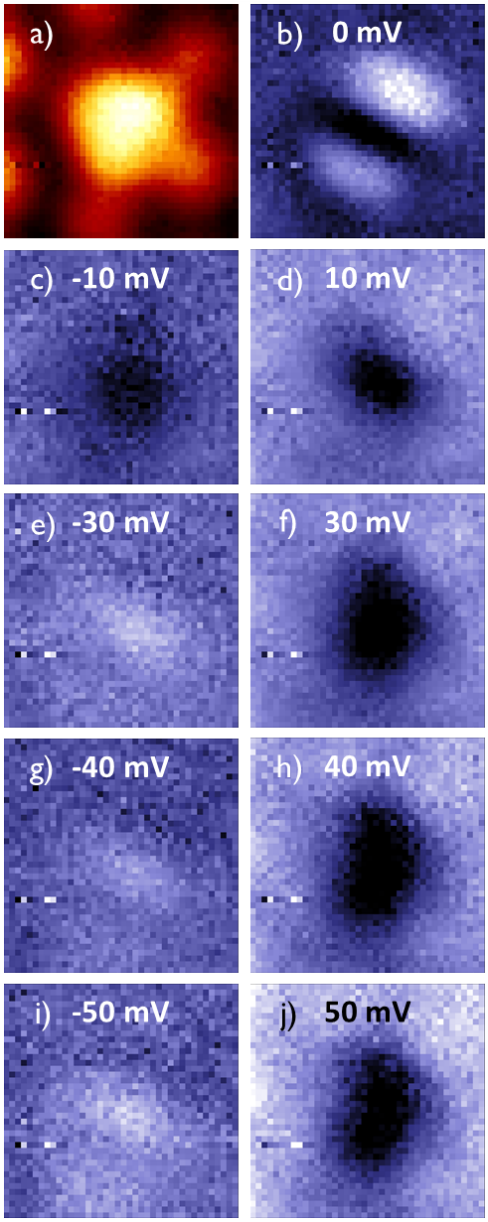

Figure 8.3: Spatially resolved spectroscopic measurements of an individual Co atom on the silicene/ZrB_2 surface.
(a) STM topographic image of an individual Co atom on silicene/ZrB_2 (1.3 nm×1.3 nm, $V_0 = -50$ mV, $I_0 = 0.5$ nA). Spatially resolved dI/dV spectra recorded simultaneously to (a) at constant energy slices of (b) 0 mV, (c)/(d)$\mp$10 mV, (e)/(f)$\mp$30 mV, (g)/(h)$\mp$40 mV, and (i)/(j)$\mp$50 mV (1.3 nm×1.3 nm, $V_0 = -50$ mV, $I_0 = 0.5$ nA.

8.1 Magnetic Field Dependence

Figure 8.4 summarises the STS results obtained for Co atoms on silicene/ZrB_2 taken with different external magnetic fields applied. In **Fig. 8.4a** STS spectra recorded with the external field perpendicular to the surface at $1\,\mathrm{T}$ (solid) and $6\,\mathrm{T}$ (dotted) are compared and in **Fig. 8.4b** a comparison of spectra for $1\,\mathrm{T}$ perpendicular (dotted) and parallel (solid) to the surface is shown. With increasing magnetic field it is expected to observe a broadening and decrease in amplitude of a Kondo resonance, and indeed the spectra recorded at $6\,\mathrm{T}$ perpendicular to the surface are less intense, but it is difficult to make a conclusive statement about any increase in width of the resonances. If it is assumed that the magnetic moment of the Co is $S = 1/2$ and that $g = 2$ then then the Zeeman effect will be of the order of $0.1\,\mathrm{mV/T}$. The FWHM of the zero bias resonance of Co atoms on silicene/ZrB_2, at $3\,\mathrm{K}$ is approximately $4\,\mathrm{mV}$ and the maximum external field that can be applied by the Omicron Cryogenic STM is $6\,\mathrm{T}$ perpendicular to the sample (see **subsection 2.6.2**). Therefore the maximal splitting of the Kondo resonances would be $\approx 0.5\,\mathrm{mV}$. Curve fitting procedures used have been used on the zero bias resonances of three Co atoms to extract information about the changes observed between $B_Z = 1\,\mathrm{T}$ and $B_Z = 6\,\mathrm{T}$. The average change in the resonance FWHM between $B_Z = 1\,\mathrm{T}$ to $B_Z = 6\,\mathrm{T}$ is $\Delta FWHM = 0.52 \pm 0.14\,\mathrm{mV}$ and is therefore considered to be suggestive, but inconclusive. The changes observed in the spectra for $B_z = 1\,\mathrm{T}$ and $B_y = 1\,\mathrm{T}$ are even less and therefore either indicate that there is no in-plane anisotropy, or that the anisotropy is significantly larger than the energy resolution of these experiments. In order to use the magnetic field dependence to characterise the zero bias resonance of Co atoms on the silicene/ZrB_2 surface a combination of lower temperatures and higher magnetic fields. However, this may not be enough if the intrinsic width of the Kondo peak is large.

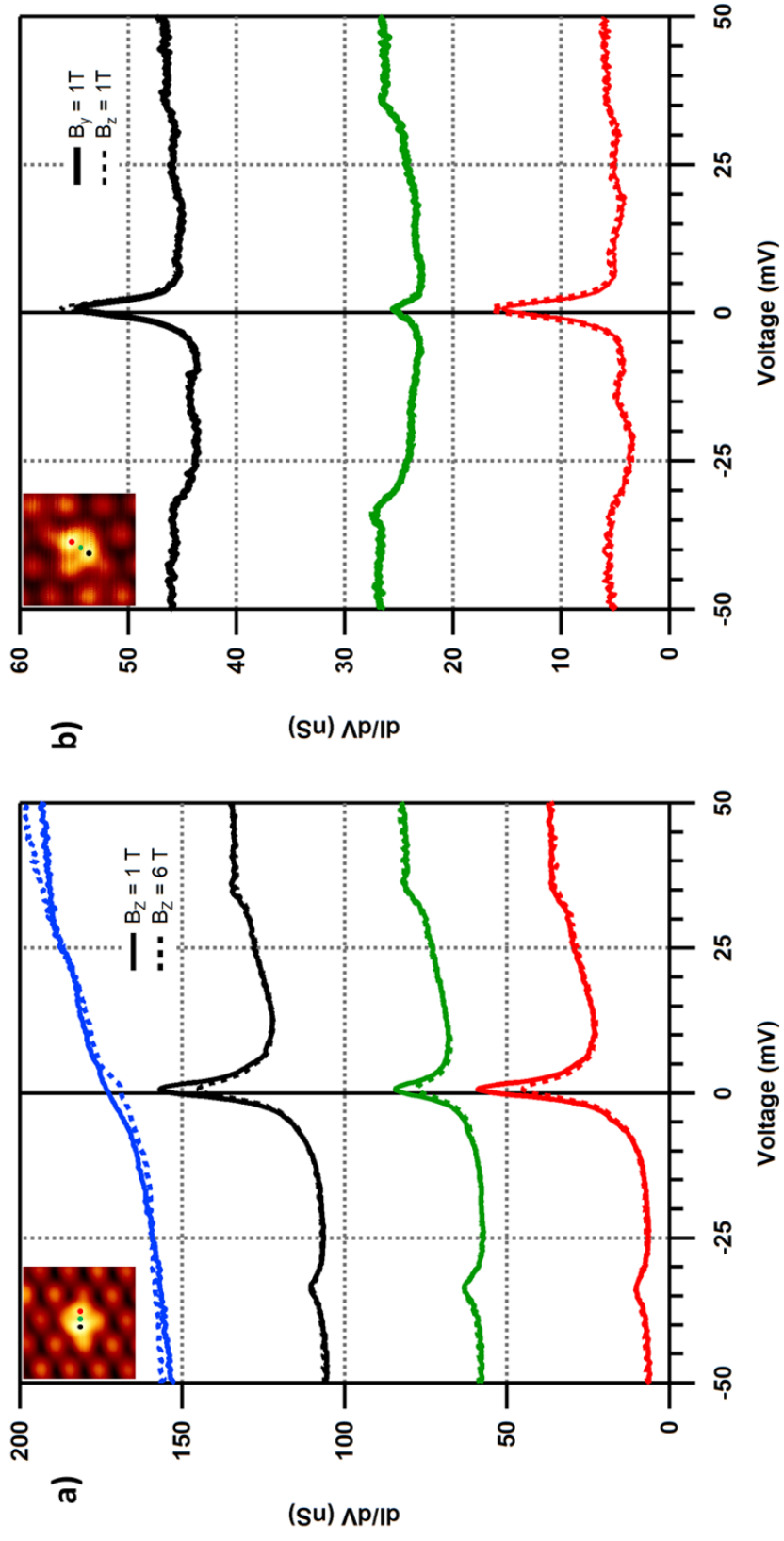

Figure 8.4: Magnetic field dependence of the Kondo resonance formed by individual Co atoms on silicene/ZrB_2.
(a) Comparison of STS curves upon the same Co atom taken at, $B_z = 1$ T (solid) and $B_z = 6$ T (dashed) ($V_0 = -50$ mV, $I_0 = 0.5$ nA, $V_{mod} = 0.5$ mV). Inset shows STM image of Cobalt atom from which STS curves are taken coloured circles correspond to spectra positions (3.5 nm×3.5 nm, V_0=-10 mV, I_0=100 pA). (b) Comparison of STS curves upon the same Co atom taken at, $B_y = 1$ T (solid) and $B_z = 1$ T (dashed)($V_0 = -50$ mV, $I_0 = 1.0$ nA, $V_{mod} = 0.5$ mV). Inset shows STM image of Cobalt atom from which STS curves are taken coloured circles correspond to spectra positions (2 nm×2 nm, V_0=-10 mV, I_0=50 pA).

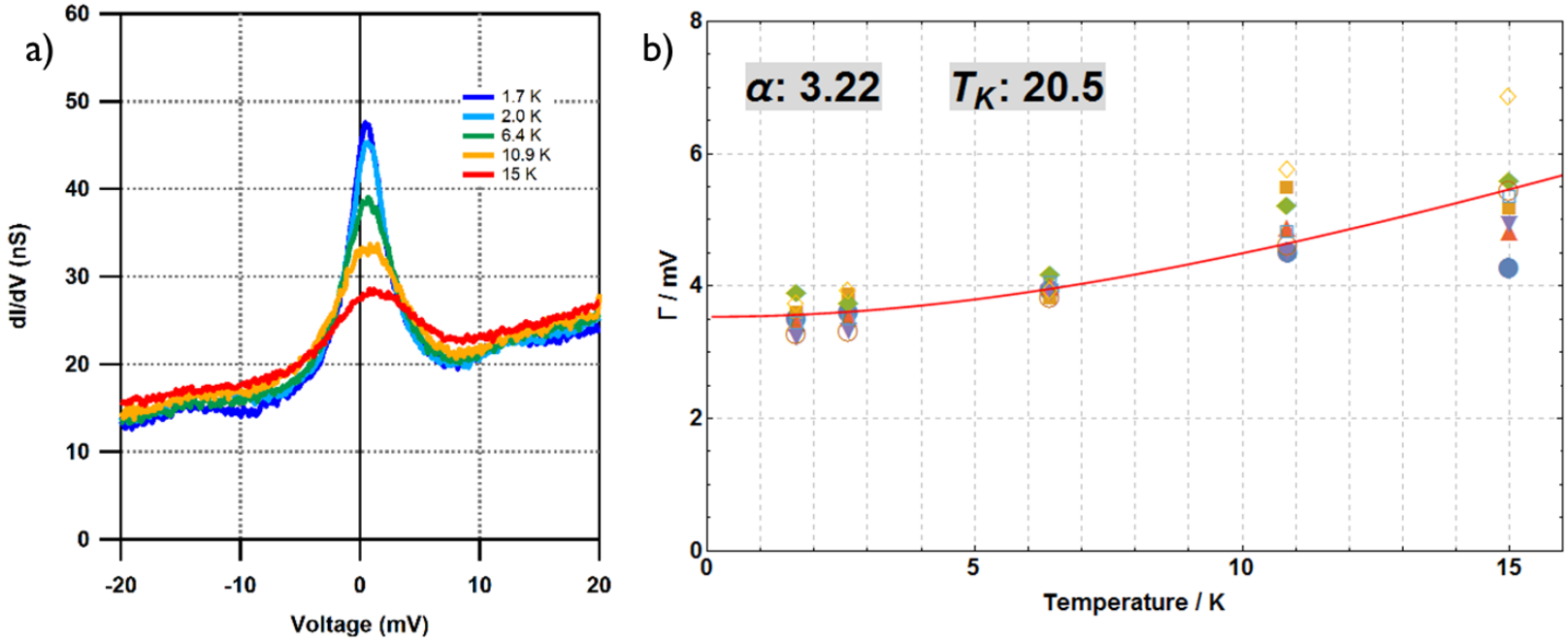

Figure 8.5: Determination of the Kondo temperature of Co atoms on silicene/ZrB_2.
(a) Example of the Kondo resonance temperature dependence from a single Co atom lobe on silicene/ZrB_2 ($I_0 = 0.5$ nA, $V_0 = 20$ mV, $V_{mod} = 0.2$ mV). (b) Graph of Co atom Kondo resonance FWHM Γ against experimental temperature. Markers show experimentally obtained data from four Co atoms, blue line is a best fit of **eqn. 8.2** with $\alpha = 2\pi$ giving a Kondo temperature $T_K = 20.3$ K. The red line denotes the standard Fermi-Dirac broadening of a simple density of states feature.

8.2 Temperature Dependence

An alternative approach to determining if a zero bias resonance is due to the Kondo effect is to perform temperature dependent measurements. Assuming that the conduction band electron states, responsible for the Kondo screening, obey Fermi liquid theory the temperature dependence of the FWHM of a Kondo resonance, after deconvolution of the tip Fermi-Dirac broadening (see **section 4.4.3**), can be expressed as [120][1],

$$\Gamma = \left[(\alpha k_B T)^2 + (2k_B T_K)^2\right]^{1/2} \tag{8.2}$$

where k_B is the Boltzmann constant, T is the temperature, T_K is the Kondo temperature, and α is a constant. The exact value of α is somewhat under contention, but strictly from Fermi liquid theory it should be equal to 2π. Deviation of α from this value can be considered an indication to whether the experimental temperature puts the system in the strong-coupling limit of the Kondo model [187]. **Figure 8.5a** shows an example of STS spectra taken from a single Co atom lobe for a range of temperatures. As is expected the amplitude decreases and the width increases with temperature. Each curve undergoes a thermal deconvolution process that extracts the intrinsic Lorentzian of the form in **eqn. 8.1** and the intrinsic FWHM are plot as a function of temperature in **Fig. 8.5b**. The temperature dependence was recorded for four Co atoms and a best fit to **eqn. 8.2** was calculated. A very good agreement to the experimental data is achieved with a Kondo temperature $T_K = 20.5\,\mathrm{K}$, and $\alpha = 3.22$ as shown by the red line in **Fig. 8.5b**. In this procedure the effect of lock-in broadening (see **section 2.6.2**) has been neglected as it is comparable or less than the thermal smearing at all temperatures investigated. The important determination from this data is that the zero bias resonance broadens intrinsically with temperature and is therefore considered to arise from the Kondo effect. However, the rate of broadening is approximately half of that expected from Fermi liquid theory [120]. A possible origin in the observed discrepancy may come from the fact that the value of $\alpha = 2\pi$ has been determined from a 3D Fermi liquid theory, however, in this work the Kondo screening may arise from the 2D states of the silicene/ZrB_2 interface, and as such a different value for α could be expected. Future work will have to look a the expected broadening of a Kondo resonance screened by a 2D Fermi liquid to confirm this.

[1] In Nagaoka's original work it is evident that the definition of T_K differs from the more standard of $k_B T_K = \frac{\Gamma}{2}$. Reworking equation 8 in Nagaoka's paper leads to the given expression.

8.3 Individual Co Atoms on Silicene/ZrB_2: A possible p-wave Kondo Effect

It has been shown that the two lobe structure of Co atoms on the silicene/ZrB_2 surface is the result of a spatially distributed Kondo resonance. The observation of a Kondo effect formed from single magnetic atoms on a conductive surface is not unusual, and indeed the determination of the Co/silicene/ZrB_2 Kondo temperature of $\approx 20\,\mathrm{K}$ is of a similar order of magnitude as metallic systems [188]. The unusual aspect of the Kondo effect here is the anisotropic spatial distribution. In previous investigations of Kondo resonances on metallic substrates spatial variations have been limited to the expected oscillations in the q-factor of the Fano interference (see **subsection 4.4.3**). Other examples of spatially dependent Kondo resonances have occurred in molecular systems where the molecular orbital that hosts the magnetic moment is itself spatially distributed [177]. However, the high voltage spectroscopy performed on Co atoms bound to the silicene/ZrB_2 surface have revealed a d-orbital that is likely the singly occupied level of the Anderson model (see **subsection 4.4.2**) that does not exhibit the two lobe structure observed for the Kondo resonance (**Fig. 7.7**).

The Anderson model outlined in **subsection 4.4.2** is commonly used to describe the observations made in single magnetic atom Kondo systems. However, it is assumed that the conduction band states responsible for the Kondo screening are s-wave like bulk states of the host metal. Silicene on ZrB_2 has an intriguing electronic structure, where bulk ZrB_2 DOS are suppressed around the Fermi level [77, 189–192]. A significant contribution to the DOS at the Fermi level comes from the 2D surface state of ZrB_2 [193, 194]. Furthermore, when silicene is grown upon the $ZrB_2(0001)$ surface the d-orbitals of the 2D state hybridise with the Si-p states of the silicene surface[84]. In p-wave Kondo models, where the conduction band is comprised of p-wave states, the hybridisation matrix element of the Anderson model becomes non-isotropic resulting in spatially non-uniform screening clouds [195, 196]. It is therefore suggested that the two-lobe spatial structure of the Kondo resonance formed by single Co atoms on the silicene/ZrB_2 surface could be caused by the p-wave nature of the silicene/ZrB_2 2D surface state responsible for the Kondo screening.

8.4 Cobalt Atom Kondo Lobe Asymmetry

Co atoms on the silicene/ZrB_2 surface exhibit an unusual spatially non-uniform Kondo effect (see **section 8**). Unlike in most Kondo systems the Kondo resonance is observed as a two lobe structure with a central nodal plane. In this section it shown that there is a further asymmetry in the Kondo effect of individual Co atoms in this system: the two Kondo lobes can differ. **Figure 8.6a** and **Fig. 8.6b** compare two low bias STM images of Co atoms on silicene, where both exhibit the two lobe structure previously detailed. However, whereas the Co atom in **Fig. 8.6a** is symmetric about the central nodal plane, the Co atom in **Fig. 8.6b** has a clear asymmetry, where one of the two lobes is much brighter than the other.

To confirm that the asymmetries observed in topographic images are due to changes in the Kondo resonance, STS spectra have been recorded upon the two lobes of asymmetric Co atoms. **Figure 8.7** summarises an example of these results. The top most lobe of the Co atom in **Fig. 8.7a** is brighter than the lower lobe, and in **Fig. 8.7c** this can be seen to result from a substantial difference in the amplitude of the Kondo resonances. To gain a greater understanding of this phenomena topographic images can be used to gather greater statisitics; since the images, at low bias, are essentially imaging the amplitude of the Kondo resonance.

Co atoms on the silicene/ZrB_2 surface have three binding sites that are 120^o rotations of one another, due to the three-fold symmetry of the silicene lattice (see **section 7.1**). Naively it may be assumed that these three configurations are equivalent, but if the striped domains of the surface are considered the three-fold symmetry is broken. The striped domains of silicene/ZrB_2 result in a two-fold symmetry of the surface, where adjacent domains are 180^o rotations of one another (see **section 7.3**). In **Fig. 8.8**

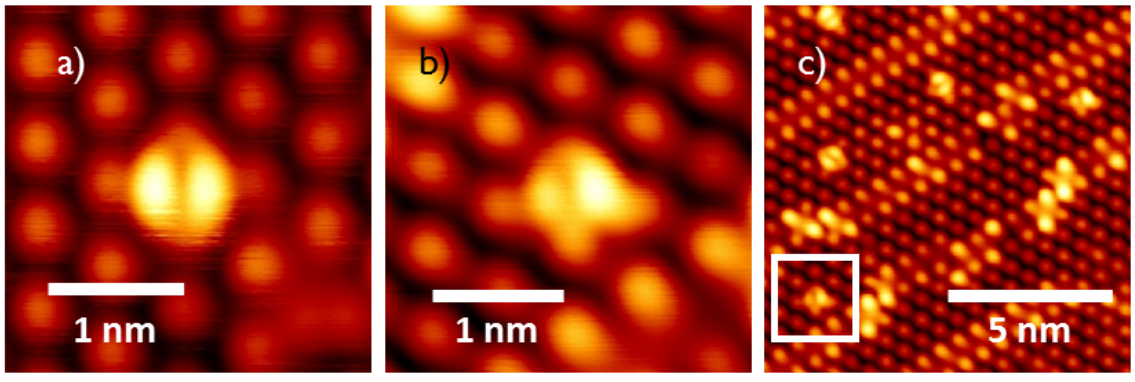

Figure 8.6: Asymmetry in the topographic height of Co atoms on silicene/ZrB_2. High resolution, low bias $-10\,\mathrm{mV} \lesssim V \lesssim 10\,\mathrm{mV}$, STM images of the Kondo lobes of Co atoms on silicene/ZrB_2, where the two lobes are (a) symmetric ($I_0 = 50, pA, V_0 = -3\,mV$)and (b) asymmetric ($I_0 = 100\,pA, V_0 = -10\,mV$) in height and spatial extent. (c) Large scale STM image that highlights the location of the Co atom in (b) with respect to the striped domain boundary structure of the silicene/ZrB_2 surface.

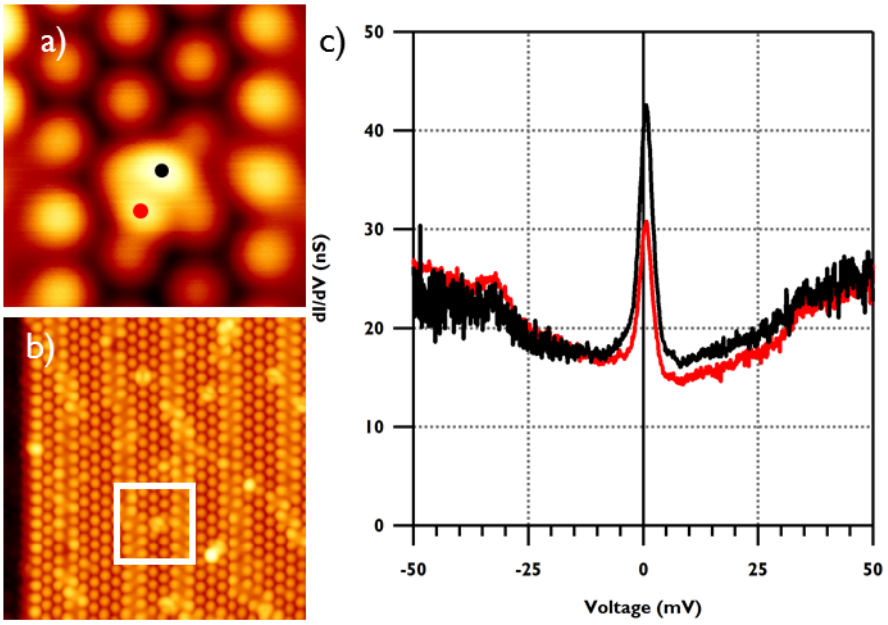

Figure 8.7: Amplitude asymmetry of the Kondo lobes of Co atoms on silicene/ZrB_2. (a) High resolution STM images of an asymmetric Co atom on silicene/ZrB_2 ($2.5\,nm \times 2.5\,nm, I_0 = 100\,pA, V_0 = -10\,mV$). (b) Large scale STM image highlighting the relative orientation of the Co atom in (a) with respect to the domain boundaries. (c) STS spectra taken upon the two Kondo lobes of the Co atom in (a), where the topographic asymmetry can be seen to result from a difference in the amplitudes of the Kondo resonance ($I_0 = 1.0\,nA, V_0 = -50\,mV, V_{mod} = 0.2\,mV$)

a model of Co atoms on silicene/ZrB_2 is given that allows for each example of a Co atom to be completely described by it's topographic image. In **Fig. 8.8a** the orientation of the Co atom binding configuration for each silicene phase (A or B), with respect to the domain boundaries, is given a label of 1, 2, or 3. Owing to the two-fold symmetry between the silicene phases it can be seen that A1(A3) is equivalent to B3(A1), and that A2 is equivalent to B2. **Figure 8.8b** is used to define the Kondo lobe asymmetry of each Co atom. In **Fig. 8.8b(i)** a ball model of the silicene ($\sqrt{3} \times \sqrt{3}$) lattice is shown that aligns with the STM image of a Co atom on the silicene surface in **Fig. 8.8b(ii)**. **Figure 8.8b(iii)** shows that for a given Co atom there are three possible cases for the two lobes: symmetric (yellow), left lobe greater (blue), or right lobe greater (white). The labelling scheme detailed here is used to map the Co atoms in large area STM images, an example of which is shown in **Fig. 8.9**.

The mapping of Co on silicene/ZrB_2 has been performed upon over 100 atoms the results of which are summarised in **table 8.1**. In addition to the orientation of the Co atoms, with respect to the domain boundaries, the distinction of whether or not the Co atom is in the middle of a domain (D) or touching/on a domain boundary (B) is included. Ignoring the Co atoms that touch or are partly on domain boundaries[2], the

[2]It will later be shown that Co atoms touching or on a domain boundary experience an additional interaction, that negates the effect detailed in this section (see **section 8.5**).

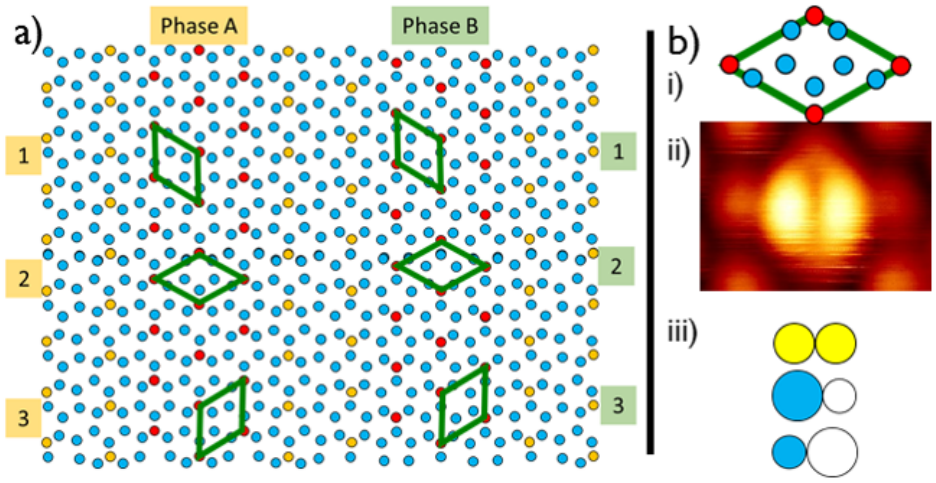

Figure 8.8: Model of the Co atom Kondo lobe asymmetry.
(a) Ball model of the silicene/ZrB_2 striped domain boundary surface. The two silicene phases are labelled A, and B. For a given phase three configurations of the Co atoms with respect to the domain boundaries can be observed, each has been labelled 1, 2, or 3. (b) (i) Zoom in mode of the silicene lattice relative to the STM image in (ii). (iii) A given Co atom can be either symmetric (top) or have its left (middle) or right (bottom) lobe brighter/larger than the other.

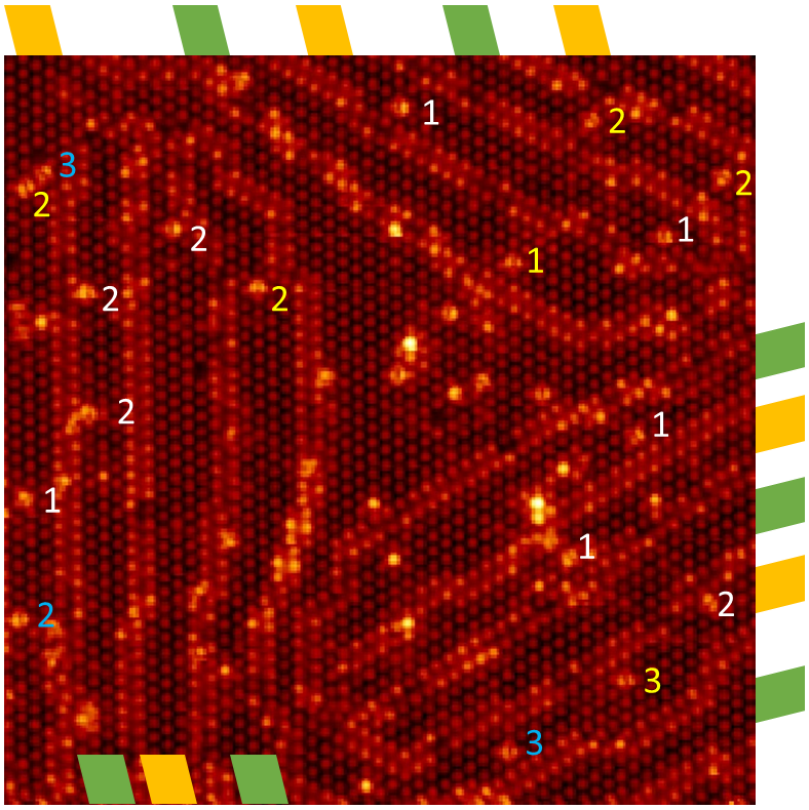

Figure 8.9: Example of the Co atoms Kondo lobe asymmetry mapping.
STM image of the silicene/ZrB_2 surface with Co atoms deposited upon the surface. Each Co atom is labelled with the designations detailed in **Fig. 8.8**

	Cobalt Atom Orientation						
Orientation	1		2		3		**Total**
	D	B	D	B	D	B	
Blue	1	0	2	12	36	2	**53**
White	34	3	1	11	0	0	**49**
Yellow	8	0	19	3	2	0	**32**
Total	**43**	**3**	**22**	**26**	**39**	**2**	**134**

Table 8.1: Summary of Co atom Kondo Lobe asymmetries.
Lobe asymmetry designations as detailed in **Fig. 8.8**. D refers to Co atoms that are in the middle of domains and B to atoms touching or partly on the striped domain boundaries. Ignoring atoms on domain boundaries (B) orientations 1, 2, and 3 are most commonly found to have the white, yellow, and blue lobe asymmetries respectively.

table reveals a clear pattern for the Co atom Kondo lobe asymmetry. Co atoms that are in configuration 2, i.e. the atoms that have the central nodal plane parallel to the domain boundaries, are symmetric. That configuration 2 is symmetric is intuitively logical as this orientation retains the two-fold symmetry of the surface. Configurations 1 and 3 then have the blue and white lobes large/brighter respectively. If one were to consider each lobe to be an oval, and to define the lobes orientation to be along the long axis of the oval then what is observed is that the lobe most perpendicular to the domain boundaries is the brightest.

The topographic images of Co atoms on the silicene/ZrB_2 surface have allowed for the asymmetry in the amplitude of the Co Kondo lobes to be mapped. To investigate whether or not any other parameters of the Kondo resonances are affected STS measurements must be used. Spectra have been taken upon a number of Co atoms with varied orientation, and the Kondo resonance of each lobe was fit to a Lorentzian curve of the form found in **eqn. 8.1**. To determine any asymmetry in a given parameter the difference of values between the two lobes is taken. **Figure 8.10a** shows the corresponding histogram for the Kondo resonance FWHM Γ, and **Fig. 8.10b** for the resonance energy position E_0. Both these histograms have distributions centred upon zero, indicating that there is negligible change in the width or position of the Kondo resonances between the two lobes of a given Co atom.

These results demonstrate that the striped domain boundaries of silicene on ZrB_2 influence the Kondo effect of Co atoms on the surface. An asymmetry in the Kondo resonances of the Co atoms two lobes is present depending on the relative orientation of the Co atoms, with respect to the domain boundaries. It has been shown that only the amplitude of the Kondo resonances are affected and from Fano theory of Kondo resonances it is known that the amplitude is a measurement proportional to the density of states of the continuum [117, 118]. To observe this asymmetry there must therefore be an underlying asymmetry in the continuum responsible for the Kondo screening. If an infinite domain free silicene sheet is considered then there would be no reason for an

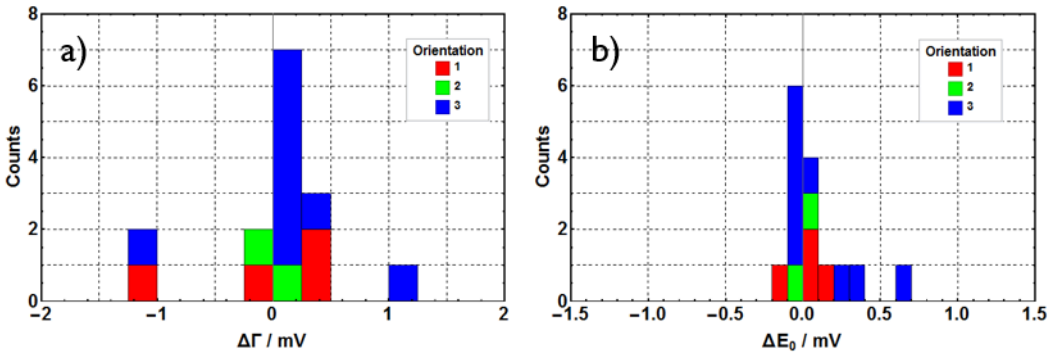

Figure 8.10: Co Kondo lobe Lorentzian fit parameter differences.
The Kondo resonances of Co atoms in different orientations with respect to the domain boundaries of silicene/ZrB_2 have been fit with Lorentzian line shapes. The difference in parameters between the two Kondo lobes are plot as histograms. (a) $\Delta\Gamma$, and (b)ΔE_0, where red, green, and blue correspond to orientations 1, 2, and 3 respectively.

asymmetry to exist. However, the striped domains of silicene on ZrB_2 break the three fold symmetry of the surface. The two lobe structure of the Kondo effect formed by Co atoms on silicene/ZrB_2 may be be due to p-wave scattering. If the electronic states of the silicene surface are different for electrons propagating parallel or perpendicular to the striped domain boundaries then it may be that the observed asymmetry in the amplitude of the two Kondo lobes is a reflection of the differences in DOS of these states.

8.5 Domain Boundary Modification of Kondo Temperature

In the previous sections it has been shown that a spatially distributed Kondo effect arises from Co atoms on the silicene/ZrB_2 surface (see **section 8**) and that the realtive orientation of the Co atoms, with respect to the striped domains, induces an asymmetry between the two Co atom Kondo lobes (see **section 8.4**). In this section the influence of the silicene domain boundaries upon the Kondo effect of individual Co atoms is investigated further. It is found that for Co atoms directly touching a silicene domain boundary there is the same spatially distributed Kondo effect, but there is a significant increase in the energetic width of the Kondo resonances. The electronic structure of the silicene surface across the domain boundaries is investigated by STM, STS, and DFT, where an enhancement in the LDOS of Si atoms in the domain boundaries around the Fermi level is found. It is suggested that the increase in the LDOS at the Fermi level increases the Co atom Kondo temperature, resulting in the observed FWHM increase for Co atoms on the domain boundaries. The modulation of the silicene surfaces electronic structure across the domain boundaries may therefore prove useful in fine-tuning the parameter space within the Kondo effect of single magnetic atoms allowing for more detailed investigations.

Figure 8.11(a-d) show STM images of four Co atoms bound upon the silicene/ZrB_2 surface. For each of them at lease one of the four Si 'up' atoms that define the silicene $(\sqrt{3} \times \sqrt{3})$ unit cell is incorporated into a domain boundary of the surface. Just like Co atoms in the centre of silicene domains the atoms are imaged as two lobes at low bias (see **section 7.2**). Similarly, Kondo resonances are observed when STS spectra are recorded upon the two lobes of the Co atoms on silicene domain boundaries (see **Fig. 8.11(e-h)**). What is different is the width of the Kondo resoances of Co atoms on the domain bounaries. The average width, as determined by fitting procedures, is 11.9 ± 4.2 mV approximately three times that of the 3.8 ± 0.4 mV width of Co atoms in the centre of domains (see **section 8**).

The striped domain boundaries of silicene on ZrB_2 are formed from a distorted honeycomb lattice linking the two adjacent silicene domains of the opposite phase; each a 180^o rotation of the other (see **section 7.3**). **Figure 8.12a** shows a DFT model of the silicene/ZrB_2 surface, where the red rectangles highlight the positions of the domain boundaries. From the side view of the surface in **Fig. 8.12b** it can be seen that the Si hollow and Si near-bridge atoms (yellow) lie in a single plane, and all the Si 'up' atoms form a second plane above that, as is the case of the domain-free *planar-like* silicene model structure (see **section 3.3**).

STM imaging of the domain boundaries on silicene/ZrB_2 reveal a bias dependent contrast difference between the silicene surface in the centre of a domain compared

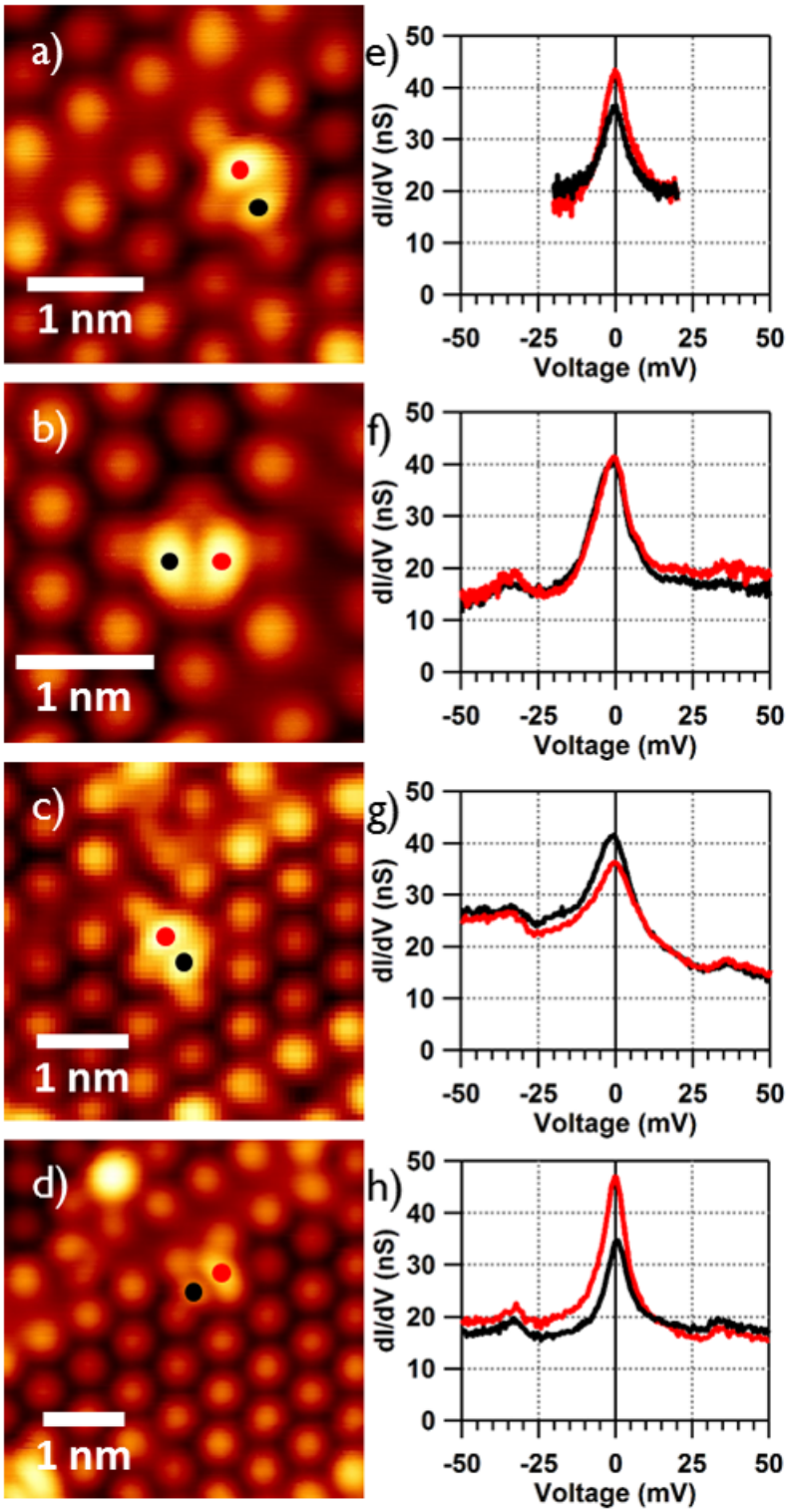

Figure 8.11: Modification of Kondo resonances from from Co atoms sat on silicene domain boundaries.
(a-d) STM images of Co atoms sat on silicene/ZrB_2 domain boundaries ($I_0 = 0.1$ nA, $V_0 = -10$ mV). (e-h) Corresponding STS spectra of Co atoms in (a-d) revealing that the primary influence of the silicene domain boundaries is to increase the width of the Kondo resonances. (e) $I_0 = 0.5$ nA, $V_0 = -20$ mV, $V_{mod} = 0.5$ mV, (f) $I_0 = 1.0$ nA, $V_0 = -50$ mV, $V_{mod} = 0.5$ mV, (g) $I_0 = 1.0$ nA, $V_0 = 50$ mV, $V_{mod} = 0.5$mV, (h) $I_0 = 1.0$ nA, $V_0 = 50$ mV, $V_{mod} = 0.5$mV

to at the boundaries. Topographic measurements taken over a -1.0 V$>$ V $>$+1.0 V range are shown in the first and last column of **Fig. 8.13**. At -1.0 V there is little contrast between the Si 'up' atoms across the surface, but as the voltage approaches the Fermi level the Si 'up' atoms of the boundary become significantly more bright than those in the centre of the domains. In the empty states, positive bias, close to the Fermi level the constrast remains, but as the voltage increases, it declines. Eventually at $+1.0$ V the contrast of the Si 'up' atoms is inverted, where the domain boundary is imaged as a depression relative to the domain centres.

Simulated STM images have been extracted from the DFT structure in **Fig. 8.12** and are shown in the central two columns of **Fig. 8.13**. There is a significant agreement between the experimental and theoretical results, where all changes in contrast are reproduced. Since the DFT structural model shows that there is no topographic difference between the Si 'up' atoms across the surface, the observed changes in STM contrast can be interpreted as changes in the electronic structure of Si atoms at the boundaries.

The bias dependent imaging of the silicene/ZrB_2 striped domain boundaries indicates that there is a notable difference in the electronic structure of Si atoms in the domain centre, versus Si atoms incorporated within the domain boundaries. In particular the enhanced contrast around the Fermi level shows that the zero voltage LDOS is increased upon the domain boundaries. **Figure 8.14a** shows an STM image of silicene on ZrB_2, within which a domain boundary runs vertically up the centre of the image. Scanning tunnelling spectroscopy curves have been recorded along the white line in **Fig. 8.14a** to produce the dI/dV line profile in **Fig. 8.14b**. Here the intensity of the dI/dV signal is plot as a function of lateral position against bias voltage. The general suppression in the LDOS within ± 0.5 V of the Fermi level does not change significantly between thee domain center and boundary. However, at $+100$ mV there is a feature centred upon the domain boundary that is approximately 200 mV wide. In addition a more subtle disappearance of a feature at approximately $+200$ mV is observed. As a result of these changes in the electronic structure the LDOS at the Fermi level is increased with respect to the centre of the domains.

To reveal more detail into the nature of the changes observed in the spectroscopic measurement of silicene domain boundaries the Si partial density of states (PDOS) have been extracted from DFT calculations of the surface. **Figure 8.15a** shows four PDOS plots taken from different Si atoms across the silicene/ZrB_2 surface as shown in **Fig. 8.15b**. Si atoms 1, 2, and 3 are hollow site, near-bridge site, and Si 'up' atoms incorporated within the striped domain boundary, while atom 4 is a Si 'up' atom in the centre of a domain. The Si 'up' atom in the centre of the silicene domain (atom 4) has a relatively sharp feature at approximately +200 mV above the Fermi level that has significant Si-s orbital contributions (black line). Qualitatively the comparative PDOS plot of the Si 'up' atom in the domain boundary (atom 3) is very similar, however

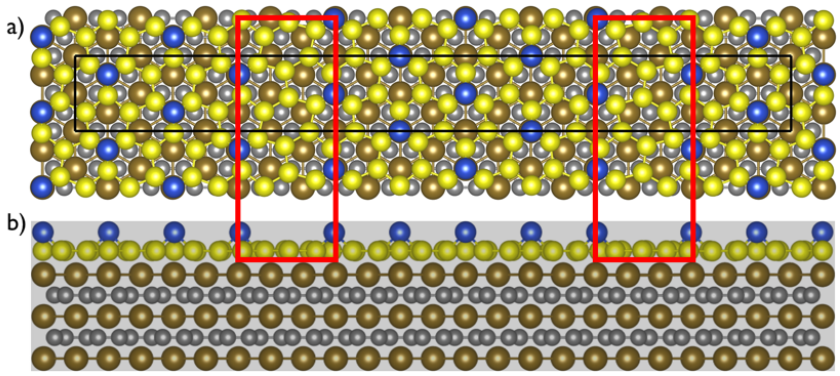

Figure 8.12: DFT calculated structure of the striped domains of silicene on ZrB_2. (a) Top and (b) side view of the silicene/ZrB_2 structure, where brown, and gray balls are Zr, and B atoms respectively. The yellow and blue balls are then both Si atoms, where the blue balls correspond to the Si 'up' atoms of the *planar-like* silicene reconstruction.

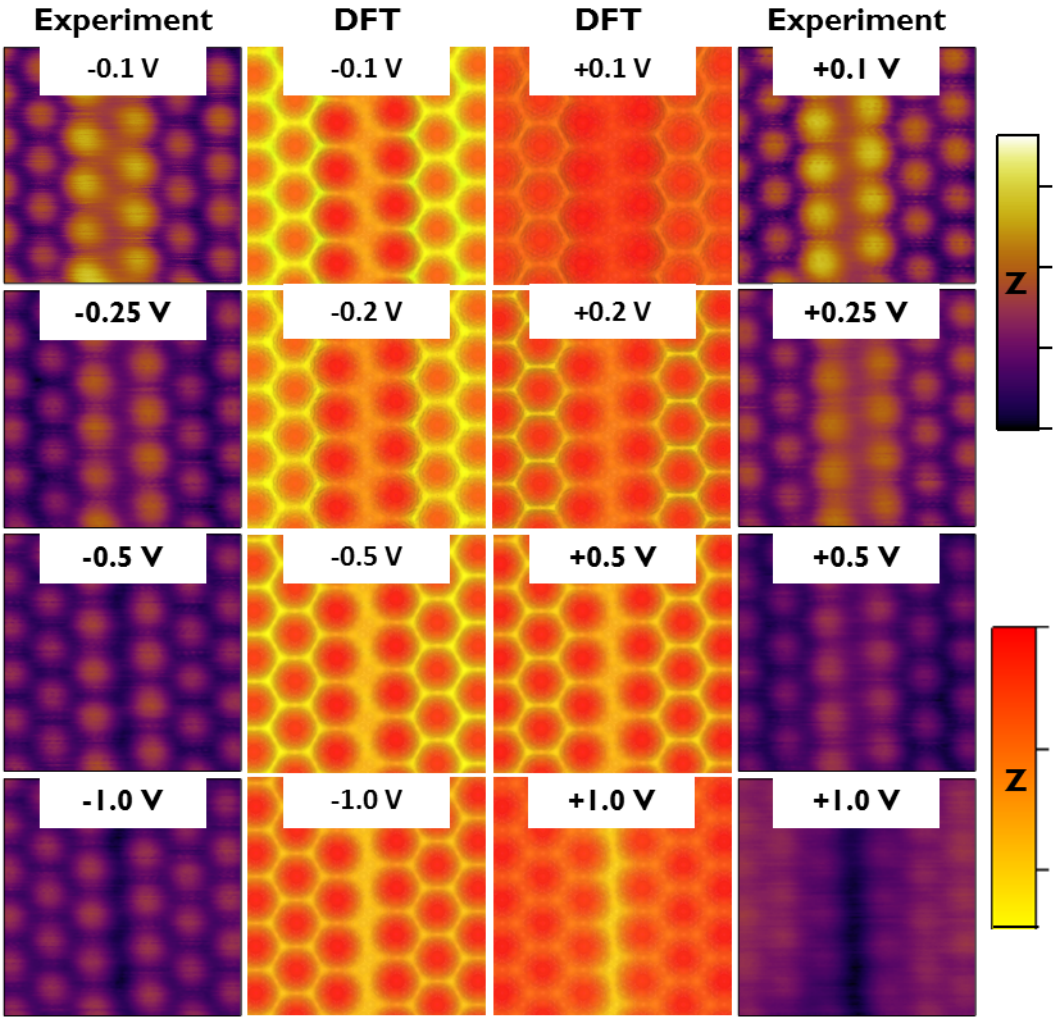

Figure 8.13: Bias dependent STM imaging of striped domains on silicene/ZrB_2. First and last column are experimentally obtained STM images of the striped domains of silicene/ZrB_2 acquired at different bias voltages ($2.98\,\mathrm{nm}\times 2.98\,\mathrm{nm}$, $I_0 = 50\,\mathrm{pA}$). The second and third columns are simulated STM images taken from a DFT calculation of the surface at comparable voltages. A good agreement is found between the two, in particular the enhancement of the Si 'up' atoms at the domain boundary close to the Fermi level.

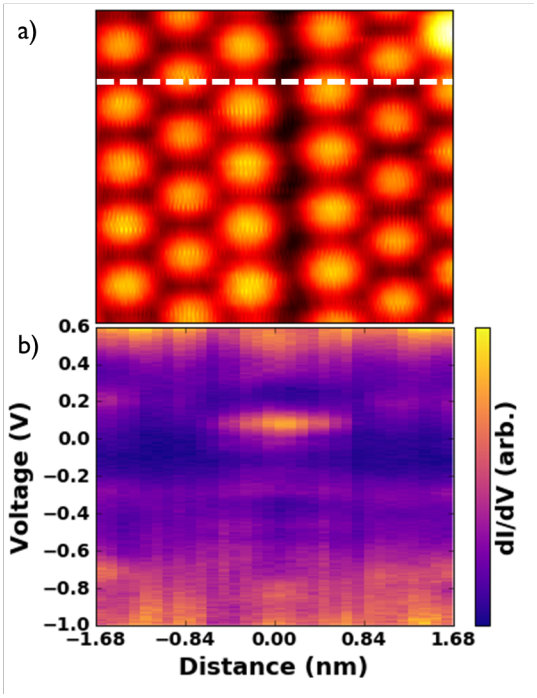

Figure 8.14: STS measurements of silicene/ZrB_2 domain boundaries.
(a) STM image of a domain boundary on the silicene/ZrB_2 surface (3.36 nm$\times$ 3.36 nm, $I_0 = 0.5$ nA, $V_0 = -1.0$ V). (b) dI/dV line profile taken along the white dotted line in (a), where the +100 mV feature localised upon the domain boundary can be seen ($I_0 = 0.5$ nA, $V_0 = -1.0$ V, $V_{mod} = ??$ mV).

close inspection of the different features reveals energetic shifts. Close to the Fermi level the features at both positive and negative voltages have significantly broadened. Furthermore, the feature that was at +200 mV in the domain centre has shifted towards the Fermi level and has diminished Si-s (black line), and increased Si-p (red, and blue lines) orbital contributions. Si atoms 1, and 2 follow this trend having even greater DOS at the Fermi level with significant Si-p orbital contributions.

The Kondo temperature of a magnetic impurity is given by $T_K \propto exp\,(-1/2J\rho_0)$, where J is the exchange coupling strength and ρ_0 is the screening continuum's DOS at the Fermi energy. The exponential dependence of T_K on the Fermi level DOS means that even small changes can alter the Kondo temperature significantly. Spectroscopic and DFT results have shown that Si atoms incorporated within the striped domains of silicene on ZrB_2 have an increased DOS at the Fermi level in comparison to Si atoms in the domain centres. The observed increase in the width of the Co atom Kondo resonances for Co atoms touching the domain boundaries can therefore qualitatively been understood as the result of the Kondo temperature being increased due to the increase in LDOS at the Fermi level.

In this section it has been shown that the Kondo temperature of Co atoms bound on the silicene/ZrB_2 surface touching a striped domain boundary is increased. Bias dependent STM and STS investigations of the domain bounadries have shown that

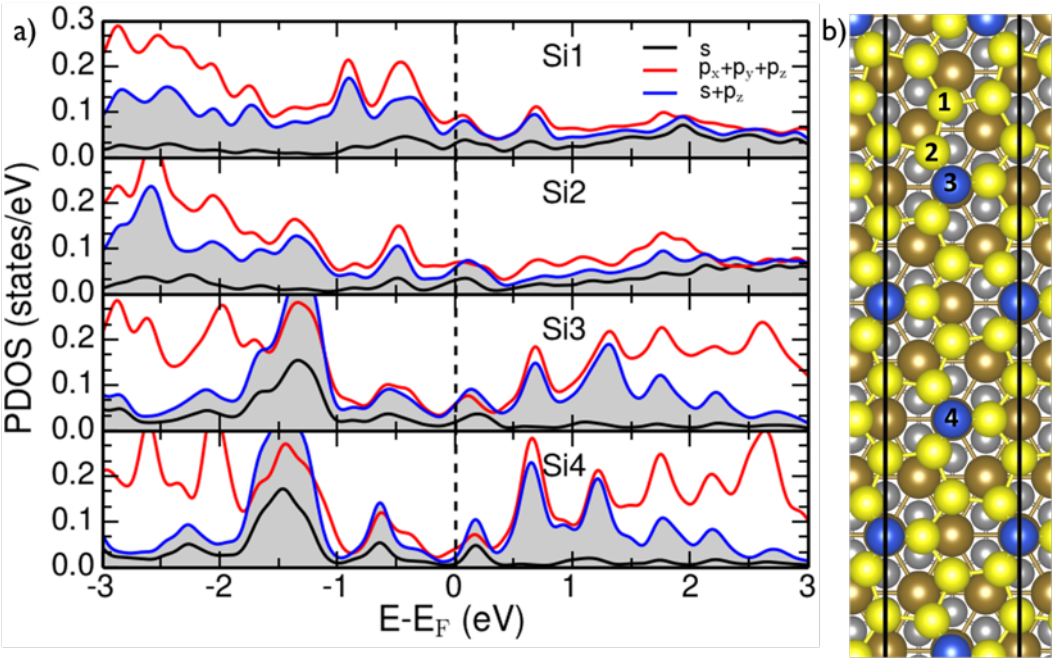

Figure 8.15: Electronic structure of domain boundaries on silicene/ZrB_2.
(a) Silicon partial density of states plots for different Si atoms in the silicene/ZrB_2 surface as labelled in the DFT model in (b). Si atoms 1, 2, and 3 are in the domain boundary, while Si atom 4 is in the centre of the domain. The Si p-orbital density of states is increased around the Fermi level in the vicinity of the domain boundary.

there is a significant change in the electronic structure of the silicene surface at the Fermi level, in comparison to the domain centres. These observations are supported by DFT calcualtions of the silicene/ZrB_2 striped domains that indicate an increase in the Fermi level DOS due to an increasingly significant Si-p orbital contribution. The observed increase in the Kondo temperature of Co atoms can therefore be explained to result from an increase in the Fermi level DOS. Interestingly this result informs on the nature of the states responsible for the screening continuum in the Kondo effect for Co atoms on silicene/ZrB_2. If the Co atoms were predominantly coupled to the bulk ZrB_2 metallic states then the modification of the electronic structure of the silicene at the surface should not have a significant impact on the observed Kondo temperature [185]. However, the observation of an increased Kondo temperature with increasing Si-p orbital DOS at the Fermi level implies that a major contribution to the screening continuum comes from the Si states. This result further emphasises the need to understand how the Kondo effect of single magnetic atoms can be influenced by the continuum states being formed from a band of p-orbital states.

8.6 Influence of Co Atom Switching on Kondo Effect

Previously, it was shown that Co atoms on silicene/ZrB_2 can be switched between two states (**section 7.4**). The changes in the the topographic images of the Co atoms after switching indicates that there is a change in the electronic structure of the atoms. **Figure 8.16** shows STS measurements performed on the top lobe (top three curves) and bottom lobe (bottom three curves) of the Co atom in **Fig. 7.10** prior to switching (black), after switching (red), and after switching back to the first state (green). Both prior to and after switching, the two lobes of the Co atom exhibit a Kondo resonance, but after the switching event the amplitude has been significantly reduced by an average ratio of $A/A_{switched} = 0.48 \pm 0.04$. Unlike the significant change in amplitude there is no determinable change in the average FWHM of $\Delta\Gamma = 0.4 \pm 0.4$ mV, nor the resonance position of $\Delta E_0 = 0.0 \pm 0.2$ mV. It can then be seen that the spectra of the re-switched atom perfectly aligns with that of the un-switched atom, confirming that the process is reversible.

The spatial depedence of the switched Co atoms Kondo effect has been mapped upon the Co atom in the STM image of **Fig. 8.17a**. **Figure 8.17b** shows the zero voltage cross section from these measurements, where just as in the case of the un-switched Co atom, the Kondo feature is clearly spatially distributed into two lobes.

The observed changes in the Kondo resonance spectroscopic features indicate that only the amplitude of the Kondo resonance is influenced by the switching event. Similarly

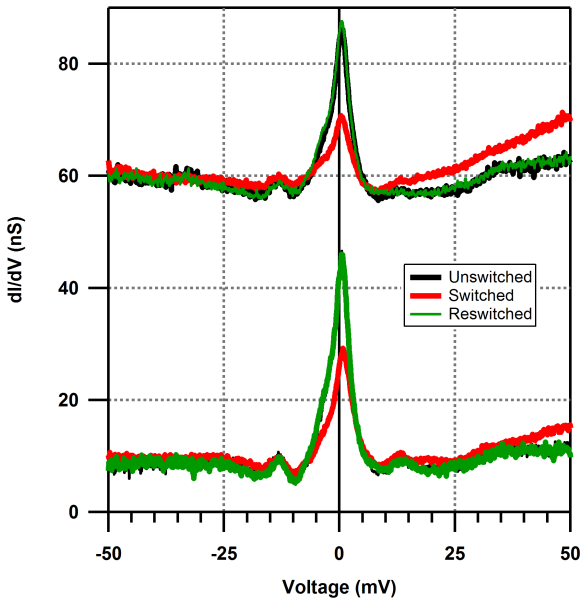

Figure 8.16: Modification of Co atoms Kondo effect upon switching.
STS spectra taken on the two lobes of the Co atom in **Fig. 7.10**, top(bottom) set of spectra correspond to the left(right) most lobe ($I_0 = 1.0$ nA, $V_0 = -50$ mV, $V_{mod} = 0.2$ mV). Spectra recorded prior to switching, after switching, and after re-switching are shown in black, red, and green respectively.

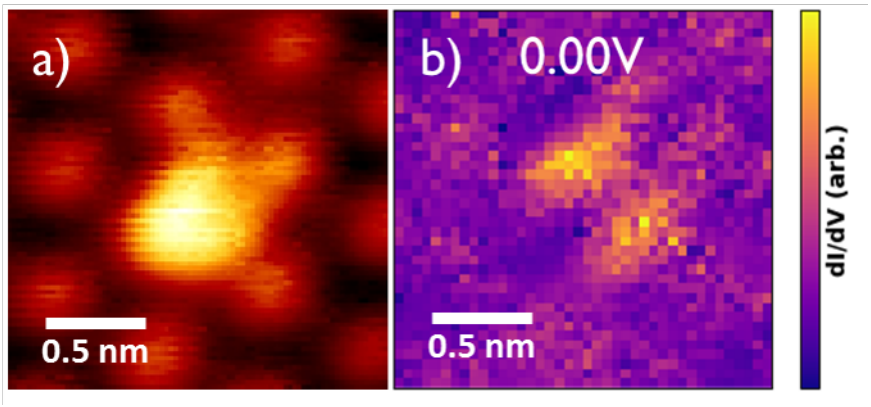

Figure 8.17: Preservation of Co atom Kondo lobes after switching.
(a) STM image of a switched Co atom on the silicene/ZrB_2 surface ($I_0 = 0.5\,nA$, $V_0 = -20\,mV$). (b) Simultaneously recorded Fermi level (0 V) dI/dV map of the switched Co atom revealing the two lobe structure of the Kondo effect.

to the arguments used to explain the lobe asymmetry in Co atoms bound at an angle to the striped domains of silicene/ZrB_2 (see **section 8.4**), this change in the amplitude of the Kondo resonance indicates that there is a change in the continuum density of states. How the switching of the Co atom can influence the background LDOS is unclear, but it may be that a change in the binding geometry could alter the surrounding silicon structure similar to the Jahn-Teller effect in molecular systems [197].

8.7 Conclusion

Spatially resolved spectroscopic measurements have been performed across Co atoms on silicene/ZrB_2 revealing that the two lobe structure arises due to an unusual spatially distributed Kondo effect with a Kondo temperature of $T_K \approx 20\,K$. The relative orientation of the Co atoms with respect to the striped domains of silicene on ZrB_2 are shown to induce an asymmetry into the amplitude of the Kondo resonance in each lobe, suggesting that there is an underlying asymmetry in the LDOS of the silicene lattice for electronic states propagating perpendicular or parallel to the boundaries. The changes in electronic structure of the silicene lattice at the domain boundaries is used to alter the magnetic coupling of the Co atoms to the surface by increasing the Kondo temperature of Co atoms on the boundaries. The increase of the Co atom Kondo temperature at the domain boundaries is an indication that the Si-p states are a significant contributor to the screening continuum, highlighting the importance of understanding the influence of these states on the spatial extent of the Kondo screening cloud. Finally it has been shown that voltage induced switching of the Co atoms between two states can alter the Kondo amplitude. These results demonstrate the rich array of interesting phenomena that can manifest when decorating 2D materials with magnetic adatoms.

8.8 Future Work

In this chapter intriguing magnetic interactions have been observed for Co atoms on the silicene/ZrB_2 surface. The spatially distributed Kondo resonance, and the influences of the domain boundaries of the surface hint towards non-trivial interactions that may have their roots in a form of p-wave Kondo screening. To be able to investigate these possibilities it will be necessary to gain further insight into how the Co atoms interact with the silicene substrate. To this end we are working with our collaborators to perform DFT calculations of Co atoms on silicene/ZrB_2. It is hoped that by understanding the orbital contributions to different electronic features a more complete picture can be developed that will then be used to guide calculations into how the silicene/ZrB_2 surface acts as a screening continuum.

Chapter 9

Parity Symmetry Breaking in the Two-Impurity Anderson Model

The physics of highly correlated phenomena are of crucial importance in many active areas of research including, high-temperature cuprate superconductors [198], heavy-fermion systems [199, 200], and frustrated magnetism [201]. In these systems small variations in the competing energy scales of different interactions can lead to greatly different physical characteristics. It is this complexity that still raises fundamental questions, as well as imposing barriers to further technological development. It is therefore key to develop a comprehensive understanding of model systems, from which to build upon.

A deceptively simple realisation of these complex interactions can be found in the two-impurity Anderson model (TIAM). Two magnetic impurities embedded in a metallic host, at a finite separation from one another, will hybridise with the host such that two competing effects arise; the Kondo effect, and the RKKY interaction [202–212].

The single impurity Kondo effect attempts to screen the magnetic moment of the individual impurities by antiferromagnetically (AFM) coupling a cloud of conduction band electrons to the impurity. The characteristic energy scale of the Kondo effect is given by the Kondo temperature T_K, a non-analytical quantity that is exponentially dependent on the strength of hybridisation between the impurity and conduction band[20].

RKKY is an indirect exchange interaction, of strength J_{RKKY}, that is mediated via the conduction electrons of the host metal [121–123]. The magnetic moment of one impurity is AFM coupled to the conduction band polarising the spin distribution in its vicinity. The spin polarisation then oscillates as the electrons propagate away from the impurity. Depending on distance to the second impurity it becomes effectively ferromagnetically (FM) or AFM coupled to the first.

Since both the Kondo and RKKY interactions arise due to hybridisation of the impurity magnetic moment with the conduction band, the two directly compete. This competition is characterised by a quantum critical point (QCP) that separates the mag-

netically ordered (RRKY dominant), and paramagnetic (Kondo dominant) phases [202–204]. By breaking the symmetry of the TIAM, either through the inclusion of non-identical impurities or paticle-hole asymmetry the QCP becomes a crossover. [205–212]. Experimentally the TIAM has been explored by STM investigations of transition metal atoms and molecules on metallic, [21–23, 25, 27, 213] and thin insulating [28, 29] surfaces, as well as in quantum dot devices [214].

In this chapter the TIAM formed from pairs of Co atoms on the surface of the two-dimensional (2D) material silicene/ZrB_2 is investigated. Individual Co atoms on silicene/ZrB_2 have been shown to undergo an unusual spatially distributed Kondo screening that is suspected to arise from p-wave hybridisation to the conduction band (see **chapter 7**). It is shown that Co dimers exhibit a highly anisotropic RKKY interaction of strengths comparable to the individual impurity Kondo temperature; this is well into the regime of the QCP in the TIAM. In the FM coupled regime the two impurities are found to still exhibit a Kondo effect, albeit with a greater resonance width. The increase in the width is attributed to a decrease in the Kondo temperature [21, 202, 205], which is an indication that the FM coupled Co atoms are in the regime of a higher spin state, under-screened Kondo interaction. Furthermore, the amplitude of the split Kondo resonances in the AFM regime are found to be highly asymmetric. It is suggested parity breaking, induced by the honeycomb silicene lattice, is responsible for the observed asymmetry [212, 215–217]. These results highlight how novel 2D materials can be used to induce new degrees of freedom into highly correlated systems. In particular the diverse asymmetries observed could be used to define parity dependent coupling extended magnetic structures.

9.1 Cobalt Dimers on the 2D material Silicene/ZrB_2

Investigations of isolated Co atoms on silicene/ZrB_2 have revealed that the two lobe structure observed at low bias is the result on an unusual spatially distributed Kondo resonance (see **chapter 7**). **Figure 9.1a** displays an STM image of a Co dimer, where the inter-atom spacing is $d = 3.17$ nm along the $ZrB_2[11\bar{2}0]$ direction. At very large separations, such as this, it is expected that the two Co atoms will behave as isolated Kondo impurities, each individually screened by the conduction electrons. The STS spectra recorded upon the two atoms are shown in **Fig. 9.1b**, where the average FWHM of the Kondo resonances from the top, and bottom Co atoms are 3.78 ± 0.07 mV, and 3.95 ± 0.12 mV respectively, within the range of expected values for isolated Co atoms of 3.8 ± 0.4 mV (see **section 8**).

Several examples of Co dimers on the silicene/ZrB_2 surface with separations, as measured between the two Si near-bridge sites, ranging from $d = 0.63$ nm to $d = 1.68$ nm are shown **Fig. 9.2** . The Co dimers in **Fig. 9.2a-c**, **Fig. 9.2d**, and **Fig. 9.2e-f**, are along the ZrB_2 $[11\bar{2}0]$, $[1\bar{1}00]$, and $[41\bar{5}0]$, directions respectively. In all cases low bias STM images reveal a two lobe structure of the Co atoms indicating that the a Kondo effect is still present at all separations.

Cobalt atoms on the silicene/ZrB_2 surface bind above the Si near-bridge atom of the silicene lattice that sits just off of the nearest Si 'up' atom (see **section ??**). Since the contrast in STM images of the surface is provided by these Si 'up' atoms, dimer configurations are labelled by the number of Si 'up' atoms that separate them. In

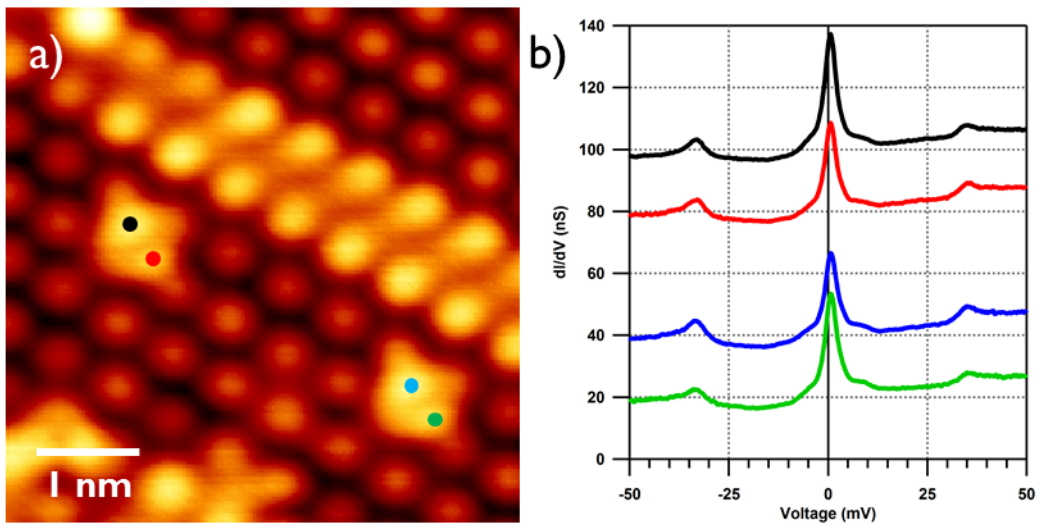

Figure 9.1: Co dimer on silicene/ZrB_2 in the single impurity Kondo screening phase. (a) STM image of a Co dimer on silicene/ZrB_2 with an inter-impurity separation of $d = 3.17$ nm along the $ZrB_2[11\bar{2}0]$direction ($I_0 = 0.1$ nA, $V_0 = -10$ mV). (b) STS spectra recorded upon each lobe of the dimer as denoted by the coloured circles in (a). The spectra are identical to those of isolated Co atoms on silicene/ZrB_2 indicating that there is negligible RKKY interaction between the pair.

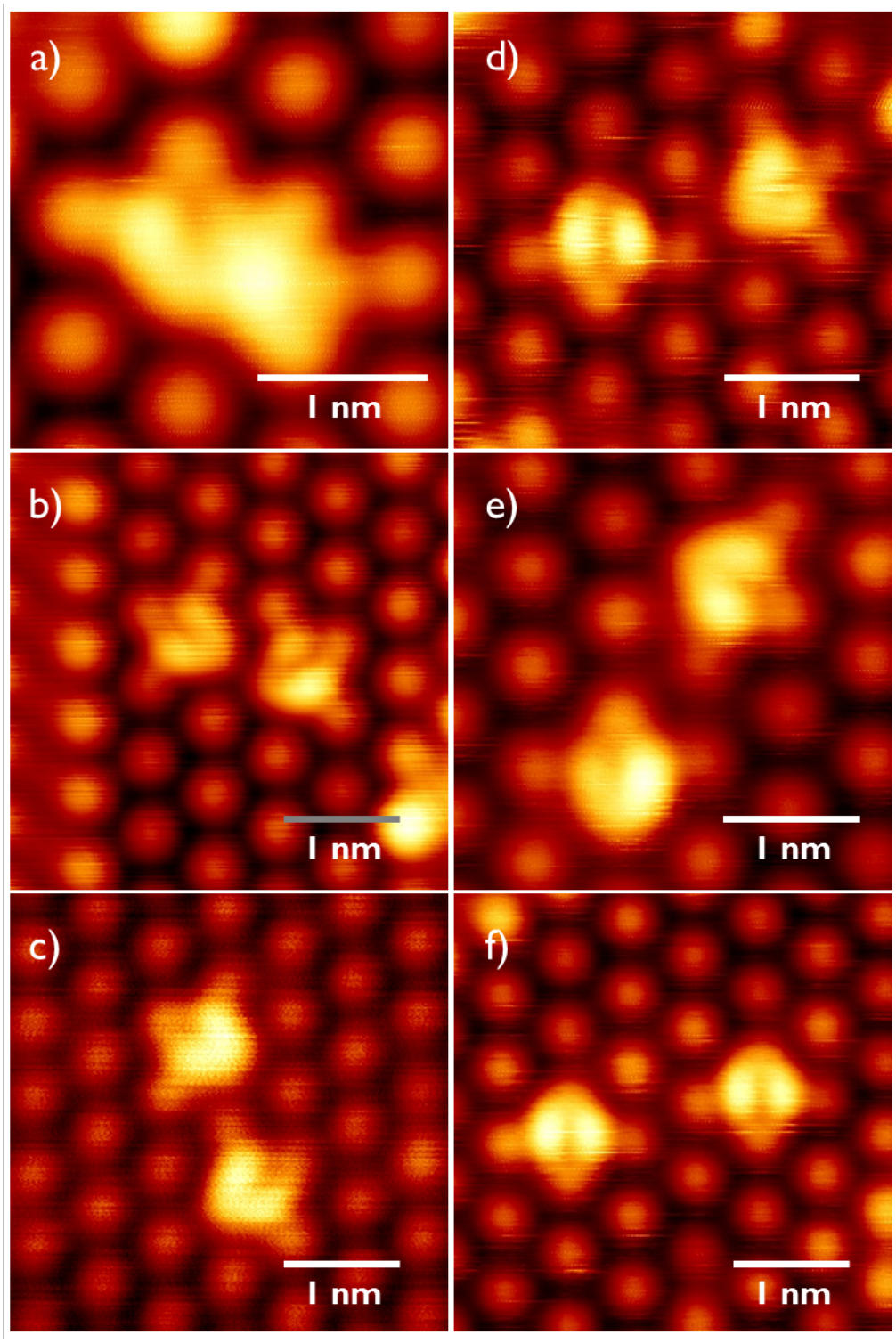

Figure 9.2: Examples of Co dimers on silicene/ZrB_2 at various separations.
STM images of pairs of Co atoms on the silicene/ZrB_2 surface at various relative orientations and separations. Along the $ZrB_2[11\bar{2}0]$ directions in (a) $d = 0.63\,\text{nm}$ ($I_0 = 0.1\,\text{nA}$, $V_0 = -10\,\text{mV}$), (b) $d = 0.91\,\text{nm}$ ($I_0 = 0.1\,\text{nA}$, $V_0 = -10\,\text{mV}$), and (c) $d = 1.30\,\text{nm}$ ($I_0 = 10\,\text{pA}$, $V_0 = -10\,\text{mV}$). Along the $ZrB_2[1\bar{1}00]$ directions in (d) $d = 1.28\,\text{nm}$ ($I_0 = 0.5\,\text{nA}$, $V_0 = -10\,\text{mV}$). Along the $ZrB_2[41\bar{5}0]$ directions in (e) $d = 1.50\,\text{nm}$ ($I_0 = 0.1\,\text{nA}$, $V_0 = -10\,\text{mV}$), and (f) $d = 1.68\,\text{nm}$ ($I_0 = 0.1\,\text{nA}$, $V_0 = -10\,\text{mV}$).

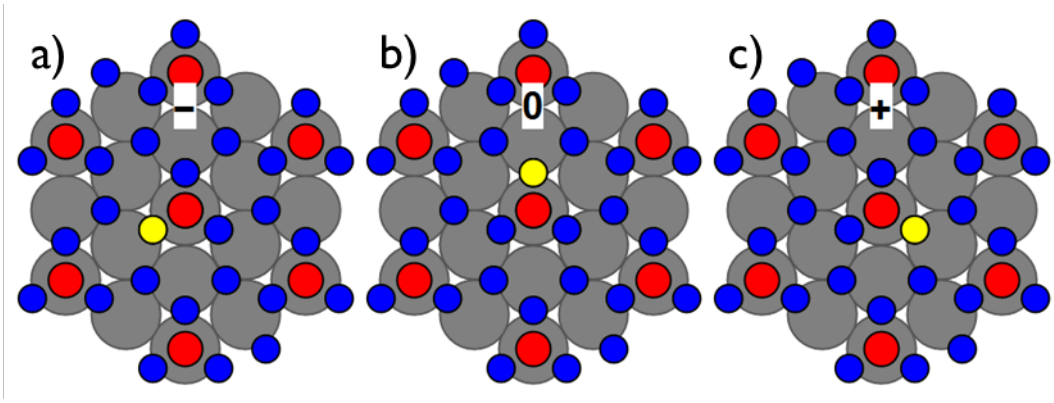

Figure 9.3: Model of the three equivalent Co atom binding sites on silicene/ZrB_2. Co atoms on the silicene/ZrB_2 surface bind above the Si near-bridge atom (yellow) of the silicene lattice. Owing to the three-fold symmetry of the silicene lattice there are three equivalent sites, labelled "-", "0", and "+" in (a), (b), and (c) respectively.

addition the crystallographic direction that joins the two atoms is denoted by the $ZrB_2(0001)$ surface directions joining the two nearest Si 'up' atoms. For a given Si 'up' atom on the silicene surface there are therefore three equivalent Co atom binding sites labelled "-", "0", and "+" (see **Fig. 9.3**). For a Co dimer at a given Si 'up' atom separation there are then 9 possible configurations. Models are shown for Co dimers along the silicene/ZrB_2 $[11\bar{2}0]$ nearest neighbour (**Fig. 9.4**), $[11\bar{2}0]$ next nearest neighbour (**Fig. 9.5**), $[1\bar{1}00]$ nearest neighbour (**Fig. 9.6**), and $[41\bar{5}0]$ nearest neighbour (**Fig. 9.7**) directions. To date reliable atom manipulation on the silicene/ZrB_2 surface has not been achieved, therefore a subset of the total number of configurations has been studied by finding them on the surface after deposition.

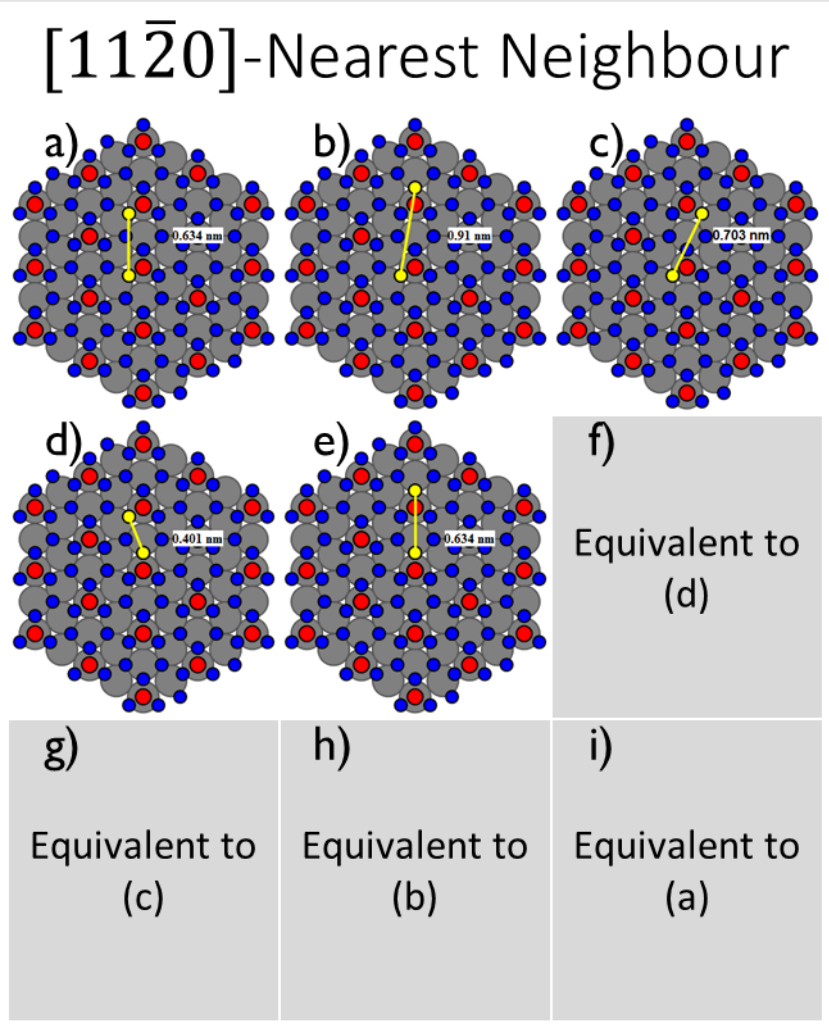

Figure 9.4: Nearest neighbour Co dimer configurations along the ZrB_2 $[11\bar{2}0]$ direction. Ball models of each possible dimer configuration, *orientation 1*:*orientation 2*. (a) -:-, (b) -:0, (c) -:+, (d) 0:-, (e) 0:0, (f) 0:+, (g) +:-, (h) +:0, (i) +:+

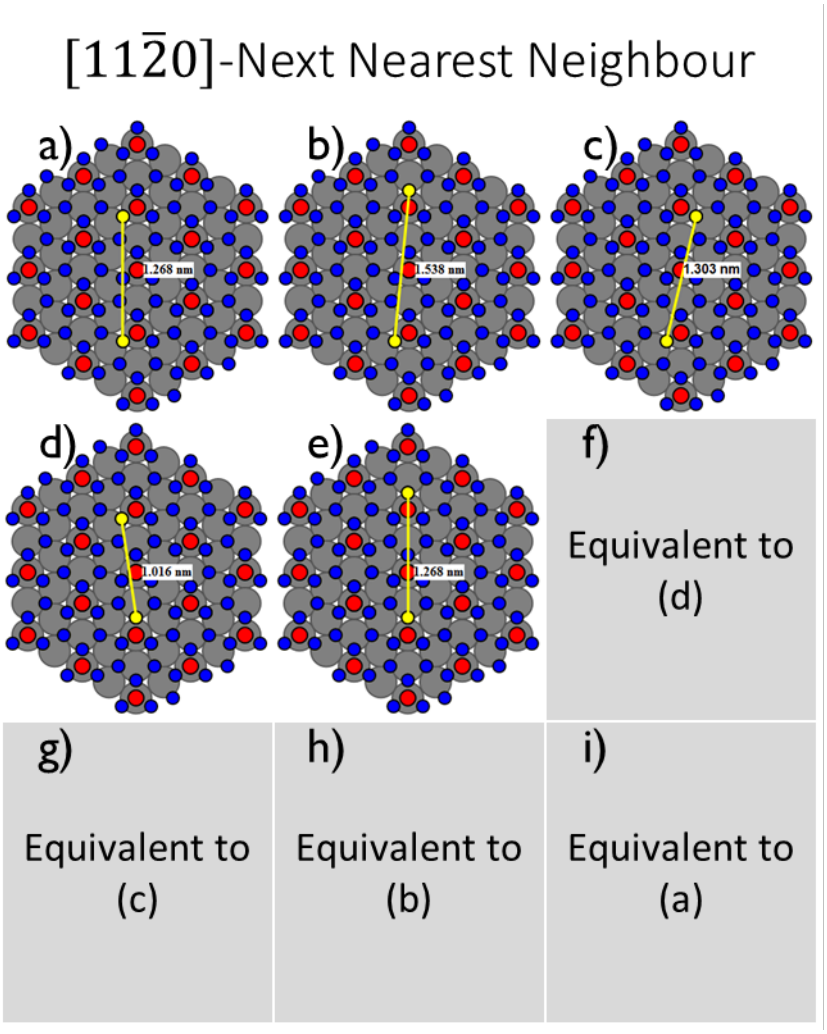

Figure 9.5: Next nearest neighbour Co dimer configurations along the ZrB_2 $[11\bar{2}0]$ direction.
Ball models of each possible dimer configuration, *orientation 1*:*orientation 2*. (a) -:-, (b) -:0, (c) -:+, (d) 0:-, (e) 0:0, (f) 0:+, (g) +:-, (h) +:0, (i) +:+

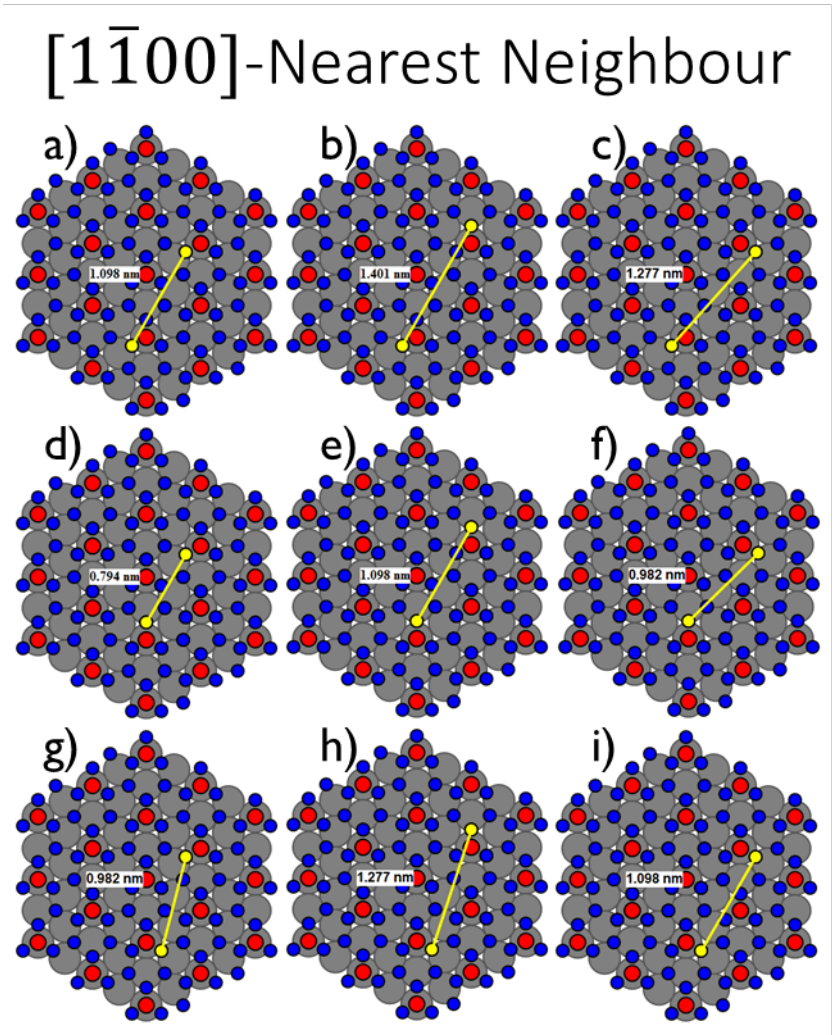

Figure 9.6: Nearest neighbour Co dimer configurations along the ZrB_2 $[1\bar{1}00]$ direction. Ball models of each possible dimer configuration, *orientation 1*:*orientation 2*. (a) -:-, (b) -:0, (c) -:+, (d) 0:-, (e) 0:0, (f) 0:+, (g) +:-, (h) +:0, (i) +:+

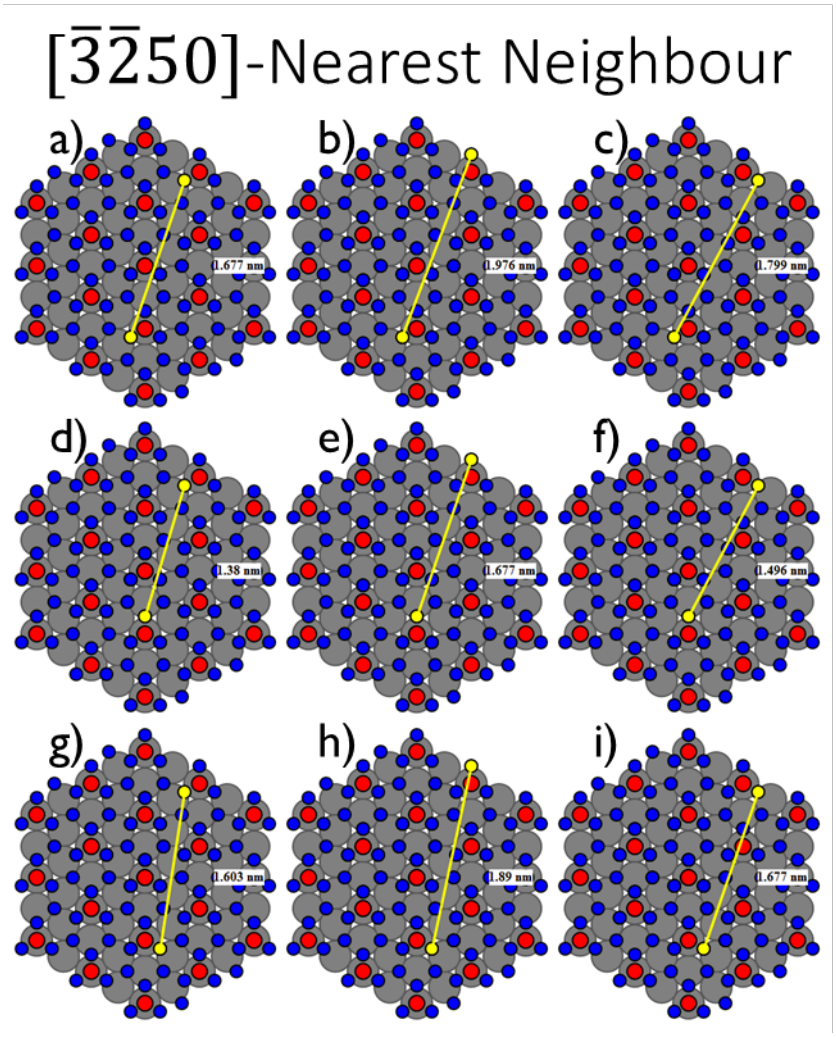

Figure 9.7: Nearest neighbour Co dimer configurations along the ZrB_2 $[\bar{3}\bar{2}50]$ direction. Ball models of each possible dimer configuration, *orientation 1*:*orientation 2*. (a) -:-, (b) -:0, (c) -:+, (d) 0:-, (e) 0:0, (f) 0:+, (g) +:-, (h) +:0, (i) +:+

9.2 Spectroscopic Measurements of Cobalt Dimers

Qualitatively, there are three intuitive regimes of the TIAM that arise depending on the sign and relative magnitude of the RKKY interaction strength J_{RKKY}, and the Kondo temperature T_K. As a result it can naively be expected to observe one of three behaviours. (i) $|J_{RKKY}| << k_B T_K$. In this regime the single impurity Kondo effect dominates and the STS spectra of the Co dimer should be equivalent to those of isolated Co atoms, as is shown in **Fig. 9.1**. (ii) $-J_{RKKY} >> k_B T_K$. In this FM regime the magnetic moments of the two impurities should effectively be coupled into an $S = 1$ (assuming $S = 1/2$ impurities) state that is usually associated with a significant decrease in the Kondo temperature of the dimer T_K^d [202]. Therefore at a constant experimental temperature it should be expected to observe a broadening or disappearance of the Kondo resonances [21]. (iii) $J_{RKKY} >> k_B T_K$. In this AFM regime the Co atom spins will couple into a $S = 0$ singlet state [203, 204] that no longer exhibit a Kondos effect. However, these three regimes neglect the important AFM crossover region in which $J_{RKKY} \approx k_B T_K$, where neither the single impurity Kondo effect and the AFM RKKY coupling dominate. In this crossover region the Kondo resonance is split around the Fermi level forming two resonances at $eV = \pm J_{RKKY}$ [22, 215].

STS measurements performed on Co dimers can be classified into one of three regimes, an example of each is shown in **Fig. 9.8**. For each dimer there are four STS curves for the four lobes from the two atoms; each is denoted by a coloured circle in the corresponding STM image. For each dimer a ball model of the complete silicene/ZrB_2 surface is shown, where the Co atom centres are highlighted by the yellow Si near-bridge atoms, and the lobes are shown by the coloured ovals.

When the Co atoms are very close, as in **Fig. 9.8ai-ii**, the STS curves (**Fig. 9.8aiii**) show that there is no longer a zero bias resonance, but rather two resonances separated symmetrically around the Fermi level. This splitting of the Kondo resonance is as would be expected for TIAM in the AFM regime, but unexpectedly there is a significant asymmetry in the amplitude of the split resonances, which is itself non-trivially different for each Co atom lobe (i.e. there is no clear pattern).

In **Fig. 9.8bi-ii** an example of a Co dimer where there is no splitting of the Kondo resonances is shown. There are two possibilities for these examples, either the magnitude of the RKKY interaction is insufficient to over come the single impurity Kondo effect, or the two Co atoms are FM coupled and the observed resonance is a manifestation of the Kondo effect for a higher spin state [202].

An example of the third class of Co dimers is shown in **Fig. 9.8c**. The third class is defined by a slight AFM splitting of the Kondo resonance, and little or no asymmetry in the amplitude of the split resonances.

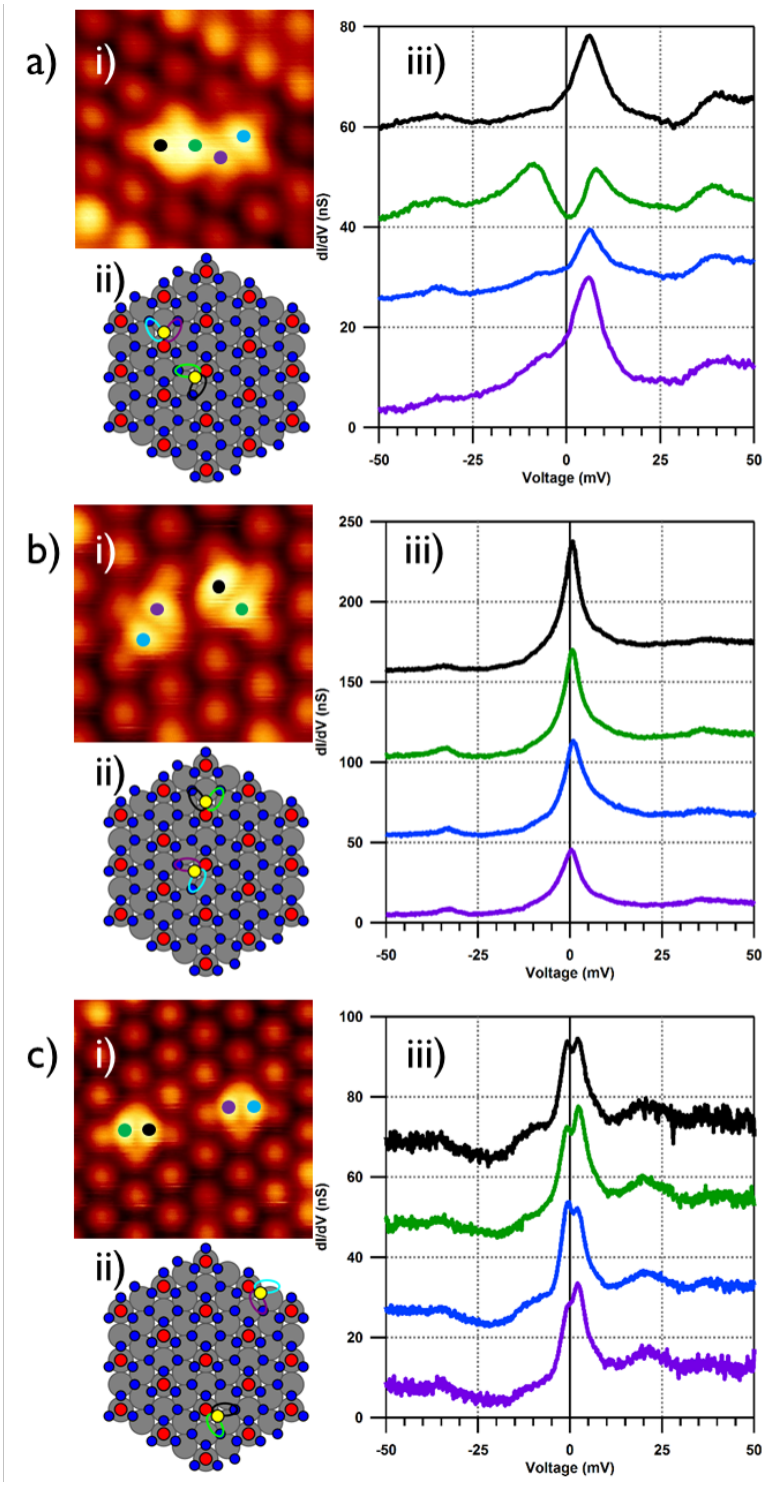

Figure 9.8: Influence of dimer separation on Co atom Kondo resonances.
STM images of Co dimers at three different separations d, on silicene/ZrB_2 (a)(i) $d = 0.70\,\text{nm}$ ($3.2\,\text{nm}\times3.2\,\text{nm}$, $I_0 = 0.1\,\text{nA}$, $V_0 = -10\,\text{mV}$), (b)(i) $d = 0.91\,\text{nm}$ ($3.0\,\text{nm}\times3.0\,\text{nm}$, $I_0 = 0.05\,\text{nA}$, $V_0 = -3\,\text{mV}$), (c)(i) $d = 1.68\,\text{nm}$ ($3.8\,\text{nm}\times3.8\,\text{nm}$, $I_0 = 0.1\,\text{nA}$, $V_0 = -10\,\text{mV}$). (a)(ii), (b)(ii), and (c)(ii) are ball models of the Co dimers in (a)(i), (b)(i), and (c)(i) respectively, where the coloured ovals correspond to the different lobes, and the yellow Si near-bridge atom highlights the Co atom centres. STS spectra taken upon each lobe of the Co dimers in (a)(i), (b)(i), and (c)(i) are shown in (a)(iii), (b)(iii), and (c)(iii).

9.3 Anisotropic RKKY interaction of Co Dimers

For RKKY interactions it is expected that J_{RKKY} will oscillate between FM and AFM as a function of separation. Using the Kondo effect to indirectly measure the RKKY interaction means that there is no measurement for $J_{RKKY} < 0$ FM interactions (unlike when using spin polarised STM [24, 26]). In **Fig. 9.9** a plot of the Co dimer Kondo resonance splitting as a function of separation is shown for 20 Co dimers. The magnitude of the splitting is seen to decrease with increasing separation, but it is difficult to make out any sinusoidal pattern. However, in **Fig. 9.10** the same plot is reproduced for Co dimers running along different $ZrB_2(0001)$ crystallographic directions. Here a clear paattern can be seen, in particular for Co dimers along the $ZrB_2[11\bar{2}0]$ direction (**Fig. 9.10a**), where more configurations have been found.

It has previously been shown that an isotropic 2D RKKY model can be used describe the interactions between magnetic adsorbates on surfaces along different crstallographic directions [24, 26]. The 2D isotropic RKKY model has a form for the interaction strength J_{RKKY} of,

$$J_{RKKY} = J_0 \frac{Cos\,(2k_F d + \alpha)}{(2k_F d)^2}, \tag{9.1}$$

where J_0 is the zero separation interaction strength, $\lambda_F = 2\pi/k_F$ is the Fermi wavelength, d is the dimer separation, and α is a phase offset. A modified version of the 2D RKKY model in **eqn. 9.1** is used to fit the experimental data for Co dimers along the $ZrB_2[11\bar{2}0]$ direction in **Fig. 9.11** giving $J_0 = 1225 \pm 215$ mV, $\lambda_F = 3.23 \pm 0.04$ nm, and α has been fixed at zero [1].

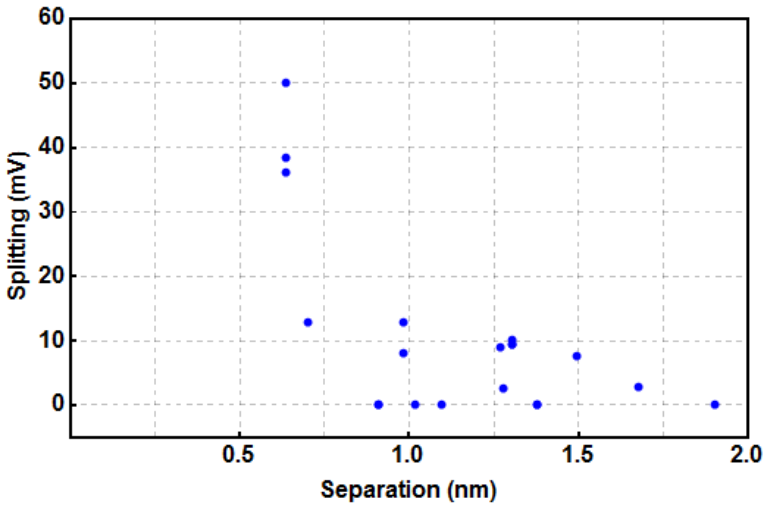

Figure 9.9: Splitting of Kondo resonances for Co atom dimers.
Values for splitting taken as an average from all four lobes. Errors estimated from range of values from all four lobes are too small to display on the scale shown.

[1] Since there is no measure for FM J_{RKKY} values, the fit is performed with J_{RKKY} given by **eqn. 9.1** for $Cos(2k_F d) > 0$ and zero for $Cos(2k_F d) < 0$

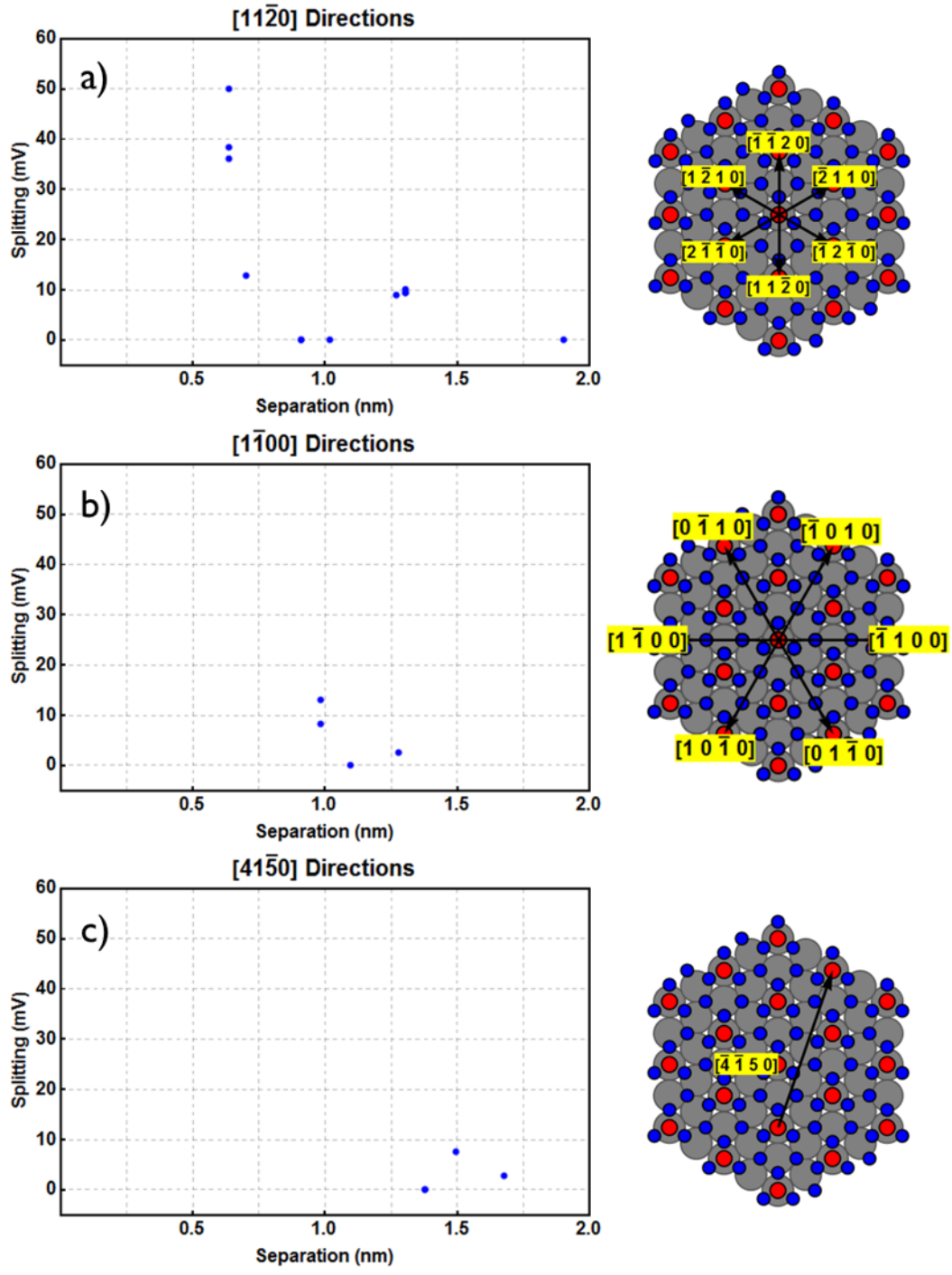

Figure 9.10: Splitting of Kondo resonances for Co atom dimers along different crystallographic directions.
Kondo resonance splitting against dimer separation along ZrB_2(a) $[11\bar{2}0]$, (b) $[1\bar{1}00]$, and (c) $[\bar{3}\bar{2}50]$, and equivalent directions. Values for splitting taken as an average from all four lobes. Errors estimated from range of values from all four lobes are too small to display on the scale shown.

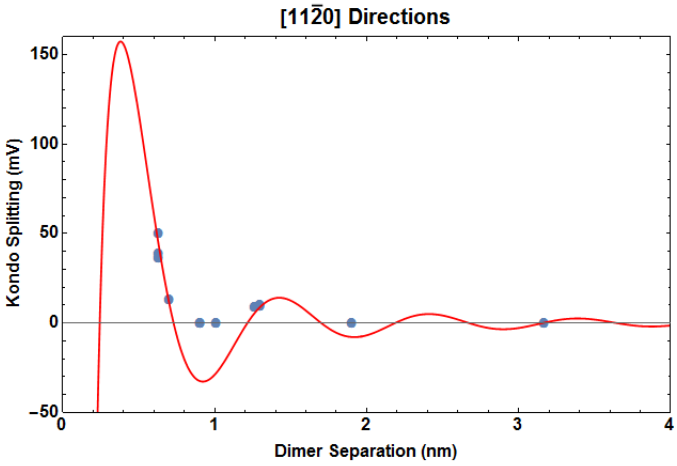

Figure 9.11: Fitting of RRKY models to Co dimer Kondo splitting.
Fit of 2D RKKY model (red line) to Kondo resonance splitting of Co dimers along the ZrB_2 $[11\bar{2}0]$ and equivalent directions (blue markers). A zero separation interaction strength of $J_0 = 1125 \pm 215$ mV and Fermi wavelength of $\lambda_F = 3.23 \pm 0.04$ nm are found, no phase shift α was used.

The determined value for the Fermi wavelength of the 2D state that mediates that RKKY interaction is similar, but larger than those of other systems. For example $\lambda_F = 1.46$ nm on Cu_2N, [28, 29], $\lambda_F = 2.0$ nm on Pt(111), [24] and $\lambda_F = 2.9$ nm on Cu(111) [26]. In comparison to these other systems the strength of the interaction between Co atoms on the silicene/ZrB_2 surface can be one, if not two orders of magnitude greater [24, 26–29]. More specifically it is the ratio of J_{RKKY} to $k_B T_K$ that is very large in the present work that allows for the clear separation of the split resonances in the AFM regime, rather than an apparent broadening of the zero bias resonance.

Although there are only a few examples of Co dimers along the $[1\bar{1}00]$ (**Fig. 9.10b**) and $[41\bar{5}0]$ (**Fig. 9.10c**) directions, and therefore fitting to **eqn. 9.1** is of limited use, the presence of dimers in both the FM and AFM regimes gives an indication to how significant the change the wavelength along the different directions is. The differences in the RKKY interaction of magnetic atoms along different directions on the surface, [24, 26] and in the bulk of metals [27] has been linked to anisotropies of the Fermi surface [27]. At present no clear description of the silicene/ZrB_2 fermi surface is known, however it is expected that the 2D surface state of ZrB_2 [193, 194] that has significant hybridisation with the Si p-states [84] will play a major role in the observed interactions. The bulk Fermi surface of ZrB_2 is highly anisotropic [190–192], and APRES measurements of the silicene/ZrB_2 surface show signigicant differences in the Fermi level states along the $[11\bar{2}0]$ and $[1\bar{1}00]$ directions [12]. The presence of such a large anisotropy could be useful in the manufacturing of complex architectures in extended magnetic structures.

9.4 Parity Breaking in the Antiferromagnetic Regime

The aspects of the TIAM formed by Co atoms on silicene/ZrB_2 that have been examined so far are consistent with other experimental observations [21–23, 25, 27–29, 213, 214]. In the FM regime a decrease in the Kondo temperature of the coupled atoms is observed, and in the AFM regime a splitting of the zero bias resonance occurs. However, Co dimers in the AFM coupled regime display a dramatic asymmetry in the amplitude of the split resonances, a few examples of which are shown in **Fig. 9.12**. In this section the importance of parity symmetry in the TIAM is outlined, and it is argued that the silicene/ZrB_2 surface breaks this symmetry. As a result a new degree of freedom is introduced that shows a complex interplay with the spatially anisotropic scattering at the individual Co atoms.

As a starting point to understanding the role of parity in the TIAM, a single Kondo impurity in the presence of a magnetic field is considered. At zero field the Kondo effect arises due to the zero energy, spin flipping, virtual excitation, of electrons from the singly occupied impurity doublet state to the doubly occupied excited singlet impurity state (see **Fig. ??**). When the magnetic field is non-zero the degeneracy of the singly occupied doublet is lifted, via the Zeeman effect, forming two singlets that are separated by an energy ΔE. When $\Delta E >> k_b T_K$, the Kondo effect is killed and spin flip inelastic excitations are observed at $\omega = \pm\Delta E$. However, when $\Delta E \approx k_b T_K$ the field is not sufficient to completely suppress the Kondo effect and so the spin flip excitations also have a non negligible contribution from the Kondo effect. This manifests as a pair of split resonances at $\omega = \pm\Delta E$ [218].

To understand the nature of the states for two magnetic impurities embedded in a metallic host at positions $\mathbf{R}_{\{1,2\}}$ the TIAM of the form, [212]

$$H = H_0^c + H_0^d + W^f + V, \tag{9.2}$$

is examined where,

$$H_0^c = \sum_{\mathbf{k},\sigma} \epsilon_{\mathbf{k}}^c c_{\mathbf{k},\sigma}^\dagger c_{\mathbf{k},\sigma}, \tag{9.3a}$$

$$H_0^d = \sum_{j,\sigma} \epsilon_{j,\sigma}^d d_{j,\sigma}^\dagger d_{j,\sigma} + \sum_{j=\{1,2\}} U_j d_{j,\downarrow}^\dagger d_{j,\downarrow} d_{j,\uparrow}^\dagger d_{j,\uparrow} + \frac{1}{2} \sum_{l\neq j,\sigma,\sigma'} U_{12}' d_{j,\sigma}^\dagger d_{j,\sigma} d_{l,\sigma'}^\dagger d_{l,\sigma'}, \tag{9.3b}$$

$$W^d = \sum_{l\neq j,\sigma} t_{lj} d_{l,\sigma}^\dagger d_{j,\sigma} - \frac{1}{2} \sum_{l\neq j} J_{lj} \mathbf{S}_l^d \cdot \mathbf{S}_j^d, \tag{9.3c}$$

$$V = \sum_{j,\mathbf{k},\sigma} \left(V_{\mathbf{k}} e^{-i\mathbf{k}\cdot\mathbf{R}_j} c_{\mathbf{k},\sigma}^\dagger d_{j,\sigma} + V_{\mathbf{k}}^* e^{i\mathbf{k}\cdot\mathbf{R}_j} d_{j,\sigma}^\dagger c_{\mathbf{k},\sigma} \right). \tag{9.3d}$$

Here H_0^c describes the conduction band of non-interacting electrons, where $c_{\mathbf{k},\sigma}^\dagger (c_{\mathbf{k},\sigma})$ is the creation(annihilation) operator of an electron with wave vector $\mathbf{k}$ and energy $\epsilon_{\mathbf{k}}^c$. H_0^d

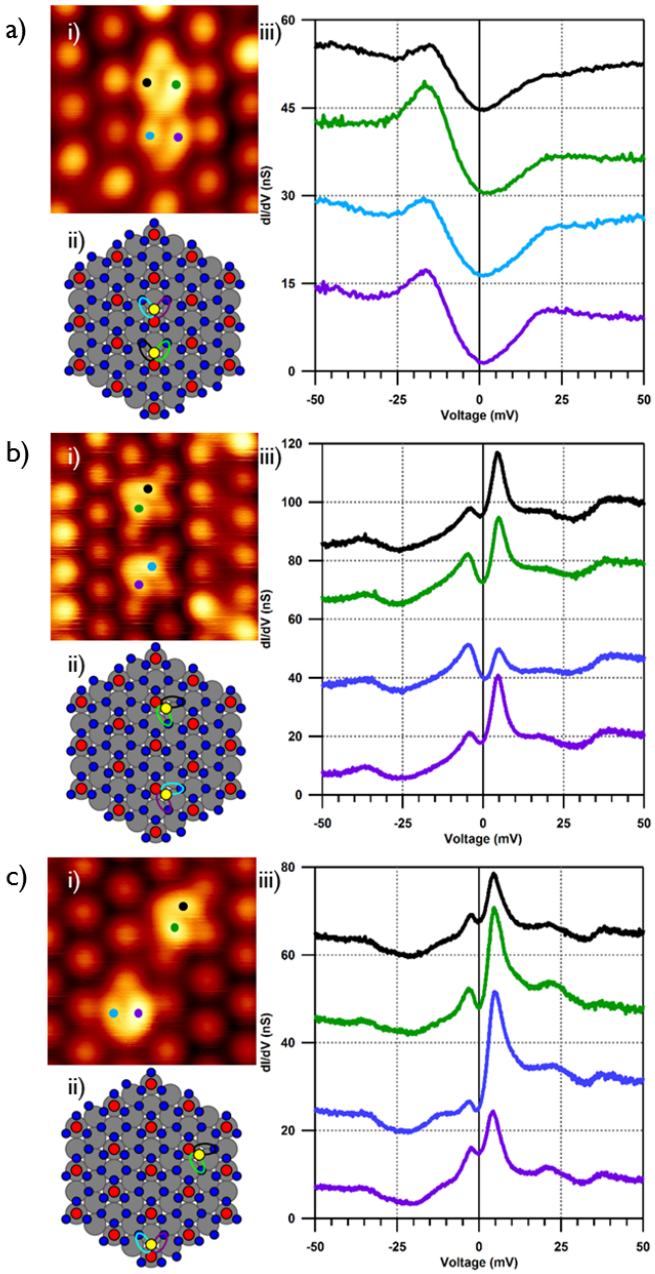

Figure 9.12: Examples of Co dimers that display significant parity symmetry breaking. (a) (i) STM image of Co dimer with $0.63\,\mathrm{nm}$ separation along the $[11\bar{2}0]$ direction ($2.6\,\mathrm{nm} \times 2.56\,\mathrm{nm}$, $\mathrm{I}_0 = 0.1\,\mathrm{nA}$, $\mathrm{V}_0 = 10\,\mathrm{mV}$). (ii) Ball model of the Co dimer configuration in (i). (iii) STS spectra recorded at the corresponding to the different coloured lobes in (i) and (ii). $J_{RKKY} = 36.1\,\mathrm{mV}$, spectra look increasingly like singlet to triplet excitations, but still with a slight parity breaking favouring the odd states.
(b) (i) STM image of Co dimer with $1.27\,\mathrm{nm}$ separation along the $[41\bar{5}0]$ direction ($3.3\,\mathrm{nm} \times 3.3\,\mathrm{nm}$, $\mathrm{I}_0 = 0.05\,\mathrm{nA}$, $\mathrm{V}_0 = -3\,\mathrm{mV}$). (ii) Ball model of the Co dimer configuration in (i). (iii) STS spectra recorded at the corresponding to the different coloured lobes in (i) and (ii). $J_{RKKY} = 9.0\,\mathrm{mV}$, the black, green, and purple spectra all show a significant parity breaking, where the even states are favoured. The blue spectra shows a roughly equal contribution from both parity states.
(c) (i) STM image of Co dimer with $1.27\,\mathrm{nm}$ separation along the $[11\bar{2}0]$ direction ($2.6\,\mathrm{nm} \times 2.6\,\mathrm{nm}$, $\mathrm{I}_0 = 0.1\,\mathrm{nA}$, $\mathrm{V}_0 = -10\,\mathrm{mV}$). (ii) Ball model of the Co dimer configuration in (i). (iii) STS spectra recorded at the corresponding to the different coloured lobes in (i) and (ii). $J_{RKKY} = 7.6\,\mathrm{mV}$, all spectra show significant parity breaking, where the even states are favoured.

corresponds to the Hamiltonian of the local impurities, where $d^{\dagger}_{j,\sigma}(d_{j,\sigma})$ is the creation(annihilation) operator of an electron at impurity $j = \{1, 2\}$ with spin σ and energy $\epsilon^{d}_{j,\sigma}$. The on-site and inter-site Coulomb interactions are U_j and $U^{'}_{12}$ respectively. W^d allows for the model to address more general couplings between the two impurities, where the first term allows direct hopping between impurities with amplitude t_{lj} and the second term is a Heisenberg exchange coupling of J_{lj} between impurity spins $\mathbf{S}^{d}_{j}$. Lastly V is the hybridisation term that mixes impurity and conduction states via $V_{\mathbf{k}}$.

When solving the TIAM it is convenient to use the symmetry of the system to define the even(+) and odd(-) parity one-particle states, [202–204, 212]

$$d_{\pm,\sigma} = \frac{1}{\sqrt{2}} \left(d_{1,\sigma} \pm d_{2,\sigma} \right), \tag{9.4}$$

and even and odd hybridisation functions, [212]

$$\Delta_{+}(\omega) = \frac{1}{N} \sum_{\mathbf{k}} |V_{\mathbf{k}}|^2 cos^2 \left(\frac{1}{2} \mathbf{k} \cdot \mathbf{d} \right) \pi \delta(\omega - \epsilon^{c}_{\mathbf{k}}), \tag{9.5a}$$

$$\Delta_{-}(\omega) = \frac{1}{N} \sum_{\mathbf{k}} |V_{\mathbf{k}}|^2 sin^2 \left(\frac{1}{2} \mathbf{k} \cdot \mathbf{d} \right) \pi \delta(\omega - \epsilon^{c}_{\mathbf{k}}), \tag{9.5b}$$

where $|\mathbf{d}| = \mathbf{R}_1 - \mathbf{R}_2$ is the impurity separation.

Within the TIAM outlined above both the single impurity Kondo effect and RKKY interactions will arise from the hybridisation terms alone [212]. However, in general studies phenomenologically simulate the RKKY interaction via a Heisenberg exchange interaction or direct hopping between the two impurities (that acts as an effective AFM coupling), with terms such as those in **eqn. 9.3c** [205–212].

When an AFM Heisenberg interaction is induced the observed splitting arises due to a suppression of the single impurity Kondo state at the Fermi level, coupled with the onset of a virtual Kondo effect experienced by the excited molecular triplet state at energies $\omega = \pm J$ [212]. When direct hopping between the two impurities is examined a splitting in the spectral function of the impurities of the order $2J_t = 8t^2/U$ is expected (**Fig. 9.13a-b**) [212]. However unlike with the Heisenberg coupling, the splitting in the hopping regime is largely due to the single-particle even-odd parity splitting of the quasiparticle excitations. This can be seen in **Fig. 9.13c**, where the spectral function for $J_t/\Delta = -0.4$ is shown decomposed into even and odd parity states.

The question is then, to what extent is the split resonance in the true RKKY interaction due to the suppression of the single impurity Kondo effect or the parity splitting of the single-particle excitations. This can be examined by the TIAM detailed in **eqn. 9.3** by setting $J_{lj} = t_{lj} = 0$ and explicitly modelling the RKKY interaction by including the hybridisation terms V up to higher orders. In **Fig. 9.14** the spectral function of the TIAM model in the AFM regime, due to RKKY interactions, is shown. The spectra have

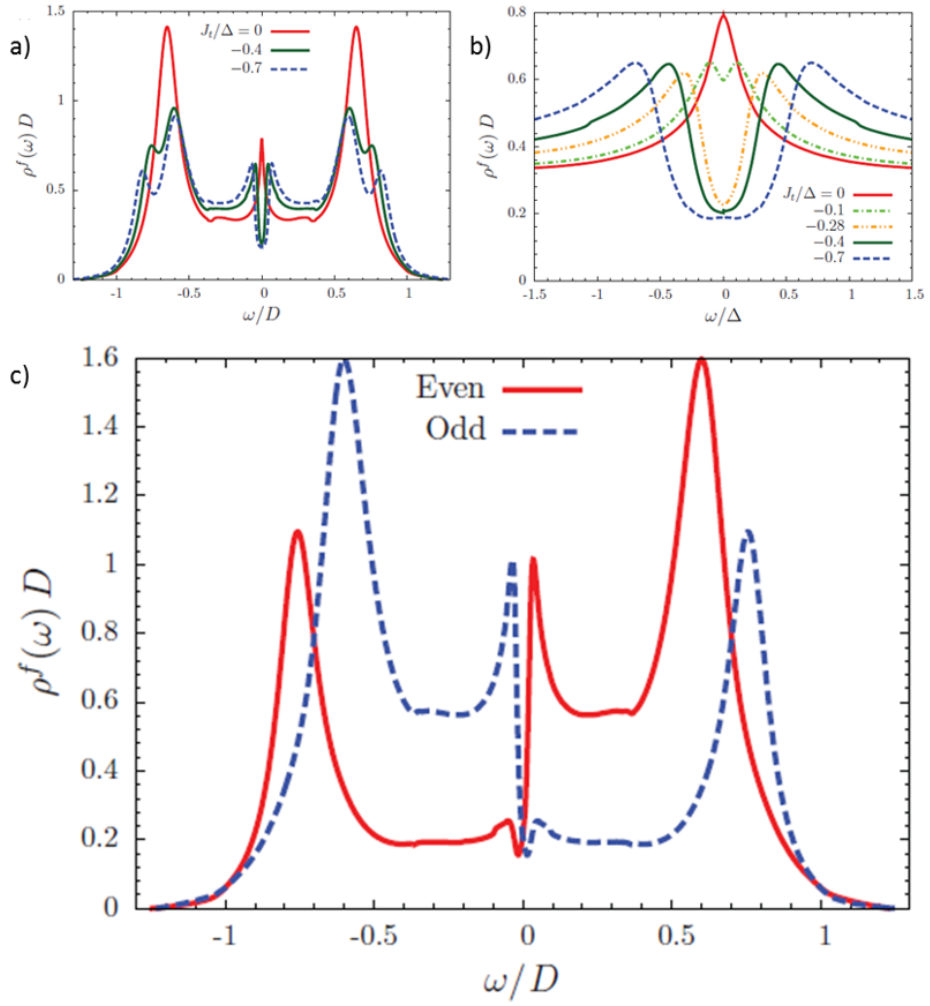

Figure 9.13: Spectral functions of the TIAM with direct hopping between impurities. (a) Spectral functions at a fixed temperature $T = 0.04\Delta$ for various values of the direct single-particle hopping t with effect AFM coupling $J_t = -4t^2/U$. (b) Shows a magnificaation of the low-energy region (in units of the Anderson width Δ). $\epsilon^d = -D/2$, $U = D$, $\Delta = 0.1D$, where D is the band width. (c) Same as in (a) with $J_t/\Delta = -0.4$ decomposed into even and odd parity contributions. [212])

.

been split into the even (**Fig. 9.14a**) and odd (**Fig. 9.14b**) parity states for different values of hybridisation strength Δ/D, where D is the bandwidth of the conduction states. At high excitation energies the parity splitting of the Hubbard bands is not as pronounced as in the purely hopping model (see **Fig. 9.13a,c**). However, the insets of **Fig. 9.14a** and **Fig. 9.14b** show that the parity splitting of the zero bias resonances is still significant.

To summarise the splitting of the resonances in the AFM regime of the TIAM can be described in analogy to the case of a single Kondo impurity in a magnetic field. When $J_{RKKY} << k_B T_K$ the single impurity Kondo effect dominates, and Kondo resonances will be observed at the Fermi level. When $J_{RKKY} >> k_B T_K$ the Kondo effect is killed and parity dependent excitations from the ground state singlet to triplet states will be

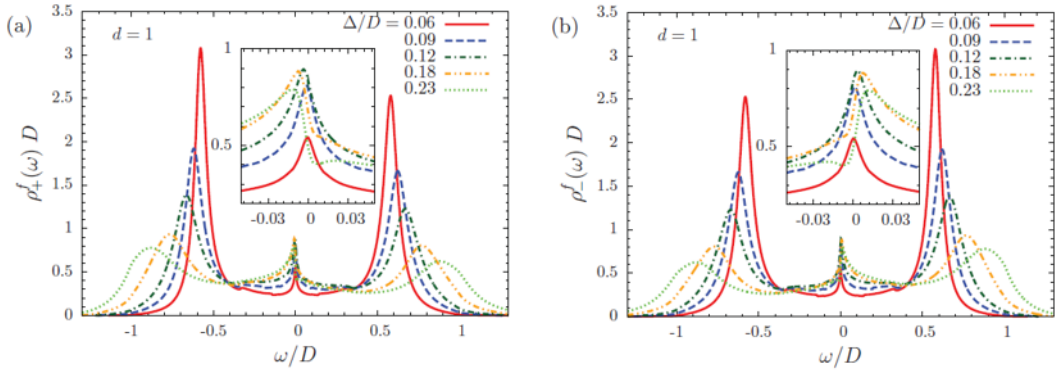

Figure 9.14: Parity resolved impurity sepctral function.
Impurity spectral functions decomposed inot even (a) and odd (b) states for AFM RKKY interactions determined through the full hybridisation model. $\epsilon^d = -D/2$, $U = D$, $T = 0.004D$, and $J = J_t = 0$. [212]

observed at $\omega = +J_{RKKY}$ for even parity and $\omega = -J_{RKKY}$ for odd parity. Finally when $J_{RKKY} \approx k_B T_K$ the parity dependent singlet to triplet excitations will contain non-negligible contributions from a Kondo effect of the excited triplet state.

It has now been demonstrated that in the AFM regime of the TIAM the split resonances around the Fermi level have a significant dependence on parity. Other experimental realisations of the TIAM on the surfaces of metallic substrates have not exhibited any measurable deviation from a parity symmetric AFM coupling [21–23, 25, 27, 213]. However, a slight asymmetry in the split resonances of Co dimers on the thin insulator Cu_2N has been observed [29], where it has been suggested that the breaking of four-fold symmetry in the Cu(001) surface is responsible for inducing a slight parity asymmetry [216].

In the present work it has been shown that there exists a significant asymmetry in the AFM regime of Co dimers on the 2D material silicene/ZrB_2 (**Fig. 9.12**). The magnitude of the splitting suggests that a significant contribution to the RKKY interaction comes from hybridisation to a 2D conduction state (see **section 9.3**). A likely candidiate for this is the 2D surface state of Zr-terminated ZrB_2(0001) [193, 194] that has been shown to hybridise with the silicene lattice [84].

Alone the ZrB_2 surface state should be symmetric under parity inversion, however, the honeycomb lattice of the silicene sheet breaks the parity symmetry. A ball model of the silicene/ZrB_2 surface is shown in **Fig. 9.15**. The two high symmetry directions of the surface are the $ZrB_2[11\bar{2}0]$ and $[1\bar{1}00]$ directions that have been associated to unit vectors $\mathbf{a}_y$ and $\mathbf{a}_x$ respectively. It can then be seen that $\mathbf{a}_x(\mathbf{a}_y)$ is symmetric(asymmetric) under parity inversion (i.e. $x \to -x$). Therefore the hybridisation between the ZrB_2 2D surface state and the silicene lattice will act to break parity symmetry. It is suggested that this parity breaking in the 2D surface state is responsible for effectively filtering the parity dependent singlet to triplet excitations in the AFM coupled Co dimers.

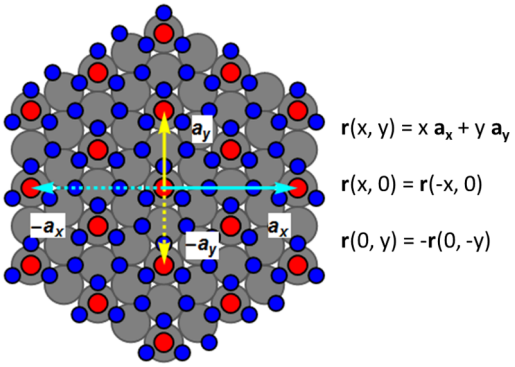

Figure 9.15: Parity Relationships of the Silicene/ZrB_2 surface.
A ball model of the silicene/ZrB_2 surface is shown, where the gray, blue, and red balls correspond to the Zr, Si near-bridge and Si hollow, and Si 'up' atoms respectively. Unit cell vectors for the $ZrB_2[11\bar{2}0]$ and $[1\bar{1}00]$ directions are labelled as $\mathbf{a}_y$ and $\mathbf{a}_x$ respectively. It can be seen that the x and y components of a given vector **r** will behave behave differently under parity inversion. $\mathbf{a}_x$ is symmetric (even) under parity inversion, whereas, $\mathbf{a}_y$ is asymmetric (odd).

9.5 Conclusion

Cobalt dimers on the silicene/ZrB_2 surface have been shown to exhibit an RKKY interaction over significant separations. The magnitude of the interaction, as measured by the splitting of the Kondo resonance in the AFM coupled regme, reaches values as high as 50 meV suggesting that the RKKY interaction is mediated by the silicene/ZrB_2 2D surface state. It is found that the RKKY interaction is highly anisotropic, heavily dependent on the crystallographic direction between the two atoms.

Unlike in other examples of FM coupled magnetic atoms on metallic surfaces, Co dimers in the FM regime of the RKKY interaction on silicene/ZrB_2 are shown to still undergo Kondo screening, albeit with an increased zero bias resonance width. The increased width is interpreted as a decrease in the Kondo temperature, with respect to the isolated atoms. It is likely that the observed Kondo effect is that of a higher spin state, and may therefore be in a underscreened regime.

AFM coupled Co dimers show a significant asymmetry in the amplitude of the split resonances that is attributed to the breaking of parity symmetry in the 2D surface state of silicene/ZrB_2. So far no clear pattern has been found that describes the observed parity asymmetries. It is considered that a complex interplay will arise between the parity breaking effect of the 2D state, and the spatially anisotropic Kondo scattering of the individual impurities (see **section 8**). However, these results highlight how the novel electronic properties of 2D materials can give rise to new degrees of freedom in the TIAM. This work may prove useful in gaining further insight into the complex interactions of heavy fermions systems, high temperature cuprate superconductors and frustrated magnetism.

9.6 Future Work

To gain further insight into the importance of parity in the RKKY interaction on silicene/ZrB_2 it will be necessary to combine existing and new experimental results with theoretical models that explicitly induce parity breaking in the conduction band states. Through these collaborative efforts it will then be possible to examine the impact of parity breaking in larger more complex magnetic structures, for example the Co trimer shown in **Fig. 9.16a**.

The Co trimer forms an equilateral triangle with sides of length d=$1.098\,$nm, as measured between the Si near-bridge binding sites, as can be seen in the comparative ball model of **Fig. 9.16b**. There is a single high symmetry mirror plane, ignoring that one of the Co atoms (top left) is touching a domain boundary, which runs through the centre of the lower Co atom along the $ZrB_2[11\bar{2}0]$ surface direction (vertical in the STM image and model). The STS measurements in **Fig. 9.16c** performed upon the different Co atom lobes show that the magnetic interactions obey the mirror symmetry. For the lower Co atom, both lobes (green and green dashed) show a zero bias Kondo resonance indicating that this atom is FM coupled. However, the spectra recorded above the lobes of the two upper Co atoms indicate that these two atoms are AFM coupled. The AFM coupling can be inferred from the highly parity filtered split resonances that only exhibit the even parity (positive bias) excitation. Furthermore, there is a symmetrical difference in the amplitude of the resonances about the mirror plane. The outer two lobes (black

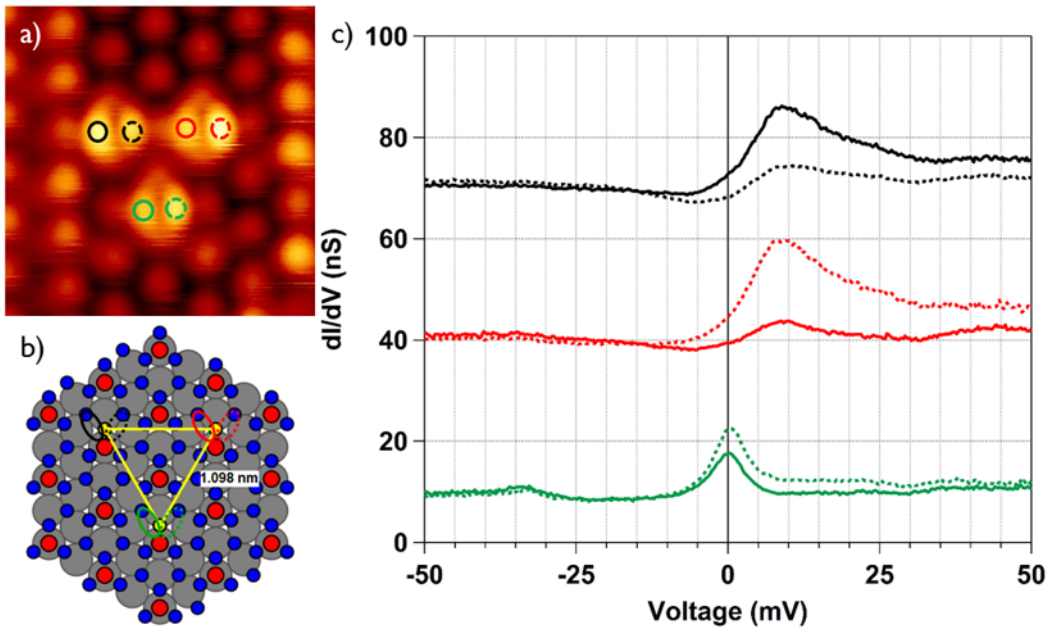

Figure 9.16: Extended magnetic structures on silicene/ZrB_2.
(a) STM image of a Co trimer on silicene/Zrb_2, ($3.2\,\mathrm{nm} \times 3.2\,\mathrm{nm}$, $I_0 = 0.1\,$nA, $V_0 = -10\,$mV,). (b) Ball model of the trimer configuration in (a). (c) STS curves taken upon the different lobes in the Co trimer as denoted by the coloured circles in (a). The top left and top right Co atoms appear to AFM coupeled, whilst the lower Co atom is FM coupled ($I_0 = 0.5\,$nA, $V_0 = -50\,$mV, $V_{mod} = 0.5\,$mV).

and red dashed) are greater in amplitude than the two central lobes (black dashed and red). From these results it is naively assumed that the bottom Co atom is FM coupled to the top two, which are in turn AFM coupled to one another. Since it is considered that the absolute separation defines the RKKY interaction, the difference in signs of the coupling is somewhat surprising given that the Co trimers forms an equilateral triangle. Challenging DFT calculations of individual Co atoms on the silicene/ZrB_2 are under way that will hopefully elucidate the Co atom spin state and hybridisation to the silicene surface. Once this is known it is possible that a simplistic Heisenberg closed chain model could help to understand the observed interactions. The preliminary results shown here indicate that there is further complexity to the magnetic interactions of Co atoms in larger coupled structures on silicene/ZrB_2. Experimentally it will therefore be of interest to investigate these phenomena in the future, perhaps on the single-domain silicene surface as this would remove the complication of the periodic domain boundaries.

In addition it will be of interest to perform measurements that probe the Kondo effect of Co atoms in the FM regime, as this area of the TIAM is known to have a complex phase space of great interest in its own right. An interesting observation in existing data is that the lobe asymmetry in the Co monomers, associated with the relative orientation with respect to the domain boundaries, no longer appears to be present in FM coupled dimers. Further experiments could focus on understanding the influence of the domain boundaries on the dimer configurations.

Chapter 10

Conclusion

In this thesis the structural, electronic, and magnetic properties of the 2D material silicene/ZrB_2 have been investigated by scanning tunnelling microscopy and spectroscopy. These experiments have used the deposition of semiconducting and magnetic adosrbates to modify the properties of the silicene surface.

Changes in structural and electronic properties that manifest when additional Si is deposited upon the silicene/ZrB_2 surface have been examined. When small amounts of Si are deposited the Si is incorporated into the silicene surface removing the striped domain boundaries unique to the silicene/ZrB_2 system. Crucially, it has been shown that this alteration does not significantly alter the structural or electronic properties of the silicene creating large single-domain sheets. In contrast, when the amount of deposited Si is increased a distinct change in both the structural and electronic properties of the silicene surface is observed. The additional Si grows as a 2D layer on top of the silicene surface, forming a new Si nanostructure, which surprisingly is metallic at room temperature. It is proposed that the atomically sharp transition to islands of metallic Si nanostructure could be utilised as an atomically precise electrical contact to the semiconducting silicene/ZrB_2 surface.

These results have shown that dramatic changes in the structural and electronic properties of the 2D material silicene/ZrB_2 can arise when sub- and mono-layer coverages of Si are deposited upon its surface. In the past few years a number of new semiconducting 2D materials have been the focus of much experimental and theoretical interest, such as germanene [63, 130, 219, 220], stanene [219, 221], and phosphorene [10, 222–225]. Some of these materials, such as germanium, can be sublimated in a similar manner to silicon. Therefore, it could be of interest to examine the changes in the structural and electronic properties when these materials are deposited in sub- and mono-layer coverages onto silicene/ZrB_2. It could also be of interest to examine how individual group III and IV dopants influence the electronic properties of silicene/ZrB_2 and Si nanostructures as these interactions have had significant impact in conventional semiconducting materials. For two reasons it would be interesting to explore the hydro-

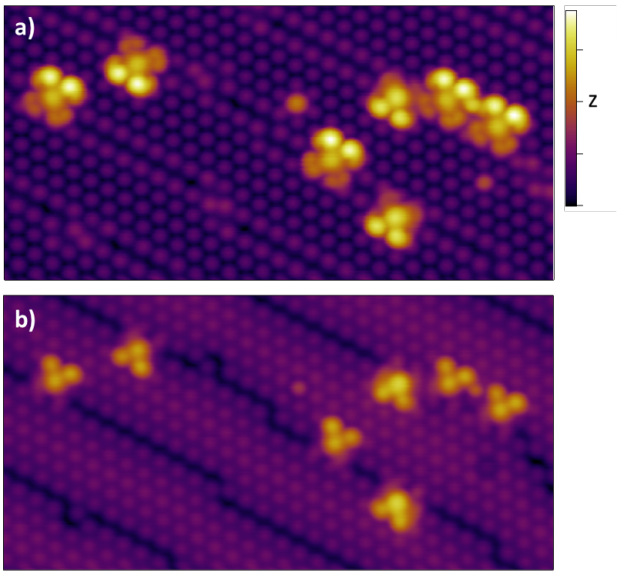

Figure 10.1: STM topographies of FePc molecules templated on silicene/ZrB_2. (a)The cross-shaped molecules can be seen to align along the linear domains of the silicene/ZrB_2 ($16.5\,\text{nm}\times8.3\,\text{nm}$, $I_0 = 0.5\,\text{nA}$, $V_0 = -1\,\text{V}$). (b) Same area as in (a), but at positive sample bias ($16.5\,\text{nm}\times8.3\,\text{nm}$, $I_0 = 0.5\,\text{nA}$, $V_0 = 1\,\text{V}$). The molecules are now observed to have a triangular profile.

gen passivation of the silicene/ZrB_2. Firstly hydrogen passivated free-standing silicene is predicted to have intriguing properties [57, 226], but secondly if selective desorption of H atoms could be achieved similarly to on the Si(100) surface [227, 228] this could provide a route to atomically precise doping on silicene/ZrB_2.

In addition to the modification of electronic and structural properties it has been a goal of this thesis to probe the magnetic properties of silicene/ZrB_2. To this end, Co atoms have been deposited on to the silicene/ZrB_2 surface at low temperature. It is shown that the structural properties of the silicene are robust to the Co deposition, but that there is significant hybridisation between two. An additional observation is that the Co atoms are bi-stable, switching between two configurations when a large bias voltage is applied. The low bias structure of the Co atoms, as observed by STM, is found to be due to an unusual spatially anisotropic Kondo effect that may result from higher angular momentum, p- or d-wave like, scattering. When Co atoms are in close proximity to one another they exhibit a substantial indirect exchange (RKKY) interaction. The magnitude of the exchange coupling indicates that the 2D surface states of silicene/ZrB_2 significantly contribute to the mediation of the interaction, which could allow for the construction of larger, more complex coupled magnetic structures. Furthermore, it is found that antiferromagnetically coupled Co dimers break parity symmetry in the two impurity anderson model, effectively parity filtering the singlet to triplet excitations. It is proposed that the silicene/ZrB_2 surface is key to the parity breaking. These results indicate that the combination of magnetic adsorbates with 2D materials can manifest potentially novel magnetic interactions, providing new pathways to probe highly correlated

physics.

Future work into the magnetic properties of adsorbates could focus around the deposition of other magnetic atoms, or molecules onto the surface. In other systems, such as Cu_2N a range of transition metal adatoms including, Co [42, 229], Mn [39, 40], and Fe [40] have been investigated. Owing to the different hybridisation and spin states of the atoms different magnetic phenomema are observed, for example, Kondo [42, 229] and inelastic spin excitations [40, 42, 229]. Furthermore, it will be of interest to investigate magnetic molecules on the surface of silicene/ZrB_2 as 2D materials have already proven useful as nanoscaled templates [230–238]. In fact other work the author has been involved in has investigated the templating of iron phthalocyanine (FePc) molecules on the silicene/ZrB_2 surface. **Figure 10.1** shows an STM image of FePc molecules on silicene/ZrB_2, where it can be seen that the molecules preferentially bind to the striped domain boundaries of the surface. The preferential binding could allow for precise templating of the molecules. No magnetic interactions were found for FePc when studied by STM, However, model DFT calculations suggest the FePc molecules are magnetic, therefore other techniques, such as X-ray magnetic circular dichroism (XMCD) may be able to probe these properties. Furthermore, other magnetic molecules may present magnetic phenomena in STM experiments.

Bibliography

[1] J. Bardeen, and W. Brattain, "Three-electrode circuit element utilizing semiconductive materials", pat. US25250305 (1948).

[2] J. Catwright, *Intel enters the third dimension*, (2011) `http://www.nature.com/news/2011/110506/full/news.2011.274.html` (visited on 09/22/2016).

[3] Intel, *Intel launches fastest processor on the planet*, (2008) `http://www.intel.com/pressroom/archive/releases/2008/20081117comp_sm.htm` (visited on 09/22/2016).

[4] A. K. Geim, and K. S. Novoselov, "The rise of graphene.", Nature materials **6**, 183–91 (2007).

[5] H. S. P. Wong, "Beyond the conventional transistor", Solid-State Electronics **49**, 755–762 (2005).

[6] K. S. Novoselov, A. K. Geim, S. V. Morozov, D. Jiang, Y. Zhang, S. V. Dubonos, I. V. Grigorieva, and A. A. Firsov, "Electric field effect in atomically thin carbon films.", Science (New York, N.Y.) **306**, 666–9 (2004).

[7] A. H. Castro Neto, N. M. R. Peres, K. S. Novoselov, and A. K. Geim, "The electronic properties of graphene", Reviews of Modern Physics **81**, 109–162 (2009).

[8] A. Splendiani, L. Sun, Y. Zhang, T. Li, J. Kim, C. Y. Chim, G. Galli, and F. Wang, "Emerging photoluminescence in monolayer MoS2", Nano Letters **10**, 1271–1275 (2010).

[9] B. Radisavljevic, A. Radenovic, J. Brivio, V. Giacometti, and A. Kis, "Single-layer MoS2 transistors", Nature nanotechnology **6**, 147–50 (2011).

[10] V. Tran, R. Soklaski, Y. Liang, and L. Yang, "Layer-controlled band gap and anisotropic excitons in few-layer black phosphorus", Physical Review B - Condensed Matter and Materials Physics **89**, 1–6 (2014).

[11] P. Vogt, P. De Padova, C. Quaresima, J. Avila, E. Frantzeskakis, M. C. Asensio, A. Resta, B. Ealet, and G. Le Lay, "Silicene: Compelling Experimental Evidence for Graphenelike Two-Dimensional Silicon", Physical Review Letters **108**, 155501 (2012).

[12]A. Fleurence, R. Friedlein, T. Ozaki, H. Kawai, Y. Wang, and Y. Yamada-Takamura, "Experimental Evidence for Epitaxial Silicene on Diboride Thin Films", Physical Review Letters **108**, 245501 (2012).

[13]S. A. Wolf, D. D. Awschalom, R. A. Buhrman, J. M. Daughton, S. von Molnar, M. L. Roukes, A. Y. Chtchelkanova, and D. M. Treger, "Spintronics: A Spin-Based Electroics Vision of the Future", Science **294** (2001).

[14]L. Meng, Y. Wang, L. Zhang, S. Du, R. Wu, L. Li, Y. Zhang, G. Li, H. Zhou, W. A. Hofer, and H.-J. Gao, "Buckled silicene formation on Ir(111).", Nano letters **13**, 685–90 (2013).

[15]T. Aizawa, S. Suehara, and S. Otani, "Silicene on Zirconium Carbide (111)", The Journal of Physical Chemistry C **118**, 23049–23057 (2014).

[16]T. Aizawa, S. Suehara, and S. Otani, "Phonon dispersion of silicene on ZrB2 (0001)", Journal of Physics: Condensed Matter **27**, 305002 (2015).

[17]F. Donati, Q. Dubout, G. Autès, F. Patthey, F. Calleja, P. Gambardella, O. V. Yazyev, and H. Brune, "Magnetic Moment and Anisotropy of Individual Co Atoms on Graphene", Physical Review Letters **111**, 236801 (2013).

[18]F. Donati, L. Gragnaniello, a. Cavallin, F. Natterer, Q. Dubout, M. Pivetta, F. Patthey, J. Dreiser, C. Piamonteze, S. Rusponi, and H. Brune, "Tailoring the Magnetism of Co Atoms on Graphene through Substrate Hybridization", Physical Review Letters **113**, 177201 (2014).

[19]J. Ren, H. Guo, J. Pan, Y. Y. Zhang, X. Wu, H.-g. Luo, S. Du, S. T. Pantelides, and H.-j. Gao, "Kondo Effect of Cobalt Adatoms on a Graphene Monolayer Controlled by Substrate-Induced Ripples", Nano letters **14**, 4011–1015 (2014).

[20]A. Hewson, *The kondo problem to heavy fermions* (Ccambridge University Ppress, 1993).

[21]W. Chen, T. Jamneala, V. Madhavan, and M. Crommie, "Disappearance of the Kondo resonance for atomically fabricated cobalt dimers", Physical Review B **60**, R8529–R8532 (1999).

[22]P. Wahl, P. Simon, L. Diekhöner, V. S. Stepanyuk, P. Bruno, M. A. Schneider, and K. Kern, "Exchange interaction between single magnetic adatoms", Physical Review Letters **98**, 98–101 (2007).

[23]D. Wegner, R. Yamachika, X. Zhang, Y. Wang, T. Baruah, M. R. Pederson, B. M. Bartlett, J. R. Long, and M. F. Crommie, "Tuning Molecule-Mediated Spin Coupling in Bottom-Up-Fabricated Vanadium-Tetracyanoethylene Nanostructures", Physical Review Letters **103**, 087205 (2009).

[24]L. Zhou, J. Wiebe, S. Lounis, E. Vedmedenko, F. Meier, S. Blügel, P. H. Dederichs, and R. Wiesendanger, "Strength and directionality of surface RudermanKittelKasuyaYosida interaction mapped on the atomic scale", Nature Physics **6**, 187–191 (2010).

[25]N. Tsukahara, S. Shiraki, S. Itou, N. Ohta, N. Takagi, and M. Kawai, "Evolution of kondo resonance from a single impurity molecule to the two-dimensional lattice", Physical Review Letters **106**, 1–4 (2011).

[26]A. A. Khajetoorians, J. Wiebe, B. Chilian, S. Lounis, S. Blügel, and R. Wiesendanger, "Atom-by-atom engineering and magnetometry of tailored nanomagnets", Nature Physics **8**, 497–503 (2012).

[27]H. Prüser, P. E. Dargel, M. Bouhassoune, R. G. Ulbrich, T. Pruschke, S. Lounis, and M. Wenderoth, "Interplay between the Kondo effect and the RudermanKittelKasuyaYosida interaction", Nature Communications **5**, 5417 (2014).

[28]A. F. Otte, M. Ternes, K. von Bergmann, S. Loth, H. Brune, C. P. Lutz, C. F. Hirjibehedin, and A. J. Heinrich, "The role of magnetic anisotropy in the Kondo effect", Nature Physics **4**, 847–850 (2008).

[29]A. Spinelli, M. Gerrits, R. Toskovic, B. Bryant, M. Ternes, and A. F. Otte, "Exploring the phase diagram of the two-impurity Kondo problem", Nature Communications **6**, 10046 (2015).

[30]G. Binnig, H. Rohrer, C. Gerber, and E. Weibel, "7 x 7 Reconstruction on Si(111) Resolved in Real Space", Physical Review Letters **50**, 120–123 (1983).

[31]A. D. Gottlieb, and L. Wesoloski, "Bardeen's tunnelling theory as applied to scanning tunnelling microscopy: a technical guide to the traditional interpretation", Nanotechnology **18**, R57 (2006).

[32]J. Tersoff, and D. R. Hamann, "Theory and Application for the Scanning Tunneling Microscope", Physical Review Letters **50**, 1998–2001 (1983).

[33]J. Tersoff, and D. R. Hamann, "Theory of the scanning tunneling microscope", Physical Review B **31**, 805–813 (1985).

[34]R. J. Hamers, "Atomic-resolution surfac spectroscopy with the scanning tunneling microscope", Annual Review of Physical Chemistry **40**, 531–559 (1989).

[35]H. Pruser, "Scanning tunneling spectroscopy of magnetic bulk impurities: from a single kondo atom towards a coupled system", PhD thesis (Gottingen, 2013).

[36]B. C. Stipe, "Single-Molecule Vibrational Spectroscopy and Microscopy", Science **280**, 1732–1735 (1998).

[37]W. Ho, "Single-molecule chemistry", J. Chem. Phys. **117**, 11033–11061 (2002).

[38]A. J. Heinrich, J. A. Gupta, C. P. Lutz, and D. M. Eigler, "Single-atom spin-flip spectroscopy", Science **306**, 466–469 (2004).

[39]C. F. Hirjibehedin, C. P. Lutz, and A. J. Heinrich, "Spin coupling in engineered atomic structures.", Science **312**, 1021–1024 (2006).

[40]C. F. Hirjibehedin, C.-Y. Lin, A. F. Otte, M. Ternes, C. P. Lutz, B. A. Jones, and A. J. Heinrich, "Large Magnetic Anisotropy of a Single Atomic Spin Embedded in a Surface Molecular Network", Science **317**, 1199–1203 (2007).

[41]N. Tsukahara, K.-i. Noto, M. Ohara, S. Shiraki, N. Takagi, S. Shin, and M. Kawai, "Adsorption-Induced Switching of Magnetic Anisotropy in a Single Iron(II) Phthalocyanine Molecule on an Oxidized Cu(110) Surface", Physical Review Letters **102**, 167203 (2009).

[42]T. Choi, C. D. Ruggiero, and J. a. Gupta, "Tunneling spectroscopy of ultrathin insulating Cu2N films, and single Co adatoms", Journal of Vacuum Science & Technology B: Microelectronics and Nanometer Structures **27**, 887 (2009).

[43]A. F. Otte, M. Ternes, S. Loth, C. P. Lutz, C. F. Hirjibehedin, and A. J. Heinrich, "Spin excitations of a kondo-screened atom coupled to a second magnetic atom", Physical Review Letters **103**, 1–4 (2009).

[44]A. A. Khajetoorians, B. Chilian, J. Wiebe, S. Schuwalow, F. Lechermann, and R. Wiesendanger, "Detecting excitation and magnetization of individual dopants in a semiconductor.", Nature **467**, 1084–7 (2010).

[45]A. A. Khajetoorians, S. Lounis, B. Chilian, A. T. Costa, L. Zhou, D. L. Mills, J. Wiebe, and R. Wiesendanger, "Itinerant nature of atom-magnetization excitation by tunneling electrons", Physical Review Letters **106**, 6–9 (2011).

[46]X. Chen, Y. S. Fu, S. H. Ji, T. Zhang, P. Cheng, X. C. Ma, X. L. Zou, W. H. Duan, J. F. Jia, and Q. K. Xue, "Probing superexchange interaction in molecular magnets by spin-flip spectroscopy and microscopy", Physical Review Letters **101**, 1–4 (2008).

[47]S. Li, A. Yu, F. Toledo, Z. Han, H. Wang, H. Y. He, R. Wu, and W. Ho, "Rotational and Vibrational Excitations of a Hydrogen Molecule Trapped within a Nanocavity of Tunable Dimension", Physical Review Letters **111**, 146102 (2013).

[48]F. D. Natterer, F. Patthey, and H. Brune, "Distinction of Nuclear Spin States with the Scanning Tunneling Microscope", Physical Review Letters **111**, 175303 (2013).

[49]J. Lambe, and R. C. Jaklevic, "Spectra by Inelastic Electron", Physical Review Letters **165**, 821–832 (1968).

[50]A. Kogan, S. Amasha, D. Goldhaber-Gordon, G. Granger, M. A. Kastner, and H. Shtrikman, "Measurements of kondo and spin splitting in single-electron transistors", Physical Review Letters **93**, 1–4 (2004).

[51]E. W. Hudson, "Atomic-Scale Quasi-Particle Scattering Resonances in Bi2Sr2CaCu2O8+", Science **285**, 88–91 (1999).

[52]K. Takeda, and K. Shiraishi, "Theoretical possibility of stage corrugation in Si and Ge analogs of graphite", Physical Review B **50**, 14916–14922 (1994).

[53]G. Guzmán-Verri, and L. Lew Yan Voon, "Electronic structure of silicon-based nanostructures", Physical Review B **76**, 075131 (2007).

[54]K. S. Novoselov, A. K. Geim, S. V. Morozov, D Jiang, M. I. Katsnelson, I. V. Grigorieva, S. V. Dubonos, and A. A. Firsov, "Two-dimensional gas of massless Dirac fermions in graphene", Nature **438**, 197–200 (2005).

[55]S. Cahangirov, M. Topsakal, E. Aktürk, H. Sahin, and S. Ciraci, "Two- and One-Dimensional Honeycomb Structures of Silicon and Germanium", Physical Review Letters **102**, 236804 (2009).

[56]T. Suzuki, and Y. Yokomizo, "Energy bands of atomic monolayers of various materials: Possibility of energy gap engineering", Physica E: Low-Dimensional Systems and Nanostructures **42**, 2820–2825 (2010).

[57]M. Houssa, E. Scalise, K. Sankaran, G. Pourtois, V. V. Afanas'ev, and A. Stesmans, "Electronic properties of hydrogenated silicene and germanene", Applied Physics Letters **98**, 223107 (2011).

[58]M. Ezawa, "Valley-Polarized Metals and Quantum Anomalous Hall Effect in Silicene", Physical Review Letters **109**, 055502 (2012).

[59]C.-C. Liu, W. Feng, and Y. Yao, "Quantum Spin Hall Effect in Silicene and Two-Dimensional Germanium", Physical Review Letters **107**, 076802 (2011).

[60]C.-C. Liu, H. Jiang, and Y. Yao, "Low-energy effective Hamiltonian involving spin-orbit coupling in silicene and two-dimensional germanium and tin", Physical Review B **84**, 195430 (2011).

[61]M. Ezawa, "Topological phase transition and electrically tunable diamagnetism in silicene", The European Physical Journal B **85**, 363 (2012).

[62]M. Ezawa, "Spin-valley optical selection rule and strong circular dichroism in silicene", Physical Review B **86**, 161407 (2012).

[63]M. Ezawa, "A topological insulator and helical zero mode in silicene under an inhomogeneous electric field", New Journal of Physics **14**, 033003 (2012).

[64]M. Ezawa, "Quasi-Topological Insulator and Trigonal Warping in Gated Bilayer Silicene", Journal of the Physical Society of Japan **81**, 104713 (2012).

[65]M. Ezawa, "High spin-chern insulators with magnetic order.", Scientific reports **3**, 3435 (2013).

[66]M. Ezawa, "Photoinduced Topological Phase Transition and a Single Dirac-Cone State in Silicene", Physical Review Letters **110**, 026603 (2013).

[67]M. Ezawa, "Quantized conductance and field-effect topological quantum transistor in silicene nanoribbons", Applied Physics Letters **102**, 172103 (2013).

[68]B. Lalmi, H. Oughaddou, H. Enriquez, A. Kara, S. Vizzini, B. Ealet, and B. Aufray, "Epitaxial growth of a silicene sheet", Applied Physics Letters **97**, 223109 (2010).

[69]H Jamgotchian, Y. Colignon, N. Hamzaoui, B. Ealet, J. Y. Hoarau, B. Aufray, and J. P. Bibérian, "Growth of silicene layers on Ag(111): unexpected effect of the substrate temperature.", Journal of physics. Condensed matter : an Institute of Physics journal **24**, 172001 (2012).

[70]L. Chen, C.-C. Liu, B. Feng, X. He, P. Cheng, Z. Ding, S. Meng, Y. Yao, and K. Wu, "Evidence for Dirac Fermions in a Honeycomb Lattice Based on Silicon", Physical Review Letters **109**, 056804 (2012).

[71]L. Chen, H. Li, B. Feng, Z. Ding, J. Qiu, P. Cheng, K. Wu, and S. Meng, "Spontaneous Symmetry Breaking and Dynamic Phase Transition in Monolayer Silicene", Physical Review Letters **110**, 085504 (2013).

[72]C.-L. Lin, R. Arafune, K. Kawahara, N. Tsukahara, E. Minamitani, Y. Kim, N. Takagi, and M. Kawai, "Structure of Silicene Grown on Ag(111)", Applied Physics Express **5**, 045802 (2012).

[73]G. Le Lay, P. De Padova, A. Resta, T. Bruhn, and P. Vogt, "Epitaxial silicene: can it be strongly strained?", Journal of Physics D: Applied Physics **45**, 392001 (2012).

[74]J. Avila, P. D. Padova, S. Cho, I. Colambo, S. Lorcy, C. Quaresima, P. Vogt, A. Resta, G. L. Lay, M. C. Asensio, P De Padova, S. Cho, I. Colambo, S. Lorcy, C. Quaresima, P. Vogt, A. Resta, G Le Lay, and M. C. Asensio, "Presence of gapped silicene-derived band in the prototypical (3 x 3) silicene phase on silver (111) surfaces.", en, Journal of physics. Condensed matter : an Institute of Physics journal **25**, 262001 (2013).

[75]R. Arafune, C.-L. Lin, K. Kawahara, N. Tsukahara, E. Minamitani, Y. Kim, N. Takagi, and M. Kawai, "Structural transition of silicene on Ag(111)", Surface Science **608**, 297–300 (2013).

[76]K. R. Knox, S. Wang, A. Morgante, D. Cvetko, A. Locatelli, T. O. Mentes, M. A. Niño, P. Kim, and R. M. Osgood, "Spectromicroscopy of single and multilayer graphene supported by a weakly interacting substrate", Physical Review B **78**, 201408 (2008).

[77]X. Zhang, X. Luo, J. Han, J. Li, and W. Han, "Electronic structure, elasticity and hardness of diborides of zirconium and hafnium: First principles calculations", Computational Materials Science **44**, 411–421 (2008).

[78]L. Zhao, R. He, K. T. Rim, T. Schiros, K. S. Kim, H. Zhou, C. Gutiérrez, S. P. Chockalingam, C. J. Arguello, L. Pálová, D. Nordlund, M. S. Hybertsen, D. R. Reichman, T. F. Heinz, P. Kim, A. Pinczuk, G. W. Flynn, and A. N. Pasupathy, "Visualizing individual nitrogen dopants in monolayer graphene.", Science (New York, N.Y.) **333**, 999–1003 (2011).

[79]S. Bera, Y. Sumiyoshi, and Y. Yamada-Takamura, "Growth of single-crystalline zirconium diboride thin film on sapphire", Journal of Applied Physics **106**, 063531 (2009).

[80]Y. Yamada-Takamura, F. Bussolotti, A. Fleurence, S. Bera, and R. Friedlein, "Surface electronic structure of ZrB$_{2}$ buffer layers for GaN growth on Si wafers", Applied Physics Letters **97**, 073109 (2010).

[81]R. Friedlein, A. Fleurence, K. Aoyagi, M. P. de Jong, H. Van Bui, F. B. Wiggers, S. Yoshimoto, T. Koitaya, S. Shimizu, H. Noritake, K. Mukai, J. Yoshinobu, and Y. Yamada-Takamura, "Core level excitations–a fingerprint of structural and electronic properties of epitaxial silicene.", The Journal of chemical physics **140**, 184704 (2014).

[82]C.-C. Lee, A. Fleurence, R. Friedlein, Y. Yamada-Takamura, and T. Ozaki, "First-principles study on competing phases of silicene: Effect of substrate and strain", Physical Review B **88**, 165404 (2013).

[83]C.-C. Lee, A. Fleurence, R. Friedlein, Y. Yamada-Takamura, and T. Ozaki, "Avoiding critical-point phonon instabilities in two-dimensional materials: The origin of the stripe formation in epitaxial silicene", Physical Review B **90**, 241402 (2014).

[84]C.-C. Lee, A. Fleurence, Y. Yamada-Takamura, T. Ozaki, and R. Friedlein, "Band structure of silicene on zirconium diboride (0001) thin-film surface: Convergence of experiment and calculations in the one-Si-atom Brillouin zone", Physical Review B **90**, 075422 (2014).

[85]S. Kumashiro, H. Tanaka, Y. Kawamata, H. Yanagisawa, K. Momose, G. Nakamura, C. Oshima, and S. Otani, "Electronic States of NbB2(0001), TaB2(0001) and ZrB2(0001) Surfaces Studied by Angle-resolved Ultraviolet Photoelectron Spectroscopy", e-Journal of Surface Science and Nanotechnology **4**, 100–104 (2006).

[86]C. H. Schwalb, S. Sachs, M. Marks, A. Schöll, F. Reinert, E. Umbach, and U. Höfer, "Electron lifetime in a Shockley-type metal-organic interface state", Physical Review Letters **101**, 1–4 (2008).

[87]K. F. Mak, C. Lee, J. Hone, J. Shan, and T. F. Heinz, "Atomically thin MoS2: A new direct-gap semiconductor", Physical Review Letters **105**, 136805 (2010).

[88]H. Fu, J. Zhang, Z. Ding, H. Li, and S. Meng, "Stacking-dependent electronic structure of bilayer silicene", Applied Physics Letters **104**, 131904 (2014).

[89]P. Pflugradt, L. Matthes, and F. Bechstedt, "Unexpected symmetry and AA stacking of bilayer silicene on Ag(111)", Physical Review B **89**, 205428 (2014).

[90]J. Liu, and W. Zhang, "Bilayer silicene with an electrically-tunable wide band gap", RSC Advances **3**, 21943 (2013).

[91]F. Liu, C.-C. Liu, K. Wu, F. Yang, and Y. Yao, "d+id' Chiral Superconductivity in Bilayer Silicene", Physical Review Letters **111**, 066804 (2013).

[92]P. De Padova, P. Vogt, A. Resta, A. J., I. Razado-Colambo, C. Quaesima, C. Ottaviani, B. Olivieri, T. Bruhn, T. Hirahara, S. Shirai, T. Hasegawa, M. Carmen Asensio, and G. Le Lay, "Evidence for Dirac fermions on multilayer silicene", Appl. Phys. Lett. **102** (2013).

[93]B. Feng, Z. Ding, S. Meng, Y. Yao, X. He, P. Cheng, L. Chen, and K. Wu, "Evidence of silicene in honeycomb structures of silicon on Ag(111).", Nano letters **12**, 3507–11 (2012).

[94]P. De Padova, J. Avila, A. Resta, I. Razado-Colambo, C. Quaresima, C. Ottaviani, B. Olivieri, T. Bruhn, P. Vogt, M. C. Asensio, and G. Le Lay, "The quasiparticle band dispersion in epitaxial multilayer silicene.", Journal of physics. Condensed matter : an Institute of Physics journal **25**, 382202 (2013).

[95]P. Vogt, P. Capiod, M. Berthe, A. Resta, P. De Padova, T. Bruhn, G. Le Lay, and B. Grandidier, "Synthesis and electrical conductivity of multilayer silicene", Applied Physics Letters **104**, 021602 (2014).

[96]A. J. Mannix, B. Kiraly, B. L. Fisher, M. C. Heram, and N. P. Guisinger, "Silicon Growth at the Two-Dimensional Limit on Ag(111)", ACS nano **8**, 7538–7547 (2014).

[97]T. Shirai, T. Shirasawa, T. Hirahara, N. Fukui, T. Takahashi, and S. Hasegawa, "Structure determination of multilayer silicene grown on Ag(111) films by electron diffraction: Evidence for Ag segregation at the surface", Physical Review B **89**, 241403 (2014).

[98]P. Atkins, and R. Friedman, *Molecular quantum mechanics* (Oxford University Press, 2011).

[99]D. Gatteschi, R. Sessoli, and J. Villain, *Molecular nanomagnets* (Oxford University Press, 2006).

[100]B. Lengeler, W. Schilling, and H. Wenzl, "Deviations from Matthiessen's rule and longitudinal magnetoresistance in cold-worked and neutron-irradiated copper", Journal of Low Temperature Physics **2**, 237–254 (1970).

[101]J. M. Ziman, *Principles of the theory of solids* (Cambridge University Press, 1972).

[102]T. L. Hill, *Introduction to statistical thermodynamics* (Dover Publications, 1986).

[103]W. De Haas, and G. Van Den Berg, "The electrical resistance of gold and silver at low temperatures", Physica **3**, 440–449 (1936).

[104]J. Kondo, "Effect of ordinary scattering on exchange scattering from magnetic impurity in metals", Physical Review **169**, 437–440 (1968).

[105]E. K. U. Gross, E. Runge, and O. Heinonen, *Many-particle theory* (Adam Hilger, 1991).

[106]J. R. Schrieffer, and P. A. Wolff, "Relation between the Anderson and Kondo Hamiltonians", Physical Review **149**, 491–492 (1966).

[107]F. D. M. Haldane, "Scaling Theory of the Asymmetric Anderson Model", Phys. Rev. Lett. **40**, 416–419 (1978).

[108]L. Kouwenhoven, and L. Glazman, "Revival of the Kondo effect", Physics World **14**, 33–38 (2001).

[109]K. G. Wilson, "The renormalization group: Critical phenomena and the Kondo problem", Reviews of Modern Physics **47**, 773–840 (1975).

[110]R. Bulla, T. a. Costi, and T. Pruschke, "Numerical renormalization group method for quantum impurity systems", Reviews of Modern Physics **80**, 395–450 (2008).

[111]T. Pruschke, and N. Grewe, "The Anderson model with finite Coulomb repulsion", Zeitschrift fur Physik B Condensed Matter **74**, 439–449 (1989).

[112]R. N. Silver, J. E. Gubernatis, D. S. Sivia, and M. Jarrell, "Spectral densities of the symmetric Anderson model", Physical Review Letters **65**, 496–499 (1990).

[113]D. Goldhaber-Gordon, J. Göres, M. Kastner, H. Shtrikman, D. Mahalu, and U. Meirav, "From the Kondo Regime to the Mixed-Valence Regime in a Single-Electron Transistor", Physical Review Letters **81**, 5225–5228 (1998).

[114]S. M. Cronenwett, T. H. Oosterkamp, and L. Kouwenhoven, "A Tunable Kondo Effect in Quantum Dots", Science **281**, 540–544 (1998).

[115]V. Madhavan, "Tunneling into a Single Magnetic Atom: Spectroscopic Evidence of the Kondo Resonance", Science **280**, 567–569 (1998).

[116]M. A. Schneider, L. Vitali, N. Knorr, and K. Kern, "Observing the scattering phase shift of isolated Kondo impurities at surfaces", Physical Review B **65**, 121406 (2002).

[117]U. Fano, "Effects of configuration interaction on intensities and phase shifts", Physical Review **124**, 1866–1878 (1961).

[118]O. Ujaghy, J. Kroha, L. Szunyogh, A Zawadowski, O. Js-Ghy, J. Kroha, L. Szunyogh, and A. Zawadowski, "Theory of the Fano Resonance in the STM Tunneling Density of States due to a Single Kondo Impurity", Physical Review Letters **85**, 2557 (2000).

[119]M. Ternes, "Scanning tunneling spectroscopy at the single atom scale", PhD thesis (Ecole Polytechnique Federale de Lausanne, 2006).

[120]K. Nagaoka, T. Jamneala, M. Grobis, and M. Crommie, "Temperature Dependence of a Single Kondo Impurity", Physical Review Letters **88**, 077205 (2002).

[121]M. A. Ruderman, and C. Kittel, "Indirect exchange coupling of nuclear magnetic moments by conduction electrons", Physical Review **96**, 99–102 (1954).

[122]T. Kasuya, "A Theory of Metallic Ferro- and Antiferromagnetism on Zener's Model", Progress of Theoretical Physics **16**, 45–57 (1956).

[123]K. Yosida, "Magnetic Properties of Cu-Mn Alloys", Physical Review **106**, 893–898 (1957).

[124]B. Warner, T. G. Gill, V. Caciuc, N. Atodiresei, A. Fleurence, Y. Yoshida, Y. Hasegawa, S. Blügel, Y. Yamada-Takamura, and C. F. Hirjibehedin, "Templating of electronically decoupled molecules using domain boundaries of the 2D material silicene on ZrB_2", In preparation for submission to Nature Communications (2016).

[125]L. Tao, E. Cinquanta, D. Chiappe, C. Grazianetti, M. Fanciulli, M. Dubey, A. Molle, and D. Akinwande, "Silicene field-effect transistors operating at room temperature", Nature Nanotechnology **10**, 227–231 (2015).

[126]A. Fleurence, T. G. Gill, R. Friedlein, J. T. Sadowski, K. Aoyagi, M. Copel, R. M. Tromp, C. F. Hirjibehedin, and Y. Yamada-Takamura, "Single-domain epitaxial silicene on diboride thin films", Applied Physics Letters **108**, 151902 (2016).

[127]R. Doering, and Y. Nishi, *Semiconductor manufacturing technology* (CRC Press, Taylor and Francis Group, 2008).

[128]M. Tahir, and U. Schwingenschlogl, "Magnetocapacitance of an electrically tunable silicene device", Applied Physics Letters **101**, 132412 (2012).

[129]N. D. Drummond, V. Zólyomi, and V. I. Fal'ko, "Electrically tunable band gap in silicene", Physical Review B **85**, 075423 (2012).

[130]Z. Ni, Q. Liu, K. Tang, J. Zheng, J. Zhou, R. Qin, Z. Gao, D. Yu, and J. Lu, "Tunable bandgap in silicene and germanene.", Nano letters **12**, 113–8 (2012).

[131]M Tahir, and U Schwingenschlögl, "Valley polarized quantum Hall effect and topological insulator phase transitions in silicene.", Scientific reports **3**, 1075 (2013).

[132]C. Berger, Z. Song, X. Li, X. Wu, N. Brown, C. Naud, D. Mayou, T. Li, J. Hass, A. N. Marchenkov, E. H. Conrad, P. N. First, and W. A. de Heer, "Electronic confinement and coherence in patterned epitaxial graphene.", Science (New York, N.Y.) **312**, 1191–1196 (2006).

[133]W. A. de Heer, C. Berger, X. Wu, P. N. First, E. H. Conrad, X. Li, T. Li, M. Sprinkle, J. Hass, M. L. Sadowski, M. Potemski, and G. Martinez, "Epitaxial graphene", Solid State Communications **143**, 92–100 (2007).

[134]S. Y. Zhou, G. H Gweon, A. V. Fedorov, P. N. First, W. A. de Heer, D. H. Lee, F. Guinea, A. H. Castro Neto, and A. Lanzara, "Substrate-induced bandgap opening in epitaxial graphene.", Nature materials **6**, 770–775 (2007).

[135]F. Varchon, R. Feng, J. Hass, X. Li, B. Nguyen, C. Naud, P. Mallet, J.-Y. Veuillen, C. Berger, E. Conrad, and L. Magaud, "Electronic Structure of Epitaxial Graphene Layers on SiC: Effect of the Substrate", Physical Review Letters **99**, 126805 (2007).

[136]I. Luk'yanchuk, and Y. Kopelevich, "Phase Analysis of Quantum Oscillations in Graphite", Physical Review Letters **93**, 166402 (2004).

[137]N. Gao, J. Li, and Q. Jiang, "Bandgap opening in silicene: Effect of substrates", Chemical Physics Letters **592**, 222–226 (2014).

[138]T. Ohta, A. Bostwick, T. Seyller, K. Horn, and E. Rotenberg, "Controlling the electronic structure of bilayer graphene.", Science (New York, N.Y.) **313**, 951–4 (2006).

[139]T. Ohta, A. Bostwick, J. McChesney, T. Seyller, K. Horn, and E. Rotenberg, "Interlayer Interaction and Electronic Screening in Multilayer Graphene Investigated with Angle-Resolved Photoemission Spectroscopy", Physical Review Letters **98**, 206802 (2007).

[140]X. Zhang, X. Luo, J. Li, J. Han, W. Han, and C. Hong, "Structure and bonding features of ZrB2(0001) surface", Computational Materials Science **46**, 1–6 (2009).

[141]R. Roucka, Y. An, A. V. G. Chizmeshya, J. Tolle, J. Kouvetakis, V. R. D'Costa, J. Menendez, and P. Crozier, "Epitaxial semimetallic Hf xZr 1-xB 2 templates for optoelectronic integration on silicon", Applied Physics Letters **89**, 242110 (2006).

[142]A. Fleurence, and Y. Yamada-Takamura, "Scanning tunneling microscopy investigations of the epitaxial growth of ZrB2 on Si(111)", Physica Status Solidi (C) **8**, 779–783 (2011).

[143]S Naji, B Khalil, H Labrim, M Bhihi, A Belhaj, A Benyoussef, M Lakhal, and A El Kenz, "Interdistance Effects on Flat and Buckled Silicene Like-bilayers", Journal of Physics: Conference Series **491**, 012006 (2014).

[144]K. Oura, V. G. Lifshits, A. Saranin, A. V. zotov, and M. Katayama, *Surface science: an introduction* (Springer-Verlag Berlin Heidelberg, 2003).

[145]Y. Lee, K.-H. Yun, S. B. Cho, and Y.-C. Chung, "Electronic properties of transition-metal-decorated silicene.", Chemphyschem : a European journal of chemical physics and physical chemistry **15**, 4095–9 (2014).

[146]H. N. Waltenburg, and J. T. Yates, "Surface Chemistry of Silicon", Chemical reviews **95**, 1589–1673 (1995).

[147]P. Y. Yu, and M. Cardona, *Fundamentals of Semiconductors: Physics and Material Properties*, 3rd Editio (Springer Berlin Heidelberg New York, 2005), p. 159.

[148]M. D. McCluskey, and E. E. Haller, *Dopants and Defects in Semiconductors* (CRC Press, Taylor & Francis Group, 2012).

[149]A. Puzder, A. J. Williamson, J. C. Grossman, and G. Galli, "Surface chemistry of silicon nanoclusters.", Physical review letters **88**, 097401 (2002).

[150]A. Cullis, L. Canham, and D. Calcott, "The structural and luminescence properties of porous silicon", Journal of Applied Physics **82**, 909–965 (1997).

[151]R. Rurali, "Colloquium: Structural, electronic, and transport properties of silicon nanowires", Reviews of Modern Physics **82**, 427–449 (2010).

[152]R. H. Wentorf, and J. S. Kasper, "Two New Forms of Silicon", Science (New York, N.Y.) **139**, 338 (1963).

[153]M. T. Yin, and M. Cohen, "Theory of static structural properties, crystal stability, and phase transformations: Application to Si and Ge", Physical Review B **26**, 5668–5687 (1982).

[154]S. Sorella, M. Casula, L. Spanu, and A. D. Corso, "Ab initio calculations for the β -tin diamond transition in silicon : Comparing theories with experiments", Physical Review B **075119**, 1–12 (2011).

[155]M. Pratzer, H. J. Elmers, M. Bode, O. Pietzsch, A. Kubetzka, and R. Wiesendanger, "Atomic-Scale Magnetic Domain Walls in Quasi-One-Dimensional Fe Nanostripes", Physical Review Letters **87**, 127201 (2001).

[156]P. Ferriani, K. Von Bergmann, E. Y. Vedmedenko, S. Heinze, M. Bode, M. Heide, G. Bihlmayer, S. Blügel, and R. Wiesendanger, "Atomic-scale Spin spiral with a unique rotational sense: Mn monolayer on W(001)", Physical Review Letters **101**, 1–4 (2008).

[157]S. Heinze, K. von Bergmann, M. Menzel, J. Brede, A. Kubetzka, R. Wiesendanger, G. Bihlmayer, and S. Blügel, "Spontaneous atomic-scale magnetic skyrmion lattice in two dimensions", Nature Physics **7**, 713–718 (2011).

[158]N. Romming, C. Hanneken, M. Menzel, L. E. Bickel, B. Wolter, K. von Bergmann, Kubetzka, André, and R. Wiesendanger, "Writing and Deleting Single Magnetic Skyrmions", Science **341**, 636–639 (2013).

[159]J. Li, W.-D. Schneider, R. Berndt, and B. Delley, "Kondo Scattering Observed at a Single Magnetic Impurity", Physical Review Letters **80**, 2893–2896 (1998).

[160]N. Y. Dzade, K. O. Obodo, S. K. Adjokatse, A. C. Ashu, E. Amankwah, C. D. Atiso, A. a. Bello, E. Igumbor, S. B. Nzabarinda, J. T. Obodo, A. O. Ogbuu, O. E. Femi, J. O. Udeigwe, and U. V. Waghmare, "Silicene and transition metal based materials: prediction of a two-dimensional piezomagnet.", Journal of physics. Condensed matter : an Institute of Physics journal **22**, 375502 (2010).

[161]X. Lin, and J. Ni, "Much stronger binding of metal adatoms to silicene than to graphene: A first-principles study", Physical Review B **86**, 075440 (2012).

[162]M. Lan, G. Xiang, C. Zhang, and X. Zhang, "Vacancy dependent structural, electronic, and magnetic properties of zigzag silicene nanoribbons:Co", Journal of Applied Physics **114** (2013) 10.1063/1.4828482.

[163]X. Sun, L. Wang, H. Lin, T. Hou, and Y. Li, "Induce magnetism into silicene by embedding transition-metal atoms", Applied Physics Letters **106**, 222401 (2015).

[164]T. P. Kaloni, N. Singh, and U. Schwingenschlögl, "Prediction of a quantum anomalous Hall state in Co-decorated silicene", Physical Review B **89**, 035409 (2014).

[165]J. Zhang, B. Zhao, and Z. Yang, "Abundant topological states in silicene with transition metal adatoms", Physical Review B **88**, 165422 (2013).

[166]P. Hohenberg, and W. Kohn, "Inhomogeneous electron gas", Physical Review B **136**, 864–871 (1964).

[167]P. E. Blöchl, "Projector augmented-wave method", Physical Review B **50**, 17953–17979 (1994).

[168]J. P. Perdew, K. Burke, and M. Ernzerhof, "Generalized Gradient Approximation Made Simple", Physical Review Letters **77**, 3865–3868 (1996).

[169]G. Kresse, and J. Hafner, "Ab initio molecular-dynamics simulation of the liquid-metalamorphous-semiconductor transition in germanium", Physical Review B **49**, 14251–14269 (1994).

[170]G. Kresse, and J. Furthmüller, "Efficient iterative schemes for ab initio total-energy calculations using a plane-wave basis set", Physical Review B **54**, 11169–11186 (1996).

[171]M. F. Crommie, C. P. Lutz, and D. M. Eigler, "Spectroscopy of a single adsorbed atom", Physical Review B **48**, 2851–2854 (1993).

[172]a. Davies, J. Stroscio, D. Pierce, and R. Celotta, "Atomic-Scale Observations of Alloying at the Cr-Fe(001) Interface", Physical Review Letters **76**, 4175–4178 (1996).

[173]R Wiesendanger, M Bode, M Kleiber, M Lohndorf, R Pascal, A Wadas, and D Weiss, "Magnetic nanostructures studied by scanning probe microscopy and spectroscopy", Journal of Vacuum Science & Technology B **15**, 1330–1334 (1997).

[174]D. Kitchen, A. Richardella, J.-M. Tang, M. E. Flatté, and A. Yazdani, "Atom-by-atom substitution of Mn in GaAs and visualization of their hole-mediated interactions", Nature **442**, 436–439 (2006).

[175]A. Richardella, D. Kitchen, and A. Yazdani, "Mapping the wave function of transition metal acceptor states in the GaAs surface", Physical Review B - Condensed Matter and Materials Physics **80**, 1–6 (2009).

[176]M. Bozkurt, M. R. Mahani, P. Studer, J.-M. Tang, S. R. Schofield, N. J. Curson, M. E. Flatté, a. Y. Silov, C. F. Hirjibehedin, C. M. Canali, and P. M. Koenraad, "Magnetic anisotropy of single Mn acceptors in GaAs in an external magnetic field", Physical Review B **88**, 205203 (2013).

[177]E. Minamitani, Y. S. Fu, Q. K. Xue, Y. Kim, and S. Watanabe, "Spatially extended underscreened Kondo state from collective molecular spin", Physical Review B - Condensed Matter and Materials Physics **92**, 1–5 (2015).

[178]H. S. Reehal, and P. T. Andrews, "An ultraviolet photoelectron spectroscopy study of some solid solutions of 3d transition metals in gold and silver", J. Phys. F: Met. Phys. **10**, 1631–1644 (1980).

[179]H. Höchst, P. Steiner, and S. Hüfner, "II. XPS Study of 3d-Metal Ions Dissolved in Noble Metals", Z. Phys. B: Condens. Matter **38**, 201 (1980).

[180]F. U. Hillebrecht, J. C. Fuggle, G. A. Sawatzky, and R. Zeller, "Split-off narrow d-band states above EF in transition-metal alloys", Physical Review Letters **51**, 1187–1190 (1983).

[181]W. Folkerts, D. van der Marel, C. Haas, G. A. Sawatzky, D. Norman, H. Padmore, H. Wright, and P. Weightman, "The use of Cooper minima effects and resonant photoemission in the study of the electronic structure of dilute alloys", J. Phys. F: Met. Phys. **17**, 657 (1987).

[182]T. Jamneala, V. Madhavan, W. Chen, and M. Crommie, "Scanning tunneling spectroscopy of transition-metal impurities at the surface of gold", Physical Review B **61**, 9990–9993 (2000).

[183]M. Etzkorn, C. F. Hirjibehedin, A. Lehnert, S. Ouazi, S. Rusponi, S. Stepanow, P. Gambardella, C. Tieg, P. Thakur, A. I. Lichtenstein, A. B. Shick, S. Loth, A. J. Heinrich, and H. Brune, "Comparing XMCD and DFT with STM spin excitation spectroscopy for Fe and Co adatoms on Cu2 N/Cu(100)", Physical Review B - Condensed Matter and Materials Physics **92**, 1–9 (2015).

[184]J. Repp, G. Meyer, F. E. Olsson, and M. Persson, "Controlling the charge state of individual gold adatoms.", Science (New York, N.Y.) **305**, 493–495 (2004).

[185]M. A. Schneider, L. Vitali, P. Wahl, N. Knorr, L. Diekhner, G. Wittich, M. Vogelgesang, K. Kern, L. Diekhöner, G. Wittich, M. Vogelgesang, and K. Kern, "Kondo state of Co impurities at noble metal surfaces", Applied Physics A **80**, 937–941 (2005).

[186]M. J. Romero, J. Van De Lagemaat, G. Rumbles, and M. M. Al-Jassim, "Plasmon excitations in scanning tunneling microscopy: Simultaneous imaging of modes with different localizations coupled at the tip", Applied Physics Letters **90**, 1–4 (2007).

[187]Y.-h. Zhang, S. Kahle, T. Herden, C. Stroh, M. Mayor, U. Schlickum, M. Ternes, P. Wahl, and K. Kern, "Temperature and magnetic field dependence of a Kondo system in the weak coupling regime", Nature Communications **4**, 1–6 (2013).

[188]P. Wahl, L. Diekhöner, G. Wittich, L. Vitali, M. A. Schneider, and K. Kern, "Kondo effect of molecular complexes at surfaces: Ligand control of the local Spin coupling", Physical Review Letters **95**, 166601 (2005).

[189]H. Ihara, M. Hirabayashi, and H. Nakagawa, "Band Structure and X-ray Photoelectron Spectrum of ZrB2", Physical Review B **16**, 726–730 (1977).

[190]H. Rosner, J. M. An, W. E. Pickett, and S. L. Drechsler, "Fermi Surfaces of Diborides: MgB2 and ZrB2", 7 (2002).

[191]R. Kumar, M. Mishra, B. Sharma, V. Sharma, J. Lowther, V. Vyas, and G. Sharma, "Electronic structure and elastic properties of TiB2 and ZrB2", Computational Materials Science **61**, 150–157 (2012).

[192]S. Sichkar, V. Antonov, and V. Antropov, "Comparative study of the electronic structure, phonon spectra, and electron-phonon interaction of ZrB2 and TiB2", Physical Review B **87**, 064305 (2013).

[193]T. Aizawa, S. Suehara, S. Hishita, S. Otani, and M. Arai, "Surface core-level shift and electronic structure on transition-metal diboride (0001) surfaces", Physical Review B **71**, 165405 (2005).

[194]C.-C. Lee, Y. Yamada-Takamura, and T. Ozaki, "Unfolding method for first-principles LCAO electronic structure calculations", Journal of Physics: Condensed Matter **25**, 345501 (2013).

[195]J. W. Rhim, and J. H. Han, "Emergent p-Wave Kondo Coupling in Multi-Orbital Bands with Mirror Symmetry Breaking", Journal of the Physical Society of Japan **82**, 104704 (2013).

[196]S. A. Jafari, and T Tohyama, "Kondo resonance from p-wave hybridization in graphene", Journal of Physics: Condensed Matter **26**, 415601 (2014).

[197]A Wachowiak, R Yamachika, K. H. Khoo, Y Wang, M Grobis, D.-H. Lee, S. G. Louie, and M. F. Crommie, "Visualization of the molecular Jahn-Teller effect in an insulating K$_4$C$_{60}$ monolayer ", Science **310**, 468–470 (2005).

[198]R. Wesche, *Physical properties of high-temperature superconductors* (Wiley, 2015).

[199]F. Steglich, "From Kondo impurities to heavy-fermion superconductivity and quantum critical points", Physica B: Condensed Matter **378-380**, 7–12 (2006).

[200]Q. Si, and F. Steglich, "Heavy Fermions and Quantum Phase Transitions", Science **329**, 1161–1166 (2010).

[201]P. Lacroix, F. Mila, and P. Mendels, *Introduction to frustrated magnetism: materials, experiments, theory* (Springer, Berlin, 2011).

[202]C. Jayaprakash, H. R. Krishna-Murthy, and J. W. Wilkins, "Two-Impurity Kondo Problem", Physical Review Letters **47**, 737–740 (1981).

[203]B. A. Jones, and C. M. Varma, "Study of two magnetic impurities in a Fermi gas", Physical Review Letters **58**, 843–846 (1987).

[204]B. A. Jones, C. M. Varma, and J. W. Wilkins, "Low-Temperature Properties of the Two-Impurity Kondo Hamiltonian", **61**, 125–128 (1988).

[205]J. Silva, W. Lima, W. Oliveira, J. Mello, L. Oliveira, and J. Wilkins, "Particle-Hole Asymmetry in the Two-Impurity Kondo Model", Physical Review Letters **76**, 275–278 (1996).

[206]O. Sakai, Y. Shimizu, and T. Kasuya, "Excitation Spactra of Two Impurity Anderson Model", Solid State Communications **75**, 81 (1990).

[207]M. Vojta, R. Bulla, and W. Hofstetter, "Quantum phase transitions in models of coupled magnetic impurities", Physical Review B **65**, 140405 (2002).

[208]O. Sakai, Y. Shimizu, and N. Kaneko, "Excitation spectra of two-impurity and multi-channel Kondo systems by the numerical renormalization group method", Physica B: Condensed Matter **186-188**, 323–327 (1993).

[209]S. Nishimoto, T. Pruschke, and R. M. Noack, "Spectral density of the two-impurity Anderson model", **981** 10.1088/0953-8984/18/3/015.

[210]D. F. Mross, and H. Johannesson, "Two-impurity Kondo model with spin-orbit interactions", Physical Review B **80**, 155302 (2009).

[211]M. Lee, M. S. Choi, R. López, R. Aguado, J. Martinek, and R. Žitko, "Two-impurity Anderson model revisited: Competition between Kondo effect and reservoir-mediated superexchange in double quantum dots", Physical Review B - Condensed Matter and Materials Physics **81**, 6–9 (2010).

[212]T. Jabben, N. Grewe, and S. Schmitt, "Spectral properties of the two-impurity Anderson model with varying distance and various interactions", Physical Review B - Condensed Matter and Materials Physics **85**, 1–15 (2012).

[213]J. Bork, Y.-h. Zhang, L. Diekhöner, L. Borda, P. Simon, J. Kroha, P. Wahl, and K. Kern, "A tunable two-impurity Kondo system in an atomic point contact", Nature Physics **7**, 901–906 (2011).

[214]N. J. Craig, J. M. Taylor, E. A. Lester, C. M. Marcus, M. P. Hanson, and A. C. Gossard, "Tunable Nonlocal Spin Control in a Coupled-Quantum Dot System", Science **304**, 565–567 (2004).

[215]O. Sakai, and Y. Shimizu, "Excitation Spectra of the Two Impurity Anderson Model. II. Interplay between the Kondo Effect and the Inter Site Interactions", Journal of the Physical Society of Japan **61**, 2348–2358 (1992).

[216]E. Minamitani, W. A. Diño, H. Nakanishi, and H. Kasai, "Effect of antiferromagnetic RKKY interaction and magnetic field in a two-impurity Kondo system", Physical Review B - Condensed Matter and Materials Physics **82**, 1–4 (2010).

[217]E. Minamitani, W. A. Dino, H. Nakanishi, and H. Kasai, "Scanning tunneling spectroscopic evidence of crossover transition in the two-impurity Kondo problem", Surface Science **604**, 2139–2149 (2010).

[218]K. von Bergmann, M. Ternes, S. Loth, C. P. Lutz, and A. J. Heinrich, "Spin Polarization of the Split Kondo State", Physical Review Letters **114**, 1–5 (2015).

[219]S. Rachel, and M. Ezawa, "Giant magnetoresistance and perfect spin filter in silicene, germanene, and stanene", Physical Review B **89**, 195303 (2014).

[220]L. C. Lew Yan Voon, E. Sandberg, R. S. Aga, and A. A. Farajian, "Hydrogen compounds of group-IV nanosheets", Applied Physics Letters **97**, 163114 (2010).

[221]J. Lado, and J. Fernández-Rossier, "Magnetic Edge Anisotropy in Graphenelike Honeycomb Crystals", Physical Review Letters **113**, 027203 (2014).

[222]L. Li, Y. Yu, G. J. Ye, Q. Ge, X. Ou, H. Wu, D. Feng, X. H. Chen, and Y. Zhang, "Black phosphorus field-effect transistors", Nature Nanotechnology **9**, 372–377 (2014).

[223]E. S. Reich, "Phosphorene excites materials scientists.", Nature **506**, 19 (2014).

[224]P. D. Ye, H. Liu, A. T. Neal, Z. Zhu, Z. Luo, X. Xu, C. Engineering, W. Lafayette, U. States, E. Lansing, U. States, M. Engineering, W. Lafayette, and U. States, "Phosphorene : An Unexplored 2D Semiconductor with a High Hole", 4033–4041 (2014).

[225]F. Xia, H. Wang, and Y. Jia, "Rediscovering black phosphorus as an anisotropic layered material for optoelectronics and electronics.", Nature communications **5**, 4458 (2014).

[226]F. Pan, R. Quhe, Q. Ge, J. Zheng, Z. Ni, Y. Wang, Z. Gao, L. Wang, and J. Lu, "Gate-induced half-metallicity in semihydrogenated silicene", Physica E: Low-dimensional Systems and Nanostructures **56**, 43–47 (2014).

[227]J. W. Lyding, T. C. Shen, J. S. Hubacek, J. R. Tucker, and G. C. Abeln, "Nanoscale patterning and oxidation of H-passivated Si(100)-21 surfaces with an ultrahigh vacuum scanning tunneling microscope", Applied Physics Letters **64**, 2010–2012 (1994).

[228]T Shen, C Wang, G. C. Abein, J. R. Tucker, J. W. Lyding, P. Avouris, and R. E. Walkup, "Atomic-Scale Desorption Through Electronic and Vibrational Excitation Mechanisms AEyfh", Science **268**, 1590–1592 (1995).

[229] J. C. Oberg, M. R. Calvo, F. Delgado, M. Moro-Lagares, D. Serrate, D. Jacob, J. Fernández-Rossier, and C. F. Hirjibehedin, "Control of single-spin magnetic anisotropy by exchange coupling.", Nature nanotechnology **9**, 64–8 (2014).

[230] M. Corso, W. Auwärter, M. Muntwiler, A. Tamai, T. Greber, and J. Osterwalder, "Boron nitride nanomesh.", Science (New York, N.Y.) **303**, 217–20 (2004).

[231] F. Schulz, R. Drost, and S. K. Ha, "Templated Self-Assembly and Local Doping of Molecules on Epitaxial Hexagonal Boron Nitride", 11121–11128 (2013).

[232] S. Joshi, F. Bischoff, R. Koitz, D. Ecija, K. Seufert, A. P. Seitsonen, J. Hutter, K. Diller, J. I. Urgel, S. H., J. V. Barth, and W. Auwärter, "Control of Molecular Organization and Energy Control of Molecular Organization and Energy Level Alignment by an Electronically Nanopatterned Boron Nitride Template", 430–442 (2013).

[233] P. Järvinen, S. K. Hämäläinen, K. Banerjee, P. Häkkinen, M. Ijäs, A. Harju, and P. Liljeroth, "Molecular self-assembly on graphene on SiO2 and h-BN substrates", Nano Letters **13**, 3199–3204 (2013).

[234] H. Dil, J. Lobo-Checa, R. Laskowski, P. Blaha, S. Berner, J. Osterwalder, and T. Greber, "Surface trapping of atoms and molecules with dipole rings.", Science (New York, N.Y.) **319**, 1824–6 (2008).

[235] J. M. Macleod, and F. Rosei, "Molecular self-assembly on graphene", Small **10**, 1038–1049 (2014).

[236] M. Bazarnik, J. Brede, R. Decker, and R. Wiesendanger, "Tailoring molecular self-assembly of magnetic phthalocyanine molecules on fe- and co-intercalated graphene", ACS Nano **7**, 11341–11349 (2013).

[237] C. Shi, C. Wei, H. Han, G. Xingyu, Q. Dongchen, W. Yuzhan, and A. T. S. Wee, "Template-Directed Molecular Assembly Comparison Between CuPc and", **4**, 849–854 (2010).

[238] H. Huany, S. L. Wong, J. Sun, W. Chen, and A. T. S. Wee, "Trapping Single Polar Molecules in SiC", 2774–2778 (2012).